

Thèse de Doctorat

en vue de l'obtention du grade de
Docteur en Sciences pour l'Ingénieur,
Aix Marseille Université

Spécialité : Mécanique et Physique des Fluides

Institut de Recherche sur les Phénomènes Hors Équilibre (IRPHE), UMR 7342
École Doctorale 353, Sciences pour l'Ingénieur : Mécanique, Physique, Micro et
Nanoélectronique

Atomisation de jets liquides : analyse statistique en champ proche et en champ lointain

Présentée et soutenue publiquement le 09 novembre 2021
par **Romain VALLON**

Directeurs de thèse : Dr. Malek ABID Aix Marseille Université & IRPHE, Marseille
Pr. Fabien ANSELMET, Ecole Centrale Marseille & IRPHE, Marseille

Devant le jury composé de :

Pr.	Caroline NORE	Université Paris Saclay & LISN, Orsay	Présidente
Pr.	Luminita DANAILA	Université de Rouen Normandie & M2C, Rouen	Rapportrice
IR.	Séverine TOMAS (HDR)	INRAE, Montpellier	Rapportrice
Pr.	Emmanuel VILLERMAUX	Aix Marseille Université & IRPHE, Marseille	Examinateur
MCF	Malek ABID (HDR)	Aix Marseille Université & IRPHE, Marseille	Directeur
Pr.	Fabien ANSELMET	Ecole Centrale de Marseille & IRPHE, Marseille	Directeur

Institut de Recherche sur les
Phénomènes Hors Équilibre (IRPHE)
49 Rue Frédéric Joliot Curie
13013 Marseille

École doctorale 353
5 rue Enrico Fermi
13013 Marseille

Ph.D. Thesis

Submitted for the degree of
Doctor in Engineering Sciences,
Aix Marseille University

Fields : Mechanics and Physics of Fluids

Institut de Recherche sur les Phénomènes Hors Équilibre (IRPHE), UMR 7342
École Doctorale 353, Sciences pour l'Ingénieur : Mécanique, Physique, Micro et
Nanoélectronique

Liquid jet atomisation: statistical analysis in the close field and in the far field

Presented and defended in public on November 9, 2021,
by **Romain VALLON**

Ph.D. supervisors : Dr. Malek Abid, Aix Marseille Université, IRPHE, Marseille
Pr. Fabien ANSELMET, Ecole Centrale Marseille & IRPHE, Marseille

Doctoral committee:

PR.	Caroline NORE	Université Paris Saclay & LISN, Paris	Chairwoman
PR.	Luminita DANAILA	Université de Rouen Normandie & M2C, Rouen	Referee
IR.	Séverine TOMAS (HDR)	INRAE, Montpellier	Referee
PR.	Emmanuel VILLERMAUX	Aix Marseille Université, Marseille	Examiner
MCF.	Malek ABID (HDR)	Aix Marseille Université & IRPHE, Marseille	Supervisor
PR.	Fabien ANSELMET	Ecole Centrale de Marseille & IRPHE, Marseille	Supervisor

La vraie prise de risque, ou disons la prise de risque pertinente, suppose d'être relevée de tous les autres risques, en tout cas du risque matériel. [...] Si l'on veut jouer gros sur un certain front, le front de la création par exemple, il est préférable d'être un peu tranquille sur les autres.

Frédéric Lordon, *Les Figures du Communisme*, 2021

À mes grands-pères, pour leur détermination,

À mes grands-mères, pour leur dévouement,

À eux quatre, pour leur réussite.

Remerciements

En premier lieu, j’aimerais remercier mes deux directeurs de thèse, Malek Abid et Fabien Anselmet, pour m’avoir donné la possibilité de faire ce doctorat. Je les remercie tout particulièrement de m’avoir fait confiance ainsi que d’avoir su me laisser l’autonomie de mener mon projet de recherche tout en restant, quand bien même leurs enseignements occupaient une large partie de leur temps en période de pandémie, toujours disponibles pour répondre à mes questions, m’aider à surmonter certains obstacles et suivre attentivement mon travail.

Je remercie l’ensemble des membres du jury qui ont accepté de rapporter et d’examiner mes travaux. Merci à Luminita Danaila et Séverine Tomas pour la précision et le détail de leurs rapports ainsi que de leurs questions et remarques lors de la soutenance. Merci à Caroline Nore et Emmanuel Villermaux pour les discussions engagées aussi bien lors de la soutenance qu’à sa suite. Je remercie particulièrement Emmanuel Villermaux pour les discussions que nous avons également pu avoir à propos de mes travaux tout au long de ma thèse.

Je tiens à remercier chaleureusement l’ensemble du personnel et des doctorants de l’IRPHE que j’ai rencontré pendant mon séjour au laboratoire, entre autre pour leur gentillesse, leur présence – dans les hauts comme dans les bas –, leur joie de vivre, la stimulation intellectuelle régnant dans le groupe et singulièrement pour leur humour. J’adresse des remerciements particuliers à Fabien Robaux, aussi bien pour ses conseils en programmation que son compagnonnage en escalade, à Amélie Gay, pour nos longues discussions sur la turbulence et tous ses trucs et astuces marseillais, à Pierre Léard, pour ses recommandations de lectures et sa détermination, à Keshav Purseed, pour ses blagues décapantes et son engagement pédagogique, à Daphné Lemasquerier, pour son engagement scientifique et ses filouteries, à Alix Bartoli, pour nos discussions sur la fragmentation et les bons moments passés à Udine et à Montpellier, et à Sarah Christin, pour sa passion du sport et son amour de la montagne. Ses remerciements aux doctorants seraient incomplets sans mentionner les personnes, chacune d’elle impressionnante par sa personnalité, qui sont arrivées au laboratoire durant ces trois ans : Calimero (Raùl), parkour man (Rémi), Kochari dude (Ahmed), running guy (Tommi), anonyme du 2.23 (Tristan), le jeune (Lucas), der ein-zwei-drei-vier Mensch (Marc), Tornado (Quentin), M. Météo (Elliot), Djidji (Djihane), padawan (Nihal), AI guy (Sélim), le massif de l’étoile (Florian) et la vieille pince (Roman).

Je remercie bien évidemment ma mère, mon père et mon frère : ma mère pour m’avoir transmis le panache de son fourmillement d’idées, mon père pour m’avoir transmis la rigueur de sa logique, mon frère pour la force de notre fraternité et évidemment tous les trois pour leur soutien intemporel. Un grand merci aussi à mes amis, d’enfance et d’après, qu’ils aient été à Bordeaux, Paris, en Malaisie, aux États-Unis ou en Chine, pour nos espaces de décompression

et d'écoute. Un merci spécial à Julien de Troullioud de Lanversin, pour les discussions que nous avons eues ensemble à Pékin qui ont attisé ma volonté de me lancer dans un doctorat, et à la team askip, pour l'espace de réflexion et de soutien que l'on partage.

Enfin, je dédie une pensée particulière à Kim avec qui j'ai partagé quatre ans intenses dont deux ans et demi pendant ce doctorat. Je la remercie pour son esprit critique aiguisé, son soutien dans les épreuves les plus dures et son intelligence engagée. Son soutien et nos échanges ont été un repère solide et sûr dans cette aventure scientifique qui est, à ce jour, après Jiuzhaigou, le plus grand défi que j'ai relevé.

Synthèse

Introduction

Qu'est-ce que l'atomisation des jets liquides ? En première approche, l'atomisation, ou fragmentation, des jets liquides est un phénomène physique durant lequel un volume initial de liquide subit des déformations et des ruptures du fait d'instabilités hydrodynamiques ou des interactions aérodynamiques avec le milieu ambiant. Cette fragmentation génère une population de gouttes ayant chacune d'elles une taille et une vitesse donnée. La compréhension de ce phénomène reste incomplète bien qu'il joue un rôle important dans le contrôle et la compréhension de la taille des gouttes dans de nombreuses applications industrielles et naturelles.



Figure 1: Déferlement d'une vague, Vallon des Auffes, Marseille.

Du côté des applications industrielles, générer une population de gouttes homogène en taille est nécessaire afin d'optimiser l'injection dans les moteurs thermiques pour le transport terrestre (Saidur *et al.*, 2011) ou les moteurs cryogéniques pour le transport aérospatial. Pour l'irrigation agricole à l'aide d'asperseurs ou l'épandage des pesticides, les plus petites gouttes sont soumises aux courants de dérive dus au vent (Al Heidary *et al.*, 2014). Ceci induit des pertes d'eau pouvant aller jusqu'à 30% (Yazar, 1984), des pollutions indésirables des zones résidentielles environnantes (Gil & Sinfot, 2005) ou une pression croissante sur les terres arables avec l'imposition de cordons sanitaires (Hilz & Vermeer, 2013). Comprendre la création des plus petites gouttes et influencer leur taille se révèle ainsi essentiel pour limiter ces effets.

Du côté des applications naturelles, la fragmentation se trouve joliment illustrée par les embruns, par exemple lors du déferlement des vagues sur la côte, voir Fig. 1. La formation d'embruns à travers les océans joue un rôle déterminant pour les écoulements atmosphériques (Kudryavtsev & Makin, 2011), la formation des ouragans (Perrie *et al.*, 2004) et le forçage radiatif dû aux aérosols, élément clé de la physique du climat (Witek *et al.*, 2016). Autrement, la taille des gouttes produites lors d'un éternuement (Fig. 2a) détermine la nature de leur trajectoire, balistique ou brownienne, et leur durée de persistance dans l'air (Duguid, 1946; Bourouiba, 2016), deux critères cruciaux pour la propagation des maladies aéroportées comme la COVID 19 (Mittal *et al.*, 2020). La fragmentation se retrouve aussi dans le contexte de la lutte contre les incendies (Kamluk *et al.*, 2020), de l'administration de médicaments (Fig. 2b), des revêtements, de l'impression à jet d'encre ou encore de la peinture par spray. Bien que les applications soient très diverses, l'objectif reste sensiblement le même : mieux comprendre

la formation des gouttes et déterminer les paramètres contrôlant leurs tailles.

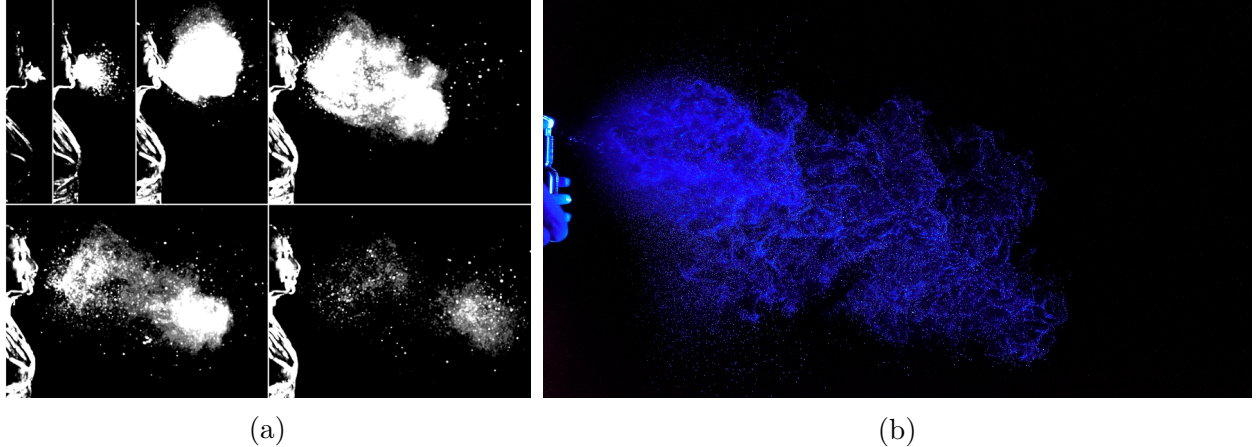


Figure 2: (a) Éternuement enregistré à 1000 images par seconde (Bourouiba *et al.*, 2014). (b) Superposition de photographies expérimentales d'un nuage de gouttelettes d'eau produit par un spray commercial de 10 centimètres de haut (Courtoisie de Lucas Rotily).

Dans ce contexte, cette thèse se concentre sur l'étude expérimentale et numérique des jets ronds afin de caractériser la population de gouttes proche et loin de la buse. L'étude expérimentale porte sur le champ lointain, à des distances de plusieurs centaines de diamètres de buse de l'injection, et reprend les données mesurées par vélocimétrie par suivi de gouttes (DTV) produites par Felis *et al.* (2020). L'étude numérique se concentre sur le champ proche, à des distances de plusieurs dizaines de diamètres de buse, et utilise les données générées par Simulations Numériques Directes (DNS) d'un écoulement diphasique à l'aide du logiciel libre Basilisk. Dans les deux cas, les configurations d'étude sont choisies telles qu'elles soient proches de celles observées pour les asperseurs utilisés en irrigation agricole. Deux théories de fragmentation de natures très différentes sont comparées dans les champs proche et lointain. La première repose sur la mécanique fine des ligaments formés lors de la fragmentation (Villermaux *et al.*, 2004; Kooij *et al.*, 2018), Sec. 1.3 et 1.5.2. La seconde repose quant à elle sur une approche statistique développée dans le cadre de la turbulence intermittente (Novikov, 1994; Novikov & Dommermuth, 1997), Sec. 1.4 et 1.5.1. Par la suite, les phases liquides et gazeuses sont indiquées par les indices l et g . Les paramètres adimensionnés gouvernant l'écoulement, Sec. 1.2.1 sont les nombres de Reynolds, de Weber et d'Ohnesorge définis tels que :

$$Re_i = \frac{\rho_i U_{inj} d_n}{\mu_i}, \quad We_i = \frac{\rho_i U_{inj}^2 d_n}{\sigma}, \quad Oh = \frac{\mu_l}{\sqrt{\rho_l \sigma d_n}} \quad (1)$$

avec d_n le diamètre de la buse d'injection, U_{inj} la vitesse d'injection, σ la tension de surface entre les deux phases, ρ_i la masse volumique de la phase i et μ_i la viscosité dynamique de la phase i . Les configurations choisies placent les jets étudiés dans le régime *second wind induced*, pour lequel $13 \leq We_g \leq 40.3$, et le régime dit d'atomisation, pour lequel $We_g \geq 40.3$, Sec. 1.2.2.

Méthodes expérimentales et numériques

L'étude expérimentale de cette thèse repose sur l'analyse approfondie des données de la phase dispersée produites par Felis *et al.* (2020). Ce dernier a réalisé une campagne de mesures simultanées du diamètre et de la vitesse des gouttes générées par un jet d'eau injecté dans l'air au repos. La configuration choisie fixe le Weber gaz à 24 et place le jet dans le régime de fragmentation *second wind induced*. Les mesures simultanées du volume et de la vitesse des gouttes ont été réalisées à l'aide de la technique de velocimétrie par suivi de gouttes par ombroscopie, Sec. 2.2. Pour la mesure du volume V , les gouttes sont supposées être des sphéroïdes. Leur diamètre équivalent est ensuite calculé tel que $d_{[30]} = \sqrt[3]{6V/\pi}$. L'ombroscopie est réalisée à l'aide d'une lumière de fond non cohérente générée par une source laser pulsée et un collimateur. Cette source lumineuse permet de projeter l'ombre de l'écoulement sur le plan de prise d'une caméra rapide qui, à chaque déclenchement, capture deux instants consécutifs. Le temps d'exposition est fixé à 4 ns et la fréquence entre deux déclenchements est fixée à 5 Hz. La durée séparant les deux instants consécutifs est choisie par rapport à la vitesse moyenne de l'écoulement dans le champ de prise, afin de capturer correctement sa dynamique, et fixée à quelques μs . Une fois les prises par ombroscopie réalisées, l'objectif est de détecter correctement les gouttes dans chaque image et de déterminer leur déplacement entre les deux instants consécutifs. Les images sont segmentées à l'aide d'un algorithme de calibration d'ombres (*shadow sizer*) développé par Felis-Carrasco (2017) et implémenté à l'aide des outils de traitement d'image de MATLAB. La procédure de calibration d'ombres est séquencée en 4 étapes : transformation en ondelettes, analyse locale de chaque objet, extraction de contour et estimation de la vitesse. Bien que cette procédure assure une bonne détection des gouttes dans le champ et hors champ, la détection des gouttes hors champ présente deux limites principales. La mesure de leur taille et la détermination de leur position dans le plan de prise 2D peuvent être biaisées. L'erreur induite lors de la mesure du diamètre $d_{[30]}$ des gouttes peut être corrigée à l'aide de la fonction de correction empirique suivante (Felis *et al.*, 2020) : $d_0/d_m = 0.9629C^{0.2166}$ avec d_0 le diamètre vrai, d_m le diamètre mesuré et C le ratio de contraste. Concernant l'erreur induite lors de la détermination de la position dans le plan de prise, et par conséquent sur la vitesse des gouttes, il est possible de mettre de côté les gouttes étant trop en avant ou en arrière du plan de prise. Ce filtrage est fait sur la valeur de profondeur de champ (*Depth Of Field, DOF*) calculé pour chaque goutte : $DOF = 0.08153d_0^{0.9321}$. Seules les gouttes telles que $DOF = DOF_{min}$ sont conservées pour l'analyse, avec DOF_{min} déterminé expérimentalement et égale à 1.61 mm. Les mesures de velocimétrie par suivi de gouttes expliquées ici sont réalisées sur 5 positions expérimentales le long de l'axe du jet, $x/d_n \in \{400, 500, 600, 700, 800\}$, avec un champ de prise de $14.73 \times 14.73\text{mm}^2$. Enfin, pour chaque position x/d_n , la dimension perpendiculaire est découpée en 5 champs de prise de 2.95 mm de hauteur. Le volume de mesure DTV est ainsi égal à $14.73 \times 2.95 \times 1.61\text{mm}^3$ pour chaque position $(x/d_n, y)$.

Pour sa part, l'étude numérique repose sur une campagne de Simulations Numériques Directes (*Direct Numerical Simulations, DNS*) réalisées à l'aide du logiciel libre Basilisk. Parmi les différentes approches numériques pour simuler les écoulements fluides, l'approche DNS est celle qui offre la meilleure approximation, Sec. 2.3.1. En effet, comparé à l'approche RANS (*Reynolds Averaged Navier Stokes*) ou LES (*Large Eddy Simulation*), les DNS ne reposent sur aucune modélisation physique, notamment pour la turbulence, et résolvent directement les équations de Navier Stokes :

$$\partial_t \rho + \nabla \cdot (\rho \mathbf{u}) = 0, \quad (2)$$

$$\rho(\partial_t \mathbf{u} + \mathbf{u} \cdot \nabla \mathbf{u}) = -\nabla p + \nabla \cdot (2\mu \mathbf{D}) + \sigma \kappa \delta_S \mathbf{n}, \quad (3)$$

avec p la pression, \mathbf{D} le tenseur de déformation, κ la courbure de l'interface, δ_S la fonction de Dirac non nulle le long de l'interface et \mathbf{n} la normale de l'interface, dirigée vers la phase gazeuse. L'approximation faite par ces simulations découle seulement de la discrétisation des équations de comportement et sa qualité dépend de la précision et de la robustesse des schémas de discrétisation choisis. En outre, les simulations DNS peuvent résoudre l'ensemble des échelles spatiales et temporelles, dans la limite des ressources de calcul disponibles. L'outil Basilisk utilisé pour la campagne de simulation est un langage haut niveau libre basé sur le langage C++ développé par S. Popinet et ses collaborateurs dans la suite du logiciel Gerris (Popinet, 2003) dont il reprend les derniers développements en les améliorant, Sec. 2.3.2. Basilisk permet de développer des solveurs d'équations aux dérivés partielles, ce qui élargit sa gamme d'application à la modélisation des tsunamis, des milieux poreux ou des écoulements multiphasiques. De plus, la versatilité de ce langage facilite l'implémentation de nouveaux solveurs pour résoudre d'autres équations aux dérivés partielles. Côté technique, Basilisk propose un spectre large de fonctions de traitement et d'automatisation, par exemple pour la gestion de la mémoire. Un avantage majeur de Basilisk par rapport à son prédecesseur Gerris est que les routines sont facilement accessibles et modifiables. En complément de sa versatilité, l'implémentation des schémas numériques et des discrétisations font de Basilisk un langage efficace en terme de temps de calcul et d'usage mémoire, notamment grâce à l'usage de grilles cartésiennes *octree*, voir le cas 2D en Fig. 3 et Sec. 2.4.2, couplées avec un raffinement adaptatif, Sec. 2.4.3.

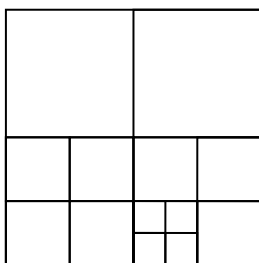


Figure 3: Exemple d'une discrétisation *quadtree*.

L'utilisation des routines de parallélisation, basée sur la librairie C++ *Message Passing Interface* (MPI), implémentées dans Basilisk permet de réduire encore le temps de calcul. Enfin, l'implémentation d'un solveur précis et adaptatif pour les écoulements à tension de surface, Sec. 2.4.4 et 2.4.5, ouvre la voie au calcul de DNS de fragmentation de jets liquides incompressibles avec Gerris (Agbaglah *et al.*, 2011) puis avec Basilisk avec les travaux de Chen *et al.* (2013) et Ling *et al.* (2017b) respectivement sur l'atomisation des jets à collision (*impinging jets*) et des jets biodiesel. Dans l'implémentation de ce solveur, les deux phases sont considérées comme composant un fluide

monophasique à viscosité et masse volumique variable, Sec. 4.2.1. Dans ce cadre, l'indicatrice de phase α est égale à 0 dans la phase gazeuse et à 1 dans la phase liquide tandis que toutes les cellules pour lesquelles $\alpha \in]0, 1[$ contiennent l'interface séparant les phases. La viscosité et la masse volumique du fluide monophasique s'expriment alors telles que $\mu = \alpha \mu_l + (1 - \alpha) \mu_g$ et $\rho = \alpha \rho_l + (1 - \alpha) \rho_g$. Dans ce contexte, l'équation de continuité, Eq. (4), peut aussi être réécrite en fonction de α telle que :

$$\partial_t \alpha + \nabla \cdot (\alpha \mathbf{u}) = 0. \quad (4)$$

Afin de calculer l'advection de l'interface, cette forme de l'équation de continuité est résolue à l'aide d'un schéma *Volume-Of-Fluid* (VOF) géométrique et linéaire par morceaux, Sec. 2.5.1. Ce type de schéma se scinde généralement en deux parties : reconstruction de l'interface et

calcul des flux géométriques le long de l’advection de l’interface. Une fois l’interface advectée, il est nécessaire de calculer le terme de tension de surface $\sigma\kappa\delta_S \mathbf{n}$ intervenant dans l’équation de conservation de quantité de mouvement, Eq. (3), ce qui est toujours un défi à ce jour (Gorokhovski & Herrmann, 2008). La résolution de ce terme dans Basilisk suit l’approche de force surfacique continue (*Continuum-Surface-Force, CSF*), Sec 2.5.2, proposée par Brackbill *et al.* (1992) pour laquelle les approximations suivantes sont faites :

$$\sigma\kappa\delta_S \mathbf{n} \approx \sigma\kappa\alpha, \quad (5)$$

$$\kappa \approx \nabla \cdot \tilde{\mathbf{n}}, \quad (6)$$

$$\tilde{\mathbf{n}} = \frac{\nabla\alpha}{\|\nabla\alpha\|}. \quad (7)$$

Cependant, cette méthode est connue pour générer de courants non physiques dans le cas de gouttes stationnaires. Afin de dépasser cette limite, deux conditions doivent être respectées. Premièrement, le calcul des gradients de pression et d’indicatrice de phase, intervenant respectivement dans les Eq. (3) et (7), doit être compatible. Cette première condition est respectée en implémentant la même procédure pour les deux gradients. Deuxièmement, l’approximation de la courbure κ de l’interface doit être constante. Cette condition dépend de la qualité de l’estimation de κ et peut être respectée à l’aide des fonctions de hauteur généralisées (*generalised height function*), Sec. 2.5.3.

Cette approche peut être complétée par l’utilisation de stencils asymétriques, voir Fig. 4, afin de capturer correctement les morceaux d’interface présentant une courbure importante tout en évitant de fixer la taille des stencils en amont de la simulation et en minimisant l’usage mémoire lors des calculs. Les fonctions de hauteur généralisées présentent toutefois deux limites. Même pour des interfaces moyennement courbées, ces fonctions peuvent générer des hauteurs inconsistantes. Leur performance s’écroule pour calculer la courbure d’une interface faiblement résolue, c-à-d lorsque le rayon de courbure est du même ordre de grandeur que la taille du maillage. Ces deux écueils peuvent être évités en conservant les hauteurs consistantes et en les utilisant pour interpoler l’interface par une parabole (2D) ou un paraboloïde (3D). La courbure peut ensuite être calculée en différenciant la fonction analytique de l’interpolation. Finalement, une fois la courbure correctement calculée et l’interface correctement advectée, l’écoulement peut évoluer, se fragmenter et générer des gouttes qu’il est possible de détecter. Cette dernière opération peut-être faite à l’aide de la routine *tag* de Basilisk, Sec. 2.5.4. À partir du champ d’indicatrice de phase α , cette routine parcourt les cellules composant la phase liquide, c-à-d pour lesquelles $\alpha \geq 10^{-6}$, et affecte un même indice aux cellules faisant partie du même voisinage, c-à-d les cellules incluses dans un volume de liquide défini par une interface. Le volume, la position du barycentre et la vitesse d’une goutte j peuvent alors être déterminés en calculant la moyenne de chaque variable pondérée par le volume des cellules ayant le même indice j .

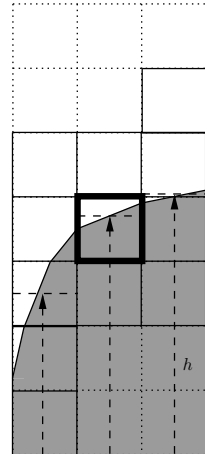


Figure 4: Schéma d’une interface avec une courbure importante capturée par un stencil asymétrique. La grille en pointillé représente un stencil symétrique de taille 3×7 . Les traits gras indiquent la cellule pour laquelle on cherche la courbure. Les flèches représentent la hauteur h .

ρ_l (kg/m ³)	ρ_g (kg/m ³)	ν_l (m ² /s)	ν_g (m ² /s)	σ (N/m)
998.3	1.205	1.004×10^{-6}	15.11×10^{-6}	0.073

Table 1: Propriétés physiques considérées par Felis *et al.* (2020) en conditions normales.

Distributions multimodales pour les jets agricoles : une analyse statistique de la population de gouttes d'un spray atomisé par pression

L'étude des jets agricoles, ou dans des configurations proches, est un défi en soi du fait de la présence d'une turbulence intense, de l'existence d'une grande variété de mécanismes de fragmentation une fois le cœur liquide pincé (Guildenbecher *et al.*, 2009) et du développement du jet sur de grandes distances, typiquement plusieurs centaines de diamètres de buse (Felis-Carrasco, 2017). La configuration dans laquelle un jet liquide est injecté dans du gaz au repos à une vitesse suffisante pour se placer dans le régime de fragmentation *second wind induced* ou d'atomisation correspond aux sprays atomisés par pression (*pressure atomised jets*). À partir des mesures expérimentales réalisées par Felis *et al.* (2020) sur un spray de cette sorte, une analyse statistique de la population de gouttes générées par la fragmentation est faite. Cette analyse met en lumière la nature multimodale des distributions en taille et en vitesse axiale des gouttes ainsi que la bonne correspondance entre les distributions en taille et la description théorique développée par Novikov & Dommermuth (1997) dans le cadre de la turbulence intermittente. Il est aussi montré que le modèle quadratique de Lee & An (2016) offre une bonne description qualitative de la ligne centrale de la distribution jointe en taille et en vitesse axiale. En outre, sur la base des propriétés des distributions marginales, cinq sous-groupes de gouttes peuvent être définis à partir de la distribution jointe, chacun des sous groupes présentant une taille et une vitesse caractéristique. Cette analyse a été publiée dans la revue *Physical Review Fluids* en février 2021, Sec. 3.2.

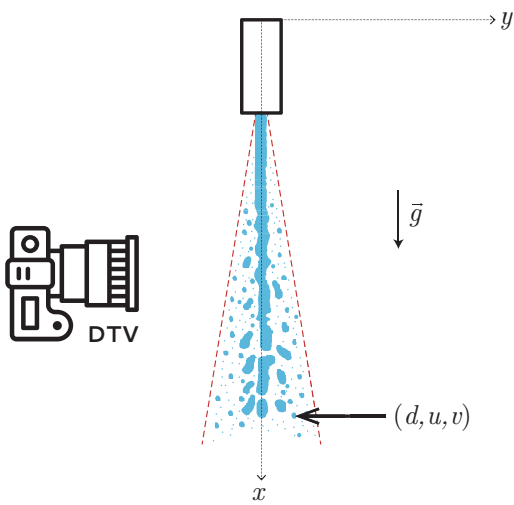


Figure 5: Schéma de l'expérience mise en place par Felis *et al.* (2020) avec \vec{g} la gravité, d le diamètre et (u, v) les vitesses axiale et transversale, suivant x et y , d'une goutte.

Le principe de l'expérience mise en place par Felis *et al.* (2020) est illustré par la Fig. 5. Dans cette expérience, la buse est circulaire de diamètre $d_n = 1.2$ mm et de longueur $L_n/d_n = 50$, ce qui assure une turbulence développée dans la conduite. La buse est orientée selon la verticale et pointe vers le bas. L'eau est injectée dans l'air à une vitesse $u_{inj} = 35$ m/s dans des conditions normales (297 K, 1 atm) et les conditions d'injection assurent qu'il n'y ait pas de cavitation dans la buse. Les propriétés physiques des phases sont résumées dans la Table 1. Pour cette configuration, les nombres adimensionnés sont tels que $Re_l = 41833$, $We_l = 20158$, $We_g = 24$ et $Oh = 0.0034$, ce qui place le jet dans le régime de fragmentation *second wind induced*.

Trois techniques de mesure sont utilisées. Une mesure par sonde optique permet d'obtenir les fractions massique et volumique moyennes de liquide. Un dispositif de vélocimétrie laser par effet Doppler (*Laser Doppler Velocimetry*, LDV) mesure séparément les

vitesses de la phase gazeuse et liquide. Enfin, la vélocimétrie par suivi de gouttes (*Droplet Tracking Velocimetry*, DTV) permet de mesurer simultanément le volume ainsi que les vitesses axiale et transversale des gouttes dans la zone dispersée du spray. Les mesures DTV sont réalisées loin de la buse : $x/d_n \in \{400, 500, 600, 700, 800\}$. Cette section présente l'analyse statistique de ce dernier jeu de mesures et met en lumière la nature multimodale de la distribution jointe en taille et vitesse ainsi que l'existence de différents sous-groupes de gouttes. Deux descriptions théoriques, de natures très différentes, de la distribution en taille des gouttes issues de la fragmentation d'un jet sont testées. La première repose sur la mécanique fine prenant place lors de la rupture des ligaments et a été proposée par Villermaux *et al.* (2004). Dans le cadre de cette description, les gouttes pouvant se fragmenter prennent une forme de ligaments du fait des interactions aérodynamiques et de la tension de surface. Les gouttes produites par la fragmentation d'un ligament présentent des tailles dont la distribution suit une loi Γ , qui est fonction de l'ordre de corrugation n du ligament (Villermaux *et al.*, 2004; Marmottant & Villermaux, 2004):

$$p(x = d/\langle d \rangle) = \frac{n^n}{\Gamma(n)} x^{n-1} e^{-nx} \quad (8)$$

Lorsque les ligaments subissant une fragmentation présentent différents diamètres, ceux-ci sont aussi Γ distribués et les gouttes issues de leur fragmentation suivent alors une loi Γ composée (Kooij *et al.*, 2018):

$$p(x = d/\langle d \rangle) = \frac{2(mn)^{(m+n)/2} x^{(m+n)/2-1}}{\Gamma(m)\Gamma(n)} \mathcal{K}_{m-n}(2\sqrt{nm}x) \quad (9)$$

La seconde description repose sur la description statistique de la turbulence intermittente. À la suite des travaux de Novikov (1990, 1994) sur l'intermittence des petites échelles de la turbulence et les distributions infiniment divisibles, Novikov & Dommermuth (1997) ont proposé une forme analytique du coefficient d'intermittence ainsi qu'une distribution en taille de gouttes pour les sprays turbulents :

$$p(y = -\ln(l/l_1)) = \frac{1}{\sqrt{2\pi}\sigma} \exp \left\{ -\frac{a}{2\sigma^2} (ay^{-1/2} - y^{1/2})^2 \right\} \quad (10)$$

où l_1 est la taille de l'élément à l'origine de la cascade, l est la taille d'un élément issu de la cascade, $a = \langle y \rangle$ et $\sigma^2 = \langle (y - a)^2 \rangle$. Dans cette description, les gouttes sont supposées suivre une cascade de fragmentation, comme la cascade de Richardson (1922), avec toute fois une correction pour prendre en compte l'intermittence de leur formation.

Concernant la description statistique de la distribution jointe en taille et vitesse axiale des gouttes à $x/d_n = O(100)$, l'approche intégrale de Lee & An (2016) dérivée dans le contexte de la combustion et proche de la buse, $x/d_n = O(10)$, est testée. Cette approche permet d'obtenir une formule quadratique du diamètre moyen de Sauter¹ $d_{[32]}$ en fonction de la vitesse des gouttes en faisant deux hypothèses. Premièrement, la phase liquide est supposée être complètement fragmentée. Deuxièmement, d'une manière similaire aux développements de Tennekes & Lumley (1972), le terme de dissipation visqueuse est supposé pouvoir être exprimé comme le ratio de la vitesse et du diamètre $d_{[32]}$ des gouttes. Il reste alors un paramètre libre K et la relation quadratique s'écrit telle que :

¹Celui-ci représente le diamètre d'une sphère ayant le même rapport volume / surface que la goutte d'intérêt.

$$d_{[32]} = \frac{3\sigma + \sqrt{9\sigma^2 + K\rho_l\mu_l\bar{u}\frac{u_{inj}^2 - \bar{u}^2}{2}}}{\rho_l\frac{u_{inj}^2 - \bar{u}^2}{2}} \quad (11)$$

Celle-ci offre une bonne description de la ligne centrale des distributions jointes obtenues pour des sprays atomisés par pression (*pressure atomised sprays*) avec et sans rotation.

Pour chaque position axiale, les mesures DTV ont été réalisées sur plusieurs positions transversales, $y/d_n \in [-20, 20]$ pour $x/d_n = 400$ et $y/d_n \in [-32, 32]$ pour $x/d_n = 800$. Dans la suite, les statistiques données à une position x/d_n agrègent l'ensemble des positions transversales y/d_n , sauf mention contraire. Par souci de clarté, la PDF en nombre d'une variable quelconque ζ est dénotée \mathcal{P}_ζ . En outre, entre la moyenne algébrique et la moyenne pondérée en volume, la seconde est retenue et a pour expression $\langle \zeta \rangle_V = \sum_{i=1}^{N_{tot}} V_i \zeta_i / \sum_{i=1}^{N_{tot}} V_i$ avec N_{tot} le nombre total de gouttes, i l'indice d'une goutte, V_i son volume et ζ_i la valeur de ζ pour cette goutte. La Fig. 6 donne les distributions $\mathcal{P}_{d/\langle d \rangle_V}$, $\mathcal{P}_{u/\langle u \rangle_V}$ et $\mathcal{P}_{v/\langle u \rangle_V}$. Étant donné que la vitesse transversale v est à moyenne nulle du fait de la symétrie de l'écoulement, elle est normalisée par la moyenne de la vitesse axiale u .

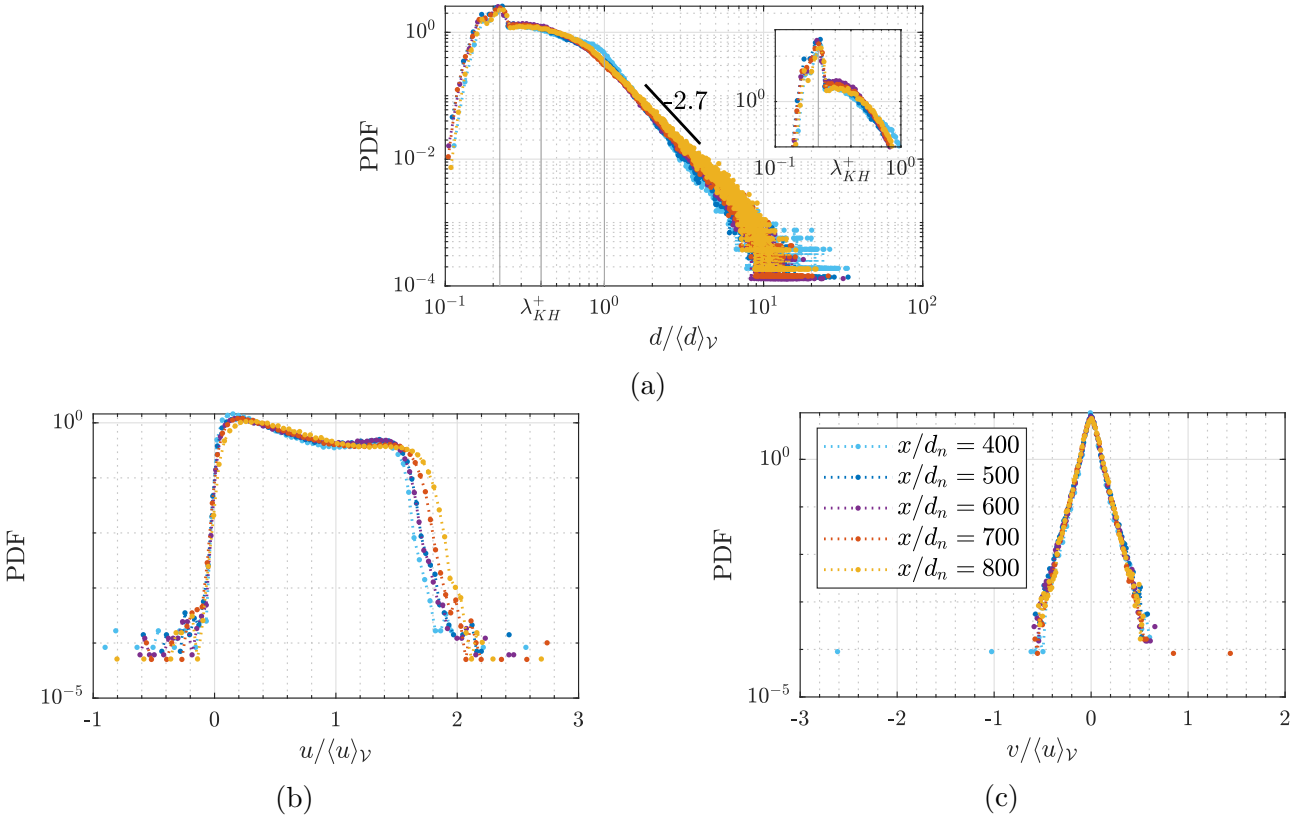


Figure 6: Distributions de (a) $d/\langle d \rangle_V$, (b) $u/\langle u \rangle_V$ et (c) $v/\langle u \rangle_V$ pour les données DTV de Felis *et al.* (2020). La distribution en taille est donnée en échelle logarithmique et les distributions en vitesse en échelle semi logarithmique.

La distribution $\mathcal{P}_{d/\langle d \rangle_V}$ présente un skewness et un kurtosis importants. Le premier diminue avec x/d_n de 10 à 5 et le second diminue de 155 à environ 35. De telles valeurs reflètent le fait que la distribution s'étend sur deux décades, $d/\langle d \rangle_V \in [0.1, 40]$, et que la majorité des tailles

sont contenues dans la première décade, ce qui est corroboré par la médiane de $d/\langle d \rangle_V$ égale à 0.51 en moyenne. En outre, la déviation standard est constante selon x/d_n . Elle est égale à 0.93 en moyenne, caractéristique d'une concentration importante des données. En outre, $\langle d \rangle_V$ est compris entre 121.7 et 129.3 μm pour les cinq positions expérimentales. Du côté des grandes tailles, la décroissance de la distribution suit une loi d'échelle $(d/\langle d \rangle_V)^{-2.7}$, ce qui diffère de la décroissance exponentielle déterminée par Simmons (1977). De plus, deux modes sont visibles à chaque position x/d_n , $d/\langle d \rangle_V \in \{0.2, 0.4\}$. À $x/d_n = 400$, un troisième mode est visible pour $d/\langle d \rangle_V = 1$. Le deuxième correspond à l'échelle caractéristique de l'instabilité de Kelvin Helmholtz (Hoyt & Taylor, 1977) : $\lambda_{KH} = \sigma/\rho_g u_{inj}^2 = d_n/We_g = 49.6 \mu\text{m}$, notée λ_{KH}^+ une fois normalisée par $\langle d \rangle_V$ et $\lambda_{KH}^+ \approx 0.4$. La distribution $\mathcal{P}_{u/\langle u \rangle_V}$ présente aussi deux modes pour tous les x/d_n , $u/\langle u \rangle_V \in \{0.2, 1.4\}$. Mise à part une légère différence pour la décroissance vers les grandes tailles, les cinq distributions montrent une bonne similarité. Cette fois, les valeurs du skewness et du kurtosis sont quasiment constantes et faibles comparées à celles de $\mathcal{P}_{d/\langle d \rangle_V}$, respectivement égales en moyenne à 0.58 et 2.14. La première s'explique par la légère dissymétrie de la distribution due à la prédominance du mode de basse vitesse. La seconde s'explique par la faible longueur du domaine de définition, du fait des conditions aux limites sur la vitesse des gouttes. En effet, le jet est globalement advecté vers les grands x/d_n , $u/\langle u \rangle_V \geq 0$, et, à x/d_n fixé, il existe un maximum de vitesse au niveau du centre du jet, $u/\langle u \rangle_V \leq U_{inj}/\langle u \rangle_V$. Enfin, les valeurs du skewness et du kurtosis diffèrent des valeurs d'un jet monophasique, -0.5 et 2.8, qui ont des distributions quasi gaussiennes. Ici, la distribution a une dissymétrie inversée et un étalement plus faible. La distribution $\mathcal{P}_{v/\langle u \rangle_V}$ présente quant à elle un seul mode pour $v/\langle u \rangle_V = 0$ et est symétrique avec un skewness égal à -0.05 en moyenne. Son kurtosis diminue avec x/d_n et est égal à 9.39 en moyenne, caractérisant une grande dispersion des ailes de la distribution et un écart important avec la distribution gaussienne. Cette distribution se comporte d'une manière plus classique que les deux distributions précédentes et est similaire à celles de la littérature de la turbulence.

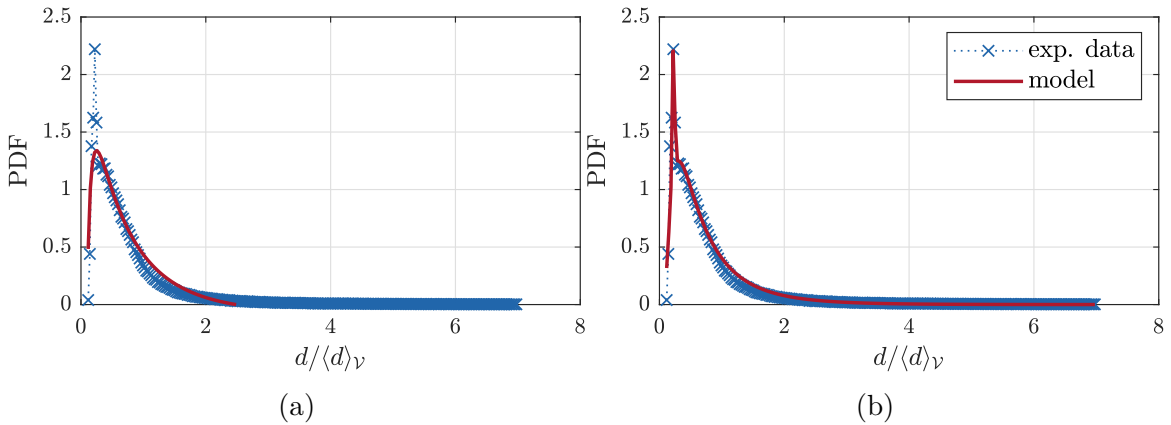


Figure 7: Ajustement de la distribution expérimentale $\mathcal{P}_{d/\langle d \rangle_V}$ à $x/d_n = 800$ par (a) la distribution de Kooij *et al.* (2018), Eq. (9), et par (b) celle de Novikov & Dommermuth (1997), Eq. (10).

Les deux descriptions théoriques de la distribution en taille sont testées sur les données expérimentales. Celles-ci montrant deux modes, la fonction d'ajustement choisie dans chaque cas est une combinaison linéaire de deux fonctions de référence. La Fig. 7 montre le résultat obtenu pour la distribution dérivée par Kooij *et al.* (2018) et Novikov & Dommermuth (1997) à

l’issue de la campagne systématique de test d’ajustement. Ici, l’accent est mis sur la région des modes, c-à-d des petites tailles. Ainsi, les ajustements sont testés par rapport à la distribution expérimentale pour $d/\langle d \rangle_V \leq 7$ et sont calculés en mode linéaire. Leur performance est mesurée par le carré du coefficient de corrélation, r^2 . Entre les deux fonctions d’ajustement, celle de Kooij *et al.* (2018) échoue systématiquement à capturer le pic à $d/\langle d \rangle_V \approx 0.2$ bien que $r^2 = 1.04$, contrairement à celle de Novikov & Dommermuth (1997) qui capture le pic et pour laquelle $r^2 = 0.97$. Cette dernière capture correctement la distribution expérimentale pour les cinq positions x/d_n .

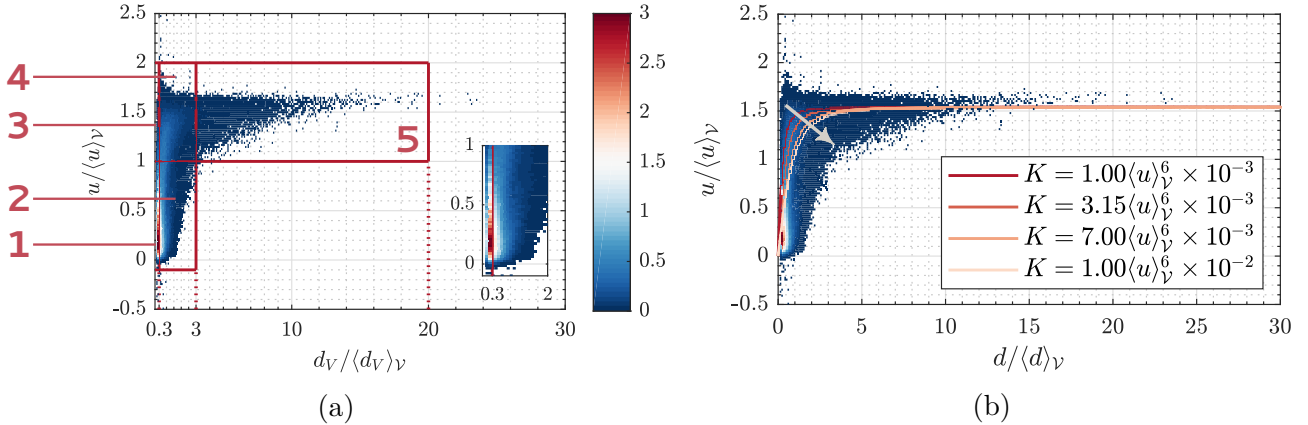


Figure 8: Distribution jointe en taille et en vitesse axiale à $x/d_n = 600$ avec (a) les sous-groupes de gouttes définis par les caractéristiques des distributions marginales et (b) l’ajustement de la ligne centrale par la fonction de Lee & An (2016).

Les distributions $\mathcal{P}_{d/\langle d \rangle_V}$ et $\mathcal{P}_{u/\langle u \rangle_V}$ sont toutes deux bimodales. Afin de connaître comment les modes sont corrélés, il est judicieux d’étudier la distribution jointe en taille et en vitesse axiale, donné par la Fig. 8 à $x/d_n = 600$. Deux tendances principales se détachent : les petites tailles montrent une dispersion importante en vitesse tandis que la dispersion en vitesse est beaucoup plus faible pour les grandes tailles, qui atteignent une asymptote en vitesse. De plus, il est possible d’observer un «chemin» de probabilités relativement larges liant ces deux régions. Sachant que chaque mode en taille et en vitesse est potentiellement marqueur de comportements physiques différents, reporter les caractéristiques de $\mathcal{P}_{d/\langle d \rangle_V}$ et $\mathcal{P}_{u/\langle u \rangle_V}$ sur la distribution jointe pourrait permettre de définir des sous-groupes de gouttes soumis à ces différents comportements. Les caractéristiques en question sont les domaines de définition de chaque distribution marginale, leur dispersion et les limites entre les modes. Prenons l’exemple à $x/d_n = 600$ donné par la Fig. 8a. Les domaines de définition délimitent directement les bords extérieurs des sous-groupes : $d/\langle d \rangle_V \in [0, 20]$ et $u/\langle u \rangle_V \in [-0.1, 2]$. La limite entre les modes de vitesse est fixée à $u/\langle u \rangle_V = 1$ et celle entre les modes de tailles à $d/\langle d \rangle_V = 0.3$. En complément, la séparation entre les deux modes en taille et la queue de la distribution est fixée à $3\sigma_d \approx 3$ où σ_d est la déviation standard de la distribution en taille. Les gouttes dont les tailles sont comprises entre 0 et $3\sigma_d$ représentent 96% du total de la distribution, une valeur proche de celle d’une distribution gaussienne. Ces délimitations font ainsi ressortir l’existence de 5 sous-groupes de gouttes dont le nombre de Stokes St , la répartition en nombre et en volume sont donnés dans la Table 2. Le nombre de Stokes est calculé avec la formule de Ferrand *et al.* (2003).

L’expression analytique de la ligne centrale de la distribution jointe proposée par Lee & An

(2016) dans le contexte de la combustion doit être légèrement adaptée. En effet, au lieu de considérer la vitesse d'injection, il est nécessaire d'utiliser une autre vitesse de référence pour capturer la tendance expérimentale loin de la buse : la vitesse du jet sur son axe. La Fig. 8b compare la distribution jointe expérimentale et l'ajustement obtenu avec l'expression de Lee & An (2016). Cette dernière offre une bonne description qualitative pour plusieurs valeurs du paramètre libre K . Le choix de K peut être affiné en comparant la distribution expérimentale en taille et celle reconstruite à partir de l'expression de la ligne centrale. De la sorte, on obtient $K = 7\langle u \rangle_V^6 \times 10^{-3}$.

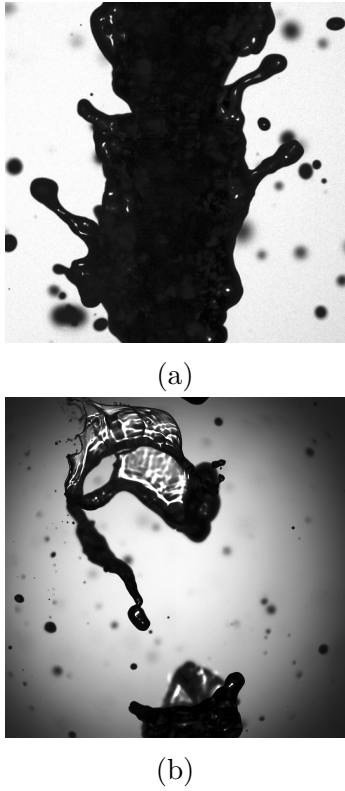


Figure 9: Photographie expérimentale (a) de ligaments le long du cœur liquide ($3d_n \times 3d_n$) et (b) d'une rupture par sac ($12d_n \times 12d_n$) dans la zone dispersée (Felis-Carrasco, 2017).

Pour finir, il est possible de s'intéresser au transfert de volume entre les sous-groupes en les associant aux différents mécanismes de fragmentation, Sec. 3.3.1. En effet, étant donné que chaque sous-groupe est associé à une vitesse et une taille moyenne, il est légitime de considérer que les gouttes perçoivent une physique différente ou sont issues de mécanismes de fragmentation différents. Les deux mécanismes de fragmentation observés expérimentalement dans le spray sont la rupture ligamentaire et la rupture par sac (*bag breakup*). La seconde fragmentation se produit sur des gouttes de grande taille ayant une vitesse importante qui prennent la forme d'un sac avec un bourrelet au niveau de l'ouverture. Une fois la goutte déformée, la fragmentation de ces gouttes se déroule en deux temps : perçage et fragmentation de l'enveloppe puis fragmentation du bourrelet toroïdal. La Fig. 9 illustre ces deux mécanismes de fragmentation. Le sous-groupe 5 contenant les gouttes les plus grandes et les plus rapides, il peut être vu comme un réservoir de liquide qui se déverse dans les autres sous-groupes. On peut conjecturer que ces gouttes subissent des ruptures par sac. D'après Rimbert & Castanet (2011), les gouttes produites par la rupture de l'enveloppe sont bien plus petites que celles produites par le bourrelet. Dans un second temps, il est possible de conjecturer que les nouvelles gouttes produites ont la même vitesse que la goutte qui se fragmente. Les gouttes produites par *bag breakup* se situent alors dans les sous groupes 3 et 4 en fonction de leur taille. Celles

#	$u/\langle u \rangle_V$	$d\langle d \rangle_V$	volume (%)	nombre (%)	St
1	$[0, 1]$	$[0, 0.3]$	$\mathcal{O}(10^{-2})$	25.2	0.83
2	$[0, 1]$	$[0.3, 3]$	3.69	48.8	7.92
3	$[1, 2]$	$[0, 0.3]$	$\mathcal{O}(10^{-3})$	1.20	0.39
4	$[1, 2]$	$[0.3, 3]$	10.8	22.2	7.61
5	$[1, 2]$	$[3, 20]$	85.5	2.55	44.0

Table 2: Répartition des sous-groupes en volume et en nombre de gouttes et leur nombre de Stokes (Ferrand *et al.*, 2003) pour la distribution jointe à $x/d_n = 600$.

du sous-groupe 3 ne subissent plus de fragmentation mais ralentissent et se retrouvent alors dans le sous-groupe 1. Les gouttes du sous-groupe 4 sont ralenties et se fragmentent par rupture ligamentaire. En fonction de la taille et de la vitesse de la goutte de ce sous-groupe, les nouveaux éléments produits se retrouveront dans les sous-groupes 1 ou 2. En complément, il est possible de regarder les distributions en taille de chaque sous-groupe, Sec. 3.3.2. Celles des sous-groupes 2, 4 et 5 montrent une décroissance exponentielle correspondant à l'argument de *random stripping* de Villermaux (2020) et indiquent que la décroissance en $(d/\langle d \rangle_V)^{-2.7}$ observée en Fig. 6a est une composition de ces décroissances exponentielles.

La dépendance de la fragmentation des jets au nombre de Weber : Simulations Numériques Directes

Les écoulements de fragmentation à grands nombres de Reynolds et de Weber présentent une grande diversité d'échelles et d'objets dont la dynamique est en partie fixée par la tension de surface et les caractéristiques de la turbulence, ce qui rend ces écoulements complexes. Réaliser des Simulations Numériques Directes (*Direct Numerical Simulations*, DNS) de ces écoulements requiert de résoudre les équations de Navier Stokes en incluant la tension de surface, Eq. (2) et Eq. (3), pour l'injection d'une phase dense dans une phase légère, Sec. 4.2.1. Une résolution fine de l'interface est cruciale et peut être obtenue à l'aide d'une utilisation optimisée des ressources de calcul, notamment grâce aux maillages adaptatifs, Sec. 4.2.2. Les phases sont dénotées par l'indice $i \in \{1, 2\}$, respectivement dense et légère. La phase 1 correspond au liquide et est injectée par une buse de diamètre d_n dans la phase 2 qui correspond au gaz au repos. L'objectif est de simuler la fragmentation d'un jet rond dans des configurations proches de la configuration expérimentale de Felis *et al.* (2020), en ciblant les régimes de fragmentation *second wind induced*, $We_2 \in [13, 40.3]$ et d'atomisation, $We_2 \geq 40.3$. Afin de compléter l'étude expérimentale de Felis *et al.* (2020) qui porte sur le champ lointain, $x/d_n \geq 400$, l'étude numérique se concentre sur le champ proche de la buse, jusqu'à $x/d_n \approx 28$. Étant donné que la simulation d'un jet d'eau dans l'air est trop gourmande en ressources informatiques, il est nécessaire de déterminer d'autres valeurs des paramètres physiques permettant de réaliser des simulations dans des temps raisonnables et en respectant les conditions sur les nombres adimensionnels définissant les régimes de fragmentation. En complément, la fragmentation peut être accélérée en excitant le mode le plus instable du jet. Cette section présente le choix des paramètres physiques et la détermination du mode le plus instable avant d'analyser les données. L'analyse des données et la comparaison des simulations, entre elles et avec l'expérience, est faite en trois temps : statistiques des gouttes, statistiques jointes en taille et en vitesse et reformulation dans l'espace des phases (Re_p, Oh_p), où Re_p et Oh_p sont basés sur le diamètre d'une particule et sa vitesse relative par rapport au gaz.

Le domaine est une boîte cubique de longueur $L_x = 28 d_n$. Un jet rond de liquide est injecté à une vitesse moyenne U_{inj} dans du gaz au repos le long de l'axe x à travers un disque de longueur l_x et de diamètre d_n , dénommé «buse» par la suite. Un signal sinusoïdal est imposé à l'injection pour exciter l'instabilité de Kelvin Helmholtz et accélérer la fragmentation. La vitesse d'injection est alors telle que $u_{inj} = U_{inj}(1 + A \sin(2\pi f t))$, $(A, f) \in \mathbb{R}^2$. Le temps d'advection est tel que $T_a = d_n/U_{inj}$. Pour simuler des configurations proches de la configuration expérimentale, les valeurs des paramètres physiques sont adaptées, Sec. 4.2.3. Par exemple, un écoulement avec un rapport de densité de l'ordre de 10^3 serait très coûteux, voire inaccessible.

ρ_1 (kg/m ³)	ρ_2 (kg/m ³)	ν_1 (m ² /s)	ν_2 (m ² /s)	σ (N/m)	d_n (m)	Oh
1	1/55	10^{-6}	10^{-6}	10^{-5}	4.48×10^{-3}	4.725×10^{-3}

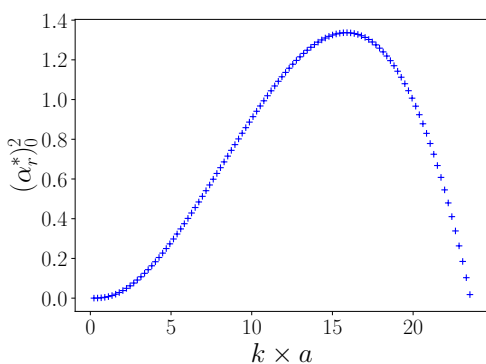
Table 3: Paramètres fixes et nombre d’Ohnesorge correspondant.

DNS	1	2	3	4	5	6	7	8	9	10
U_{inj} (m/s)	1.357	1.567	1.787	1.919	2.073	2.216	3.0	3.5	4.0	4.5
We_2 ($\times 10^1$)	1.5	2.0	2.6	3.0	3.5	4.0	7.33	9.98	13.03	16.5
Re_1 ($\times 10^3$)	6.1	7.0	8.0	8.6	9.3	10.0	13.4	15.7	17.9	20.2

Table 4: Vitesses d’injection et nombres de Weber gaz et de Reynolds liquide correspondants.

Les contraintes numériques imposent $\rho_1/\rho_2 \leq 100$, $\max(Re) = O(10^4)$ et $\sigma = O(10^{-5})$ N/m, respectivement dénotées \mathcal{C}_0 , \mathcal{C}_1 et \mathcal{C}_2 . De plus, l’attention est portée sur l’obtention de nombres adimensionnels proches des valeurs expérimentales, même si les paramètres physiques sont très différents. Afin de simuler une fragmentation dans les régimes *second wind induced* et d’atomisation, We_2 est respectivement tel que $We_2 \in [13, 40.3]$ et $We_2 \geq 40.3$, ce qui fait une contrainte supplémentaire \mathcal{C}_3 . En complément des régimes de fragmentation, reproduire des déformations de gouttes, définies par Oh , similaires à l’expérience est intéressant, soit \mathcal{C}_4 : $Oh = O(10^{-3})$. Du côté du rapport de viscosité, reproduire la valeur expérimentale $\nu_2/\nu_1 = 15$ ralentirait le processus de fragmentation, ce qui va à l’encontre de l’optimisation des ressources de calcul. À la place, il est possible de conserver le rapport des viscosités dynamiques $\mu_1/\mu_2 = (\rho_1\nu_1)/(\rho_2\nu_2) = Ca_1/Ca_2$ où $\rho_i\nu_id_n$ est homogène à un débit massique et Ca_i dénote le nombre capillaire de la phase i . Expérimentalement, $\mu_1/\mu_2 = 55$, ce qui impose la dernière contrainte physique \mathcal{C}_5 . La liste des contraintes est telle que :

$$\left\{ \begin{array}{l} \mathcal{C}_0 : \rho_1/\rho_2 < 100 \\ \mathcal{C}_1 : \max(Re) = O(10^4) \end{array} \right. , \quad \left\{ \begin{array}{l} \mathcal{C}_2 : \sigma = O(10^{-5}) \text{ N/m} \\ \mathcal{C}_3 : We_2 \geq 13 \end{array} \right. , \quad \left\{ \begin{array}{l} \mathcal{C}_4 : Oh = O(10^{-3}) \\ \mathcal{C}_5 : \rho_1\nu_1/\rho_2\nu_2 = 55 \end{array} \right. . \quad (12)$$

Figure 10: Taux de croissance temporel normalisé (α_r^*)₀ pour $U_{inj} = 3.0$ m/s avec $a = d_n$.

intéressant de déclencher l’instabilité de Kelvin Helmholtz en excitant le mode axisymétrique

Une fois ceci posé, les paramètres ρ_1 , ρ_2 , ν_1 , σ , U_{inj} et d_n sont libres. La géométrie est fixée pour les différentes simulations et seule U_{inj} varie. La table 3 donne les valeurs des paramètres fixes et la table 4 les valeurs des vitesses d’injection choisies et les nombres de Weber gaz et de Reynolds liquide correspondants.

Le nombre d’Ohnesorge étant constant pour les 10 DNS, le nombre de Weber critique pour lequel la fragmentation d’une goutte se déclenche est fixe (Hinze, 1955) et les régimes de fragmentation des gouttes durant l’atomisation secondaire sont définis sur la même gamme de Weber gaz (Faeth *et al.*, 1995). Afin d’accélérer la fragmentation, il est

le plus instable du jet, Sec. 4.2.4. Les travaux de Yang (1992) permettent de calculer le taux de croissance temporel en fonction de la fréquence des modes de déformation d'un jet. La fréquence du mode le plus instable correspond au taux de croissance maximum et est notée f . La fig 10 illustre l'évolution du taux de croissance temporel normalisé $(\alpha_r^*)_0^2$ du mode axi-symétrique d'un jet rond en fonction de son nombre d'onde. La fréquence du mode le plus instable est déterminée pour chaque vitesse d'injection.

La configuration numérique et les performances des calculs sont données dans la Sec. 4.2.5. Le niveau de raffinement du maillage est fixé à 12, ce qui donne une taille de cellule minimale telle que $\Delta_{min} = L_x/2^{12} = 30.5 \mu\text{m}$ et $d_n/\Delta_{min} = 146.8$. Par conséquent, les gouttes les plus petites ayant un sens physique ont un volume V tel que $V \geq \Delta_{min}^3$. Cette limite impose un diamètre minimum pour les gouttes $d_{min} = \sqrt[3]{6/\pi}\Delta_{min} \approx 37.8 \mu\text{m}$, soit environ 3 fois le diamètre minimum obtenu expérimentalement (Vallon *et al.*, 2021). Le pas de temps est fixé par la condition CFL avec le nombre de Courant égal à 0.8. 431 256 heures scalaires ont été nécessaires pour calculer les 10 simulations. Les DNS 3 à 10 ont nécessité 50 400 heures chacune et les DNS 1 et 2 uniquement 12 600 et 15 456 heures. Toutes les DNS ont été calculées sur le supercalculateur Occigen du Centre Informatique National de l'Enseignement Supérieur (CINES).

La stationnarité de l'écoulement est démontrée par l'étude de l'énergie cinétique turbulente, Sec. 4.3.1. L'étude de l'interface du jet permet de comparer le développement du mode instable et du front du jet pour les 10 DNS, Sec. 4.3.2. Les moments statistiques des populations de gouttes générées par les DNS sont analysés et comparés en Sec. 4.3.3. Parmi eux, l'évolution temporelle du moment d'ordre 0, c-à-d le nombre total d'éléments N_{tot} , est illustré pour chaque DNS en Fig 11a. Avant toute chose, il est à noter que moins de 1000 gouttes sont produites dans les DNS 1 et 2, ce qui est insuffisant pour étudier les statistiques de ces deux populations. Ces deux DNS sont ainsi mises de côté par la suite. A contrario, le nombre de gouttes générées pour les DNS 3 à 10 est suffisant pour faire une étude statistique. L'évolution de N_{tot} se distingue pour les deux régimes de fragmentation du jet, *second wind induced* et d'atomisation, avec $N_{tot} = O(10^3)$ et $N_{tot} = O(10^4)$ respectivement. Cependant, ces évolutions collaborent une fois le nombre de gouttes normalisé par $We_2^{1.8}$ et tendent vers $N_{tot}We_2^{-1.8} = 6$.

Une fois les moments statistiques étudiés, il est possible de passer à l'étude des distributions des tailles et des vitesses, Sec. 4.3.4. Comme précédemment, la distribution d'une variable ζ est dénotée \mathcal{P}_ζ et les distributions des variables normalisées par leur moyenne sont étudiées. Du fait de la symétrie de l'écoulement, $\langle u_y \rangle \approx 0$ et $\langle u_x \rangle$ est utilisé pour normaliser la vitesse transversale u_y . La Fig 11 donne les distributions de $d/\langle d \rangle$, $u_x/\langle u_x \rangle$ et de $u_y/\langle u_x \rangle$ à $t/T_a = 15$. $\mathcal{P}_{u_y/\langle u_x \rangle}$ collapse pour les deux régimes de fragmentation tandis que $\mathcal{P}_{d/\langle d \rangle}$ et $\mathcal{P}_{u_x/\langle u_x \rangle}$ montrent un collapse différent pour chacun des régimes. Les ailes de $\mathcal{P}_{u_y/\langle u_x \rangle}$ suivent une loi exponentielle de coefficient ± 3 en régime *second wind induced* et de coefficient ± 6 en régime d'atomisation. La différence entre ces deux coefficients, et par conséquent l'épaisseur des ailes entre les deux régimes, peut s'expliquer par l'augmentation du cisaillement entre les deux phases avec l'augmentation de We_2 . $\mathcal{P}_{d/\langle d \rangle}$ présente des modes très différents entre les deux régimes. Pour le régime d'atomisation, un seul mode existe, $d/\langle d \rangle = 0.5$, tandis qu'il en existe 3 pour le second régime, $d/\langle d \rangle \in \{0.2, 1, 2\}$. Bien que le mode principal semble translaté vers les petits $d/\langle d \rangle$ lorsque We_2 augmente, il correspond à la même gamme de tailles, $d \in [47, 58] \mu\text{m}$. Dans le régime d'atomisation, la distribution décroît en suivant une loi puissance de coefficient -2.7 , identiquement à la distribution expérimentale (Vallon *et al.*, 2021), ce qui va à l'encontre de la décroissance en loi exponentielle observée expérimentalement par Simmons (1977). Le passage

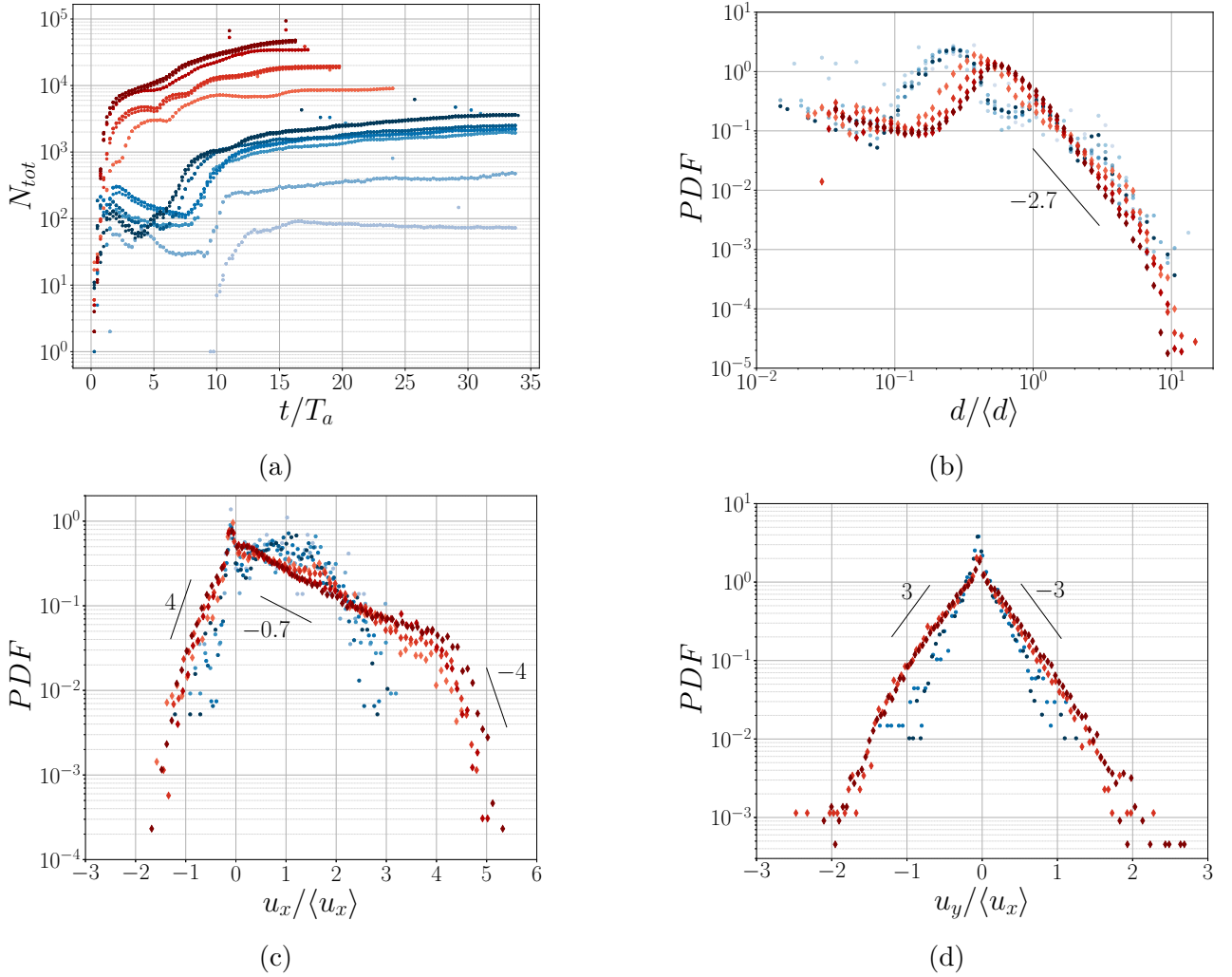


Figure 11: (a) Évolution temporelle du nombre de gouttes et distributions numériques (b) des tailles $d/\langle d \rangle$, (c) des vitesses axiales $u_x/\langle u_x \rangle$ et (d) des vitesses transversales $u_y/\langle u_x \rangle$ à $t/T_a = 15$. Les DNS dans le régime *second wind induced* sont indiquées par les points bleus et celles dans le régime d'atomisation par losanges rouges.

en échelle loglog indique l'existence de deux décroissances exponentielles avec une transition entre les deux suivant $(d/\langle d \rangle)^{-2.7}$, ce qui permet de retrouver le résultat de la littérature. En outre, les distributions théoriques en taille, Eq (8) à (10), sont testées, Sec. 4.3.5. Il ressort que, sur les données disponibles, la distribution de Kooij *et al.* (2018) offre la meilleure description quantitative tandis que celle de Novikov & Dommermuth (1997) offre une meilleure description qualitative. $\mathcal{P}_{u_x/\langle u_x \rangle}$ montre des spécificités inattendues. En fragmentation des jets, la vitesse axiale des gouttes est positive, le spray étant globalement advecté vers les x/d_n croissants, et inférieure à U_{inj} . Ici, la distribution présente un pic pour $u_x/\langle u_x \rangle = 0$ et des probabilités non négligeables pour $u_x/\langle u_x \rangle \in [-2, 0]$. Dans le régime *second wind induced*, la distribution est centrée sur $u_x/\langle u_x \rangle = 1$. En outre, l'aile droite de la distribution correspond à des vitesses supérieures à U_{inj} . Par exemple, pour la DNS 6 où $We_2 = 40$, $\mathcal{P}(u_x/\langle u_x \rangle \in [2, 3]) \geq 0$. Or $\langle u_x \rangle \approx 1 \text{ m/s}$ soit $\langle u_x \rangle \approx 0.5 \times U_{inj}$, donc $\mathcal{P}(u_x/U_{inj} \in [1, 1.5]) \geq 0$. Concernant les ailes de la distribution, celles-ci suivent une loi exponentielle de même coefficient, ± 4 , dans le régime

d'atomisation mais de coefficients différents, 7 et -2.5, dans le régime *second wind induced*. Les vitesses négatives et supérieures à U_{inj} correspondent principalement aux gouttes localisées dans la zone de recirculation, derrière le front du jet. Les développements de Saffman (1992) sur les anneaux de vorticité permettent de quantifier la vitesse de rotation de la recirculation et par conséquent d'expliquer ces vitesses de gouttes particulières, Sec. 4.4.1.

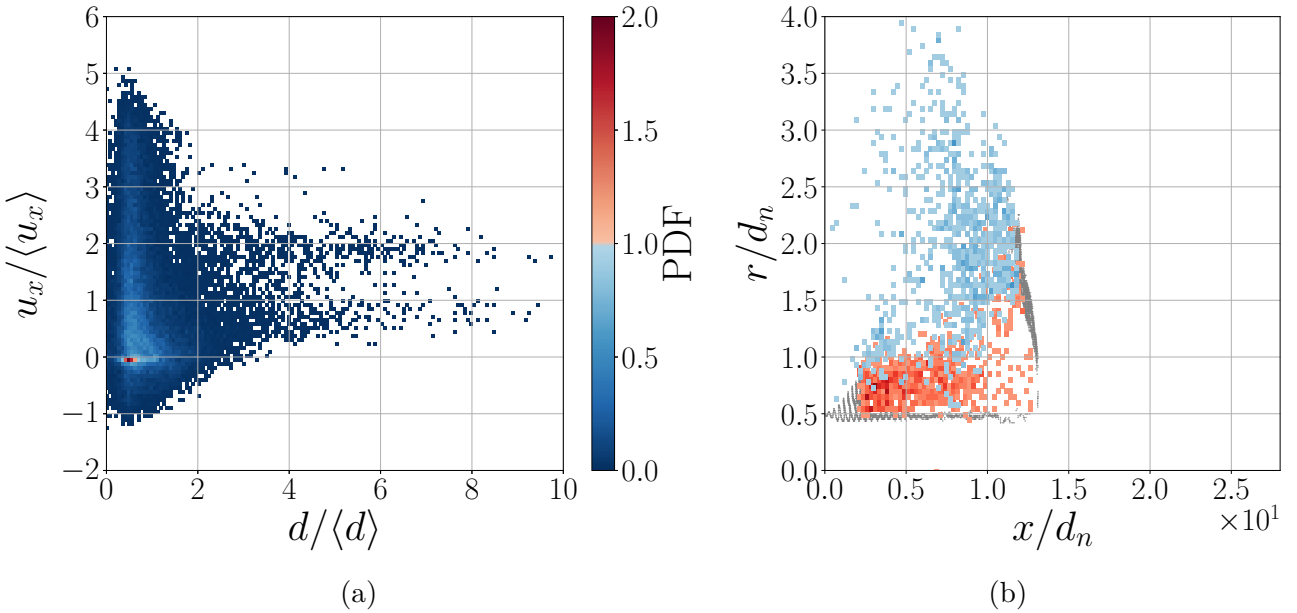


Figure 12: (a) Distribution jointe en taille et vitesse axiale pour $We_2 = 130.3$ (DNS 9) à $t/T_a = 15$ et (b) évolution spatiale des probabilités $\mathcal{P}(d/d_n \geq 0.075, u_x/U_{inj}) \leq 0.4$ (bleu) et $\mathcal{P}(d/d_n \geq 0.075, u_x/U_{inj}) \geq 0.4$ (rouge) pour $We_2 = 99.8$ (DNS 8) à $t/T_a = 15$ en coordonnées cylindriques. Pour ce dernier, les probabilités sont intégrées le long de la direction orthoradiale θ et le contour gris représente l'interface moyenne du jet, voir Sec. 4.3.2.

Une fois les spécificités de $\mathcal{P}_{u_x/\langle u_x \rangle}$ expliquées, il est intéressant de regarder les distributions jointes en taille et en vitesse axiale, Sec. 4.4.2. La Fig. 12a donne la distribution jointe pour $We_2 = 130.3$ à $t/T_a = 15$. Contrairement à l'expérience, Fig. 8, la distribution jointe est moins régulière. Les excursions de la distribution jointe vers les vitesses négatives et les grandes valeurs de vitesses ont été expliquées précédemment. En revanche, là où l'expérience ne montre qu'une asymptote vers les grandes tailles, il existe deux asymptotes pour les données numériques, ce qui est à expliquer. Ces deux asymptotes sont observables pour toutes les DNS du régime d'atomisation, existent pour $d/d_n \geq 0.075$ et se scindent à $u_x/U_{inj} = 0.4$. La Fig. 12b donne l'évolution spatiale des probabilités jointes des gouttes ayant un diamètre supérieur à $0.075 d_n$. Il apparaît que les gouttes telles que $u_x/U_{inj} \geq 0.4$, asymptote supérieure, sont générées par la fragmentation au niveau de la buse et sont localisées dans la couche limite du jet. Les gouttes telles que $u_x/U_{inj} \leq 0.4$ sont quant à elles localisées à l'arrière de la nappe de front et préférentiellement au niveau de son extrémité. Enfin, les deux groupes de gouttes se recouvrent en partie dans la région de recirculation. Ceci permet de montrer que chacune des asymptotes correspond à une source de fragmentation distincte : celle de la nappe de front et celle due au forçage du mode le plus instable.

Les distributions jointes donnent des informations sur la dynamique des gouttes. Cependant, comparées à l'expérience, les tendances sont différentes, plus complexes et ne permettent pas de

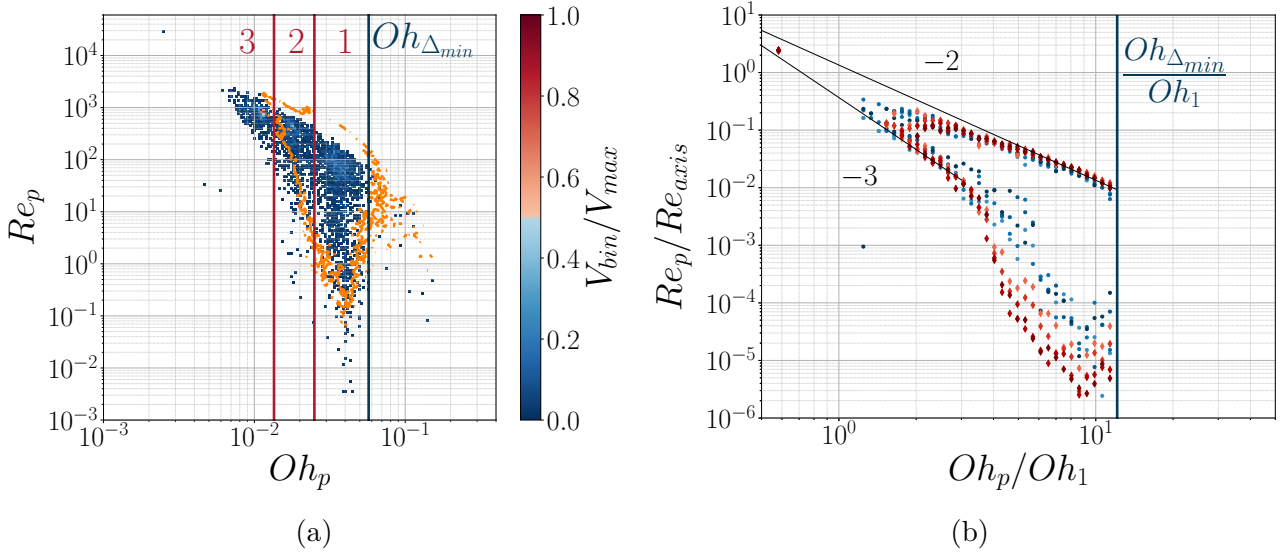


Figure 13: (a) Histogramme joint en Re_p et Oh_p pour $We_2 = 40$ (DNS 6) à $t/T_a = 30$ avec le contour de l'histogramme joint pour $We_2 = 165$ (DNS 10) et (b) superposition des contours des histogrammes joints normalisés à $t/T_a = 15$. Les DNS dans le régime *second wind induced* sont indiquées par les points bleus et celles dans le régime d'atomisation par les losanges rouges. Les 3 modes en taille observés pour le régime *second wind induced* sont numérotés de 1 à 3 dans le sens de d croissant. $Oh_{\Delta min}$ correspond au Ohnesorge calculé sur la taille minimale de maille.

distinguer différents sous-groupes de gouttes comme en Fig. 8a. Afin d'obtenir des informations sur l'écoulement perçu par les gouttes, il est possible de s'intéresser aux nombres de Reynolds et d'Ohnesorge particulaires, Sec. 4.4.3 s'écrivant tels que :

$$Re_p = \frac{|u_{p,x} - U_{g,x}| d}{\nu_l}, \quad Oh_p = \frac{\mu_l}{\sqrt{\rho_l \sigma d}} \quad (13)$$

avec d le diamètre de la goutte, $u_{p,x}$ sa vitesse axiale et $|u_{p,x} - U_{g,x}|$ sa vitesse relative par rapport à $U_{g,x}$, la vitesse moyenne de la phase gazeuse selon x . La Fig 13a donne l'histogramme en volume joint en Re_p et Oh_p en régime *second wind induced* pour $We_2 = 40$ (DNS 6) à $t/T_a = 30$. Cet histogramme présente des frontières marquées et un comportement plus régulier que les distributions jointes précédentes, aussi bien pour cette valeur de We_2 que pour les autres. En complément, lorsque le contour de l'histogramme obtenu en régime d'atomisation pour $We_2 = 165$ à $t/T_a = 15$ est reporté sur cet histogramme, il apparaît que les deux existent dans le même espace (Re_p, Oh_p) bien que les régimes de fragmentation du jet soient différents. Afin d'approfondir la comparaison des histogrammes joints en fonction de We_2 , la Fig. 13b montre la superposition des contours obtenus pour les 10 valeurs de We_2 . Ici, les données sont observées dans l'espace $(Re_p/Re_{axis}, Oh_p/Oh_1)$ avec Re_{axis} le nombre de Reynolds liquide calculé avec la vitesse axiale du jet sur l'axe et Oh_1 le nombre d'Ohnesorge liquide. Cette normalisation permet d'obtenir le collapse des contours. Quelque soit la valeur de We_2 , les contours existent sur la même gamme $Oh_p/Oh_1 = \sqrt{d_n/d}$. Le long de l'axe Re_p/Re_{axis} , la dispersion vers les petites valeurs augmente avec We_2 pour $(Oh_p/Oh_1) \in [4, 10]$, ce qui peut s'expliquer par l'augmentation du cisaillement entre les phases avec la vitesse d'injection. Cette dispersion mise à part, les histogrammes existent dans le même espace $(Re_p/Re_{axis}, Oh_p/Oh_1)$ pour les deux régimes de fragmentation. En outre, deux segments des contours suivent des lois

puissance de coefficient -2 et -3. Étudier l'histogramme joint en Re_p/Re_{axis} et Oh_p/Oh_1 permet d'obtenir des frontières régulières et indépendantes de We_2 bien qu'il existe une dynamique complexe et que les histogrammes évoluent au sein de ces frontières.

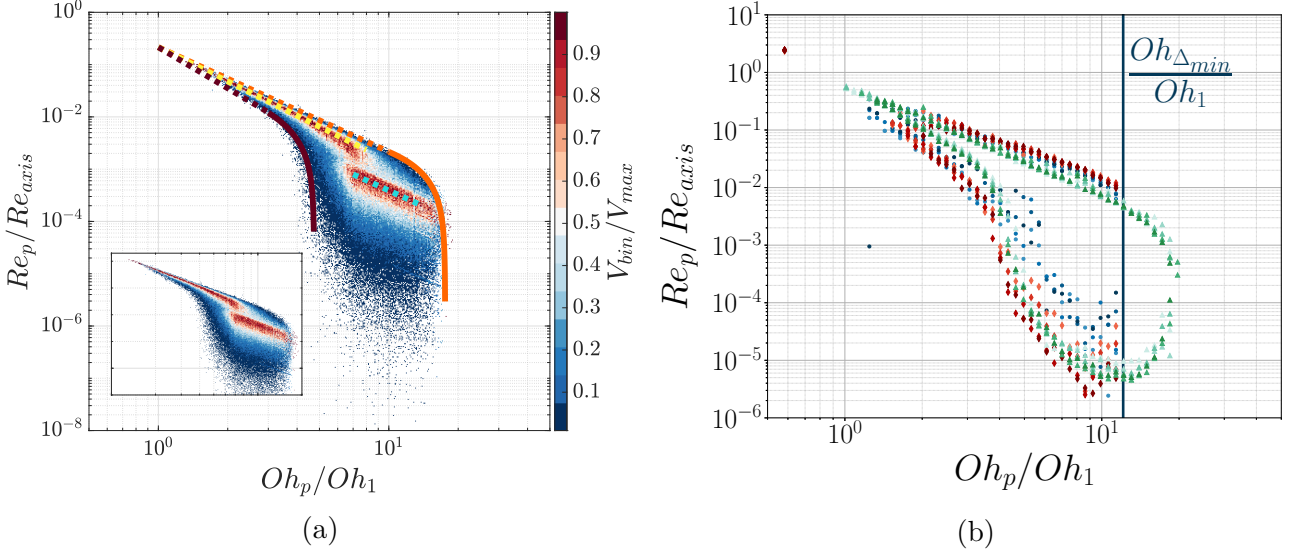


Figure 14: (a) Histogramme expérimental joint en Re_p/Re_{axis} et Oh_p/Oh_1 à $x/d_n = 800$ et (b) superposition du contour des histogrammes joints numériques, pour les 10 valeurs de We_2 , et expérimentaux, pour les 5 positions x/d_n . Ces derniers sont translatés d'un offset multiplicatif de 3. Les DNS dans le régime *second wind induced* sont indiquées par les points bleus, celles dans le régime d'atomisation par les losanges rouges et les données expérimentales par les triangles verts.

Afin d'aller plus loin dans l'analyse de ces histogrammes joints, il est possible de les comparer avec les données expérimentales, Sec. 4.4.4. La Fig. 14a donne l'histogramme joint en Re_p/Re_{axis} et Oh_p/Oh_1 calculé sur les données expérimentales de Felis *et al.* (2020) à $x/d_n = 800$. Comme pour les données numériques, les frontières de l'histogramme sont bien définies. Il est possible de les décrire par des lois puissances dont le coefficient évolue entre -2 et -2.61 pour $Re_p/Re_{axis} \geq 10^{-2}$ et par des lois exponentielles pour $Re_p/Re_{axis} \leq 10^{-2}$. Dans la région $Re_p/Re_{axis} \geq 10^{-2}$, le Reynolds particulaire évolue tel que $Re_p = C Oh_p^{-2-\alpha}$, $(C, \alpha) \in \mathbb{R}^2$. Or $Re_p = \sigma^{-1} \mu_l |u_{p,x} - U_{g,x}| Oh_p^{-2}$. Ainsi, on obtient $|u_{p,x} - U_{g,x}| = \sigma C Oh_p^{-\alpha}$ soit $|u_{p,x} - U_{g,x}| \propto d^{\alpha/2}$, ce qui donne, dans cette région, la loi d'évolution de la vitesse relative des gouttes par rapport à leur diamètre. Sachant que la vitesse relative augmente lorsque le diamètre augmente, α appartient nécessairement à \mathbb{R}^+ . La frontière supérieure, évoluant telle que $Re_p/Re_{axis} = 0.215(Oh_p/Oh_1)^{-2}$, résulte de cette contrainte, représente une limite dynamique et correspond aux gouttes se comportant comme des traceurs, c-à-d telles que $|u_{p,x} - U_{g,x}| \approx 0$.

La Fig. 14b compare les contours des histogrammes joints issus des DNS et de l'expérience. Il est important d'avoir à l'esprit que les premiers sont calculés pour différents We_2 dans le champ proche de la buse tandis que les seconds sont calculés pour $We_2 = 24$ à différentes positions x/d_n dans le champ lointain, c-à-d la zone dispersée. En outre, les contours expérimentaux sont multipliés par 3, ce qui les translatent vers les Re_p croissants et permet d'obtenir le collapse entre les contours numériques et expérimentaux. Un premier fait marquant est que, avec ou sans offset multiplicatif, les histogrammes joints sont similaires et s'expriment tous sur

le segment $Oh_p/Oh_1 \in [1, 10]$. En suite, du fait de l'offset multiplicatif, les contours vérifient $(Re_p/Re_{axis})_{num} = C \times (Re_p/Re_{axis})_{exp}$ avec $C \approx 3$. Ceci se réécrit tel que

$$\frac{|u_{p,x} - U_{g,x}|_{num} d_{num}}{|u_{p,x} - U_{g,x}|_{exp} d_{exp}} = C \frac{d_{n,num} \times u_{x,axis,num}}{d_{n,exp} \times u_{x,axis,exp}} \quad (14)$$

et donne $|u_{p,x} - U_{g,x}|_{num} d_{num} \approx 1.8 |u_{p,x} - U_{g,x}|_{exp} d_{exp}$ avec $u_{x,axis,exp} = 0.8 \times U_{inj,exp} = 28 \text{ m/s}$ et $u_{x,axis,num} = U_{inj,num} = 4.5 \text{ m/s}$. De plus, les contours s'expriment sur la même gamme Oh_p/Oh_1 donc $d_{exp}/d_{n,exp} \approx d_{num}/d_{n,num}$, ce qui permet de calculer

$$\frac{d_{num}}{d_{exp}} \approx 3.73, \quad \frac{|u_{p,x} - U_{g,x}|_{num}}{|u_{p,x} - U_{g,x}|_{exp}} \approx 0.48. \quad (15)$$

Les tailles moyennes expérimentale et numérique sont respectivement $\langle d \rangle_{exp} = 95 \mu\text{m}$, moyen-née sur les 5 positions x/d_n , et $\langle d \rangle_{num} \approx 300 \mu\text{m}$, à $t/T_a = 34$ en régime *second wind induced*. Le ratio des moyennes est égal à 3.16, ainsi $\langle d \rangle_{num}/\langle d \rangle_{exp} \approx d_{num}/d_{exp}$ et vérifie le résultat précédent. L'interprétation du ratio de tailles et de vitesses relatives doit être faite avec précaution du fait des différences dans la manière de mesurer la taille et la vitesse des gouttes numériquement et expérimentalement et aussi du fait que les données numériques et expérimentales correspondent à deux régions de l'écoulement qui sont radicalement différentes, le champ proche ($x/d_n \leq 28d_n$) et la zone dispersée ($x/d_n \in [400, 800]$). L'offset multiplicatif entre les contours des deux régions spatiales pourrait révéler l'existence d'une dynamique à l'échelle du jet, comme par exemple le ralentissement global du spray le long de l'axe. Même avec ces considérations en tête, il semble correct de conclure que les contours numériques et expérimentaux sont autosimilaires. Enfin, la différence au niveau de l'asymptote vers les petits Oh_p/Oh_1 et grands Re_p/Re_{axis} pourrait s'expliquer par la présence de ruptures par sac dans l'expérience alors que ce type de rupture n'est pas observé dans les DNS. Une estimation de la vitesse de glissement entre les phases est aussi proposée, Sec. 4.4.5, et s'élève à environ 90% de la vitesse d'injection.

Conclusions et perspectives

L'objectif de cette thèse est l'étude de la population de gouttes générées par la fragmentation d'un jet rond liquide dans les régions proche et lointaine de la buse. Pour ce faire, des mesures expérimentales jointes de la taille et de la vitesse des gouttes ont été réalisées par DTV dans le champ lointain. Le champ proche est quant à lui étudié numériquement à l'aide de DNS utilisant le solveur des équations de Navier Stokes implémenté dans le langage Basilisk, libre et de haut niveau, développé en C++. Pour chaque champ, l'attention est portée sur la distribution en taille et en vitesse des gouttes. Deux modèles théoriques de natures très différentes, dérivés de la turbulence intermittente (Novikov & Dommermuth, 1997) et de la fragmentation ligamentaire (Villermaux *et al.*, 2004), sont testés dans les deux champs pour décrire la distribution en taille.

L'analyse des mesures DTV de Felis *et al.* (2020) illustre la nature multimodale des distributions en taille et en vitesse pour les jets proches des configurations agricoles en régime *second wind induced*, $We_2 = 24$, loin de la buse, $x/d_n \in [400, 800]$. Une fois les statistiques des gouttes décrites, la campagne systématique d'ajustement indique que la distribution en taille issue de l'intermittence de la turbulence offre une meilleure description quantitative. En outre, un modèle est aussi proposé pour la distribution en vitesse. À partir de la distribution jointe en taille et en vitesse et des propriétés statistiques des distributions marginales, il est

possible de définir 5 sous-groupes de gouttes présentant une vitesse et une taille caractéristique et représentant un pourcentage en volume ou en nombre de gouttes conséquent. Enfin, la ligne centrale de la distribution jointe est modélisée par la relation quadratique proposée par Lee & An (2016), qui permet aussi de retrouver la tendance de la distribution en taille.

La campagne DNS se concentre sur les jets ronds liquides jusqu'à $x/d_n = 28$ pour différents We_2 , ce qui permet de parcourir les régimes *second wind induced* et d'atomisation. Aussi bien la distribution en taille que les distributions en vitesse diffèrent entre les deux régimes. Pour les tailles, le premier régime montre une distribution trimodale tandis que la distribution est unimodale pour le second. De nouveau, les statistiques et les distributions sont détaillées et une campagne d'ajustement est menée pour tester les deux distributions théoriques. Il en ressort que la distribution issue de la fragmentation ligamentaire offre la meilleure description quantitative. Celle issue de la turbulence intermittente offre une moins bonne description quantitative mais sa description qualitative de la distribution, notamment pour les petites tailles, est meilleure. Les spécificités, à première vue, inattendues de la distribution marginale en vitesse et de la distribution jointe en taille et vitesse sont respectivement expliquées par la théorie des anneaux de vorticité de Saffman (1992) et par l'existence de deux sources de fragmentation, l'une au niveau de la buse et l'autre à l'extrémité de la nappe de front. L'histogramme en volume joint en nombres de Reynolds et d'Ohnesorge particulaires montre des frontières bien définies, invariantes avec le nombre de Weber du gaz et vérifiées par les données expérimentales. Enfin, la vitesse de glissement entre les phases est estimée s'élever à 90% de la vitesse d'injection.

La Sec. 5.2 propose plusieurs pistes pour étendre le travail fait ici et la Sec. 5.3 le conclut. Entre autres, des éléments sont apportés pour différencier la fragmentation continue d'une goutte ou ligament et la fragmentation complète d'un jet qui pourrait, dans certaines circonstances, montrer une forme d'intermittence. Enfin, des références sont données pour l'étude de l'écoulement perçu par les gouttes et la possibilité de faire le suivi lagrangien des ligaments toroïdaux observés à $We_2 = 40$ est démontrée.

Contents

Contents	xxix
List of Figures	xxxii
List of Tables	xxxv
1 Introduction	1
1.1 What is liquid jet atomisation?	2
1.2 Describing fragmentation flows	4
1.2.1 Governing parameters of the flow	4
1.2.2 Breakup regimes	6
1.3 Hydrodynamic instabilities	9
1.3.1 Stability of an interface between two fluids	9
1.3.2 Classic hydrodynamic instabilities	11
1.4 Turbulence	15
1.4.1 Fragmentation flows and turbulence	15
1.4.2 Predictions of Kolmogorov	16
1.4.3 Intermittency	18
1.5 Aggregation & cascade: two theories of fragmentation for the drop size distribution	21
1.5.1 From internal turbulence intermittency to the droplet sizes	21
1.5.2 Aggregation scenarii	25
1.6 Objectives and outlines of the thesis	30
2 Experimental and numerical methods	31
2.1 Introduction	32
2.2 Droplet Tracking Velocimetry by shadowgraphy	33
2.3 How to simulate flow dynamics?	35
2.3.1 Numerical simulations for fluid dynamics	35
2.3.2 Basilisk: a C-based high level language for the computational dynamics of fluid	36
2.4 A numerical description of multiphase flows with surface tension	37
2.4.1 Flow configuration and governing equations	37
2.4.2 Discretisation of the physical space: a hierarchical octree mesh	38
2.4.3 Adaptative mesh refinement	39
2.4.4 Time discretisation of the governing equations	40
2.4.5 Spatial discretisation of the governing equations	42
2.5 A numerical description of the interface	44

CONTENTS

2.5.1	Tracking the interface with a Volume-Of-Fluid approach	44
2.5.2	Computing the interfacial forces: a balanced force surface tension calculation	46
2.5.3	Computing the interface curvature	48
2.5.4	Droplet detection	52
2.6	Conclusion	54
3	Multimodal distributions of agricultural-like sprays: A statistical analysis of drop population from a pressured-atomized spray	55
3.1	Preamble	56
3.2	Multimodal distributions of agricultural-like sprays	57
3.3	Connecting the size-velocity joint distribution and the fragmentation mechanisms	82
3.3.1	Conjectures for the volume transfer between the droplet subgroups . . .	82
3.3.2	Exploring the size distributions of the subgroups	85
4	Weber dependency of jet fragmentation: a DNS investigation	89
4.1	Introduction	90
4.2	Flow modeling and parameter framing	92
4.2.1	Governing equations	92
4.2.2	Numerical methods	92
4.2.3	Physical configuration and parameters	93
4.2.4	Most unstable modes for triggering the jet fragmentation	94
4.2.5	Numerical configuration and computational cost	97
4.3	Overall flow characteristics and droplet statistics	99
4.3.1	Turbulent kinetic energy	99
4.3.2	Close up on the jet interface	100
4.3.3	Statistics of the droplet population	103
4.3.4	Distributions of the size and the velocity	106
4.3.5	Modeling the droplet size PDF	108
4.4	Dynamics of the jet and the droplets: a two speed fragmentation	115
4.4.1	The axial velocity PDF and the jet head vortex ring	115
4.4.2	Joint distribution of the droplet size and axial velocity	118
4.4.3	Governing parameters at the droplet scale	119
4.4.4	Droplet phase space: simulations and experiments	123
4.4.5	Drift between the gas and liquid phases	126
4.5	Conclusion	128
5	Conclusions and perspectives	131
5.1	Main results	132
5.2	Thinking further	134
5.3	Closing words	142
References		143
A	Estimation of the sheet thickness in the region of the jet head	157
A.1	A simple model of the jet head development	158

CONTENTS

A.2 Estimation of the sheet thickness at its feet	160
A.3 Estimation of the sheet thickness at its edge	163

List of Figures

1	Déferlement d'une vague, Vallon des Auffes, Marseille.	ix
2	Éternuement enregistré à 1000 images par seconde (Bourouiba <i>et al.</i> , 2014) et Superposition de photographies expérimentales d'un nuage de gouttelettes d'eau produit par un spray commercial de 10 centimètres de haut (Courtoisie de Lucas Rotily).	x
3	Exemple d'une discréétisation <i>quadtree</i>	xii
4	Schéma d'une interface avec une courbure importante capturée par un stencil asymétrique.	xiii
5	Schéma de l'expérience mise en place par Felis <i>et al.</i> (2020).	xiv
6	Distributions de $d/\langle d \rangle_V$, $u/\langle u \rangle_V$ et $v/\langle u \rangle_V$ pour les données DTV de Felis <i>et al.</i> (2020).	xvi
7	Ajustement de la distribution expérimentale $\mathcal{P}_{d/\langle d \rangle_V}$ à $x/d_n = 800$ par les distributions de Kooij <i>et al.</i> (2018) et de Novikov & Dommermuth (1997).	xvii
8	Distribution jointe expérimentale en taille et en vitesse axiale à $x/d_n = 600$ avec les sous-groupes de gouttes définis par les caractéristiques des distributions marginales. Ajustement de la ligne centrale par la fonction de Lee & An (2016).	xviii
9	Photographies expérimentales de ligaments et d'une rupture par sac (Felis-Carrasco, 2017).	xix
10	Taux de croissance temporel normalisé (α_r^*) ₀ pour $U_{inj} = 3.0$ m/s avec $a = d_n$	xxi
11	Évolution temporelle du nombre de gouttes et distributions de $d/\langle d \rangle$, $u_x/\langle u_x \rangle$ et $u_y/\langle u_x \rangle$ pour les données obtenues par DNS à $t/T_a = 15$	xxiii
12	Distribution jointe numérique en taille et vitesse axiale pour $We_2 = 130.3$ à $t/T_a = 15$ et évolution spatiale des probabilités $\mathcal{P}(d/d_n \geq 0.075, u_x/U_{inj}) \leq 0.4$ et $\mathcal{P}(d/d_n \geq 0.075, u_x/U_{inj}) \geq 0.4$ pour $We_2 = 99.8$ à $t/T_a = 15$ en coordonnées cylindriques.	xxiv
13	Histogramme joint numérique en Re_p et Oh_p pour $We_2 = 40$ à $t/T_a = 30$ avec le contour de l'histogramme joint pour $We_2 = 165$. Superposition des contours des histogrammes joints numériques normalisés à $t/T_a = 15$	xxv
14	Histogramme expérimental joint en Re_p/Re_{axis} et Oh_p/Oh_1 à $x/d_n = 800$. Superposition du contour des histogrammes joints numériques, pour les 10 valeurs de We_2 , et expérimentaux, pour les 5 positions x/d_n	xxvi
1.1	Illustration of fuel injection (Smith & Sick, 2006).	2
1.2	A wave crashing on the rocky shore at Vallon des Auffes, Marseilles.	2
1.3	High-speed images of a sneeze (Bourouiba <i>et al.</i> , 2014) and photographs of a water droplet cloud produced by a commercial spray (Courtesy of Lucas Rotily).	3
1.4	Jet stability curve (Lefebvre & McDonell, 2017) and photographs of jets in each stability region (Dumouchel, 2008).	7

1.5	Schema of an unidirectional flow of two fluids with an interface.	9
1.6	Illustrations of the Kelvin Helmholtz instability on a cloud sheet (Guyon <i>et al.</i> , 2012), the Rayleigh Taylor instability in an experimental setup (Wilkinson & Jacobs, 2007) and the Rayleigh Plateau instability during the fragmentation of a ligament (Eggers & Villermaux, 2008).	12
1.7	Schema of the evolution from a cylinder to a varicose cross-section due to surface tension.	13
1.8	Schema of the turbulent energy cascade.	16
1.9	Exponent ζ_p of the structure functions in the time domain of order p vs p , comparison of the experimental data and several models of intermittent turbulence, taken from Frisch (1995).	20
1.10	Schema of a ligament and its composing blobs.	26
2.1	Example of a quadtree discretisation and its corresponding tree representation.	38
2.2	Scheme of an interface with a small curvature captured by a 3×3 symmetric stencil and with a stronger curvature captured by an asymmetric stencil.	48
3.1	Size-velocity joint distribution for $x/d_n = 600$ and the droplets subsets discriminated with the characteristics of the marginal distributions.	82
3.2	Photographs of ligaments ($3d_n \times 3d_n$).	83
3.3	Photographs of bag break-ups ($12d_n \times 12d_n$).	84
3.4	Size distribution of the droplets separated by subset for the five experimental positions.	86
4.1	Evolution of the adimensional temporal growth rate $(\alpha_r^*)_m^2$ for $U_1 = 3.0$ m/s.	96
4.2	Atomisation and adaptative grid for $We_2 = 165$ at $t/T_a = 16.2$	98
4.3	Temporal evolution of the jet length L_j relatively to the theoretical jet length $L_{j,\text{theo}}$ for the 10 DNS.	99
4.4	Turbulent kinetic energy in the gas phase for $We_2 = 40$	100
4.5	Superposition of the interface sliced at $z = 0$ in the region of the nozzle in both the second wind induced and atomisation regimes.	102
4.6	Superposition of the interface sliced at $z = 0$ in the region of the jet head in both the second wind induced and atomisation regimes at $t/T_a = 15$	103
4.7	Joint distribution of the interface points in the $(x/d_n, r/d_n)$ space for $We_2 = 99.8$ at $t/T_a = 15$ and the interface filtered with a threshold of 0.2.	104
4.8	Total number of detected droplets, unscaled and scaled by $We_2^{-1.8}$	105
4.9	Temporal evolution of the mean $\langle \cdot \rangle$, unscaled and scaled by We_2 , of the droplet size d , the axial velocity u_x and the transverse velocity u_y	111
4.10	Evolution of $\langle \cdot \rangle$, σ , S , κ , the minimum and maximum against We_2 for the size d , the axial velocity u_x and the transversal velocity u_y	112
4.11	Distributions of $d/\langle d \rangle$, $u_x/\langle u_x \rangle$ and $u_y/\langle u_x \rangle$ at $t/T_a = 15$ and $t/T_a = 25$ in both the second wind induced and the atomisation regime.	113
4.12	Distribution of $d/\langle d \rangle$ in semi-logarithmic scale at $t/T_a = 15$ and $t/T_a = 20$ in both the second wind induced and atomisation regimes.	114
4.13	Fit of $\mathcal{P}_{d/\langle d \rangle}$ by f_Γ , $f_{\Gamma B}$ and f_ϵ in the second wind induced regime and the atomisation regime at $t/T_a = 15$	114

LIST OF FIGURES

4.14 Spatial evolution of the probabilities $\mathcal{P}(u_x/U_{inj} < 0)$ and $\mathcal{P}(u_x/U_{inj} > 1)$ for $We_2 = 99.8$ at $t/T_a = 15$ in cylindrical coordinates.	115
4.15 Distribution of u_x/U_{inj} at $t/T_a = 15$ in the second wind induced regime and in the atomisation regime.	116
4.16 Joint distributions of the size and the axial velocity of the droplets for $We_2 = 40$ in second wind induced regime and for $We_2 = 130.3$ in atomisation regime.	118
4.17 Spatial evolution of the probabilities $\mathcal{P}(d/d_n > 0.075, u_x/U_{inj} < 0.4)$ and $\mathcal{P}(d/d_n > 0.075, u_x/U_{inj} > 0.4)$ for $We_2 = 99.8$ at $t/T_a = 15$ in cylindrical coordinates.	120
4.18 Joint volume histogram of Re_p and Oh_p for the droplet population for $We_2 = 40$ at $t/T_a = 30$ and for $We_2 = 165$ at $t/T_a = 15$	121
4.19 Edges of the joint volume histograms, raw and normalised, at $t/T_a = 15$ in both the second wind induced and atomisation regimes.	122
4.20 Experimental joint volume histogram of Re_p/Re_{axis} and Oh_p/Oh_1 at $x/d_n = 800$	124
4.21 Comparison of the joint volume histograms obtained from the DNS campaign and from the experimental data of Felis <i>et al.</i> (2020), not corrected and corrected by a multiplicative factor of 3.	125
4.22 Velocity difference between the liquid and the gas phase averaged over the computational domain not normalised and normalised.	127
 5.1 Examples of intermittent ligament fragmentation.	136
5.2 Visualisation of the jet head ($2d_n \times 3d_n$) for $We_2 = 165$ and of the spatial correlation between droplets and vortices.	138
5.3 Illustration of the Lagrangian tracking of the corollas and of the rims.	139
5.4 Time evolution of a corolla and the corresponding rim for $We_2 = 40$	140
5.5 Relationship between the cumulative CO ₂ emissions and the increase in global surface temperature (Masson-Delmotte <i>et al.</i> , 2021).	142
 A.1 Schematic representation of a simple model for the jet head development.	159
A.2 Schematic representation of the cylinder jet in the theoretical initial state with the different pressures at play in the control volume.	160
A.3 Schematic representation of the initial deformation of the cylinder jet head.	161
A.4 Scheme of an infinitesimal element in cylindrical coordinates in the (r, θ) plane and in the (x, r) plane.	163

List of Tables

1	Propriétés physiques considérées par Felis <i>et al.</i> (2020) en conditions normales.	xiv
2	Répartition des sous-groupes en volume et en nombre de gouttes et leur nombre de Stokes (Ferrand <i>et al.</i> , 2003) pour la distribution jointe à $x/d_n = 600$.	xix
3	Paramètres fixes et nombre d'Ohnesorge correspondant.	xxi
4	Vitesses d'injection et nombres de Weber gaz et de Reynolds liquide correspondants.	xxi
1.1	Breakup regimes and related transition criteria (Lin & Reitz, 1998).	8
4.1	Fixed parameters and corresponding Ohnesorge number.	94
4.2	Injection velocities and corresponding gas Weber and liquid Reynolds numbers.	94
4.3	Pulsation and frequency of the most unstable mode for each jet configuration.	97
4.4	Numerical performances of the DNS.	97
4.5	Strouhal number Sr based on the forcing and We_2 for the 10 DNS.	101
4.6	Estimation of the Taylor micro scale λ and its normalised values at $t/T_a = \{15, 25\}$.	107
4.7	Final parameters and r^2 , truncated at the third decimal, for the best fits given by f_Γ , $f_{\Gamma B}$ and f_ϵ at $t/T_a = 15$.	109

Chapter **1**

Introduction

Contents

1.1	What is liquid jet atomisation?	2
1.2	Describing fragmentation flows	4
1.3	Hydrodynamic instabilities	9
1.4	Turbulence	15
1.5	Aggregation & cascade: two theories of fragmentation for the drop size distribution	21
1.6	Objectives and outlines of the thesis	30

1.1 What is liquid jet atomisation?

At first blush, those three words let think of a mass of liquid which, in a way or another, breaks into pieces and potentially produces elements of the atomic size. Fluids and solids are constituted by millions of molecules and atoms, each of them interact locally with its neighbours in a play of attraction and repulsion, described by the van der Waals forces. Those interactions have for consequence the existence of cohesive forces within a material. For solids, those forces are of such amplitudes that no internal motion is possible. In fluids, the molecules can move freely, more or less easily depending on the internal friction.

Those cohesive forces also lead to the formation of an interface between two immiscible fluids, like water in air or oil in water. Waves or droplets are typical examples. Under some conditions, a mass of liquid can have a motion leading some fluid particles to burst through the interface. If the ejection energy is sufficient, the particles will detach from the main core and create new liquid fragments. It is very unlikely that the fragments will be of the atomic scale, as the energy needed for breaking the chemical bonds in a molecule are of order of hundreds of kJ/mol , or of the molecule scale as the cohesive forces between molecules is of order of $10\ kJ/mol$ for the hydrogen bonds and of $1\ kJ/mol$ for the van der Waals forces. For instance, the chemical bond between the atoms of hydrogen and oxygen in a water molecule (H_2O) has an averaged energy of $429.76 \pm 0.03\ kJ/mol$ (Haynes, 2017). Let us consider 1 litre of water, representing $55.6\ mol$, knowing that 1 ton of petroleum is equivalent to $4.186 \times 10^{10}\ J$ (European Union *et al.*, 2019) or 7.33 barrels of 159 litres, dissociating all the atoms requires a theoretical energy approximately equivalent to 0.67 litres of petroleum. Compared to this, the energy bonding the water molecules to each other is negligible. Following the thoughts of Néel (2018), “fragmentation” might be a more appropriate wording than atomisation. Even so, two main questions arise here: what sizes the newly created fragments have? Why so?



Figure 1.2: A wave crashing on the rocky shore at Vallon des Auffes, Marseilles.

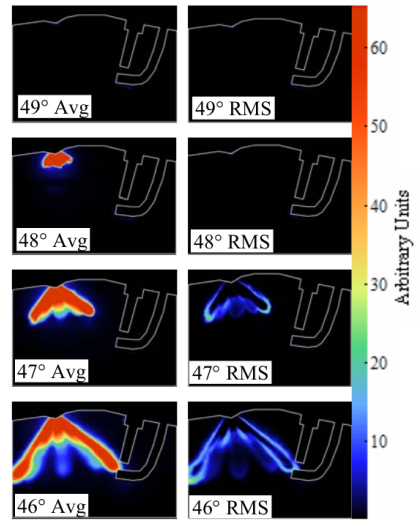


Figure 1.1: 100 cycle averages (left) and rms (right) at the beginning of the fuel injection (Smith & Sick, 2006).

Researching an answer absorbed a large number of scientists across the globe for decades. Far from being only theoretical, those two questions are of most importance in the large spectrum of processes in which fragmentation takes place. In classic combustion engines or cryogenic combustion engines, in rockets for instance, the fuel is injected at high pressure in a gas chamber, Fig. 1.1. The smaller and the more homogeneous are the droplet sizes the more efficient the explosion is, e.g. through droplet micro explosions in bio fuels (Saidur *et al.*, 2011; Wang & Lee, 2007). In agricultural farming or pesticide spraying, smaller droplets are subjected to wind drift (Al Heidary *et al.*, 2014) which can lead to 30% of water losses (Yazar, 1984) in a context of increasing worldwide population and water use (Jiménez

Cisnero *et al.*, 2014) or to pollute neighbour residential or agricultural areas (Gil & Sinfort, 2005) and impose no-spray buffer zones which increases the pressure on land use (Hilz & Vermeer, 2013). Ocean sprays play an important role at the scale of the planet, for example by influencing either the dynamics of the marine atmospheric boundary layer (Kudryavtsev & Makin, 2011), the radiative forcing of aerosol and its impact on climate (Witek *et al.*, 2016) or the heat and momentum fluxes in hurricanes (Perrie *et al.*, 2004). Finally, while sneezing, Fig. 1.3a, the droplet size sets, among other, the nature of the trajectory which can Brownian or ballistic, i.e. rather random or fully determined, and the air carriage duration in the atmosphere (Duguid, 1946; Bourouiba *et al.*, 2014), two parameters being relevant for airborne disease transmission, like for COVID 19 (Mittal *et al.*, 2020). This list of processes where fragmentation takes part is far from being exhaustive and includes many other applications like firefighting (Kamluk *et al.*, 2020), medical drug delivery, similarly to Fig. 1.3b, small and large scale coatings, inkjet printing or spray painting. Thus, liquid jet “atomisation” or fragmentation globally depicts a liquid core in a gaseous medium undergoing break-ups which eventually generate droplets of different sizes.

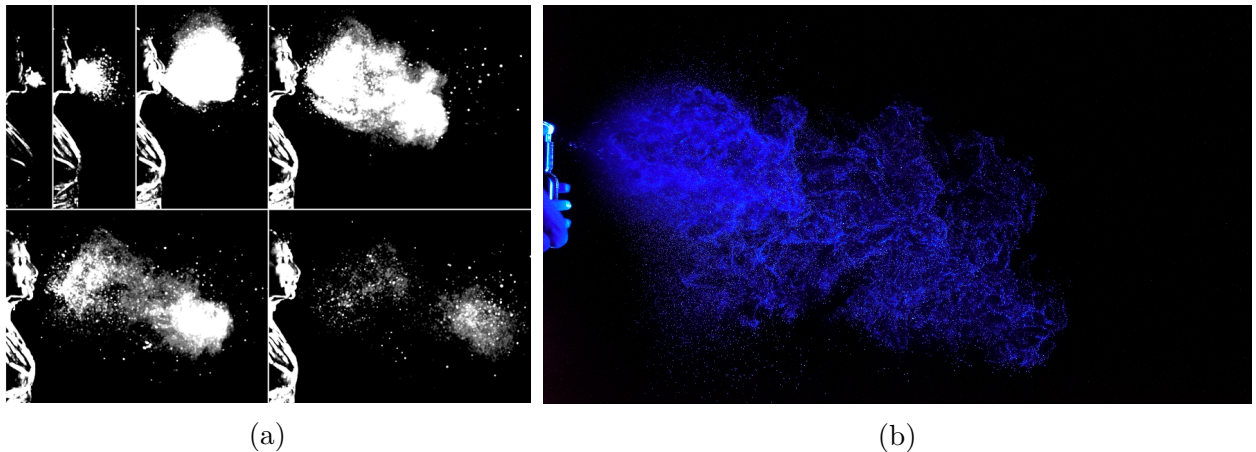


Figure 1.3: (a) High-speed images of a sneeze recorded at 1000 frames per second (Bourouiba *et al.*, 2014), (b) Superposition of experimental photographs of a water droplet cloud produced by a commercial spray of 10 centimetres height (Courtesy of Lucas Rotily).

In this work, the focus will be given to cylindrical round jets studied both experimentally and numerically. The study of the former jet will be carried out far away from the nozzle, typically at distances around several hundreds of nozzle diameters d_n . The latter jet is investigated close to the nozzle at distances around dozens of nozzle diameters. In both cases, the configurations are chosen to reproduce as much as possible those observed for sprinklers in farming irrigation. In the following, Sec. 1.2 tackles the question of the description of fragmentation flows. Sec. 1.3 and 1.4 recall the theory relative to hydrodynamic instabilities and turbulence while Sec. 1.5 introduces two theories for modelling the droplet size distribution resulting from fragmentation flows. The first one being based on turbulence cascade whilst the second one on aggregation dynamics, they both will be the red line of this work. Finally, Sec. 1.6 gives the objectives and the outlines of the thesis.

1.2 Describing fragmentation flows

Fragmentation generates new elements from one, or potentially several, source core. If each source core is immiscible, several phases will then coexist in the form of a multiphase flow. For liquid jet fragmentation in the context of this thesis, a biphasic flow is considered and composed of a liquid phase denoted with the subscript l and a gas phase denoted with the subscript g , the former being injected into the latter through a nozzle. Due to its fragmentation, the liquid phase becomes disperse. Beside, the newly generated fragments of the disperse phase can show properties, like their size or velocity, being different from each others, making the liquid phase polydisperse (Marchisio & Fox, 2013). Fragmentation flows are mainly governed by three dimensionless parameters: the Reynolds number, the Weber number and the Ohnesorge number. Each of them characterizes the balance between specific forces.

1.2.1 Governing parameters of the flow

Forces at play

Before explaining the role of the governing dimensionless parameters of the flow, it is worth recalling what forces are relevant in a fragmentation flow. Obviously, all possible forces act and interact in a flow, starting from quantum effects to the sun or galaxy gravitational forces, passing by large scale magnetic interactions or the previously mentioned intermolecular van der Waals forces. However, only a short range of forces are relevant to the description of the main fragmentation flow physics:

- the inertial forces derived from the injection of the liquid phase,
- the viscous forces resulting from each fluid viscosity,
- the aerodynamic interactions related to the surface tension and the interface deformation.

Inertia can be seen as the tendency of a body to keep its velocity and is directly related to its mass, or its density in a volume based approach. Conversely, viscosity can be seen as the tendency of a fluid to resist to internal motion or motion induced by contact with an interface or other external surface. While inertia and viscosity are quite common and straight forward to understand, surface tension is slightly more complex. The surface tension between two immiscible fluids, or a fluid and a solid, results from the intermolecular van der Waals forces, i.e. the internal cohesive forces of the fluid, as a macroscopic effect with an action range of several centimetres. Surface tension is the key element to explain the shape of a liquid interface in capillary tubes or the wetting angle of a droplet on a solid. Depending on the intensity of each force relatively to the others, the flow evolves differently, if not dramatically differently. Using dimensionless numbers helps to quantify relevant forces relatively to each other and to define general flow regimes.

Reynolds number

The Reynolds number is defined such that:

$$Re_i = \frac{\rho_i U_i L_i}{\mu_i} = \frac{U_i L_i}{\nu_i} \quad (1.1)$$

where ρ_i , μ_i and ν_i denote the density, the dynamic viscosity and the kinematic viscosity, U_i and L_i are the characteristic velocity and length scales of the phase i . Here, both scales are free to choose and “characteristic” denotes the idea of relevance of the scales. For Re to be

meaningful, each scale has to be chosen carefully and be representative of the flow physics, or at least part of it. In his seminal papers, Osborne Reynolds (1883) studied laminar and turbulent flows in a pipe and used the aforementioned ratio to assess the transition between the two regimes. This ratio was later named after Osborne Reynolds by Sommerfeld (1908) (Rott, 1990) and quantifies the ratio of the inertial forces, $\rho_i U_i L_i$, over the viscous forces, μ_i , and thus enables to characterise the regime of the flow under consideration. Low Reynolds numbers, $Re \ll 1$, indicate flows for which viscosity is dominant and inertia negligible. These flows are typically experienced by micro swimmers. The flow physics is radically different from what a human experiences while swimming (Purcell, 1976) and specific strategies like helical propulsion or wave like beating flagellum are the keys to motility (Lauga, 2016; Rode *et al.*, 2019). Conversely, high Reynolds numbers, $Re \gg 1$, indicate that inertial forces dominate viscous forces and are commonly found in aerodynamics research, e.g. for drag reduction of cars (Katz, 2006; Choi *et al.*, 2014) or aircraft (Cattafesta & Sheplak, 2011; Corke *et al.*, 2010).

Weber number

The Weber number is defined such that:

$$We_i = \frac{\rho_i U_i^2 L_i}{\sigma} \quad (1.2)$$

where σ is the surface tension between the liquid and gas phases and the other parameters are the same as for the Reynolds number. Introduced by Constantin Weber (1931) (Villermaux, 2020), this number quantifies the ratio between the inertial forces and the superficial forces resulting from the surface tension. Low Weber objects would thus be almost not deformable, if not at all, as in some high Reynolds bubbly flows (Kumaran & Koch, 1993) or in the context of fragmentation with weak aerodynamic forces (Dumouchel *et al.*, 2005a,b). Conversely, still in the context of jet fragmentation, a large Weber number indicates strong aerodynamic interactions between the gas phase and the liquid phase, either disperse or not, as in so called the bag break-up regime of fragmentation in which the droplets take a bag-like shape before bursting (Rimbert & Castanet, 2011).

Ohnesorge number

The Ohnesorge number is defined such that:

$$Oh = \frac{\mu_l}{\sqrt{\rho_l \sigma L_l}} \quad (1.3)$$

Introduced by Ohnesorge (1936) in his doctoral thesis, this number quantifies the ratio of the viscosity forces over the ratio of the inertial forces and the surface tension and rewrites as: $Oh = \sqrt{We_l}/Re_l$. Even if it is dependent on the last two dimensionless parameters, the Ohnesorge number helps to quantify the deformation of droplets and bubbles. Lefebvre (1989) & Lefebvre & McDonell (2017) also describe it as an indicator of the jet stability. Variations in the Ohnesorge number lead to significant changes in fluid fragment dynamics like for the droplet fragmentation (Marcotte & Zaleski, 2019; Radhakrishna *et al.*, 2021) or the ligament retraction (Notz & Basaran, 2004; Hoepffner & Paré, 2013; Constante-Amores *et al.*, 2020).

Choosing the relevant scales

Now that the definitions of the governing dimensionless parameters are given, the characteristic

velocity and length scales U_i and L_i remain to be chosen. A common choice is to pick the scales related to the injection: the injection velocity U_{inj} and the nozzle diameter d_n . Doing so enables to compare directly the injection conditions of different flows. Note that for a liquid jet with a coaxial gas stream, it is more appropriate to pick the difference between the injection velocities of the gas and liquid phases. In this thesis, the experimental and numerical liquid jets are both injected in a quiescent gaseous medium and the velocity difference between the phases is equal to U_{inj} . The injection dimensionless parameters then give global information on the flow and write as:

$$Re_i = \frac{U_{inj}d_n}{\nu_i}, \quad We_i = \frac{\rho_i U_{inj}d_n}{\sigma}, \quad Oh = \frac{\mu_l}{\sqrt{\rho_l \sigma d_n}}, \quad \forall i \in \{l, g\} \quad (1.4)$$

Note that, it is possible to refine their interpretation by picking scales related to specific phenomenology, like the Kolmogorov scale for turbulence. At last, computing the particulate dimensionless numbers can also be relevant in order to characterize the flow locally or the flow perceived by the elements of the disperse phase. The relevant velocity and length scales are then the droplet size and relative velocity compared to the gas phase. More details about the particulate dimensionless parameters and their relevant scales are given in the following chapters.

1.2.2 Breakup regimes

This section is largely inspired by the work of Lefebvre (1989) and Lefebvre & McDonell (2017).

Consider a liquid round jet injected into a quiescent gaseous medium, the two phase flow resulting from the injection undergoes fragmentation once the conditions are met to get out of the dripping regime. This fragmentation is not unique and depends on the flow configuration and relevant dimensionless parameters. For instance, the jet length, defined as the length of the continuous portion of the jet measured from the nozzle to the break-up point where drop formation occurs, depends on the injection velocity. This dependency is a first key for defining different fragmentation regimes and was extensively studied. The evolution of the jet length with the injection velocity is called the jet stability curve and is given in Fig. 1.4. The dashed portion below the point A corresponds to drip flows and point A denotes the lower critical velocity at which the drip flow changes to jet flow. From A to B, the break-up length increases linearly with the velocity. This portion corresponds to the fragmentation of the jet due to surface forces as studied by Rayleigh and Weber. Point B corresponds to the change in the break-up mechanism from varicose to sinuous and opens a transition region towards turbulent jets, point C to point D, and fully developed sprays, from point D towards larger jet velocities. Lin & Reitz (1998) state that it is generally believed that the break-up length, or core length, depends on the liquid/gas density ratio and only weakly on the fluid properties and the jet velocity. They back up their argument with the analysis of Taylor (1940) of high-speed liquid jet break-up for which he derived an expression of the break-up length L :

$$L/d_n = B(\rho_l/\rho_g)^{1/2} / f(T) \quad (1.5)$$

where T is the Taylor parameter and writes as $T = (\rho_l/\rho_g)(Re_l/We_l)^2 = (\rho_l/\rho_g)[\sigma/(\mu_l U_{inj})]^2$, the function $f(T)$ has been approximated from Taylor's numerical results as $f(T) = \sqrt{3}/6[1 -$

$\exp(-10T)$] by Dan *et al.* (1997) and B is a constant equal to 4.04 for diesel spray nozzles (Chehroudi *et al.*, 1985).

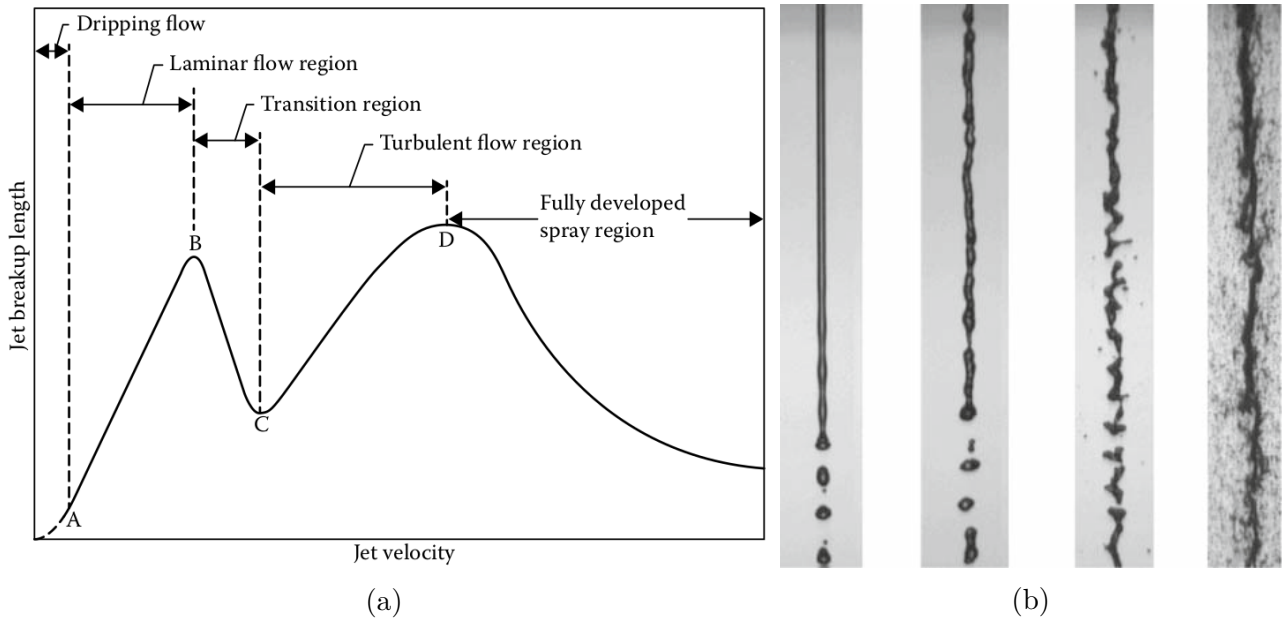


Figure 1.4: (a) Jet stability curve (Lefebvre & McDonell, 2017) and (b) photographs of jets respectively in the laminar flow, transition, turbulent flow and fully developed spray regions (Dumouchel, 2008).

Based on his analysis on diesel sprays, Reitz (1978) listed the different break-up regimes encountered when the injection velocity is increased:

1. Rayleigh jet break-up, caused by the growth of axisymmetric instabilities due to surface tension.
2. First wind-induced break-up, the relative velocity between the phases strengthens the surface tension effects, thus producing a static pressure distribution across the jet.
3. Second wind-induced break-up, the relative velocity between the phases induces the unstable growth of short-wavelength surface waves on the jet interface.
4. Atomization, the jet disrupts completely at the nozzle exit and the spray properties are strongly influenced by the development of the turbulence in the nozzle.

Concatenating the work of Miesse (1955), Ranz (1956), Sterling & Sleicher (1975), Reitz (1978), & Dan *et al.* (1997), Chigier & Reitz (1996) and Lin & Reitz (1998) reviewed the criteria for predicting the onset of break-up regimes, latter recalled in a review by Dumouchel (2008). The different regimes and the related onset criteria are given in Table 1.1. Note that, for the atomisation regime, the parameter K empirically accounts for the effect of initial disturbances in the flow caused by the internal nozzle walls and depends on the aspect ratio of the nozzle l_n/d_n , with l_n is the nozzle length. Note that, typical configurations for farming irrigation or pesticide spraying lead to a second wind-induced or an atomisation regime (Stevenin *et al.*, 2016; Felis *et al.*, 2020).

Breakup regimes	Jet velocity range	Criteria
Dripping	$0 - A$	$We_l < 8$
Rayleigh	$A - B$	$\begin{cases} We_l > 8, \\ We_g < 0.4 \text{ or } We_g < 1.2 + 3.41 Oh \end{cases}$
First wind-induced	$B - C$	$1.2 + 3.41 Oh < We_g < 13$
Second wind-induced	$C - D$	$13 < We_g < 40.3$
Atomisation	$D - \infty$	$\begin{cases} 40.3 < We_g, \\ \rho_g/\rho_l > Kf(T)^{-2}, \\ K = (0.53\sqrt{3 + l_n/d_n} - 1.15)/744 \end{cases}$

Table 1.1: Breakup regimes and related transition criteria (Lin & Reitz, 1998) where $f(T) = \sqrt{3}/6[1 - \exp(-10T)]$ (Dan *et al.*, 1997).

1.3 Hydrodynamic instabilities

Sec. 1.2.2 introduced the different break-up regimes which can occur during jet fragmentation, each of them relying on hydrodynamic instabilities. Far from describing all the details of linear stability of jets, this section recalls the theoretical background of the stability of an interface between two fluids before detailing three very classic hydrodynamic instabilities taking place in fragmentation flows: the Kelvin Helmholtz, Rayleigh Taylor and Rayleigh Plateau instabilities. This section follows the work of Drazin & Reid (2004), Charru (2007), Guyon *et al.* (2012), & Abid *et al.* (2017).

1.3.1 Stability of an interface between two fluids

Consider the unidirectional flow of two incompressible inviscid fluids with densities ρ_1 and ρ_2 and uniform velocities U_1 for $y < 0$ and U_2 for $y > 0$ under an acceleration field \vec{g} , as depicted in Fig. 1.5.

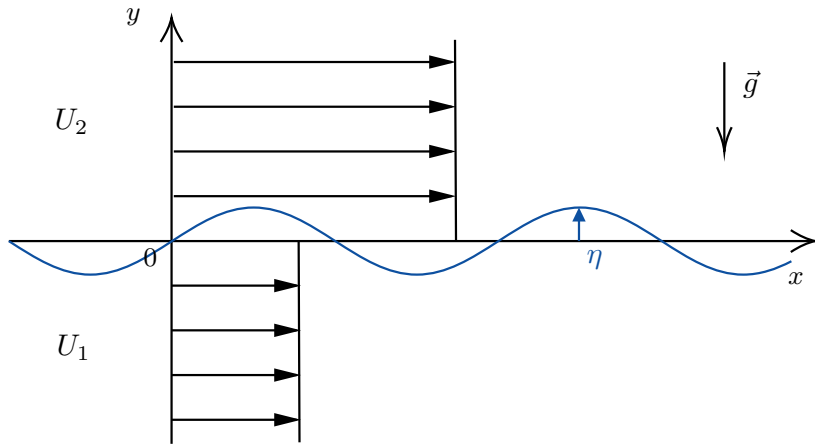


Figure 1.5: Schema of an unidirectional flow of two fluids with an interface.

The base flow is described by:

$$\mathbf{U} = \begin{cases} U_1 \mathbf{x} & , \quad \rho = \begin{cases} \rho_1 & , \quad P = \begin{cases} P_0 - \rho_1 g y, & y < 0 \\ P_0 - \rho_2 g y, & y > 0 \end{cases} & , \end{cases} \\ U_2 \mathbf{x} & \end{cases} \quad (1.6)$$

where P_0 is the pressure at the interface. Over this base flow, it is possible to superimpose small unsteady disturbances \mathbf{u} . For the sake of simplicity and following the initial work of Kelvin (1871), let us consider an irrotational initial disturbance. Drazin & Reid (2004) state that it is possible to do so while keeping in mind that it allows a proof of instability but not a proof of stability as no conclusion about rotational disturbances can be drawn. Even so, this condition is necessary as well as sufficient for instability. Charru (2007) recalls the results of Batchelor (1967) that, in the case of inviscid fluids, the vorticity field related to a rotational disturbance respects the linearised Helmholtz equation and then is advected by the base flow, thus the rotational part of any disturbance is neutral. Under the assumption of an irrotational initial disturbance, it exists a velocity potential Φ such that $\mathbf{u} = \nabla\Phi$. The interface elevation is measured relatively to the undisturbed interface, $y = 0$, and is such that $y = \eta(x, t)$ with η being infinitesimal. Due to incompressibility, the velocity potentials satisfy the Laplace equation:

$$\begin{cases} \Delta\Phi_1 = 0, & y < \eta \\ \Delta\Phi_2 = 0, & y > \eta \end{cases} \quad (1.7)$$

The boundary conditions are:

- (a) the initial disturbance occurs in a finite region at any time instant, implying Eq. (1.8).
- (b) the fluid particles at the interface must move with the interface without crossing it, which implies the kinematic equation (1.9).

$$\nabla\Phi \xrightarrow[y \rightarrow \pm\infty]{} \mathbf{U} \quad (1.8)$$

$$\frac{\partial\Phi_i}{\partial y} = \frac{D\eta}{Dt} = \frac{\partial\eta}{\partial t} + \frac{\partial\Phi_i}{\partial x} \frac{\partial\eta}{\partial x}, \quad y = \eta, \quad i = \{1, 2\} \quad (1.9)$$

Complementary to those two boundary conditions, the dynamic pressure condition has to be satisfied as well. For small disturbances of the interface, the pressure difference on each side of the interface balances with the capillary pressure: $P_2 - P_1 = \sigma/R$ for $y = \eta$, where σ is the surface tension and R the interface radius of curvature expressed as $R^{-1} = \eta_{xx}/(1+\eta_x^2)^{3/2}$. Knowing that the disturbances are infinitesimal, the radius of curvature becomes $R \approx \eta_{xx}$. Furthermore, the pressures P_i are given by the Bernoulli's theorem for irrotational flows, therefore

$$\rho_1 \left[gy + \frac{1}{2}(\nabla\Phi_1)^2 + \frac{\partial\Phi_1}{\partial t} + C_1 \right] - \rho_2 \left[gy + \frac{1}{2}(\nabla\Phi_2)^2 + \frac{\partial\Phi_2}{\partial t} + C_2 \right] = \sigma\eta_{xx} \quad (1.10)$$

Also, the dynamic condition relates the constants C_1 and C_2 such that

$$\rho_1 \left(\frac{1}{2}U_1^2 + C_1 \right) = \rho_2 \left(\frac{1}{2}U_2^2 + C_2 \right). \quad (1.11)$$

Here, the non linear problem of instability of the base flow is set. For the linear stability, we assume that the velocity potentials follow

$$\begin{cases} \Phi_1 = U_1 x + \phi_1, & y < \eta \\ \Phi_2 = U_2 x + \phi_2, & y > \eta \end{cases} \quad (1.12)$$

and neglect the products of the small increments ϕ_1 , ϕ_2 and η . Note that ϕ_i is the potential due to the velocity disturbance in the fluid i . Such a linearisation can be justified if the interface displacement and its slope are small, i.e. $\partial\eta/\partial x \ll 1$ and $g\eta \ll U_1^2, U_2^2$. Equations (1.7)–(1.10) then rewrite as

$$\Delta\phi_i = 0, \quad (1.13)$$

$$\nabla\phi_i \xrightarrow[y \rightarrow \pm\infty]{} 0, \quad (1.14)$$

$$\frac{\partial\phi_i}{\partial t} = \frac{\partial\eta}{\partial t} + U_i \frac{\partial\eta}{\partial x}, \quad y = 0, \quad i \{1, 2\}, \quad (1.15)$$

$$\rho_1(U_1 \frac{\partial\phi_1}{\partial x} + \frac{\partial\phi_1}{\partial x} + g\eta) = \rho_2(U_2 \frac{\partial\phi_2}{\partial x} + \frac{\partial\phi_2}{\partial x} + g\eta), \quad y = 0. \quad (1.16)$$

All the coefficients in this linear partial differential system are constant. It is then possible to use the method of normal modes assuming that the disturbances respect:

$$(\eta, \phi_1, \phi_2) = (\hat{\eta}, \hat{\phi}_1, \hat{\phi}_2) e^{ikx+st} \quad (1.17)$$

and Eqs. (1.13) give:

$$\begin{cases} \hat{\phi}_1 = B_1 e^{ky}, \\ \hat{\phi}_2 = B_2 e^{-ky} \end{cases} \quad (1.18)$$

Using the kinematic equations (1.15) leads to the following expression for B_1 and B_2

$$\begin{cases} B_1 = (s + ikU_1)\hat{\eta}/k, \\ B_2 = -(s + ikU_2)\hat{\eta}/k \end{cases} \quad (1.19)$$

while the linearised dynamic equation (1.16) gives the eigenvalue relation,

$$s(\rho_1 B_1 - \rho_2 B_2) + ik(\rho_1 U_1 B_1 - \rho_2 U_2 B_2) + (\rho_1 - \rho_2)g\hat{\eta} = -\sigma k^2 \hat{\eta}. \quad (1.20)$$

The resolution of this quadratic relation gives two modes $s = is_i \pm |s_r|$ with:

$$s_i = -k \frac{\rho_1 U_1 + \rho_2 U_2}{\rho_1 + \rho_2}, \quad (1.21)$$

$$s_r^2 = \frac{-\sigma k^3}{\rho_1 + \rho_2} + \frac{k^2 \rho_1 \rho_2 (U_1 - U_2)^2}{(\rho_1 + \rho_2)^2} - \frac{(\rho_1 - \rho_2)gk}{\rho_1 + \rho_2} \quad (1.22)$$

and the general instability condition then writes as $s_r^2 > 0$, i.e.:

$$\frac{k\rho_1 \rho_2 (U_1 - U_2)^2}{\rho_1 + \rho_2} > (\rho_1 - \rho_2)g + \sigma k^2 \quad (1.23)$$

where the phase velocity is such that $c = (\rho_1 U_1 + \rho_2 U_2)/(\rho_1 + \rho_2)$. Now that the general instability condition for an interface with surface tension between two fluids with a relative motion and submitted to the gravitational acceleration is derived, we can focus on the Kelvin Helmholtz, Rayleigh Taylor and Rayleigh Plateau instabilities. The following subsections use the same configuration and notations as the ones of this section.

1.3.2 Classic hydrodynamic instabilities

This section details three classic hydrodynamic instabilities by considering them independently from each other. In the context of fragmentation flows, it is very unlikely that those instabilities are truly independent and it is more common to observe their superposition, like in Fig. 1.6b. Even so, the independent evaluation of each one helps to understand the underlying physics. Note that all the relevant quantities related to these instabilities and fragmentation are recalled by Villermaux (2020). The reader interested into a more detailed historical timeline of the research progress about these three instabilities, in relation with fragmentation flows, could also find satisfaction with the latter reference.

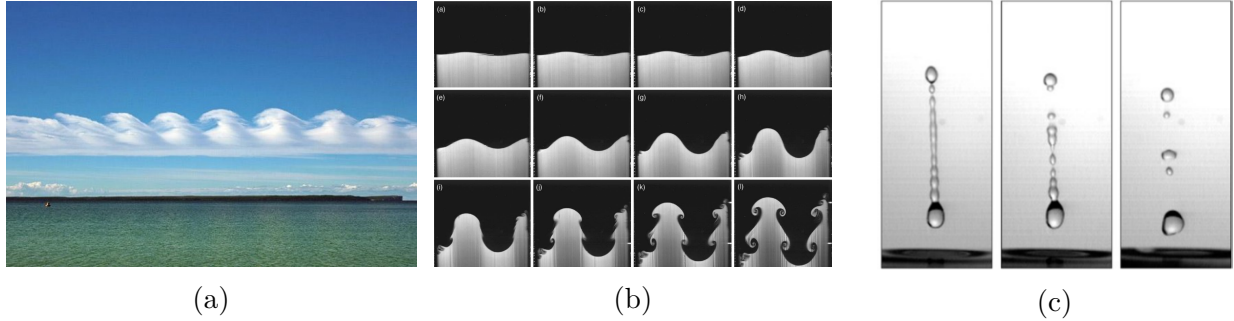


Figure 1.6: (a) Kelvin Helmholtz instability on a cloud sheet, Jervis Bay, New South Wales, Australia by G. Goloy taken from Guyon *et al.* (2012). (b) Rayleigh Taylor instability with Kelvin Helmholtz instability at latter stages (Wilkinson & Jacobs, 2007). (c) Rayleigh Plateau instability during the fragmentation of a ligament (Eggers & Villermaux, 2008).

1.3.2.1 Kelvin Helmholtz instability

Roaming around outdoor, the Kelvin Helmholtz instability can be observed in a large variety of flows, from clouds (Dalin *et al.*, 2010), particularly visible in Fig. 1.6a, to geophysical flows (Wilson *et al.*, 2012; Li *et al.*, 2018). Initially remarked and described by Helmholtz (1868), the formulation of the instability problem was first posed by Kelvin (1871). This instability is said to be convective, i.e. the disturbances develop or attenuate in a finite size area while being convected by the base flow.

Consider the two fluids with the heavier fluid being below and without any acceleration field \vec{g} nor surface tension: $\rho_1 > \rho_2$, $\vec{g} = \vec{0}$ and $\sigma = 0$. The general instability condition, Eq. (1.23), and the instability growth rate, Eq. (1.22) then reduce to:

$$(U_1 - U_2)^2 > 0, \quad (1.24)$$

$$s_r = \frac{k|U_1 - U_2|\sqrt{\rho_1\rho_2}}{\rho_1 + \rho_2}, \quad (1.25)$$

and thus the flow is always unstable for any non zero velocity difference between the two fluids and for any disturbance of wavenumber k , with a growth rate increasing linearly with k . Note that this conclusion does not hold for a viscous fluid. Indeed, due to viscosity, the large wavenumbers, such that $k \geq (U_1 - U_2)/2\nu$, or equivalently the small wavelengths, are fully attenuated and the analysis does not hold for such values of k .

1.3.2.2 Rayleigh Taylor instability

Initially described by Rayleigh (1883) in the development of his theory of stability of stratified fluids submitted to gravity, it was generalised to any acceleration perpendicular to the interface by Taylor (1950). An illustration of a developing Rayleigh Taylor instability is given in Fig. 1.6b. Consider the two fluids at rest without surface tension: $U_1 = U_2 = 0$ and $\sigma = 0$. The general instability condition, Eq. (1.23), and the instability growth rate, Eq. (1.22) then reduce to:

$$\rho_2 > \rho_1, \quad (1.26)$$

$$s_r = \frac{\rho_2 - \rho_1}{\rho_1 + \rho_2} gk, \quad (1.27)$$

and thus lead to the trivial conclusion that the configuration is unstable when the heavier fluid is above the lighter one. What is more interesting here is to generalize the idea of acceleration field from gravity to the combination of accelerations resulting from various motions, e.g. while considering the acceleration of a liquid sheet in the gravitational field. Note that in such cases, only the apparent acceleration perpendicular to the interface accounts for triggering the instability.

1.3.2.3 Rayleigh Plateau instability

Consider the two fluids at rest with non zero surface tension and the heavier fluid below while there is no acceleration field: $\sigma \neq 0$, $\rho_1 > \rho_2$ and $\vec{g} = \vec{0}$. The general instability condition and the instability growth rate, Eqs. (1.23) and (1.22) then reduce to:

$$-\sigma k^2 > 0, \quad (1.28)$$

$$s_r = i \sqrt{\frac{\sigma k^3}{\rho_1 + \rho_2}}, \quad i \in \mathbb{C}, \quad (1.29)$$

and thus the configuration is stable as the instability condition can not be realised. The surface tension stabilises the plane interface between the two fluids. Even so, the perturbation induced by an initial disturbance is proportional to $e^{st} = e^{i\omega t}$ with $\omega = \sqrt{\frac{\sigma k^3}{\rho_1 + \rho_2}}$ and the interface oscillates at the pulsation ω .

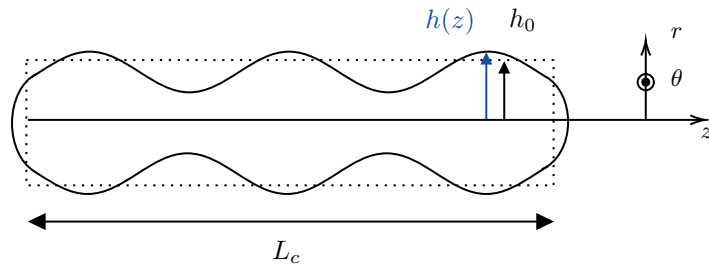


Figure 1.7: Schema of the evolution from a cylinder (dashed line) to a varicose (solid line) cross-section due to surface tension.

In the case of a plane interface, Fig. 1.5, the Rayleigh Plateau instability cannot be captured as there is no characteristic scale. Looking at the water jet coming from a tap with a low injection velocity, typically in the Rayleigh regime described in Sec. 1.2.2, one can notice the interface deformation leading to the pinching of the water jet and the generation of droplets, the three of them being the consequence of the capillary instability. Fig. 1.6c illustrates the development of the Rayleigh Plateau instability in the case of a liquid ligament. Let us consider the destabilisation of a ligament showing a characteristic scale h_0 , see Fig. 1.7. Villermaux

(2020) explains that, when distorted by a long wavelength varicose modulation of its cross-section a cylinder lowers its surface area at constant volume and, consequently the energy associated to the surface, until it reaches a minimum and eventually fragment. In the case of a cylinder, the perturbation can be of two kinds: longitudinal, i.e. along the z axis, or azimuthal, i.e. along the θ axis. Chandrasekhar (1961) recalls the result of Plateau that the liquid jet is stable for all purely non axisymmetric deformations but it is unstable for symmetric varicose deformations with wavelengths exceeding the circumference of the cylinder. Thus azimuthal disturbances are stable and the perturbation can be written in term of longitudinal deformation, such that: $h(z) = \langle h \rangle + \epsilon \cos(kz)$. Let us as well denote $V_c = \pi h_0^2 L_c$ the volume of the initial cylinder.

The energy associated to the surface is given by:

$$E = 2\pi\sigma \int_{L_c} h \sqrt{1 + h'^2} dz \quad (1.30)$$

Furthermore, in order to respect the volume conservation, the mean radius $\langle h \rangle$ follows:

$$V_c = \int_{L_c} \pi h^2 dz = \pi h_0^2 \int_{L_c} dz \quad (1.31)$$

which leads to:

$$\langle h \rangle = h_0 - \frac{\epsilon^2}{4h_0}, \quad (1.32)$$

meaning that the mean radius of the disturbed cylinder is smaller than the initial cylinder radius h_0 . Let us denote the mode wavelength $\lambda = 2\pi/k$. The difference of energy between the disturbed and undisturbed states is then $\Delta E = E - E_0$ with $E_0 = 2\pi h_0 \sigma \int dz$:

$$\frac{\Delta E}{E_0} = \frac{\epsilon^2}{4h_0^2} [(kh_0)^2 - 1] \quad (1.33)$$

$$(1.34)$$

The surface energy decreases for $\Delta E/E_0 < 0$, i.e. for $\lambda > 2\pi h_0$. This indicates that the modes of wavelengths larger than the cylinder perimeter are potentially unstable. In the inviscid limit, the most amplified wavelength is $\lambda \approx 9h_0$. More details about the determination of this wavelength and the mode stability can be found in Villermaux (2020). Finally, the inviscid growth rate of the Rayleigh Plateau instability writes (Chandrasekhar, 1961)

$$s_r^2 = \frac{\sigma}{\rho_l h_0^3} \frac{\mathcal{I}_1(kh_0)}{\mathcal{I}_0(kh_0)} (1 - (kh_0)^2) \quad (1.35)$$

where \mathcal{I}_0 and \mathcal{I}_1 are the modified Bessel functions of zero and first order. Note as well that the characteristic time of the Rayleigh Plateau stability is given by $\tau_c = \sqrt{\rho_l h_0 / \sigma}$.

1.4 Turbulence

The hydrodynamic instabilities previously introduced, Sec. 1.3, are fundamental in the fragmentation of a jet. Typically, the droplet formation in the Rayleigh regime, defined in Sec. 1.2.2, is fully determined by the Rayleigh Plateau instability. However, the complexity of the fragmentation mechanisms increases with the break-up regimes. For instance, the second wind-induced and the atomisation regimes imply strong aerodynamic interactions between the gas phase and either the liquid core or the droplets. They can turn out to be turbulent. Sec. 1.4.1 quantifies the turbulence in jet flows in typical irrigation configuration while Sec. 1.4.2 and 1.4.3, respectively, introduce the predictions of Kolmogorov and the intermittency of turbulence.

1.4.1 Fragmentation flows and turbulence

To quantify the turbulence engendered in regimes like the second wind-induced or the atomisation regime, it is necessary to have a look at the liquid Reynolds number based on the Taylor micro scale. The Taylor micro scale, denoted λ , expresses such that $\lambda^{-2} = \langle (\partial_x u_x)^2 \rangle / u_{rms}^2$. It was first defined by Taylor (1935b) who interpreted it as the length that determines the scale of the eddies responsible for the dissipation of energy. While the definition is of most relevance for experimental measurements of the strain rate $s_{i,j}$ or the energy dissipation rate ϵ in turbulent flows, the interpretation appears wrong. Tennekes & Lumley (1972) stated that λ is not a characteristic length scale of the strain rate field, does not represent a group of eddy sizes in which dissipative effects are strong nor is a dissipation scale. Indeed, the definition of λ relies on the chosen velocity scale u_{rms} with “no physical reason at all for this choice” (Tennekes & Lumley, 1972). Nonetheless, the Taylor micro scale enables a better understanding of turbulence, notably with the Reynolds number based on λ writing as $Re_\lambda = u_{rms}\lambda/\nu$ and which can be seen as the ratio of the large eddy time scale and the time scale of the strain rate fluctuation (Corrsin, 1959; Tennekes & Lumley, 1972). Under the assumption of isotropic turbulence, Re_λ rewrites as $Re_\lambda = (10/3)^{1/2}E/(\Omega^{1/2}\nu)$ where E and Ω are the mean energy and enstrophy, the energy related to vorticity, of the flow. A second scale of importance in turbulent flows is the integral scale L , commonly defined as the scale at which the energy is injected in the flow and firstly introduced by Taylor (1935a).

In the literature, turbulence is classically considered as fully developed when $Re_\lambda > 250–300$ (Pearson & Antonia, 2001). The Taylor micro scale Reynolds number is related to the integral scale Reynolds number Re_L such that $Re_\lambda \sim Re_L^{1/2}$ (Frisch, 1995). Even if this relation seems handy, the integral scale and the rms fluctuation velocity cannot be directly estimated from the injection Reynolds number Re_l , defined in Eq. (1.4), and further work is required to do so. Complementary, Ruffin *et al.* (1994) derived an analytical relation between the Taylor micro scale Reynolds number and the injection scale Reynolds number for round jet flows. When considering the turbulence in the liquid phase composed of a monofluid, the relation reduces to $Re_\lambda = A \times Re_l^{1/2}$ and the experiments give $A \approx 1.3$. Using this result and knowing that the injection Reynolds numbers for typical irrigation configurations in second wind-induced or atomisation regimes are larger than 40 000 (Felis *et al.*, 2020), it comes first that the lower bound of Re_l ensuring fully developed turbulence, $Re_\lambda > 250$, is equal to 3.6×10^4 and second that turbulence cannot be discarded in the study of fragmentation in agricultural like jets.

1.4.2 Predictions of Kolmogorov

Big whirls have little whirls that feed on their velocity,
and little whirls have lesser whirls and so on to viscosity
– in the molecular sense.

Lewis Fry Richardson, 1922

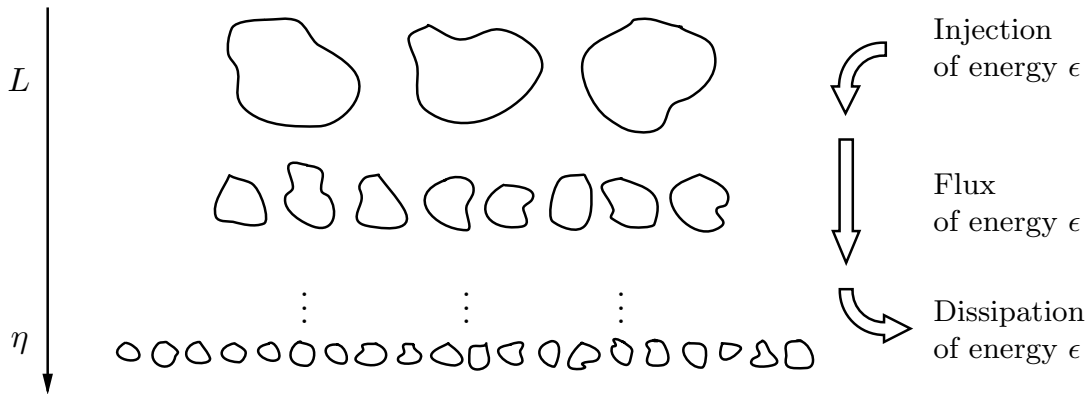


Figure 1.8: Schema of the turbulent energy cascade.

Following the idea of Richardson (1922), Kolmogorov (1941a,c) theorized the idea of vortex cascade, illustrated in Fig. 1.8, in the context of isotropic turbulence. Complementarily to the Taylor micro scale λ and the integral scale L introduced in Sec. 1.4.1, a third scale characterizes turbulent flows: the Kolmogorov scale η . This scale is the typical size of the energy dissipating scales, defined by $\eta = (\nu^3/\epsilon)^{1/4}$ (Kolmogorov, 1941c), at which the eddies die away because of viscosity. In those seminal papers, Kolmogorov defined the mean energy dissipation rate $\langle \epsilon \rangle$ between the different flow scales and proposed two hypotheses of similarity for describing isotropic turbulence. These hypotheses read as (Anselmet *et al.*, 2001):

1. The Reynolds number is very large, presumably infinite.
2. In the limit of infinite Reynolds number, turbulence properties are universal since the hierarchy of scales is then sufficiently large to generate a range of small scales whose properties are no longer influenced by the way energy is produced by the large scales, at which the energy is injected and which are specific to the flow configuration. These small scales are isotropic since their properties do not depend on any particular direction within the flow.
3. For this range of scales with universal properties, two subranges can be drawn:
 - (a) a subrange of scales whose properties only depend on $\langle \epsilon \rangle$ which equals the rate of energy finally dissipated by the kinematic viscosity ν , referred to as the inertial range scale
 - (b) smaller scales which properties depend on both ν and $\langle \epsilon \rangle$, referred to as the dissipation range.

The assumptions (2) and (3) are respectively called the first and second hypotheses of similarity.

Several predictions can be derived from the latter hypotheses. Let us consider a scale l in the inertial range, i.e. $\eta \ll l \ll L$. In order to capture the phenomenology of interest, new

key observables have to be introduced here: the velocity increments $\delta\mathbf{u}(\mathbf{r}, \mathbf{l}, t)$ and the velocity structure function $S_p(l)$ defined as

$$\delta\mathbf{u}(\mathbf{r}, \mathbf{l}, t) = \mathbf{u}(\mathbf{l} + \mathbf{r}, t) - \mathbf{u}(\mathbf{r}, t), \quad (1.36)$$

$$S_p(l) = \langle \|\delta\mathbf{u}(\mathbf{r}, \mathbf{l}, t)\|^p \rangle_{\mathbf{r}, t}. \quad (1.37)$$

where $\delta\mathbf{u}(\mathbf{r}, \mathbf{l})$ is the difference of velocity between two points of space separated by a scale \mathbf{l} while $S_p(l)$ is a function of $p \in \mathbb{R}_*$ with $l = \|\mathbf{l}\|$ and represents the statistical moment of order p of the distribution of velocity increments. The subscript \parallel is commonly used to indicate when a longitudinal separation is considered, typically the longitudinal velocity increment $\delta u_{\parallel}(r, l)$. In addition, the superscript $*$ denotes the normalisation by η and/or the Kolmogorov velocity scale defined by $U_k \equiv (\nu\langle\epsilon\rangle)^{1/4}$, then $\delta u_{\parallel}^* \equiv \delta u_{\parallel}/U_k$ and $l^* \equiv l/\eta$. A first prediction regards the variance of the longitudinal velocity increments, i.e. its statistical moment of order 2, $S_2(l)$. It is predicted to follow a power law in the physical space such that

$$\langle (\delta u_{\parallel}^*)^2 \rangle_{\mathbf{r}, t} = C_2 l^{*-2/3} \quad (1.38)$$

where C_2 is the Kolmogorov constant. This indicates that larger scales have more dispersed velocity increments than the smaller scales or, equivalently, that the velocity increments of the small scales relatively to the ones of the large scales are more grouped around their mean value. The homologue of Eq. (1.38) in the spectral space relates the one dimensional energy spectrum $E(k_{\parallel})$ of u_{\parallel} with the one dimensional wavenumber k_{\parallel} as

$$E^*(k_{\parallel}^*) = \alpha_{u_{\parallel}} k_{\parallel}^{*-5/3} \quad (1.39)$$

which is the well-known $-5/3$ decay of the Kolmogorov cascade spectrum. It is classically considered in the turbulence community that C_2 has a magnitude of about 2 (Yaglom, 1981). The constant $\alpha_{u_{\parallel}}$ is related to C_2 via the isotropic relation $C_2 = 4.02\alpha_{u_{\parallel}}$ (Monin *et al.*, 1975). A third prediction from the theory of isotropic turbulence extends Eq. (1.38) and gives the expression of the statistical moments of higher order of the longitudinal velocity increments which writes as:

$$\langle (\delta u_{\parallel}^*)^p \rangle = C_p l^{*-p/3} \quad (1.40)$$

Note that the Kolmogorov (1941a) four-fifths law is retrieved from (1.40) for $p = 3$ and $C_3 = -4/5$, which is a truly universal constant as the fourth-fifth law is directly derived from the Navier Stokes equation. Conversely to C_3 , the universality of the coefficients C_p , $p \neq 3$, is questioned by Landau & Lifshitz (1959) and Frisch (1995) pointed out that they may depend on the flow if the turbulence production mechanism of the latter implies at least two scales. Finally, it is worth taking notice of the possibility to consider an assumption of scale invariance to avoid the pitfall of the coefficient universality (Frisch, 1995), §6.4.3. More details on the phenomenology of isotropic turbulence and the K41 theory can be found in the work of Monin *et al.* (1975) & Frisch (1995). For an English translation of the seminal papers of Kolmogorov, the reader can refer to Kolmogorov (1991a,b).

Nonetheless, some limits exist to the K41 theory. The following ones are the ones summarized by Anselmet *et al.* (2001). First of all, the assumption that the Reynolds number should be very large is not verified under most laboratory conditions. Some experimental data indicate

that the magnitude of the scaling exponent ζ_p , such that $S_p(l) \propto l^{\zeta_p}$, decreases for increasing values of l , meaning that an inertial range of scales in the sense of K41 cannot be unambiguously defined. Local isotropy is also not strictly satisfied over the so called scaling-range and could only be valid asymptotically, as for the inertial range. Finally, ϵ is a random function and the use of $\langle \epsilon \rangle$ is not sufficient to describe the cascade of energy and its inherent intermittency. While equations (1.38) and (1.39) are slightly affected by small-scale intermittency, equation (1.40) becomes poorer for increasing order.

1.4.3 Intermittency

Internal intermittency is a key feature of fully turbulent flows. At first sight, it can be seen as the non-uniform distribution of eddy formations in a stream and can be depicted by indicators like the square of the vortex field or the energy dissipation velocity (Novikov, 1970). Two kinds of intermittency can be observed and have to be distinguished: the intermittency in a sporadically turbulent stream, for example at the limit between turbulent and non turbulent regions in a jet flow (Corrsin & Kistler, 1955; Borrell & Jiménez, 2016), and the intermittency in a developed turbulent stream, which is under consideration here.

1.4.3.1 The historical logarithmic model (Kolmogorov, 1962)

Following the theoretical remarks of Landau & Lifshitz (1959) on the universality of scale properties in the inertial and dissipation ranges, reformulated in its accepted modern form by Kraichnan (1974), and the work of Obukhov (1962), Kolmogorov (1961, 1962) introduced a third hypothesis, known as the refined similarity hypothesis, where $\langle \epsilon \rangle$ is replaced by the local average of ϵ over a sphere of radius r and of volume V . The new fluctuating quantity, $\epsilon_r \equiv (1/V) \int \epsilon(x) dx$, is such that the stochastic variable $x_{u_{||}} \equiv \delta u_{||}(r)/(r\epsilon_r)^{1/3}$ is universal for sufficiently small r in the limit of infinitely large Reynolds number. Furthermore, the author also assumed that ϵ_r follows a logarithmic normal distribution and that the variance of $\ln(\epsilon_r)$ is given by:

$$\sigma_{\ln \epsilon_r}^2 = A + \mu \ln \left(\frac{L}{r} \right) \quad (1.41)$$

where μ is the intermittency parameter, assumed to be universal, and A is a constant likely to depend on the flow macro structure.

To explain the assumption of a logarithmic distribution for ϵ_r , let us consider the energy cascade depicted in Sec. 1.5.2 and assume that it undergoes n break-ups with $n \rightarrow +\infty$. In addition, consider that it is a random cascade such that the size l_n at the step n equals $l_{n-1} \times b_{n-1}$ where b_{n-1} is a random breakdown coefficient. Thus, l_n can be expressed depending on the initial size l_0

$$l_n = l_0 \prod_{i=1}^n b_i \quad (1.42)$$

and, according to the Central Limit Theorem, the distribution of the breakdown coefficients b_i should follow a logarithmic normal density.

However the logarithmic normal model raises two major inconsistencies. Firstly, Novikov (1970) showed that the logarithmic normal model implies a quadratic dependence of ζ_p over the

order of moment p , which violates properties of the scaling exponent and mass conservation, see Eq. (1.50) and 1.61. Secondly, this model implies supersonic velocities at high Reynolds number (Frisch, 1995). Frisch (1995) also recalled that random cascade models fail to respect the inequality of Novikov because of the non conservative character of the cascade and questions the logarithmic model by asserting that “a mere product of a large number of independently and equally distributed positive random variables does not have an approximately logarithmic normal distribution”. Furthermore, Kraichnan (1974) stated as well that it is doubtful that small scales exhibit asymptotic logarithmic normal distribution because of the non linearity of the dynamical processes and because the sum of independent logarithmic normal variables is not logarithmic normal. Thus, although the distribution of the breakdown coefficients tends toward the logarithmic normal distribution, the moments do not tend towards the expression which results from the asymptotic distribution. Last but not least, even if the moments cannot be calculated from the asymptotic distribution, under the assumption of scale similarity and thanks to the Carleman condition Eq. (1.52), Novikov (1970) pointed that the distribution of the breakdown coefficients is uniquely defined by its moments.

1.4.3.2 Going beyond the shortcomings of the logarithmic normal model

In order to overcome the two inconsistencies of the logarithmic normal model, a large range of models has been developed to attempt to describe the intermittency of turbulence. Among the consequent list, let us mention several: the most famous β -model of Frisch *et al.* (1978), the multifractal model of Parisi & Frisch (1985) following the pioneer work of Novikov & Stewart (1964), the shell model of Desnyansky & Novikov (1974), the model of Jiménez (1998) based on the geometry of the vortex filaments and the multifractal model in connection with vortex filaments of She & Leveque (1994). Fig. 1.9 recalls the agreement of several models tested against the experimental measurements of ζ_p from Anselmet *et al.* (1984). It is worth noting that the logarithmic Poisson model, which agrees remarkably well with the extended scale similarity data of Benzi *et al.* (1995), directly comes from the model of She & Leveque (1994) who derived a relation for ζ_p without any adjustable parameters: $\zeta_p = p/9 + 2 - 2(2/3)^{p/3}$. It is named so because the latter relation of ζ_p corresponds to a logarithmic Poisson distribution (Dubrulle, 1994). Finally, bridging the gap between the multifractal approach and the vortex filament point of view seems possible by coming back to the circulation of vorticity, notably with the formalism of Migdal (1994). Proposing a comprehensive review of the previously mentioned intermittency models outreaches the scope of this thesis. Instead, the focus will be given to the logarithmic model of Novikov (1970) and its connection with drop size modelling (Novikov & Dommermuth, 1997), both laid out in Sec. 1.5.2.

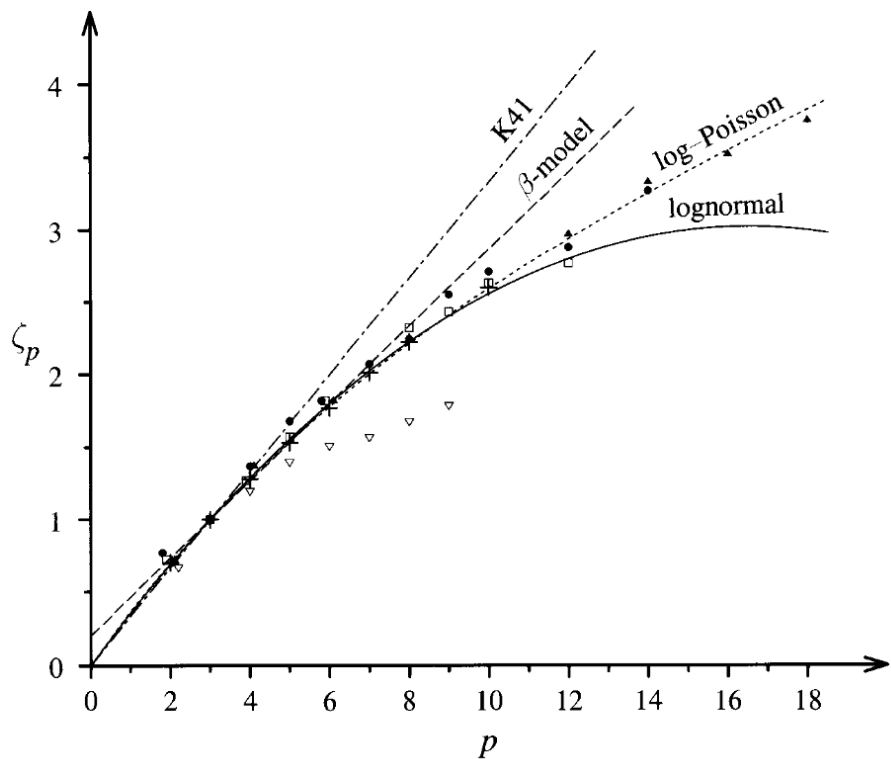


Figure 1.9: Exponent ζ_p of the structure functions in the time domain of order p vs p . ∇ : data from Van Atta & Park (1972); \bullet , \square and \blacktriangle : data from Anselmet *et al.* (1984) with $Re_\lambda \in \{515, 536, 852\}$; $+$: data processed by extended self similarity (Benzi *et al.*, 1995); Straight chain line: $\zeta_p = p/3$ (K41); dashed line: β -model with $D = 2.8$; solid line: logarithmic normal model with $\mu = 0.2$, Eq. (1.41); dotted line: logarithmic Poisson model. Taken from Frisch (1995).

1.5 Aggregation & cascade: two theories of fragmentation for the drop size distribution

At first sight, the fragmentation of a jet or a droplet conveys the idea of a straightforward cascade from a source object to a population of smaller elements, in a similar fashion to the Richardson (1922) cascade, see Fig. 1.8, or to solid particle grinding as described by Kolmogorov (1941b). Looking closer to the dynamics of liquid ligaments in fragmentation flows though highlighted that those ligaments undergo a reverse cascade before their break-up, i.e. some parts of the ligament aggregate before the ligament breaks (Marmottant & Villermaux, 2004). Numerous studies and droplet size models were carried over the last decades, a large part being reviewed in Villermaux (2007, 2020) and presented in the references therein. Among those, the focus is given here on two models of very different, opposite nature respectively relying on aggregation dynamics and intermittency of the turbulence cascade.

Taking benefits from the analytical framework of hydrodynamic instabilities, notably the ones introduced in Sec. 1.3.2, and the experimental observations of aggregation dynamics during the fragmentation of a liquid ligament, the aggregation based model enables to derive a universal law for the size distribution of droplets generated by a ligament break-up and, on this basis, proposes a droplet size distribution for the overall spray. Conversely, the intermittency based model is a purely statistical model derived from the scope of turbulence intermittency modelling and proposes a size distribution in tight connection with the distribution of energy breakdown coefficients in a mathematical framework which overcomes the shortcomings of random cascade models presented in Sec. 1.4.3. To encapsulate concisely the difference between the two, let us say that the intermittency based model derives from the statistical framework of turbulence cascade with intermittency correction of fine scale structures while the aggregation based model derives from the analytical framework of hydrodynamic instabilities and aggregation dynamics. Each of them is respectively introduced in Sec. 1.5.1 and 1.5.2.

1.5.1 From internal turbulence intermittency to the droplet sizes

Novikov & Dommermuth (1997) pointed out the effect of intermittency on the size of droplets generated by a turbulent spray. By implementing an intermittency correction they observed an increase of 18% in the typical drop size in the spray and, thus, highlighted the close connection between the distribution of the droplet sizes and of the energy dissipation in a fully turbulent spray. On the basis of this claim, the authors derived a droplet size distribution from the framework of intermittency in turbulence cascade relying on breakdown coefficients similar to what is introduced in Sec. (1.4.3), however with a mathematical apparatus overcoming the shortcomings of random cascades. The following sections introduce the developments of Novikov and co-workers to model the turbulence intermittency and its connection with drop size distribution in a turbulent spray.

1.5.1.1 Modelling intermittency with the breakdown coefficients

Let us consider a scale r in the inertial range of scales : $l_* \ll r \ll L$, where l_* is an inertial scale which can differ from the Kolmogorov scale due to the intermittency correction. Three segments of size r , ρ and l are chosen from the inertial range such that they are inserted in one another and $r < \rho < l$. Let us consider the breakdown coefficients as defined by Novikov (1970)

and consider a non negative random function $y(x)$, which could be the square of the vorticity or the square of the longitudinal derivative along the streamwise direction. The definition of the breakdown coefficient between the scale r and l is then

$$q_{r,l}(h, x) = y_r(x')/y_l(x), \quad r < l, \quad (1.43)$$

$$y_l(x) = \frac{1}{l} \int_{x-l/2}^{x+l/2} y(x_1) dx_1, \quad (1.44)$$

$$|h| \leq \frac{1}{2}, \quad h = \frac{x' - x}{l - r} \quad (1.45)$$

where the condition on h implies that the smaller section is included in the larger one. Indeed the left and the right hand sides of the inequality respectively rewrite as $x - l/2 \leq x' + r/2$ and $x' + r/2 \leq x + l/2$. h accounts for the non homogeneity of the breakdown but can be discarded by assuming an homogeneous breakdown (Novikov, 1970). Two consequences arise from this definition. Firstly, by construction, the coefficients verify $q_{r,l} = q_{r,\rho} q_{\rho,l}$. Secondly, knowing that y is non negative, the breakdown coefficients also respect

$$q_{r,l} \leq l/r. \quad (1.46)$$

In addition, let us define the moments of the distribution of the breakdown coefficients such that

$$a_p(r, l, h) = \langle q_{r,l}^p(h, x) \rangle \quad (1.47)$$

In order to take benefit of a scale similarity hypothesis, two conditions have to be respected: (i) the probability distribution of the breakdown coefficients depends only on the ratio of the corresponding scales, (ii) $q_{r,\rho}$ and $q_{\rho,l}$ are statistically independent. From those conditions and Eq. (1.47), it comes that the moments of the breakdown coefficient distribution follow a power law in l/r scaling as

$$a_p(l/r) = \left(\frac{l}{r}\right)^{\mu(p)} \quad (1.48)$$

Additional constraints on $\mu(p)$ can be derived. Combining Eq. (1.46) and Eq. (1.48) gives

$$\mu(p) - \mu(p + \delta) \leq \delta, \quad \delta \geq 0, \quad (1.49)$$

which leads to a first constraint on $\mu(p)$, setting that by definition $\mu(0) \equiv 0$, such that

$$\mu(p) \leq p \quad (1.50)$$

Furthermore, disregarding the non homogeneity of the breakdown implies that $\mu(1) = 0$ and $0 < \mu(2) < 1$ (Novikov, 1970) with $\mu(2) = \mu$ the intermittency coefficient of the logarithmic normal model, Eq. (1.41) (Kolmogorov, 1962). Thus, Eq. (1.49) gives a stronger constraint on $\mu(p)$

$$\mu(p) \leq \mu + p - 2, \quad p \geq 2 \quad (1.51)$$

Novikov (1970) noted that the inequality (1.50) ensures the fulfilment of the Carleman condition, given by

$$\sum_{p=1}^{+\infty} (a_{2p})^{-1/2p} = +\infty \quad (1.52)$$

which is a sufficient condition for the breakdown coefficient distribution to be uniquely defined by moments of integer orders, property that the limiting logarithmic normal distribution from the Central Limit Theorem does not have. Using the early experimental measurement set of atmospheric surface layer of Wyngaard & Pao (1972), Atta & Yeh (1973) investigated the accuracy of the predictions drawn by Novikov (1970) and found out a systematic departure between the predicted statistics and the experimental data.

Now that general considerations were drawn about $\mu(p)$, let us say that y is the energy dissipation at the scale r , denoted ϵ_r . The distribution of the breakdown coefficient is denoted $W(q, l/r)$ and the coefficients now express as

$$q_{r,l} = \epsilon_r / \epsilon_l \quad (1.53)$$

Let also $Q(\ln q_{r,l})$ be the probability density of the breakdown coefficient logarithm and $\psi(s, l/r)$ be the corresponding characteristic function, defined by $\psi(s, l/r) = \langle \exp(is \ln q_{r,l}) \rangle$. Q and ϕ are related such that $\psi(s, l/r) = \int_0^{l/r} Q(\ln q_{r,l}) dq$. Note as well that Q and W respect $Q(\ln q) = qW(q)$ (Feller, 1971). If $\mu(p)$ has analytical continuation in the complex domain, then $\psi(s, l/r)$ and $W(q, l/r)$ are related by (Novikov, 1994)

$$\begin{cases} \psi(s, l/r) = \int_0^{l/r} q^{is} W(q, l/r) dq = (l/r)^{\mu(is)} \\ W(q, l/r) = \frac{1}{2\pi q} \int_{-\infty}^{+\infty} \exp[-is \ln(q) + \mu(is) \ln(l/r)] ds \end{cases} \quad (1.54)$$

where the expression of $W(q, l/r)$ is the inverse Fourier transform of $\psi(s, l/r)$. One could then calculate $W(q, l/r)$ from Eq. (1.54). However, in order to ensure that the model has a physical and mathematical meaning, the probability density $W(q, l/r)$ has to be non negative and properly normalized by integration over the finite interval $[0, l/r]$ for arbitrary l/r (Novikov, 1994). Generally speaking, verifying those conditions analytically or numerically is not easy.

To overcome this issue, Novikov (1994) proposed to embed the concept of scale similarity into the theory of infinitely divisible probability distributions, opening up the opportunity to use the related mathematical apparatus. Novikov observed that, for arbitrary l/r and arbitrary integer n , Eq. (1.54) verifies

$$\psi(s, l/r) = \psi^n(s, (l/r)^{1/n}) \quad (1.55)$$

meaning that the random variable $\ln q_{r,l}$ has an infinitely divisible probability distribution. The Lévy-Baxter-Shapiro theorem gives the general form of the characteristic function of an infinitely distribution concentrated on $[0, +\infty[$

$$\chi(s) = \exp \left[ibs - \int_0^{+\infty} \frac{1 - e^{isx}}{x} P(dx) \right], \quad b \geq 0, \quad (1.56)$$

where P is a measure on the open interval $]0, +\infty[$ such that $(1+x)^{-1}$ is integrable in respect to P . The definition of an infinitely divisible distribution and the Lévy-Baxter-Shapiro theorem can be found in Chapter 17 of Feller (1971). Let us consider the variable $z_{r,l} = -\ln[(r/l)q_{r,l}]$

and denote $p = -is$. Replacing $q_{r,l}$ by $z_{r,l}$ in the definition of ψ and using Eqs. (1.54) and (1.56) gives:

$$\mu(p) = \kappa p - \int_0^{+\infty} \frac{1 - e^{-px}}{x} F(dx) \quad (1.57)$$

$$\int_0^{+\infty} \frac{1 - e^{-x}}{x} F(dx) = \kappa, \quad \kappa \leq 1 \quad (1.58)$$

where $\kappa = 1 - b/\ln(l/r)$ and $F(dx) = P(dx)/\ln(l/r)$ has the same properties as P . The condition (1.58), derives from the assumption of homogeneity of the breakdowns, which imposes $\mu(1) = 0$ and $0 < \mu(2) < 1$. Thus, the intermittency coefficient can be modelled differently by choosing a measure F . For example, choosing $F'(x) = Ax^{\alpha-1} \exp(-x/\sigma)$ with A , α and σ three positive constants, Novikov (1994) derived:

$$\mu(p) = \kappa \left[p - \frac{(p\sigma + 1)^{1-\alpha} - 1}{(\sigma + 1)^{1-\alpha} - 1} \right], \quad \alpha \neq 1 \quad (1.59)$$

$$\mu(p) = \kappa \left[p - \frac{\ln(p\sigma + 1)}{\ln(\sigma + 1)} \right], \quad \alpha = 1 \quad (1.60)$$

Finally, once $\mu(p)$ is modelled, it is possible to derive the corresponding energy distribution $W(q, l/r)$ using equation (1.54) without making any assumption on W . This was done by Saito (1992) and Vanyan (1996) who respectively considered $(\alpha, \kappa, \sigma) = (1, 1, 0.283)$ and $(\alpha, \kappa) = (1, 1/2)$ and obtained satisfactory agreement with experimental data. Note that considering $(\kappa, \alpha) = (1, 1)$ gives a Γ distribution of the logarithm of the breakdown coefficients, $z_{r,l} = -\ln[(r/l)q_{r,l}]$.

1.5.1.2 Connecting the intermittency model with the droplet size distribution

Novikov & Dommermuth (1997) showed the effect of the intermittency correction on the evaluation of the typical droplet size in turbulent spray and stated that there is a close connection between the drop size and the energy dissipation. Assuming that the droplets in a turbulent spray undergo a sequential break-up cascade and that this process can be described similarly to the energy dissipation in a turbulent flow, the authors propose a law to describe the drop size distribution. Let us consider a disintegrating water fragment of size l_1 which undergoes a sequential cascade of break-ups. At the stage n , the final size l of an individual droplet is $l \equiv l_{n+1} = l_1 \prod_{k=1}^n b_k$ where $b_k = l_{k+1}/l_k$ are random break-up coefficients. We can then define a non negative random variable y such that $y \equiv -\ln(l/l_1) = -\sum_{k=1}^n \ln b_k$ whose distribution and characteristic function are denoted P and ψ_y . As shown in the context of energy dissipation (Novikov, 1970), it cannot be concluded that, for large n , the drop size distribution is a logarithmic normal distribution. In fact, the moments given by a such a law are:

$$\langle (l/l_1)^p \rangle = \exp(-ap + \sigma^2 p^2) \quad (1.61)$$

and, for large p , this equality exceeds unity, contradicts the condition $b_k \leq 1$ and breaches the mass conservation. By choosing a measure $F'(x) = \sum_i A_i \Gamma(\alpha_i)(x/\sigma_i)^{\alpha_i-1} \exp(-x/\sigma_i) + \sum_j B_j x_j \delta(x - x_j)$ with A_i , α_i , σ_i , B_j and x_j being positive constants, thus ensuring the non

negativity of $F'(x)$, and substituting this expression in Eq. (1.57), Novikov & Dommermuth (1997) were able to derive an analytical expression of $\mu(p)$

$$\mu(p) = \kappa p - \sum_i A_i \left[\frac{(p\sigma_i + 1)^{1-\alpha_i} - 1}{1 - \alpha_i} \right] - \sum_j B_j (1 - e^{-px_j}) \quad (1.62)$$

For $\alpha_i = 1$, the expression in the square brackets must be replaced by $\ln(p\sigma_i + 1)$. The probability density P of y is then given by the inverse Fourier transform of the characteristic function ψ_y , in the same fashion as Eq. (1.54). In the case $\alpha_1 = 1/2$, the distribution of y writes as:

$$P(y) = \frac{a^{3/2}}{\sqrt{2\pi}\sigma y^{3/2}} \exp\left(-\frac{a}{2\sigma^2}(ay^{-1/2} - y^{1/2})^2\right), \quad y \geq 0 \quad (1.63)$$

where $a = \langle y \rangle$ and $\sigma^2 = \langle (y - a)^2 \rangle$. Hence, this directly connects the droplet size distribution in a fully turbulent spray and the internal intermittency of turbulence. A decade after the developments of Novikov, Rimbert & Sero-Guillaume (2004) simplified the approach of infinitely divisible distributions by considering log-stable distributions for high Weber sprays. Using this simplified way, but still offering a wide mathematical apparatus, Rimbert & Castanet (2011) were able to model the multimodal distribution resulting from the droplet fragmentation in the bag break-up regime, a regime where the droplets deform in a bag-like shape before bursting, with a crossover between the Rayleigh Taylor instability and the turbulent cascade mechanism.

1.5.2 Aggregation scenarii

Contrary to the well known cascade process, a close look to the dynamics of liquid ligaments points out a process of aggregation during the ligament break-up, and this in a large variety of configurations, as for ligaments modelled by magnetic necklaces (Vledouts A. *et al.*, 2015, 2016) or produced by a fragmenting coaxial jet (Marmottant & Villermaux, 2004; Villermaux *et al.*, 2004), by a conical sheet (Kooij *et al.*, 2018) or during the impact of a drop on a solid surface (Villermaux & Bossa, 2009; Villermaux & Bossa, 2011). After a general introduction on the aggregation dynamics, the description of the drop size distribution in the context of ligament-mediated spray formation is presented.

1.5.2.1 Introduction to aggregation dynamics

Let us consider an initial population of small elements which undergoes an aggregation process. Those elements can coalesce and form clusters, whose sizes increase timewise in average. The detailed description of the dynamics of such processes was given for the first time by von Smoluchowski (1917). The number of clusters with a volume between v and $v + dv$ is denoted $n(v, t)$ while the aggregation frequency between the clusters of volume v and v' is denoted $K(v, v')$. The total number of clusters is $N(t) = \int_0^{+\infty} n(v, t)dv$ and the aggregation kinetics respects a population balance equation (PBE) without advection term:

$$\partial_t n(v, t) = -n(v, t) \int_0^\infty K(v, v') n(v', t) dv' + \frac{1}{2} \int_0^v K(v', v - v') n(v', t) n(v - v', t) dv' \quad (1.64)$$

The first integral describes the loss rate of particles of volume v , which disappear because they aggregate with other elements. The second integral describes the growth rate of particles of

volume v resulting from the aggregation of particles of volume v' and $v - v'$. Friedlander (2000) defines the collision rate between elements by $K(v, v')n(v)n(v')dvdv'$.

1.5.2.2 Spray formation

When a jet is injected into a gaseous medium, the shear between the two phases triggers instabilities of Kelvin Helmholtz and forms waves on the jet interface, see Sec. 1.3.2.1. The amplitude of those undulations grows until it reaches a tipping value at which they undergo a transverse Rayleigh Taylor destabilization, see Sec. 1.3.2.2, due to the acceleration of the Kelvin Helmholtz waves pointing towards the gas phase and perpendicularly to the interface (Marmottant & Villermaux, 2004). The corrugations issuing from the Rayleigh Taylor instability then elongate to form ligaments which detach from the core and break instantly due to the capillary instability (Villermaux *et al.*, 2004; Eggers & Villermaux, 2008). In the aggregation scenarii, those ligaments are the fundamental cornerstone of the generation of droplets and the control of their size.

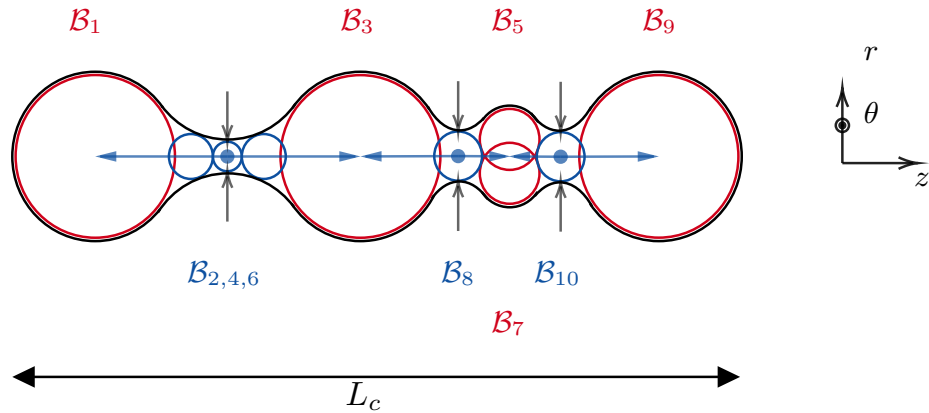


Figure 1.10: Schema of a ligament and its composing blobs. The black and blue arrows respectively indicate the direction of the surface tension forces and the direction of the liquid motion. The blue dots represent the centres of the liquid bridges. The red and blue colours for the blobs respectively indicate stable and unstable configurations.

Before diving in the dynamics of ligament break-ups, let us first have a look on their composition. It is possible to consider the ligaments to be constituted of blobs having different sizes. Here, the designation “blob” corresponds to a volume encapsulated between the interface corrugations and which can be seen as a candidate droplet. We call it candidate droplet as, depending on the evolution of the ligament, it could eventually lead to the generation of a droplet when the ligament breaks. While all the droplets originate from a blob, all the blobs do not necessarily generate a droplet. Fig. 1.10 illustrates the case of a simple ligament composed of ten blobs \mathcal{B}_i , $i \in [1, 10]$. During the ligament break-up, the blobs can interact with each other by aggregating or detaching. Two kinds of blobs can be distinguished, hinging on their position relatively to the interface curvature. Depending on the sign of the curvature, positive or negative, the blobs are coloured and numbered differently, respectively in red with odd indices and in blue with even indices. The sections of negative curvature are liquid bridges connecting the maxima of the varicose undulation. Due to the Rayleigh Plateau instability, see Sec. 1.3.2.3, the surface tension forces, indicated by the black arrows, are directed towards the centre of the liquid bridges, making them unstable and directing the liquid motion, indicated

by the blue arrows, outwards the bridges. As a consequence, the blue blobs pour into the neighbouring red blobs, the liquid bridges pinch off and the remaining blobs become actual droplets. The case of the blobs \mathcal{B}_5 and \mathcal{B}_7 requires a little more attention. On a first step of the ligament break-up, they will absorb part of the volume of the neighbouring blue blobs $\mathcal{B}_{8,10}$ and eventually merge together. On a second step, depending on the force equilibrium during the break-up, they could generate a droplet or merge with a larger, neighbour red blob. If both liquid bridges pinch off at some point, $\mathcal{B}_{5,7}$ could generate a droplet. If one of the liquid bridge remains, then $\mathcal{B}_{5,7}$ would pour into the larger blob they are still connected to. Besides, not only it is possible to consider the ligaments to be composed of blobs but also to be composed of several independent, adjacent layers of sub-blobs covering all the ligament volume (Villermaux *et al.*, 2004).

Let us denote $n(d, t)$ the number PDF of blobs of size d and $n(d, t)dd$ the number of blobs of size between d and $d + dd$ at an instant t . The total number of blobs in a ligament $N(t)$, the ligament length $L(t)$ and the ligament volume $V(t)$ then write as:

$$N(t) = \int_0^{+\infty} n(d, t)dd, \quad L(t) = \int_0^{+\infty} dn(d, t)dd, \quad V(t) = \int_0^{+\infty} d^3 n(d, t)dd \quad (1.65)$$

and the initial volume of a ligament is denoted $V_0 = d_0^3$. The random motion in the ligament is supposed to result in Λ independent layers composed of sub-blobs, where Λ reads as a quantification of the ligament corrugation: $\Lambda = O(1)$ for a very corrugated interface whilst Λ tends to $+\infty$ for a perfectly smooth interface. The size of the sub-blobs in the Λ layers is denoted d' and the sub-blob size distribution in each layer is denoted $q(d', t)$, with q satisfying $\int_0^{+\infty} q(d', t)dd' = 1$. During the evolution of the ligament, the sub-blobs of the different layers can interact with each other, similarly to the simple case described in Fig. 1.10. Under the assumption of random interactions between the sub-blobs of the Λ layers, the evolution of $q(d', t)$ follows a convolution process (Friedlander, 2000). Consequently, the distribution of the blob sizes d derives from the convolution of the distribution q by itself as many times as there are layers in the ligaments, i.e. Λ times, and writes as $n(d, t) = N(t) \cdot q(d', t)^{\otimes \Lambda}$, where \otimes denotes the convolution product. Subsequently, the evolution equation of $n(d, t)$ is given by

$$\partial_t n(d, t) = -n(d, t)N(t)^{\gamma-1} + \frac{1}{3\gamma - 2} n(d, t)^{\otimes \gamma} \quad (1.66)$$

where $\gamma = 1 + 1/\Lambda$. In his work, von Smoluchowski (1917) noted that processes evolving by self-convolution, as the one discussed here, generate exponential distributions. This implies that Eq. (1.66) admits a Γ distribution as asymptotic solution (Villermaux *et al.*, 2004). Let us detail this non trivial result. Recalling that the ligament break-up is governed by the auto convolution process of $n(d, t)$ and that the distributions $q(d', t)$ in the ligament layers are supposed independent, the size distribution $p_B = n(d, t)/N(t)$ of the droplets at the instant t_b of the ligament break-up can be expressed as the Λ -convolution of an elementary distribution $p_1(d) = q(d, t_b)$:

$$p_B(d) = p_1(d)^{\otimes \Lambda} \quad (1.67)$$

Choosing a kernel $K(v, v')$, homogeneous in v and v' , to solve the equation of the aggregation kinetics (1.64), leads to an exponential function for the asymptotic solution when t tends towards $+\infty$ (Friedlander & Wang, 1966; van Dongen & Ernst, 1985; Friedlander, 2000). Also,

this solution is attractive whatever is the initial distribution. Furthermore, when a ligament detaches from the liquid core, the only known parameter is its diameter at break-up ξ_B . Besides, ξ_B characterizes the average size of the subsequent droplets (Villermaux *et al.*, 2004) and it makes it a good candidate to parametrise the droplet distribution resulting from the ligament break-up. Having those arguments in mind, it is possible to model p_1 as an exponential function parametrised by ξ_B

$$p_1(d) = \frac{1}{\xi_B} \exp\left(-\frac{d}{\xi_B}\right). \quad (1.68)$$

The size distribution p_B of the droplets after the ligament break-up then rewrites as (Feller, 1971)

$$p_B(d/\langle d \rangle) = \frac{1}{\langle d \rangle} \frac{\Lambda^\Lambda}{\Gamma(\Lambda)} x^{\Lambda-1} e^{-\Lambda x} \quad (1.69)$$

where $\langle d \rangle = \frac{1}{N(t)} \int_0^{+\infty} d n(d, t) dd$ is the instantaneous average drop size and $\langle d \rangle = \Lambda \xi_B$. The distribution given by (1.69) is a Γ distribution parametrized by Λ , the number of independent layers composing a ligament. Such a distribution illustrates that the subsequent droplet population is monodisperse with a narrow size distribution when the ligament shows a smooth envelope, $\Lambda \rightarrow \infty$. Conversely, when the ligament envelope is corrugated, $\Lambda = O(1)$, the population is polydisperse with a broad size distribution. This description of the drop size distribution p_B after the break-up of a ligament is claimed to be universal (Villermaux *et al.*, 2004; Marmottant & Villermaux, 2004).

Eq. (1.69) models the sizes of the droplets generated at a ligament break-up on the basis of the ligament diameter ξ_B . But, depending on the flow configuration, the ligaments are not necessarily monodisperse in size and can show a narrow or broad distribution of diameters ξ_B . In order to describe the size distribution $p(d)$ of the droplets produced overall the jet, the distribution p_B has to be combined with the size distribution of the ligaments, p_L , such that:

$$p(d) = \int_0^{+\infty} p_L(d_0) p_B(d/d_0) \frac{dd_0}{d_0} \quad (1.70)$$

In order to explore the distribution of the ligament sizes p_L during fragmentation, Villermaux & Bossa (2011) carried out complementary analyses on drop impact. In the case of a drop impacting a solid surface, the drop creates a sheet and ligaments are expelled from the sheet outer rim. Stating that the rim is a toroidal ligament, the authors argue that the ligament size distribution follows the distribution of the rim corrugations and conclude that p_L is gamma distributed. The distributions p_L and p_B thus express as:

$$p_L(d_0/\langle d_0 \rangle) = \frac{1}{\langle d_0 \rangle} P_\Gamma(m, d_0/\langle d_0 \rangle), \quad p_B(d/d_0) = \frac{1}{d_0} P_\Gamma(n, d/d_0) \quad (1.71)$$

where P_Γ represents the Γ distribution given in Eq. (1.69). The parameters m and n represent the order of the size distribution of respectively the ligaments and the droplets resulting from the ligament break-ups. n also denotes the ligament corrugation, previously denoted Λ . Injecting those two distributions into (1.70) gives the global size distribution of the droplets generated by the fragmentation flow (Villermaux & Bossa, 2011):

$$p(x = d/\langle d \rangle) = \frac{2m^m n^{(m+n)/2} (mx)^{(n-m)/2} x^{m-1}}{\Gamma(m)\Gamma(n)} \mathcal{K}_{m-n}(2\sqrt{nmx}) \quad (1.72)$$

1.5. Aggregation & cascade: two theories of fragmentation for the drop size distribution

where \mathcal{K}_{m-n} is the modified Bessel function of second kind of order $m - n$. Even if this distribution is derived in the context of drop impact, a configuration radically different from the one of jet fragmentation, the underlying mechanism selecting the sizes of the ligament is considered to be universal. Assuming that the size of the ligaments are Γ distributed, Kooij *et al.* (2018) obtained a good agreement between this model and the experimental droplet size distribution for the fragmentation of conical and flat sheets produced by commercial nozzles.

1.6 Objectives and outlines of the thesis

We have seen in the previous sections how to describe the fragmentation flows in different regimes using the three dimensionless numbers of Reynolds, Weber and Ohnesorge as well as the main concepts of the hydrodynamic instabilities and turbulence which underlie jet fragmentation. Furthermore, the extensive presentation of the theory of ligament-mediated fragmentation and intermittency driven sprays highlighted two different, conceptually opposed ways for modelling the size distribution of the subsequent droplets. Now that the general frame of the thesis is set, it is possible to draw the questions we will try to answer.

Focusing on agricultural like configurations, the aim is to explore fragmentation of a round liquid jet in a quiescent gaseous medium in the fields far away from and close to the nozzle, respectively experimentally and numerically with the help of Direct Numerical Simulations (DNS). For each region, the analysis is carried out in three parts. Firstly, the question of the droplet size modelling will be tackled by testing the ligament-mediated and intermittency driven spray theories with the objective of discussing their relevance of application along the spray evolution. Secondly, complementary to the droplet size distribution, attention is also paid to the droplet velocity distribution in order to model it and bring further elements to the question of the flow regime perceived by the elements of the disperse phase.

To do so, the thesis is structured as follows. Chapter 2 introduces the methods used for the experimental and DNS campaigns. The results obtained from the analysis of the experimental measurements are presented in Chapter 3 while those obtained from the analysis of the numerical campaign are presented in Chapter 4. Finally, Chapter 5 highlights the main results of the thesis and opens the way for further research work.

Chapter 2

Experimental and numerical methods

Contents

2.1	Introduction	32
2.2	Droplet Tracking Velocimetry by shadowgraphy	33
2.3	How to simulate flow dynamics?	35
2.4	A numerical description of multiphase flows with surface tension	37
2.5	A numerical description of the interface	44
2.6	Conclusion	54

2.1 Introduction

This PhD thesis is dedicated to the analysis of experimental data and numerical experiments of liquid jet fragmentation. Detailing the tool and the methods behind it is of utmost importance to frame their robustness and accuracy in order to set the validity perimeter of the experiments and of the subsequent conclusions. This chapter is dedicated to the presentation on the first hand of the Droplet Tracking Velocimetry (DTV) by shadowgraphy and on the second hand of the discretisation of the flow equations and the numerical methods used in the Basilisk's solver for the Navier Stokes equations. Note that the latter presentation does not provide a review of the existing methods to simulate multiphase flows with surface tension nor gives an extensive introduction to Computational Fluid Dynamics (CFD) but limits itself to the schemes implemented in Basilisk. The presentation of the basics of CFD can be found in the handbooks of Anderson (1995) and Lomax *et al.* (2001). An extended presentation of the finite volume method can be found in the book of Versteeg & Malalasekera (2007) while the numerical methods for Direct Numerical Simulations in the context of gas liquid multiphase flows are detailed in the one of Tryggvason *et al.* (2011).

2.2 Droplet Tracking Velocimetry by shadowgraphy

This section presents the underlying experimental apparatus and protocol used to carry out the DTV measurements achieved by Felis *et al.* (2020) and further analysed in the present thesis. The presentation largely follows the details given in Felis-Carrasco (2017) and Felis *et al.* (2020).

In order to measure the diameter and velocity of the droplets in the disperse region, one can run a Droplet Tracking Velocimetry (DTV) algorithm on shadow images. Shadow images result from the shadowgraphy technique in which a non coherent background light is used to project the flow shadows on a camera. The background light is generated by a double-pulsed laser source and conducted via an optical fiber to a diffuser / collimator which generates the non-coherent uniform background. The system captures two consecutive image frames at high speed which will be used to compute the velocity of the objects. While the exposition time is roughly 4 ns and the frequency between the instant when two consecutive frames are captured is set to 5 Hz, extra care is required to set the time between the capture of the two frames, named time between pulses and denoted t_{bp} . This time should not be too small in order to let the objects evolve in space nor too large in order to limit the changes of the overall form and location of the objects. The time between pulses is typically of $O(\mu s)$ and is set depending on the mean velocity of the objects inside the frame. The space orientation on the picture is such that the z -axis is perpendicular to the photographs and the x axis is parallel to the jet axis and included in the photograph.

Once the region where the liquid core pinches off is determined, it is possible to carry out DTV measurements in the disperse region, i.e. after the core pinch off. The objective is then to accurately detect the droplets in the shadow images and compute their velocity using the double frame acquisition. To do so, the shadow images are segmented thanks to a custom shadow sizer algorithm developed and implemented by Felis-Carrasco (2017) with the Image Processing Toolbox of MATLAB. The shadow sizer procedure is split into four main steps which are a wavelet transform operation, a local analysis of each object, the contour extraction and the velocity estimation.

Starting from the shadow image, the wavelet transform operation detects the changes in the image gradient thanks to a Mexican-hat kernel and amplifies the droplet boundaries without considering defocusing issues. A binary mask is used on the top of this to detect the objects and segment them. The detected objects are then candidate droplets. Each candidate droplet is isolated in a sub-image and locally analysed. The local analysis mainly corresponds to the computation of the contrast ratio C defined as the difference between the contrast extrema over their sum. The candidate droplets are kept only if $C \geq 0.1$. Once the contrast filter passed, the contrast of the local image is first normalised and the grey contours for the values in $\{0.25, 0.5, 0.61, 0.77\}$ are extracted. Using the 0.61 contour and assuming that all the droplets are ellipsoids, it is possible to compute the droplet volume $V_{0.61}$ and then to compute the diameter $d_{[30]}$ based on this volume such that $d_{[30]} = \sqrt[3]{6V_{0.61}/\pi}$. The positions of the droplet centroids in the two consecutive frames are then matched by using a point matching algorithm. This algorithm does not match nearest neighbours together as it leads to inconsistency for small droplets clustered together. Instead, it minimises a target cost function by applying 2D shear, rotation and translation to the cloud of points detected between the frames. Finally, the droplet velocities are computed knowing the distance between the successive centroid positions, the time between pulses and the scale resolution, equal to $7.194 \mu m$ by pixel.

Even if the shadow sizer procedure well detects the objects being out of focus, detecting such objects has some limits. Firstly, their size can be misestimated. Secondly, the out-of-focus droplets in the background and the foreground can be far from the measurement plane. Hence, the 2D (x, y) location of their projection will not correspond to the actual 3D (x, y, z) location of the droplet and be biased. If not accounted for, those two limits can infer consequent biases in the measurements of the granulometry and the velocimetry of the jet. The misestimation of the droplet size can be corrected thanks to a size correction function. This correction function can be derived experimentally by measuring the size of round objects which nominal diameters d_0 are known. The calibration measures can be fitted by the function $d_0/d_m = 0.9629 C^{0.2166}$ with d_m the measured diameter and C the contrast ratio (Felis *et al.*, 2020). The latter function is used to correct the measured diameter $d_{[30]}$. Additionally, it is possible to filter out the detected droplets being too far from the measurement plane by computing the depth of field (DOF) such that $DOF = 0.08153 d_0^{0.9321}$ (Felis *et al.*, 2020). The minimum DOF is set by the smallest particle which can be detected by the DTV system, experimentally $DOF_{min} = 1.61$ mm (Felis-Carrasco, 2017). Lastly, the droplets are validated only if their locations are included in the thin slice such that $DOF = DOF_{min}$. The latter condition ensures that all the droplets detected by the DTV apparatus belong to the same virtual measurement environment.

The DTV measurements depicted are carried out on 5 positions along the jet axis, $x/d_n = \{400, 500, 600, 700, 800\}$ with d_n the diameter of the injection nozzle. 1000 pairs of frames are acquired for each measurement position with a Field-Of-View (FOV) of 14.73×14.73 mm 2 . Each frame pair at each position is treated as an independent event. Finally, the images are split into 5 stripes of width equal to 2.95 mm along y . Doing so enables a better resolved analysis in the y direction as well as sets the effective measurement volume of the DTV to $14.73 \times 2.95 \times 1.61$ mm 3 .

2.3 How to simulate flow dynamics?

2.3.1 Numerical simulations for fluid dynamics

Several types of simulations exist nowadays, the three most common being the Reynolds Averaged Navier Stokes (RANS) simulations, the Large Eddy Simulations (LES) and the Direct Numerical Simulations (DNS). All of them aim to simulate flows under specific configurations but with very different strategies and outcomes. Both RANS simulations and LES rely on modelling part of the flow physics. For the former, the flow quantities are expressed following the Reynolds decomposition, i.e. as the sum of a mean and a fluctuating part. For instance, the Reynolds decomposition of the velocity would be such that $\mathbf{u} = \mathbf{U} + \mathbf{u}'$ with \mathbf{U} and \mathbf{u}' the velocity mean and fluctuations. Using this decomposition, the Navier Stokes equations can then be written in terms of mean quantities and simulations can be run. The strong limitation of this strategy is that the Reynolds stresses, writing as $\rho\overline{u'_i u'_j}$ with (i, j) indicating the spatial directions, require to be modelled in order to close the system of equations and actually run any simulation. Specifically, the description of turbulence strongly relies on the closure of the Reynolds stress which led to the development of a wide range of models with their respecting closure parameters, among them are the famous standard $k - \epsilon$ (Launder & Spalding, 1974) and $k - \omega$ (Wilcox, 1993) models. The major drawbacks of the RANS approach are the strong dependence on the model closure, the exploration work which is needed to figure out the correct closure parameters for the configuration of interest and the fact that the flow turbulence is fully modelled. However, that kind of simulations can be run efficiently and be useful to get some insights on the global flow structure, particularly for flows showing a low turbulence intensity or applications for which the knowledge of time averaged properties is sufficient.

Initially proposed by Smagorinsky (1963), Large Eddy Simulations partly overcome the main issues of the RANS simulations. Instead of modelling the overall turbulent behavior of the flow, the large scales of turbulence are resolved while the small scales are spatially filtered out and taken into account through sub-grid-scales stresses (Versteeg & Malalasekera, 2007). This enables to let the turbulent large scales evolve naturally while cutting off the computational cost related to the resolution of the small scales. However, those small scales are key dynamical elements for reactive flows (Pitsch, 2006), multiphase flows (Fox, 2012) or in near wall regions (Agostini & Leschziner, 2018). As a consequence, LES represent with a better accuracy the macro structure of turbulence but require the modelling of turbulent small scales when they are relevant for the flow dynamics. Even so, it can be an interesting compromise for engineering applications.

Contrary to the latter two, Direct Numerical Simulations (DNS) aim to resolve all the spatial and time scales of the flow and thus do not model any dynamics. Even if no physical models are used, limitations can arise from the mathematical models needed to operate the discretisation of the Navier Stokes equations. For instance, the simulation of surface-tension driven flows still relies on ongoing algorithm challenges (Gorokhovski & Herrmann, 2008). Even if limitations exist, this approach enables to finely resolve the flow dynamics in various configurations like turbulent MHD flows in the Von Kármán Sodium experiment (Nore *et al.*, 2016), fully turbulent channel flows down to the Kolmogorov scale (Agostini & Leschziner, 2014) or turbulent flows in porous media down to scales smaller than the Kolmogorov's one (Jin *et al.*, 2015). Note that the gain of accuracy in the flow description goes along with a consequent increase of computational resources, making DNS not practical for industrial needs but of great relevance for research purposes.

In this work, the simulations which are carried out are DNS based on the open-source C-based high-level programming language Basilisk (Popinet & collaborators, 2013–2021). After introducing the Basilisk language, the numerical methods implemented to solve the Navier Stokes equations and to account for the interface dynamics are detailed.

2.3.2 Basilisk: a C-based high level language for the computational dynamics of fluid

Basilisk is an open source programming langage initially developed by Popinet & collaborators (2013–2021). It is implemented for resolving partial difference equations over adaptative Cartesian grids, i.e. grids which can be dynamically refined during the simulations. This language takes over from the free and open source software Gerris (Popinet, 2003) from which it takes most of the developments and improves them. The application range of Basilisk is relatively large with solvers enabling the simulation of tsunamis, flows in porous medium or multiphase flows and it can grow in the future with the implementation of new solvers by the Basilisk community. Indeed, contrary to Gerris, the versatility of the language enables to implement relatively easily solvers for any kind of partial derivative equations. Based on the C++ programming language, Basilisk offers a wide spectrum of processing functions and automation routines, as for memory management or parallel computation, making this language high-level and handy for developing simulation cases. An important plus of Basilisk compared to Gerris is that all the routines are accessible and can be easily adapted, e.g. to new mathematical formulations or flow configurations.

Additionally of being versatile, the strength of Basilisk also lies in the implementation of numerical schemes and discretisation improving the overall efficiency of the simulations in terms of time and memory usage. Particularly, the use of octree Cartesian grids with an adaptative mesh refinement (Popinet, 2003) reduces drastically the memory usage and the computational time by refining the mesh in the region of interest, like along an interface, and keeping a coarse grid elsewhere. The computational time can be further reduced with parallel computation using the Message Passing Interface (MPI) C library, and this without more development work as a consequent part of the Basilisk routines include a MPI implementation. Finally, the implementation of an accurate adaptative solver for surface-tension-driven interfacial flows (Popinet, 2009) opens the way to carry out DNS of incompressible liquid jet fragmentation. This way started to be explored by Agbaglah *et al.* (2011) on Gerris with the air-assisted atomisation of planar liquid sheet ($\rho_l/\rho_g = 833.3$, $Re_l = 1730$, $We_g = 3.52$). It continued on Basilisk with the works of Chen *et al.* (2013) and Ling *et al.* (2017b) who carried out high fidelity simulations respectively of impinging jets ($\rho_l/\rho_g = 828.5$, $Re_l = 11724$, $We_g = 3.61$) and atomizing biodiesel jets ($\rho_l/\rho_g = 78.2$, $Re_l = 1450$, $We_g = 12.9$) which validate the accuracy of the numerical schemes. As a comparison and reminder, the experimental configuration studied by Felis *et al.* (2020) is characterised by $\rho_l/\rho_g = 828.5$, $Re_l = 41833$ and $We_g = 24$, which highlights the difficulty to simulate experimental configurations of diphasique turbulent flows even with today's state of the art methods. With this in mind, the open source code for liquid jet fragmentation implemented with the Basilisk language was chosen to carry out the Direct Numerical Simulations considered in this work.

2.4 A numerical description of multiphase flows with surface tension

The following sections largely follow the work of Popinet (2003) and Popinet (2009).

2.4.1 Flow configuration and governing equations

In the frame of this thesis, we aim to numerically study the injection of a liquid round jet injected into a quiescent gaseous medium, respectively the dense and light phases denoted 1 and 2, at different injection Weber numbers. Both fluids are assumed to be incompressible, viscous and immiscible. An interface then exists between the two phases and its dynamics is partly governed by the surface tension forces. Additionally, gravity is neglected and the gravitational forces are set to zero. Instead of considering the two phases apart from each other, a way to handle this kind of configuration is to assimilate the biphasic flow to a single phase flow with a spatially and timewise variable density. The Navier Stokes equations, namely the continuity and momentum equations, can be respectively written as

$$\partial_t \rho + \nabla \cdot (\rho \mathbf{u}) = 0, \quad (2.1)$$

$$\rho(\partial_t \mathbf{u} + \mathbf{u} \cdot \nabla \mathbf{u}) = -\nabla p + \nabla \cdot (2\mu \mathbf{D}) + \sigma \kappa \delta_S \mathbf{n}, \quad (2.2)$$

with $\mathbf{u} = (u_1, u_2, u_3)$ the fluid velocity, p the pressure, $\rho = \rho(\mathbf{x}, t)$ the fluid density at the location \mathbf{x} and time instant t , $\mu = \mu(\mathbf{x}, t)$ the fluid dynamic viscosity and the deformation tensor $\mathbf{D}_{i,j} = (1/2)(\partial_i u_j + \partial_j u_i)$, $(i, j) \in \{1, 2, 3\}^2$. The last term on the right hand side of the momentum equation depicts the interfacial forces acting along the normal direction \mathbf{n} of the interface and deriving from the surface tension σ and the interface curvature κ . The Dirac function δ_S is used here to depict that the surface tension forces are concentrated on the interface and zero elsewhere. In addition to the two Navier Stokes equations, the assumption of the flow incompressibility leads to

$$\nabla \cdot \mathbf{u} = 0, \quad (2.3)$$

In order to account for the biphasic nature of the flow, an additional quantity has to be added to the single fluid approach: the phase volume fraction $\alpha(\mathbf{x}, t)$ of the phase 1. This quantity enables to depict the presence of each phase across the computational domain. When $\alpha(\mathbf{x}, t) = 1$ only the phase 1 is present and only the phase 2 is present when $\alpha(\mathbf{x}, t) = 0$. It also defines both the density ρ and the viscosity μ of the single fluid as

$$\rho(\tilde{\alpha}) = \tilde{\alpha}\rho_1 + (1 - \tilde{\alpha})\rho_2, \quad (2.4)$$

$$\mu(\tilde{\alpha}) = \tilde{\alpha}\mu_1 + (1 - \tilde{\alpha})\mu_2 \quad (2.5)$$

where ρ_i and μ_i are the density and the viscosity of the phase i , $i \in \{1, 2\}$. Here the field $\tilde{\alpha}$ is a numerical variable which is either identical to α or resulting from a smoothing spatial filter applied on α . Using a smoothed field can improve the outcomes of the simulations (Popinet, 2009). Injecting the expression of ρ and μ in the continuity equation (2.1) and noting that $\partial_t \rho_1 = \partial_t \rho_2 = 0$ leads to a formulation of the continuity equation in terms of α

$$\partial_t \alpha + \nabla \cdot (\alpha \mathbf{u}) = 0 \quad (2.6)$$

which can also be seen as the advection equation of the volume fraction. The initial problem of biphasic flows is now written in terms of a single phase flow with variable density and viscosity. It is worth noting here that instead of resolving the Navier Stokes equations for each phase, this approach allows to resolve one set of equations. This, though, implies the implicit assumption that the velocity field \mathbf{u} evolves continuously in space. In order to run numerical simulations, it is necessary to be able to compute the flow quantities step by step both timewise and spatially. To do so, the partial derivatives constitutive of the governing equations have to be discretised, for instance thanks to the finite volume method for the spatial derivatives.

2.4.2 Discretisation of the physical space: a hierarchical octree mesh

The domain is spatially discretised using cubic finite volumes organised hierarchically as an octree. Fig. 2.1 gives the representation of the 2D equivalent of this 3D discretisation with square finite volumes organised as a quadtree. Each finite volume is further called a cell and the size of the cell edge is denoted Δ . One cell can be refined by splitting it into 4 children cells (4 in 2D). The base of the hierarchical tree is called the root cell. It has no parent cell and it is the unique ancestor of all the cells of the tree. On the other side, the cells without child, the ones at the tip of each branch, are called leaf cells. As we descend in the tree, the grid is more refined. The level of the cells in the tree is defined relatively to the root cell, whose level is conventionally set to 0. The cell level increases by one for each new generation of cells. The refinement level of the grid is equal to the maximum cell level. In the case example of Fig. 2.1, the level of refinement is equal to 3. The neighbours of each cell can be accessed through the cell faces. In order to deal with interfaces, we also define mixed cells which are cells cut by an interface. Additional constraints are set on the grid structure in order to simplify the calculations at the cell boundaries:

1. the levels of direct neighbouring cells cannot differ by more than one,
2. the levels of diagonally neighbouring cells cannot differ by more than one neither,
3. all the cells directly neighbouring a mixed cell must be at the same level.

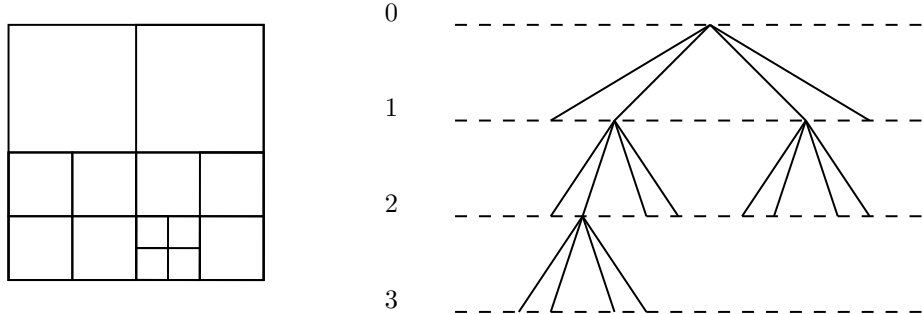


Figure 2.1: Example of a quadtree discretisation and its corresponding tree representation.

The constraints (1) and (2) have little impact on the discretisation flexibility but the constraint (3) imposes a tighter restriction by forcing all the cells cut by an interface to be at the same level, thus enforcing the same resolution all along the interface. Complementary, a major restriction

of octree structures is the spatially isotropic refinement that it imposes locally, which can be limiting for highly anisotropic flows but overcome with rectangular cells.

Practically, the data structure to choose for representing the tree has to respect several requirements:

1. for any given cell, the access to the neighbouring cells has to be efficient,
2. for any given cell, the access to the level and the spatial coordinates of the cell must be efficient,
3. the traversal of all the leaf cells, the cells at a given level and the mixed cells must be efficient.

To ensure so, the structure of *fully threaded tree* introduced by Khokhlov (1998) was implemented in the Basilisk routines. This structure enables the requirements (a) and (b) to be done in $O(1)$ operations instead of $O(\log(N))$ operations with a standard pointer based tree, where N is the number of cells traversed. For its part, the requirement (c) is performed in $O(N \log(N))$ operations with a standard pointer based tree.

Finally, all the variables are collocated at the center of each discretisation volume. The interface in the mixed cells is defined through the Volume-Of-Fluid (VOF) approach based on the volume fraction field α , see Sec.2.5.1. Consistently with the finite volume formulation, the variables are taken as the values averaged over the cell volume. Using collocated variables is a necessary choice in order to use the Godunov momentum advection scheme of Bell *et al.* (1989) and simplifies the implementation of the Crank-Nicholson discretisation of the viscous terms. However, extra care needs to be paid to avoid the decoupling of the pressure and velocity field, see Sec. 2.4.5.

2.4.3 Adaptative mesh refinement

One key feature of Basilisk is its ability to refine the mesh while running a simulation. The adaptative mesh refinement used in this work is the same as the one implemented by Popinet (2015) and used by van Hooft *et al.* (2018) for atmospheric boundary layer simulations. Formally based on the theory of wavelet thresholding used for fluid dynamics simulations (Schneider & Vasilyev, 2009), the implementation relies on the estimation of the discretisation error to decide if a cell has to be refined or coarsened. Consider a 1D signal f and its discretisation f_N over an even number N of elements. The value of f taken at the i -th element of the discretisation is denoted f_N^i . Let us denote \mathcal{D} and \mathcal{U} a downsampling and an upsampling operator. \mathcal{D} approximates a signal on a coarser grid made of $N/2$ elements while \mathcal{U} approximates a signal on a discretisation with the same number of elements as f_N . In Basilisk, the downsampling operation is defined as the local volume average of the signal value over the cells related to one descendant, i.e. contained in the next coarser level cell. For its part, the upsampling operation is defined as a linear interpolation between the grid point at the coarse level, which ensures the operation to be second-order accurate, consistently with the accuracy of the solver.

Applying first \mathcal{D} and then \mathcal{U} on the discretised signal f_N leads to a new signal g_N :

$$g_N = \mathcal{U} \circ \mathcal{D}(f_N) \quad (2.7)$$

where $\mathcal{D}(f_N) = f_{N/2}$. In the general case, the signals f_N and g_N are different. It is possible to define the discretisation error χ for each cell i in a grid of N elements as:

$$\chi_N^i = \|f_N^i - g_N^i\|. \quad (2.8)$$

Given an error threshold ι , named refinement criterion latter on, van Hooft *et al.* (2018) set the following rules to control the grid adaptation:

$$\begin{array}{lll} \text{if} & \iota < \chi_N^i & \text{then the } i\text{-th cell is too coarse.} \\ & \frac{2\iota}{3} < \chi_N^i < \iota & \text{fine.} \\ & \chi_N^i < \frac{2\iota}{3} & \text{too fine.} \end{array}$$

where ι has the same units as f . Using those rules, the grid can be refined dynamically in respect of the refinement criterion. The different field values in the newly refined or coarsened cells can be computed using the operators \mathcal{D} and \mathcal{U} defined above. Even if the explanations were given for a 1D signal, the method generalised to 2D and 3D signals is similar. Finally, adapting the grid while running a simulation in parallel imposes to balance the computation load by modifying the domain decomposition between the processors, which is done with a natural decomposition of a Z-ordering space-filling curve applied to the octree structure (Griebel & Zumbusch, 2002).

2.4.4 Time discretisation of the governing equations

Let us consider two time instants n and $n + 1$ separated by a time step Δt which can vary during the simulation, under the constraint of the Courant–Friedrichs–Lewy (CFL) condition. A classic way to compute an approximation of the first time derivative of a quantity ζ at the time instant $n + 1$ is to consider the first order backward finite difference

$$\partial_t \zeta = \frac{\zeta_{n+1} - \zeta_n}{\Delta t}. \quad (2.9)$$

The term backward relates here to the fact that the time derivative at $n + 1$ is evaluated with the knowledge of ζ at $n + 1$ and the previous time instant n . The time discretisation implemented in Basilisk relies on a discretisation staggered in time for the volume fraction and the pressure. While “stagger” would be familiar to the English readers, it might not be for those who English is not their mother tongue. Here, “staggered” in time means that some flow quantities are evaluated in between two time steps. Let us denote $n + 1/2$ the moment when this evaluation is done. Note that $n + 1/2$ is not an actual time instant but only a numerical construction representing the computation, or the update, of some flow quantities between two actual time steps. With this choice of staggering, the time derivative of α in Eq. (2.6) writes as

$$\partial_t \alpha = \frac{\alpha_{n+1/2} - \alpha_{n-1/2}}{\Delta t} \quad (2.10)$$

Complementary, the deformation tensor is evaluated as its average between the instants n and $n + 1$: $\mathbf{D} = (\mathbf{D}_n + \mathbf{D}_{n+1})/2$. As a result, the time discretisation of the Navier Stokes equations is second-order accurate (Popinet, 2009). The equations and the incompressibility conditions are discretised as

$$\frac{\alpha_{n+1/2} - \alpha_{n-1/2}}{\Delta t} + \nabla \cdot (\alpha_n \mathbf{u}_n) = 0, \quad (2.11)$$

$$\begin{aligned} \rho_{n+1/2} \left[\frac{\mathbf{u}_{n+1} - \mathbf{u}_n}{\Delta t} + \mathbf{u}_{n+1/2} \cdot \nabla \mathbf{u}_{n+1/2} \right] \\ = -\nabla p_{n+1/2} + \nabla \cdot \left[\mu_{n+1/2} (\mathbf{D}_n + \mathbf{D}_{n+1}) \right] + (\sigma \kappa \delta_S \mathbf{n})_{n+1/2}. \end{aligned} \quad (2.12)$$

$$\nabla \cdot \mathbf{u}_n = 0 \quad (2.13)$$

It is possible to further simplify this system of equations thanks to a classic time-splitting projection method. Instead of resolving directly the velocity at the instant $n + 1$ issuing from both the velocity and the pressure fields, that kind of method splits the convective and diffusive momentum terms from the pressure gradient. Practically, a provisional velocity \mathbf{u}_\star is defined following the Hodge decomposition as

$$\mathbf{u}_\star = \mathbf{u}_{n+1} + \frac{\Delta t}{\rho_{n+1/2}} \nabla p_{n+1/2} \quad (2.14)$$

The provisional velocity \mathbf{u}_\star can be seen as a general solution of the velocity field. The velocity at the time instant $n + 1$ is then the sum of the solution from the velocity field to which the pressure gradient is subtracted. The wording “projection” refers here to the projection of the provisional velocity onto the space of the divergence free velocities. The discretisation then rewrites as

$$\mathbf{u}_{n+1} = \mathbf{u}_\star - \frac{\Delta t}{\rho_{n+1/2}} \nabla p_{n+1/2} \quad (2.15)$$

$$\frac{\alpha_{n+1/2} - \alpha_{n-1/2}}{\Delta t} + \nabla \cdot (\alpha_n \mathbf{u}_n) = 0, \quad (2.16)$$

$$\rho_{n+1/2} \left[\frac{\mathbf{u}_\star - \mathbf{u}_n}{\Delta t} + \mathbf{u}_{n+1/2} \cdot \nabla \mathbf{u}_{n+1/2} \right] = \nabla \cdot \left[\mu_{n+1/2} (\mathbf{D}_n + \mathbf{D}_\star) \right] + (\sigma \kappa \delta_S \mathbf{n})_{n+1/2}, \quad (2.17)$$

$$\nabla \cdot \mathbf{u}_{n+1} = 0. \quad (2.18)$$

Ensuring that \mathbf{u}_{n+1} is divergent free, i.e. taking the divergence of Eq. (2.15) and considering Eq. (2.18), leads to the Poisson equation:

$$\nabla \cdot \left[\frac{\Delta t}{\rho_{n+1/2}} \nabla p_{n+1/2} \right] = \nabla \cdot \mathbf{u}_\star \quad (2.19)$$

This splitting method enables to compute the provisional velocity field \mathbf{u}_\star with Eq. (2.17), then to compute the pressure field thanks to Eq. (2.19) and finally get the divergence free velocity \mathbf{u}_{n+1} by applying the pressure correction on the provisional velocity field using Eq. (2.15). Eq. (2.17) can be reorganised by grouping the terms evaluated at the fractional time instant

$$\frac{\rho_{n+1/2}}{\Delta t} \mathbf{u}_\star - \nabla \cdot \left[\mu_{n+1/2} \mathbf{D}_\star \right] = \nabla \cdot \left[\mu_{n+1/2} \mathbf{D}_n \right] + (\sigma \kappa \delta_S \mathbf{n})_{n+1/2} + \rho_{n+1/2} \left[\frac{\mathbf{u}_n}{\Delta t} - \mathbf{u}_{n+1/2} \cdot \nabla \mathbf{u}_{n+1/2} \right] \quad (2.20)$$

and the quantities at the fractional time step can be computed with the knowledge of the quantities at the time steps n and $n + 1/2$. The momentum equation is then an Helmholtz type equation. Note that the Crank-Nicholson discretisation of the viscous term is formally second-order accurate and unconditionally stable. In Basilisk, both Eq. (2.19) and (2.20) are solved using an octree based multilevel solver with a V-cycle implementation. The reader can refer to Popinet (2003) for a detailed presentation of the multilevel solver. For its part, once spatially discretised, the velocity advection term is estimated using the numerical scheme of Bell *et al.* (1989). This scheme relies on a Godunov procedure, i.e. uses the leading terms, up to order one in space and time, of a Taylor series of the velocity. The time and space derivatives taking part in the series are discretised by using upwind finite differences. In the last steps of the advection scheme implemented in Basilisk, a pressure correction is applied to ensure that the resulting velocity field is divergence free, thus respecting the incompressibility condition, before estimating the velocity advection term.

2.4.5 Spatial discretisation of the governing equations

Sec. 2.4.2 concludes on the attention needed to avoid the decoupling between the velocity and the pressure fields. To circumvent such a situation, an approximation projection method (Popinet, 2003) can be used for the spatial discretisation of Eq. (2.15) and the associated divergence in the Poisson equation (2.19). At first, Eq. (2.20) is used to compute the auxiliary cell centered velocity field \mathbf{u}_\star^c . Then, the auxiliary face centered velocity field \mathbf{u}_\star^f is computed by averaging the cell centered values on all the faces of the discretisation volume, while guarantying the consistency of the volume fluxes between the cells of different level. On a third step, the divergence of the auxiliary velocity field taking part in the Poisson equation is discretised like the finite volume approximation

$$\nabla \cdot \mathbf{u}_\star = \frac{1}{\Delta} \sum_f \mathbf{u}_\star^f \cdot \mathbf{n}^f \quad (2.21)$$

where \mathbf{n}^f is the normal unit vector to the face f and Δ is the edge cell size. After solving the Poisson equation with the multilevel solver, the pressure correction can be applied to both the face centered and cell centered auxiliary velocities

$$\mathbf{u}_{n+1}^f = \mathbf{u}_\star^f - \frac{\Delta t}{\rho_{n+1/2}^f} \nabla^f p_{n+1/2} \quad (2.22)$$

$$\mathbf{u}_{n+1}^c = \mathbf{u}_\star^c - \left| \frac{\Delta t}{\rho_{n+1/2}^f} \nabla^f p_{n+1/2} \right|^c \quad (2.23)$$

with ∇^f being a simple face centered gradient operator and $|\cdot|^c$ being the average operator over all the faces delimiting the control volume. As a consequence, the resulting face centered velocity \mathbf{u}_{n+1}^f is exactly non divergent and the resulting cell centered velocity \mathbf{u}_{n+1}^c is approximately divergence free.

At this stage of the discretisation, one important point stayed in the corner. The Poisson equation (2.19), the advection diffusion equation (2.20) and the pressure corrections (2.22) and (2.23) rely on the estimation of the face centered density $\rho_{n+1/2}^f$ and viscosity $\mu_{n+1/2}^f$ from Eq. (2.4) and (2.5), themselves depending upon the volume fraction $\alpha_{n+1/2}^f$. The latter is estimated differently hinging on the configuration of the grid. If the face delimits two cells of the same

level, the volume fraction is computed as the average of the cell centered values. If the face delimits two cells with different level, the volume fraction field is computed thanks to a second order interpolation.

2.5 A numerical description of the interface

The following sections largely follow the work of Popinet (2009).

2.5.1 Tracking the interface with a Volume-Of-Fluid approach

In order to solve the advection equation (2.6) of the volume fraction field α , a piecewise linear geometrical Volume-Of-Fluid (VOF) scheme is implemented in Basilisk for octree spatial discretisations. Such schemes classically proceed in two steps with, first, reconstructing the interface and, second, computing the geometrical flux along with the interface advection. The main focus is given here on the first step. More details about the second step can be found in the work of Popinet (2009).

For piecewise linear geometrical VOF schemes, the interface is represented by a plane in 3D and a line in 2D described by

$$\mathbf{n} \cdot \mathbf{x} = a \quad (2.24)$$

with \mathbf{n} the local normal to the interface at the position \mathbf{x} . When both \mathbf{n} and the volume fraction α are known, if the volume contained in the cell and lying below the interface plane is equal to α , then the coefficient a is uniquely defined. In the implementation of this scheme in Basilisk, it is assumed that given a normal \mathbf{n} , a volume fraction α and a coefficient a in a coordinate system centered on the cell and of unit length the cell size, those three quantities are related by a bijective function \mathcal{V} such that

$$\alpha = \mathcal{V}(\mathbf{n}, a), \quad (2.25)$$

$$a = \mathcal{V}^{-1}(\mathbf{n}, \alpha). \quad (2.26)$$

Practically, the routines of Scardovelli & Zaleski (2000) are used to implement \mathcal{V} and \mathcal{V}^{-1} . Generally speaking, the schemes for estimating the interface normal only need information in a compact neighbourhood of the cell, for instance regular Cartesian stencils of size $3 \times 3 \times 3$. With this stencil, the normal can be estimated by using finite difference estimates or minimisation techniques. The generalisation of those schemes to octree grid is straightforward if the discretisation in the compact neighbourhood reduces to a regular Cartesian discretisation. Thus, reconstructing such regular discretisation when the cells in the stencil vary in size is a key element. For the sake of simplicity, the following algorithms are explained for a 2D quadtree discretisation.

Consider a cell \mathcal{C} centered on \mathbf{x}_0 of size Δ and containing the interface, $0 < \alpha < 1$. The notation \mathcal{N} denotes a neighbouring cell of \mathcal{C} . Algorithm 1 gives the procedure for the stencil computation. For setting the volume fraction $\alpha_{i,j}$ of the cell \mathcal{N}_Δ on line 6 of Algorithm 1, several cases must be considered depending if the neighbour cells are of the same size as or larger than \mathcal{C} .

Algorithm 2 gives the procedure to set $\alpha_{i,j}$ for both cases. In this algorithm, when \mathcal{N} and \mathcal{C} have the same size, \mathcal{N} is not necessarily a leaf cell. Even so, the volume fraction can be computed at all the levels of the tree by defining the cell volume fraction as the average of the volume fraction of the children cells. For processing the case when the cell \mathcal{N} is larger than \mathcal{C} and contains the interface, the interface equation (2.24) is assumed to be known for the fragment of interface in \mathcal{N} , then $\mathbf{n} \cdot \mathbf{x} = a_{\mathcal{N}}$. Prior to computing the equivalent volume fraction

of the virtual cell \mathcal{N}_Δ , the interface equation has to be transformed into the coordinate system centered on \mathcal{N}_Δ using

$$\mathbf{x}' = \frac{n\Delta\mathbf{x} + \mathbf{x}_{\mathcal{N}} - \mathbf{x}_{i,j}}{\Delta} \quad (2.27)$$

where $n\Delta$ and $\mathbf{x}_{\mathcal{N}}$ are the size and the position of \mathcal{N} . Eq. (2.24) then rewrites as

$$\mathbf{n} \cdot \mathbf{x}' = n a_{\mathcal{N}} + \frac{\mathbf{n}}{\Delta} \cdot (\mathbf{x}_{\mathcal{N}} - \mathbf{x}_{i,j}) \quad (2.28)$$

and the corresponding stencil volume fraction writes as

$$\alpha_{i,j} \mathcal{V}(\mathbf{n}, n a_{\mathcal{N}} + \frac{\mathbf{n}}{\Delta} \cdot (\mathbf{x}_{\mathcal{N}} - \mathbf{x}_{i,j})). \quad (2.29)$$

In the description of the physical space discretisation, Sec. 2.4.2, several requirements and constraints were set on the grid. Among them, the difference of level between neighbour cells cannot be larger than 1, thus setting n to 2 in the later expression of $\alpha_{i,j}$.

Now that $\alpha_{i,j}$ is known over the stencil, the Mixed Youngs Centered (MYC) implementation of Aulisa *et al.* (2007) is used to compute the normal \mathbf{m} and the interface is reconstructed by evaluating $a = \mathcal{V}^{-1}(\mathbf{m}, \alpha_{0,0})$. Finally, the interface reconstruction can be achieved by following the procedure given in Algorithm 3.

Regarding the interface advection, its implementation relies on the direction-split scheme from DeBar (1974). A major question to consider in the interface advection is the one of the computation of the volume fluxes of the first phase through the cell boundaries. The classic analytical schemes could be used but, in practice, they lead to the numerical diffusion of the interface. In order to compensate this diffusion, the initial VOF scheme developed by Hirt & Nichols (1981) included diffusive / non diffusive advection schemes. Contrary to the analytical approach, the volume fluxes can be estimated thanks to the geometry of the reconstructed interface. This method is efficient and simple to implement on a Cartesian grid or to generalise to octree structures. However, this geometrical scheme is not strictly conservative due to the occurrence of small over- or undershoots of the volume fraction. In order to keep the consistency of the volume fraction field, and mainly ensure that $\alpha \in [0, 1]$, any volume fraction violating the field bounds has to be reset, which can lead to the loss of exact mass conservation. The tests of the implementation of a geometrical scheme, and of the above mentioned limits, for the volume fraction fluxes in an octree structure carried out by Popinet (2009) indicated that mass conservation is not an issue.

Algorithm 1 Stencil computation (\mathcal{C})

Require: $(i, j) \in \mathbb{Z}^2$
Require: $(i, j) \in [-1, 1]^2$

- 1: $\mathbf{X} \leftarrow (1, 0)$
- 2: $\mathbf{Y} \leftarrow (0, 1)$
- 3: **for** each pair (i, j) **do**
- 4: Set the position $\mathbf{x}_{i,j} \leftarrow \mathbf{x}_0 + \Delta(i\mathbf{X} + j\mathbf{Y})$.
- 5: Locate the smallest cell \mathcal{N} of size larger than or equal to Δ containing $\mathbf{x}_{i,j}$.
- 6: Set the stencil volume fraction $\alpha_{i,j}$ to the volume fraction of a (virtual) cell \mathcal{N}_Δ of size Δ centered on $\mathbf{x}_{i,j}$ and entirely contained in \mathcal{N} .

Algorithm 2 Equivalent volume fraction ($\mathcal{C}, \mathbf{x}_{i,j}, \mathcal{N}$)

- 1: **if** \mathcal{N} has the same size as \mathcal{C} **then**
- 2: $\mathcal{N}_\Delta \leftarrow \mathcal{N}$
- 3: $\alpha_{i,j} \leftarrow$ the value of α in \mathcal{N}
- 4: **else if** \mathcal{N} is larger than \mathcal{C} **then** ▷ Case when \mathcal{N} is a leaf cell coarser than \mathcal{C} .
- 5: **if** \mathcal{N} does not contain the interface **then**
- 6: $\alpha_{i,j} \leftarrow$ the value of α in \mathcal{N} (0 or 1)
- 7: **else if** \mathcal{N} contains the interface **then**
- 8: By definition, \mathcal{N}_Δ does not exist and volume fraction has to be computed from the interface reconstructed cell \mathcal{N} .

Algorithm 3 Interface reconstruction

- 1: **for** each non leaf cell (traversing from leaf to root) **do**
- 2: $\alpha \leftarrow$ average of the children's volume fractions
- 3: **for** each cell \mathcal{C} containing the interface (traversing from root to leaf) **do**
- 4: Compute $\alpha_{i,j}$ over the stencil using Algo. 1.
- 5: Compute \mathbf{n} using $\alpha_{i,j}$ and the MYC scheme.
- 6: Compute $a = \mathcal{V}^{-1}(\mathbf{n}, \alpha_{0,0})$.
- 7: Store \mathbf{n} and a as state variables of \mathcal{C} .

2.5.2 Computing the interfacial forces: a balanced force surface tension calculation

Estimating accurately the surface tension term $(\sigma\kappa\delta_S \mathbf{n})_{n+1/2}$ in the momentum equation (2.2) is an ongoing challenge for the VOF method in the context of surface-tension-driven flows (Gorokhovski & Herrmann, 2008). The two major scheme families are the front tracking methods (Popinet & Zaleski, 1999) and level set with the Ghost Fluid Methods (GFM) (Kang *et al.*, 2000; Hong *et al.*, 2007). However, both families present major drawbacks. The front tracking methods cannot deal simply with topology changes while the level set methods show difficulties to ensure mass conservation (Popinet, 2009).

One of the original ideas proposed to deal with the surface term in the context of VOF methods was introduced by Brackbill *et al.* (1992) who proposed a Continuum-Surface-Force (CSF) approach based on an approximation of the surface tension term and of the curvature κ such that

$$\sigma\kappa\delta_S \mathbf{n} \approx \sigma\kappa\nabla\tilde{\alpha}, \quad (2.30)$$

$$\kappa \approx \nabla \cdot \tilde{\mathbf{n}}, \quad (2.31)$$

$$\tilde{\mathbf{n}} = \frac{\nabla\tilde{\alpha}}{\|\nabla\tilde{\alpha}\|}, \quad (2.32)$$

where $\tilde{\alpha}$ is a spatially filtered volume fraction field. The CSF approach suffers from spurious currents when it is applied to the case of a stationary droplet in theoretical equilibrium (Scardovelli & Zaleski, 1999). In the case of a stationary droplet, the discretised momentum equation reduces to (Renardy & Renardy, 2002; Francois *et al.*, 2006)

$$-\nabla p_{n+1/2} + \sigma\kappa(\delta_S \mathbf{n})_{n+1/2} = \mathbf{0} \quad (2.33)$$

and, when using the CSF approximations, becomes

$$-\nabla p_{n+1/2} + \sigma\kappa(\nabla\alpha)_{n+1/2} = \mathbf{0}. \quad (2.34)$$

Even if spurious currents appear around the interface of the droplet, the exact discrete equilibrium between the surface tension and the pressure gradient can be recovered if

1. the discrete approximations of both gradients taking part in Eq. (2.34) are compatible.
2. the estimated curvature κ is constant.

Respecting those two conditions leads to the exact discrete equilibrium solution $p_{n+1/2} = \sigma\kappa\alpha_{n+1/2} + \text{constant}$. In the actual scheme, the computation of the cell centered pressure gradient is done by averaging the face centered pressure gradient, see Eq. (2.23). To make the gradient operators compatible and respect the condition 1, it is required first to apply the surface tension force to the auxiliary face centered velocity field \mathbf{u}_\star^f as

$$\mathbf{u}_\star^f = \mathbf{u}_\star^f + \frac{\Delta t \sigma \kappa_{n+1/2}^f}{\rho(\alpha_{n+1/2}^f)} \nabla^f \alpha_{n+1/2} \quad (2.35)$$

and second to apply the corresponding cell centered surface tension force to \mathbf{u}_\star^c as

$$\mathbf{u}_\star^c = \mathbf{u}_\star^c + \left| \frac{\Delta t \sigma \kappa_{n+1/2}^f}{\rho(\alpha_{n+1/2}^f)} \nabla^f \alpha_{n+1/2} \right|^c \quad (2.36)$$

On the practical side, the implementation of the last two conditions is identical to the implementation of the pressure corrections, Eq. (2.22) and (2.23). Thus, the routines used to compute the pressure corrections and the surface tension corrections are the same in Basilisk. Now that the condition 1 is respected, it is possible to focus on the condition 2. The second one depends on the accuracy of the curvature estimation which raised numerous difficulties regarding the developments of VOF methods. The next section details how the calculation of the curvature with a generalised height function can provide an accurate estimation.

2.5.3 Computing the interface curvature

Once again, several methods exist to estimate the curvature of the interface. Complementary to the approximation of Brackbill *et al.* (1992), Eq. (2.31), it was proposed to estimate the curvature thanks to the differentiation of exact level set functions (Cummins *et al.*, 2005) or high order methods based on parabolic fitting, like the PROST method (Renardy & Renardy, 2002), or on spline interpolation (Ginzburg & Wittum, 2001). Following the curvature calculation based on height functions (HF) proposed by Torrey *et al.* (1985), the curvature estimation is done in Basilisk thanks to a height function calculation generalised to octree structure. HF calculations demonstrated inconsistency in cases for which the radii of the interface curvature is of the order of the mesh size. Thus, extra care is required to handle under-resolved interfaces which can occur during topology changes. The following introduces first the HF calculation for octree structures and then the procedure for estimating the curvature of under-resolved interfaces. The algorithms presented here are those of Popinet (2009). Further information about surface tension models is available in the review of Popinet (2018).

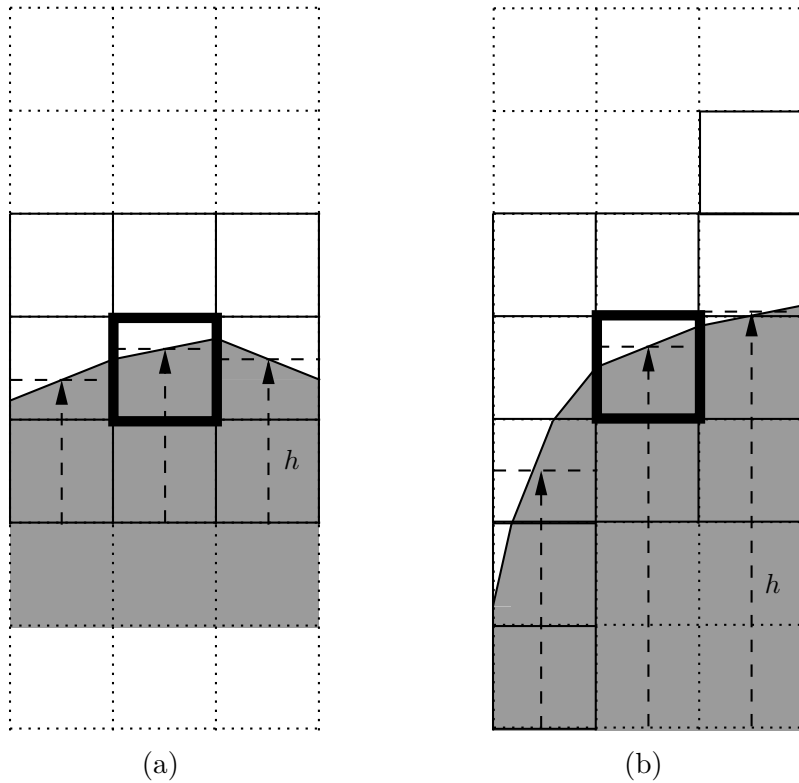


Figure 2.2: Scheme of an interface with a small curvature captured by a 3×3 symmetric stencil (a) and with a stronger curvature captured by an asymmetric stencil (b). The dotted grids represent a 3×7 stencil, the thick lines cell represent the target cell \mathcal{C} and the arrows correspond to the interface height h in a stencil column.

2.5.3.1 Height function and octree structures

The classic height function calculation on a 2D Cartesian grid (Cummins *et al.*, 2005) relies on 3×7 or 7×3 stencils from which a discrete estimation of the interface height h is derived. The curvature κ is then computed thanks to the derivatives of h : $\kappa = h''/(1 + h'^2)^{3/2}$. Algorithm

[1](#) could be used to reconstruct similar symmetric stencil in octree grids but several limitations raise here. Symmetric stencils with predefined size are not the most suitable to evaluate the curvature interface. For instance, depending on the interface topology, some columns within a same stencil might need to be higher or could be smaller than 7 cells, leading to reconstruct ill calibrated symmetric stencils. Considering instead local asymmetric stencils for which the size of each column can be adapted to the topology of the interface overcomes the latter issue. Fig. [2.2](#) illustrates the benefits of not predefining the stencil size as well as the difference between a symmetric and asymmetric stencil. For both stencils, the interface is captured and their sizes are smaller than a 3×7 . While the symmetric stencil can capture the weakly curved interface, the asymmetric stencil can capture stronger curvature requiring less cells than a symmetric stencil, and reducing pressure on the memory usage. Evaluating the interface height in a stencil column is then the elementary operation of the HF procedure. This operation is done by the Algorithm [4](#).

In this algorithm, \mathcal{C} can be understood as an initial guess of the interface location. Then, starting from \mathcal{C} , it is possible to explore the cells in the top and the bottom directions, i.e. the cells above and below, until the interface is captured. Those directions are defined relatively to the interface orientation. The interface is said to be consistent when the top cells of the column are empty, $\alpha = 0$, while the bottom cells are filled, $\alpha = 1$. The first part of the algorithm, the first while loop from line 8 to line 13, consists of summing the volume fraction in the top direction until the interface is found, $\mathcal{I} = \text{true}$, and a full or empty cell, $\alpha \in [0, 1]$, is reached. If the lastly explored cell is full, $\alpha = 1$, then a consistent interface cannot be computed with the current stencil and an error is returned, line 14. In the second part, the second while loop from line 21 to line 26, the operation is repeated along the bottom direction, this time looking for a full cell. With a correct guess of the initial cell \mathcal{C} , the algorithm is equivalent to using optimal local asymmetric stencils (Popinet, [2009](#)). Additionally, no prior assumption on the stencil height is required. The generalisation of Algorithm [4](#) is achieved by considering virtual cells in the case of coarse-fine neighbours, as in Algorithm [1](#).

Once the local asymmetric stencil is computed, it is possible to compute the curvature with the full height function curvature estimation given in Algorithm [5](#). Setting a common origin at line 5 is most needed as the stencils columns are formed independently and do not necessarily have the same origin. Note that the function $h(\mathcal{C})$ returns the absolute height of the center of \mathcal{C} and that \mathcal{P}_\perp denotes the plane perpendicular to the top direction.

2.5.3.2 Handling the case of under-resolved interfaces

As mentioned in the introductory paragraph of the subsection, height functions show difficulty to compute the interface curvature when the curvature radii are of the order of the mesh size. Besides, even moderately curved interfaces can lead to inconsistent interface heights (Popinet, [2009](#)). To overcome this issue, a solution is to use the heights which are consistent, returned by Algorithm [5](#) on line 9, and perform a parabola (2D) or a paraboloid (3D) fitting through those heights. The resulting analytical fit function can then be differentiated in order to estimate the interface curvature κ . Generally speaking, consider a cell \mathcal{C} and N estimated interface positions $\{\mathbf{x}_1, \mathbf{x}_2, \dots, \mathbf{x}_N\}$, the curvature of the under-resolved interface can be estimated with Algorithm [6](#).

The first condition of Algorithm [6](#), line 1, considers the number of independent interface positions instead of the total number of positions N . Two positions \mathbf{x}_i and \mathbf{x}_j are said independent when $\|\mathbf{x}_i - \mathbf{x}_j\| \geq \Delta$. This is necessary in order to have a well conditioned minimisation

Algorithm 4 Interface height (\mathcal{C} , top direction)

```

1:  $H \leftarrow \alpha(\mathcal{C})$                                      ▷ Initialise height.
2:  $\mathcal{N} \leftarrow \mathcal{C}$ 
3:  $\alpha_{top} \leftarrow \alpha(\mathcal{C})$ 
4: if  $\alpha_{top} < 1$  then                                ▷ Test if the cell contains the interface.
5:    $\mathcal{I} \leftarrow true$ 
6: else
7:    $\mathcal{I} \leftarrow false$ 
8: while  $\mathcal{I} = false$  or  $\mathcal{N}$  contains the interface do      ▷ Process the cells above  $\mathcal{C}$ .
9:   Replace  $\mathcal{N}$  with its top neighbour.
10:   $\alpha_{top} \leftarrow \alpha(\mathcal{N})$ 
11:   $H \leftarrow H + \alpha_{top}$ 
12:  if  $\mathcal{N}$  contains the interface then
13:     $\mathcal{I} \leftarrow true$ 
14: if  $\alpha_{top} \neq 0$  then return inconsistent height.
15:  $\mathcal{N} \leftarrow \mathcal{C}$ 
16:  $\alpha_{bottom} \leftarrow \alpha(\mathcal{C})$ 
17: if  $\alpha_{bottom} > 0$  then                                ▷ Test if the cell contains the interface.
18:    $\mathcal{I} \leftarrow true$ 
19: else
20:    $\mathcal{I} \leftarrow false$ 
21: while  $\mathcal{I} = false$  or  $\mathcal{N}$  contains the interface do      ▷ Process the cells below  $\mathcal{C}$ .
22:   Replace  $\mathcal{N}$  with its bottom neighbour.
23:    $\alpha_{bottom} \leftarrow \alpha(\mathcal{N})$ 
24:    $H \leftarrow H + \alpha_{bottom}$ 
25:   if  $\mathcal{N}$  contains the interface then
26:      $\mathcal{I} \leftarrow true$ 
27: if  $\alpha_{bottom} \neq 0$  then return inconsistent height.
      return  $H$  and  $\mathcal{N}$ 

```

Algorithm 5 Height function curvature (\mathcal{C} , top direction)

```

1:  $h_0, \mathcal{N}_0 \leftarrow \text{Interface height}(\mathcal{C}, \text{top direction})$           ▷ Process the column of  $\mathcal{C}$ 
2: for each column  $i$  neighbouring  $\mathcal{C}$  do                                ▷ Process the other stencil columns
3:   Define  $\mathcal{N}$  as the closest neighbouring (virtual) cell to  $\mathcal{C}$  in  $\mathcal{P}_\perp$ .
4:    $h_i, \mathcal{N}_i \leftarrow \text{Interface height}(\mathcal{N}, \text{top direction})$ 
5:   Set a common origin  $h_i \leftarrow h_i + h(\mathcal{N}_i) - h(\mathcal{N}_0)$ .
6: if all heights are consistent then
7:    $\kappa \leftarrow \text{estimation using the finite difference approximations of the derivatives of the}$ 
    $\text{discretised height function } h_i$ 
8:   return  $\kappa$ 
9: else
10:   return all the interface positions deduced from the consistent heights.

```

Algorithm 6 Parabola fitted curvature ($\mathcal{C}, \{\mathbf{x}_1, \mathbf{x}_2, \dots, \mathbf{x}_N\}$)

- 1: **if** there is not enough independent positions ($N < 3$ (2D), $N < 6$ (3D)) **then**
- 2: a meaningful least squares fit cannot be achieved, **return** an error
- 3: Retrieve the normal \mathbf{n} to the interface in \mathcal{C} , precomputed with Algo. 3.
- 4: $\mathcal{O} \leftarrow$ coordinates of the barycentre of the reconstructed interface fragment in \mathcal{C} .
- 5: Define an orthonormal coordinates system $\mathcal{R} = \{\mathcal{O}, (\mathbf{i}, \mathbf{m})\}$ ($\mathcal{R} = \{\mathcal{O}, (\mathbf{i}, \mathbf{j}, \mathbf{m})\}$ in 3D)
- 6: $\{\mathbf{x}'_1, \mathbf{x}'_2, \dots, \mathbf{x}'_n\} \leftarrow$ transformed coordinates of the interface positions in \mathcal{R} .
- 7: fit a parabola (a paraboloid in 3D) by minimising

$$\mathcal{F}(c_i) = \sum_{j=1}^N [z'_j - f(c_i, \mathbf{x}'_j)]^2 \quad (2.37)$$

$$f(c_i, \mathbf{x}) = \begin{cases} c_0x^2 + c_1x + c_2 & \text{(2D)} \\ c_0x^2 + c_1y^2 + c_2xy + c_3x + c_4y + c_5 & \text{(3D)} \end{cases} \quad (2.38)$$

return the mean curvature κ at the origin \mathcal{O} of \mathcal{R} such that:

$$\kappa = \begin{cases} 2c_0[1 + c_1^2]^{-3/2} & \text{(2D)} \\ 2[c_0(1 + c_4^2) + c_1(1 + c_3^2) + c_2c_3c_4][1 + c_3^2 + c_4^2]^{-3/2} & \text{(3D)} \end{cases} \quad (2.39)$$

problem. Additionally, the minimum number of independent interface positions is set to 3 (2D) or 6 (3D) because the minimisation problem requires the solution of 3×3 (2D) or 6×6 (3D) linear systems. Even if this procedure is sufficient to compute the curvature of most under resolved interfaces, it can happen that the number of independent positions is too small, like for complicated topology at coarse resolution. In this case, a new set of interface positions is constructed by computing the barycentres of the reconstructed interface fragments in each cell of a 3×3 (2D) or $3 \times 3 \times 3$ (3D) stencil. If this approach fails as well to provide enough independent positions \mathbf{x}_i , the considered cell probably contains an isolated or degenerate interface fragment. Its curvature is then simply set to 0. With the previous considerations in mind, the mean curvature of the interface contained in a cell \mathcal{C} can be computed by following Algorithm 7.

In terms of performance, the parabola fitting step is more expensive than the standard HF method. Even though, most of the cases will be dealt within the for loop, line 3 to 7, in couples of iterations. A large part of the remaining cases will be dealt within the parabola fitting procedure and seldom cases will be dealt using the barycentre construction on line 11. Thus the computational cost is mainly dominated by the cost of the standard HF method. The balanced force surface tension given in Eq. (2.35) requires the face centered interface curvature estimates. Those values are computed either by averaging the cell centered curvatures of the neighbouring cells when they both contain the interface or by taking the value of the cell centered curvature in either cell containing the interface.

Algorithm 7 Curvature (\mathcal{C})

```

1: Retrieve the normal  $\mathbf{n}$  to the interface in  $\mathcal{C}$ , precomputed with Algo. 3.
2:  $\mathcal{S} \leftarrow$  set of 2 spatial directions (3 in 3D) in decreasing order of alignment with  $\mathbf{n}$ .
3: for each top direction in  $\mathcal{S}$  do
4:    $\kappa \leftarrow$  Height function curvature( $\mathcal{C}$ , top direction)
5:   if  $\kappa$  is consistent then return  $\kappa$ 
6:   else
7:      $\mathcal{I} \leftarrow \mathcal{I} +$  set of the interface positions deduced from the consistent heights
8:    $N \leftarrow$  number of independent positions in  $\mathcal{I}$ .
9:   if  $N < 3$  in 2D or  $N < 6$  in 3D then
10:    reset  $\mathcal{I}$ 
11:     $\mathcal{I} \leftarrow$  set of interface positions built from the barycentres of the reconstructed interface
      fragments in a  $3 \times 3$  (2D) or  $3 \times 3 \times 3$  stencil centered on  $\mathcal{C}$ .
12:     $N \leftarrow$  the number of independent positions in  $\mathcal{I}$ 
13:   if  $N$  is still too small then return 0
        return Parabola fitted curvature ( $\mathcal{C}, \mathcal{I}$ )

```

2.5.4 Droplet detection

Once the surface tension term is correctly discretised and estimated, the multiphase flow can evolve and potentially presents a disperse phase, i.e. a phase which would be split into different volumes like droplets in gas or bubbles in a liquid. Consider the volume fraction field α . By choosing a threshold value, one can filter the computational domain and separate the two phases. However, nothing would be known about the droplets as the filtering only results in a group of gas cells and a second group of liquid cells, without more distinction. Complementary to solver's routines for solving the governing equations, a routine in Basilisk enables to detect the cells connected into neighbourhoods. Not only the detection is carried out but also the cells of the same neighbourhood are tagged with an unique index, which can be seen as the index of the neighbourhood. The scheme to do so follows Algorithm 8 where N_N and α_f denote the total number of neighbourhoods and the filtered volume fraction field in which all the values less than a chosen threshold are set to 0. At the beginning of the procedure, the indices of the cells are used to initialise the *tag* values. The cells see their *tag* value being refined first by setting it as the *tag* of its parent cell and second by setting it as the minimum *tag* of the neighbouring cells. The operation is repeated until all the cells of the same neighbourhood have the same index, i.e. when the list of *tag* stops evolving. The resulting indices can then range from one to the total number of leaf cells. They need to be reduced so they range from 1 to the total number of neighbourhoods. Finally, it is possible to compute quantities of the neighbourhood such as its volume by adding the volume of the contained cells weighted by the volume fraction or the coordinates of its velocity by adding the velocities in the contained cells weighted by the cell volume and volume fraction.

Algorithm 8 Tag (α_f)

```
1: for each leaf cell do                                ▷ Initialise the tag values.  
2:   if  $\alpha_f \neq 0$  then  
3:      $tag \leftarrow$  cell index  
4:   else  
5:      $tag \leftarrow 0$   
6: while the  $tag$  values change do                  ▷ Set a unique index to neighbouring cells.  
7:   for each cell (traverse from root to leaves) do  
8:     if the parent cell's  $tag \neq 0$  then          ▷ First  $tag$  refinement  
9:       children's  $tag \leftarrow$  parent's  $tag$ .  
10:    if  $tag >$  neighbours'  $tag$  then           ▷ Second  $tag$  refinement  
11:       $tag \leftarrow$  minimum  $tag$  of the neighbour cells.  
12: Reduce the range of  $tag$  indices to  $\llbracket 1, N_N \rrbracket$ .
```

2.6 Conclusion

Among the three main types of simulations, Direct Numerical Simulations were retained to carry out numerical experiments in this Ph.D thesis due to their ability to reproduce natural phenomena with a satisfying accuracy. Additionally, the open source C-based high level programming language Basilisk was chosen to simulate the fragmentation of liquid round jets. Explaining the numerical methods used in Basilisk is of utmost importance in order to picture their accuracy as well as to frame the limits of the DNS and of the subsequent conclusions.

The fragmentation mechanism under consideration occurs at low Mach numbers without any gravitational forces and involves two immiscible, viscous, incompressible fluids. The flow dynamics is then governed by the unsteady Navier-Stokes equations with surface tension. The governing equations can be expressed in the theoretical framework of a single fluid flow with variable density and viscosity in which the two phases are taken into account through the volume fraction field.

The Navier-Stokes equations are solved for a biphasic flow with a constant surface tension using numerical schemes similar to Popinet (2003) & Lagrée *et al.* (2011). The resolution of the equations relies on time steps limited by the Courant-Friedrichs-Lowy (CFL) condition, the advection scheme of Bell-Collela-Glaz (Bell *et al.*, 1989) and a multilevel solver for the Poisson equation. The gas-liquid interface is tracked with a Volume-Of-Fluid (VOF) scheme which is geometric, conservative and non diffusive (López-Herrera *et al.*, 2015). Regarding the surface tension, the interfacial forces are estimated thanks to the Continuum-Surface-Force (CSF) method of Brackbill *et al.* (1992) and an estimation of the interface curvature based on height functions (Popinet, 2009, 2018). A projection method is used to compute the centered pressure gradient. The VOF scheme is combined with an octree adaptative grid (Agbaglah *et al.*, 2011) while the grid adaptation algorithm relies on a wavelet estimated discretisation error, described by Popinet (2015) and used for atmospheric boundary layer simulations by van Hooft *et al.* (2018). Such grids present the advantage of finely resolving the gas-liquid interface while having a coarser resolution away from the interfaces, and thus enable an increase of the computational velocity. Finally, the droplet detection is achieved by a tag function which associates a different tag to each neighbourhood of connected cells respecting a threshold condition on the fraction field and opens the way for studying bubbles or droplets numerically.

Chapter 3

Multimodal distributions of agricultural-like sprays: A statistical analysis of drop population from a pressured-atomized spray

Contents

3.1	Preamble	56
3.2	Multimodal distributions of agricultural-like sprays	57
3.3	Connecting the size-velocity joint distribution and the fragmentation mechanisms	82

3.1 Preamble

Studying agricultural-like sprays is a challenging task because of the intense flow turbulence, see Sec. 1.4.1, the multiplicity of fragmentation mechanisms once the liquid core pinched off (Guildenbecher *et al.*, 2009) and the large distances on which the jet and spray can evolve, typically up to several meters (Felis-Carrasco, 2017). The classic case of jet fragmentation involving the injection of a liquid at high velocity - high enough to make the configuration lie in the second wind induced or atomisation regime, see Sec. 1.2.2 - in a quiescent gaseous medium is called a pressure atomized spray (Lefebvre, 1989). Using the experimental measurements of Felis *et al.* (2020) performed on such sprays, we carry out a statistical analysis on the resulting droplet population. The multimodal nature of the size and axial velocity distributions is highlighted as well as the good agreement with the experimental data of the intermittency based size distribution of Novikov & Dommermuth (1997). Furthermore, a quadratic model is shown to describe qualitatively well the trend of the size-velocity joint distribution and, based on the marginal distribution properties, several droplet subsets with a characteristic size and velocity are derived from the latter joint distribution.

This analysis was published as an article in Physical Review Fluids. Sec. 3.2 reproduces the article and Sec. 3.3 proposes further connections between the droplet population distributions and the fragmentation mechanisms.

3.2 Multimodal distributions of agricultural-like sprays

Multimodal distributions of agricultural-like sprays: A statistical analysis of drop population from a pressure-atomized spray

Romain Vallon *, Malek Abid †, and Fabien Anselmet ‡
Aix Marseille University, CNRS, Centrale Marseille, IRPHE, Marseille, France



(Received 9 April 2020; accepted 13 January 2021; published 11 February 2021)

This paper focuses on the statistical analysis of a droplet population produced by a pressure-atomized jet spray, laying in the second-wind-induced regime, far behind the nozzle. The droplet size and axial velocity derived from droplet tracking velocimetry measurements are shown to follow bimodal distributions and their modeling is tackled in the framework of turbulence and of combustion applications, respectively. In addition, the existence of subsets of droplets showing specific behaviors is brought to light from the analysis of the experimental droplet-size–velocity joint probability distribution function (PDF). Such subsets can be precisely defined using the properties of the size and axial-velocity distributions. Finally, the trend of the joint PDF is depicted due to a quadratic relationship which is derived in the context of combustion and shown to work here as well, far behind the nozzle.

DOI: [10.1103/PhysRevFluids.6.023604](https://doi.org/10.1103/PhysRevFluids.6.023604)

I. INTRODUCTION

Liquid jet atomization is at the heart of numerous natural and industrial systems such as ocean sprays, medication administration, and farming irrigation by aspersion. Widely used across Europe, the latter application would benefit performance gain by better understanding the atomization phenomenon. This application relies on the injection in quiescent air of a round water jet at a velocity u_{inj} through a nozzle of diameter d_n and falls in the scope of both multiphase flows and polydisperse sprays. The phases are denoted by the subscript k , which takes the value l for the liquid phase and g for the gas phase. Classically, atomization flows are controlled by the Reynolds, Weber, and Ohnesorge numbers

$$\text{Re}_k = \frac{\rho_k u_{inj} d_n}{\mu_k}, \quad \text{We}_k = \frac{\rho_k u_{inj}^2 d_n}{\sigma_{l-g}}, \quad \text{Oh} = \frac{\mu_l}{\sqrt{\rho_l d_n \sigma_{l-g}}}, \quad (1)$$

where ρ_k and μ_k represent the density and the dynamic viscosity of the phase k , respectively, while σ_{l-g} is the surface tension between the two phases.

Previous experiments showed the existence of five different regimes for nonassisted cylindrical liquid jets [1]. Among those, the second-wind-induced regime is not too far from the industrial application of aspersion irrigation and offers a more controlled environment for laboratory research. This high gas Weber regime is characterized by a large nozzle diameter $d_n > 1$ mm and sharp limits on the gas Weber number $13 < \text{We}_g < 40.3$. Physically, jets belonging to this regime show a characteristic primary atomization for which small droplets are peeled off the interface near the nozzle exit. Studies have been carried out to extensively characterize this primary breakup along

*romain.vallon@univ-amu.fr

†malek.abid@univ-amu.fr

‡fabien.anselmet@univ-amu.fr

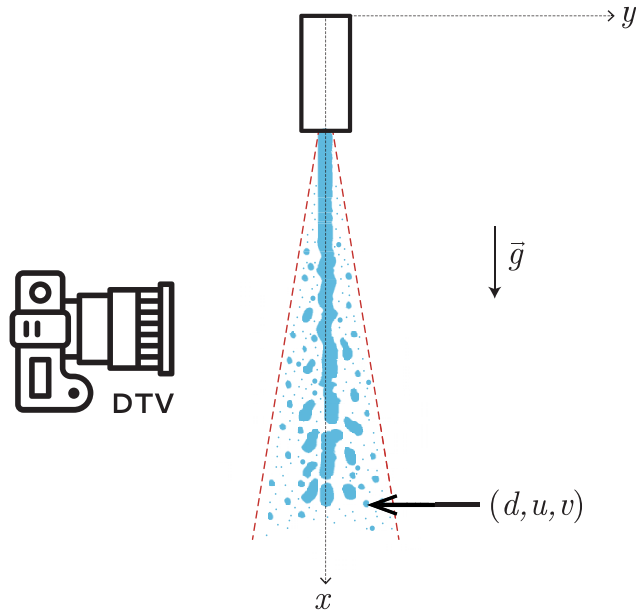


FIG. 1. Schematic of the experimental setup used by Felis *et al.* [8], with \vec{g} the gravity field, d the droplet diameter, and (u, v) the droplet axial and transversal velocities, respectively, along x and y .

the jets, before the breakup of the liquid core, including work of great importance by Faeth and co-workers [2–6], who particularly emphasized the role of turbulence by deriving a correlation for the Sauter mean diameter $d_{3,2}$ as a function of the distance to the nozzle x , its diameter d_n , the liquid Weber number We_l , and the integral length scale of turbulence L . Several subregimes with different characteristic behaviors have been precisely depicted using the jet density ratio ρ_l/ρ_g , the liquid Weber number We_l , the ratio between the Rayleigh breakup time and the aerodynamic secondary breakup time, and the degree of development of turbulence, quantified by the ratio of the nozzle length L_n and the nozzle diameter d_n .

Following along the lines of Faeth and co-workers, later works focused on the region away from the nozzle, between the breakup of the jet liquid core and the jet dispersion zone, to study the polydisperse droplet population produced by atomization. A specific droplet tracking velocimetry (DTV) technique was used by Stevenin *et al.* [7] to obtain original joint size-velocity measurements which include at the same time two velocity components and the diameter, covering a large size range, for each droplet. Insights into the turbulent multiphase flow common in the irrigation problem were derived that allow a comparison between the Reynolds stresses from the DTV and the turbulent kinetic energy from a turbulent Reynolds-averaged Navier-Stokes model. Felis *et al.* [8] further developed this method by establishing a reproducible study case and by coupling this technique with laser Doppler velocimetry (LDV) and optical probe (OP) techniques.

The latter experimental setup implements a circular nozzle of diameter $d_n = 1.2$ mm and length $L_n/d_n = 50$, which ensures a fully developed turbulent pipe flow. The nozzle is made of borosilicate glass and the interior wall roughness is considered negligible. A vertical liquid water jet is injected with an average bulk velocity $u_{inj} = 35$ m/s pointing downward into quiescent air (see Fig. 1). The campaign was made under normal conditions (297 K and 1 atm); the corresponding physical properties are given in Table I. The chosen injection velocity ensures that there is no cavitation in the nozzle. The dimensionless numbers of the case-study conditions are $Re_l = 41\,833$, $We_l = 20\,158$, $We_g = 24.3$, and $Oh = 0.0034$, which makes the jet lie in the second-wind-induced regime detailed above. An estimation of the Taylor-scale Reynolds number at the nozzle exit, based on the results from Ruffin *et al.* [9], gives $Re_\lambda = 400$, typical for fully developed turbulence in monophasic flow. The OP provides the mean liquid mass fraction and volume fraction. A specific LDV apparatus allows us to measure separately the liquid and gas velocities. Finally, a custom DTV algorithm

TABLE I. Physical properties considered by Felis-Carrasco [10], under normal conditions and in SI units.

Property	Definition	Value
ρ_l	water density	998.3 kg/m ³
ρ_g	air density	1.205 kg/m ³
ν_l	water kinematic viscosity	1.004×10^{-6} m ² /s
ν_g	air kinematic viscosity	15.11×10^{-6} m ² /s
σ_{l-g}	water-air surface tension	0.073 N/m

can capture the liquid velocity in the dispersion area of the spray. The DTV measurements are carried out to determine the radial profiles for $x/d_n \in [400, 800]$ while paying special attention to the depth-of-field estimations to reduce the bias on the droplet-size–velocity correlation. Details are given in [10].

Among the results from this study, it appears that the droplet-size distribution greatly impacts the mean velocity and the Reynolds stress field. This opens the way for a possible segregation of the droplets into several subgroups, as the Reynolds stress tensor shows different behaviors depending on the droplet size. A size class repartition highlights that small droplets tend to show large velocity fluctuations and a Stokes number of $O(1)$, like passive tracers in turbulence, while bigger droplets show a high axial mean velocity with almost zero fluctuations with a Stokes number of $O(100)$, like ballistic objects. However, the statistical analysis is not fine enough to depict precisely any specific group in the overall population.

Furthermore, the question of the drop size and velocity joint distribution remains open for this kind of flow. On the one hand, Villermaux [11] alleged that drop-size distributions are described by a universal Γ law, derived from a fine analysis of the ligament dynamics in low-turbulence fragmentation flows. While this law showed good agreement with experiments showing unimodal [12,13] or bimodal size distributions [14], it is legitimate to question its validity in fragmentation flows where turbulence plays a major role. On the other hand, Novikov and Dommermuth [15] used a phenomenological approach based on turbulence to describe the droplet-size distribution. Starting from the idea of similarity, i.e., the cascade process, they proposed a size distribution for turbulent flows based on infinitely divisible distributions [16] and turbulence intermittency [17]. Later on, Rimbert and Sero-Guillaume [18] simplified this approach by considering log-stable distributions, which are easier to handle than infinitely divisible distributions, and Rimbert and Castanet [19] were able to describe the multimodal size distribution produced in a bag-breakup regime with a crossover between Rayleigh-Taylor instability and the turbulent cascading atomization mechanism. Finally, in the context of combustion, Lee and An [20] derived, from the energy balance of a pressure-atomized spray, a quadratic formula for the droplet size as a function of the liquid velocity. Given the short distances over which jets develop in combustion applications, it is natural to wonder about the performance of this formula for agricultural-like configurations.

The present paper focuses on the DTV measurements by Felis *et al.* [8] and Felis-Carrasco [10]. It offers an analysis of the multimodal size-velocity joint probability distribution function (PDF) and a determination of different subgroups among the overall droplet population. Section II presents the three models cited above. Section III is dedicated to the analysis of the size and velocity distributions and their modeling. Section IV focuses on the determination of the droplet subgroups based on the size-velocity joint PDF and on the investigation of the validity of the quadratic formula proposed by Lee and An [20] for x/d_n between 400 and 800.

II. MODELING THE SIZE DISTRIBUTION OF SPRAY-GENERATED DROPLETS

In the context of multiphase flows, the governing equations must be derived using a phase indicator α_k , which indicates the presence of the phase k at any position \mathbf{x} and instant t . Assuming

there is no mass exchange between the phases, the governing equations for a phase k are then [21]

$$\frac{\partial \rho_k \alpha_k}{\partial t} + \frac{\partial \rho_k \alpha_k u_{j,k}}{\partial x_j} = 0, \quad (2a)$$

$$\frac{\partial \rho_k \alpha_k u_{i,k}}{\partial t} + \frac{\partial \rho_k \alpha_k u_{i,k} u_{j,k}}{\partial x_j} = \frac{\partial \alpha_k \sigma_{ij,k}}{\partial x_j} + f_{s,i,k-k'} \sigma_k^s, \quad (2b)$$

where $u_{j,k}$ stands for the j -velocity component of phase k , $f_{s,i,k-k'}$ represents the friction force between the phases k and k' which applies on the interface s of volumetric density σ_k^s , and $\sigma_{ij,k}$ stands for the Cauchy stress tensor associated with phase k . Deriving the droplet-size distribution directly from Eqs. (2) is not possible yet and models are needed in order to depict and predict such a distribution. The following sections introduce the different approaches and corresponding droplet-size distributions of Villermaux *et al.* [22], Novikov and Dommermuth [15], and Lee and An [20].

A. Ligament-mediated spray formation

In contrast to the classical cascade process in which large elements generate smaller ones, Villermaux *et al.* [22] proposed an aggregation scenario in which ligaments are the cornerstone. This processus relies on the aggregation kinematics developed by Smoluchowski [23] for solid colloidal particles in Brownian motion. Let $n(v, t)$ be the number of clusters of volume between v and $v + dv$ at the instant t . In addition, $N(t)$ is the total number of clusters and $K(v, v')$ is the frequency of aggregation between clusters of volumes v and v' . The aggregation kinetics is then governed by

$$\partial_t n(v, t) = -n(v, t) \int_0^\infty K(v, v') n(v', t) dv' + \frac{1}{2} \int_0^v K(v', v - v') n(v', t) n(v - v', t) dv'. \quad (3)$$

When talking about droplets, it is common to assume that the elements are spherical. The element size is then given by the diameter d and one can consider $n(d, t)$ instead of $n(v, t)$. In [12,22] the ligaments were supposed to consist of v independent sublayers resulting from a random particulate motion. Each sublayer consisted of subblobs of size d' and their size distribution was denoted by $q(d', t)$. The interaction between the sizes was assumed to be both random and uncorrelated. According to [24], the evolution of $q(d', t)$ was governed by a convolution process and the distribution of size d was such that $n(d, t) = N(t)q(d', t)^{\otimes v}$, where \otimes denoted the convolution product. Equation (3) then becomes

$$\partial_t n(d, t) = -n(d, t)N(t)^{\gamma-1} + \frac{1}{3\gamma-2} n(d, t)^{\otimes\gamma}, \quad (4)$$

where $\gamma = 1 + 1/v$, with v the number of ligament layers. Knowing that the process is governed by successive autoconvolutions and that the distribution $q(d, t)$ in each layer is assumed to be independent, the droplet-size distribution p_B along the ligament after detachment from the bulk flow is thus described by a v convolution

$$p_B(d) = p_1(d)^{\otimes v}, \quad (5)$$

where $p_1(d)$ is an elementary distribution corresponding to the size distribution along a ligament layer, once the ligament is detached from the bulk flow. It can be chosen as an exponential distribution characterized by the diameter ξ_B of the detached ligament before its breakup [22]. The distribution p_B is rewritten as

$$p_B(x = d/\langle d \rangle) = \frac{v^v}{\Gamma(v)} x^{(v-1)} e^{-vx}, \quad (6)$$

where $\langle d \rangle = \frac{1}{N(t)} \int dn(d, t) dd$ is the instantaneous mean droplet diameter. Finally, the droplet-size distribution of the spray is given by the composition of the ligament size distribution $p_L(d_0)$, with

d_0 the size of a ligament, and the droplet-size distribution after the ligament breakup $p_B(d/d_0)$,

$$p(d) = \int_0^\infty p_L(d_0)p_B\left(\frac{d}{d_0}\right)\frac{dd_0}{d_0}. \quad (7)$$

Furthermore, the distribution p_L of the ligament size is also Γ distributed [25] and Kooij *et al.* [26] derived the droplet-size distribution of a spray as

$$p(x = d/\langle d \rangle) = \frac{2(mn)^{(m+n)/2}x^{(m+n)/2-1}}{\Gamma(m)\Gamma(n)} \mathcal{K}_{m-n}(2\sqrt{nm}x), \quad (8)$$

with \mathcal{K}_{m-n} the modified Bessel function of the second kind. The parameter m sets the order of the ligament size distribution and n the ligament corrugation, previously denoted by ν .

B. Small-scale intermittency and droplet size

In his seminal work, Kolmogorov [27,28] stated two main assumptions about isotropic turbulence, which are the scale invariance of eddies and the scale localness of interaction, allowing quantitative predictions for the energy distribution among the scales of the flow. This led to the image of the turbulent process as a cascading process where the turbulent energy injected at a rate ϵ at larger scales cascades down the smaller scales before being eventually removed due to dissipation, still at a rate ϵ . Following the theoretical remark of Landau and Lifshitz [29], a refinement of the hypothesis on the local structure of turbulence was proposed to take into account the small-scale intermittency of turbulence [30–32]. More details about intermittency are given in [33] and a review of intermittency models is available in [34].

Novikov and Dommermuth [15] proposed a statistical description of droplets in turbulent spray connected with the turbulent dissipation resulting from small-scale intermittency. Similarly to the context of turbulent energy dissipation, the authors proposed that liquid fragments go through a sequential cascade mechanism such that

$$l \equiv l_{N+1} = l_1 \prod_{k=1}^N b_k, \quad b_k = \frac{l_{k+1}}{l_k} \leq 1, \quad (9)$$

where l_1 is the initial size of a liquid fragment, N the number of breakups, and l the final size of a droplet at the end of the process. Equation (9) is rewritten as

$$y \equiv -\ln\left(\frac{l}{l_1}\right) = -\sum_{k=1}^N \ln(b_k). \quad (10)$$

Assuming that the coefficients b_k are independent or weakly dependent, if N is large enough, then it follows from the central limit theorem [35] that the distribution of y is normal. Thus the moments of the distribution of l/l_1 are given by

$$\left\langle \left(\frac{l}{l_1}\right)^p \right\rangle = \exp(-ap + \sigma^2 p^2). \quad (11)$$

Note that the right-hand side of Eq. (11) is larger than 1 when p tends towards $+\infty$, which contradicts Eq. (9). Physically speaking, this implies that Eq. (10) breaks the mass conservation. Mathematically speaking, in this situation, the properly normalized characteristic function of the probability function will tend to normal, but not the probability function [15]. Thus, even if the fragmentation process is supposed to be a sequential breakup cascade, the distribution of l/l_1 is not log-normal.

It follows from the refinement of Kolmogorov hypotheses that the turbulent energy dissipation is not uniformly distributed among the scales. The dissipation average rate over the distance r is denoted by ϵ_r . Consider the inertial range of scales $L \gg r \gg l_*$, where L is the integral scale and

l_* is an inertial scale which can differ from the Kolmogorov internal scale because of intermittency correction. For three scales r , ρ , and l in this range such that $r < \rho < l$, we can introduce the corresponding breakdown coefficients (BDCs)

$$q_{r,l} = \frac{\epsilon_r}{\epsilon_l}, \quad q_{r,l} \leqslant \frac{l}{r}, \quad q_{r,l} = q_{r,\rho} q_{\rho,l}. \quad (12)$$

The scale similarity in a turbulent flow is determined by the following conditions: (i) The probability distribution of BDCs depends only on the ratio of the corresponding scales and (ii) $q_{r,\rho}$ and $q_{\rho,l}$ are statistically independent. From those conditions and Eq. (12) we have, for the moments of the BDCs,

$$\langle q_{r,l}^p \rangle = \left(\frac{l}{r} \right)^{\mu(p)}, \quad \mu(0) = 0, \quad (13)$$

with the quantity $\mu(p)$ respecting additional properties given in [17]. Note that $\mu(2) = \mu$, with μ the classic intermittency coefficient [34]. By definition, the characteristic function for $\ln(q_{r,l})$ is $\psi(s, l/r) = \langle \exp[is \ln(q_{r,l})] \rangle$. By inverting this formula, it could be possible to determine directly the probability distribution of $q_{r,l}$, but it requires costly verifications to ensure the non-negativity of the distribution in order to enforce physical and mathematical meaning [16].

Deriving the distribution of $q_{r,l}$ can be achieved by noting that, for arbitrary ratio l/r and arbitrary integer n , Eq. (13) can be written in the form

$$\psi\left(s, \frac{l}{r}\right) = \psi^n\left(s, \left(\frac{l}{r}\right)^{1/n}\right), \quad (14)$$

which defines infinitely divisible distribution. The Lévy-Baxter-Shapiro theorem [35] gives the general form of such distributions concentrated on $[0, +\infty[$. Using this theorem allows us to derive a general form of $\mu(p)$ [16],

$$\mu(p) = \kappa p - \int_0^{+\infty} \frac{1 - e^{-px}}{x} F(dx), \quad (15)$$

where F is a measure on the open interval $[0, +\infty[$ such that $(1+x)^{-1}$ is integrable with respect to F . Knowing $\mu(p)$, it is thus possible to reconstruct the distribution W of $q_{r,l}$ from

$$W\left(q, \frac{l}{r}\right) = \frac{1}{2\pi q} \int_{-\infty}^{+\infty} \exp\left[-is \ln(q) + \mu(is) \ln\left(\frac{l}{r}\right)\right] ds. \quad (16)$$

Note that the distribution of $\ln(q_{r,l})$ is $Q[\ln(q)] = qW(q)$. Keeping in mind that $r\epsilon_r/L\epsilon_L$ is analogous to l/l_1 in Eq. (9), it is possible to use the distribution of ϵ_r/ϵ_l to model the distribution of l/l_1 . Doing so, Novikov and Dommermuth [15] gave one example of a distribution for $y = \ln(l/l_1)$ which only depends on the average $a = \langle y \rangle$ and the standard deviation $\sigma^2 = \langle (y - a)^2 \rangle$ of the population:

$$p(y) = \frac{a^{3/2}}{\sqrt{2\pi}\sigma y^{3/2}} \exp\left\{-\frac{a}{2\sigma^2}(ay^{-1/2} - y^{1/2})^2\right\}, \quad y \geqslant 0. \quad (17)$$

C. Integral approach from combustion

Lee and An [20] followed an integral approach in order to derive a relationship between the droplet diameter and velocity. This approach allowed them to relate the physical quantities at the nozzle exit to the ones downstream, in the jet dispersion zone where atomization is achieved. Consider a control volume V_s enveloping the overall spray volume. The argumentation relies on two main assumptions. First, the liquid phase is assumed to achieve the transition from its initial state to the final state of a fully atomized group of spherical droplets within the specified control volume. Second, it is assumed that the viscous dissipation can be written in terms of known parameters such

as the liquid velocity and dissipation length scale. The integral form of the conservation equations of mass and energy for the liquid phase in the control volume are given by

$$\rho_l u_{inj} A_{inj} = \iint \rho_l \frac{\pi d^3}{6} u A n \bar{p}(d, u) dd du \approx n \rho_l \frac{\pi}{6} \bar{u} A \sum_i^N p(d_i) d_i^3 \Delta d_i, \quad (18a)$$

$$\rho_l \frac{u_{inj}^3}{2} A_{inj} = n \rho_l \frac{\pi}{12} \bar{u}^3 A \sum_i^N p(d_i) d_i^3 \Delta d_i + n \bar{u} A \pi \sigma_{l-g} \sum_i^N p(d_i) d_i^2 \Delta d_i + K' \mu_l \left\langle \left(\frac{\partial u}{\partial y} \right)^2 \right\rangle V_s, \quad (18b)$$

where V_s is the spray volume. The mass conservation is achieved by equating the injected mass flow rate with the mass of the droplets contained in a volume swept by the mean velocity \bar{u} over a spray area A . The velocity distribution is simplified to an average drop velocity. The cross-sectional area A represents the physical extent of the spray at a plane where full atomization is achieved and can be calculated from the spray cone angle. The quantities n , d_i , $p(d_i)$, and Δd_i denote the droplet number density, the droplet diameter, the droplet-size distribution, and the droplet-size bin width, respectively. The authors considered that the fragmentation of the jet liquid core into droplets occurs at some velocity scale, taken as the mean liquid velocity \bar{u} , and at the length scale of the droplets, taken as the Sauter mean diameter $d_{3,2}$ since it is the scale at which droplets are created. This approach is similar to the classic one of Tennekes and Lumley [36] in which $(\partial u / \partial y)^2$ is linked to the Taylor microscale, taken here as $d_{3,2}$. This leads to the estimation of the average viscous dissipation as

$$\mu_l \left\langle \left(\frac{\partial u}{\partial y} \right)^2 \right\rangle V_s \sim \mu_l \left(\frac{u}{d_{3,2}} \right)^2 V_s. \quad (19)$$

Finally, the model has one adjustable parameter K' , as the exact relationship between the viscous dissipation term and the spray volume is approximated. After solving Eq. (18a) for n , substituting Eq. (19) into Eq. (18b) gives a quadratic equation for the $d_{3,2}$ -velocity relationship

$$\rho_l \left(\frac{u_{inj}^2 - \bar{u}^2}{2} \right) d_{3,2}^2 - 6\sigma_{l-g} d_{3,2} - K \mu_l \bar{u}^2 = 0, \quad (20)$$

where K absorbs the spray volume term for the sake of simplicity. After discarding the negative solution, this leads to a quadratic relationship between $d_{3,2}$ and the velocity

$$d_{3,2} = \frac{3\sigma_{l-g} + \sqrt{9\sigma_{l-g}^2 + K \rho_l \mu_l \bar{u}^2 \frac{u_{inj}^2 - \bar{u}^2}{2}}}{\rho_l \frac{u_{inj}^2 - \bar{u}^2}{2}}. \quad (21)$$

Equation (21) shows good agreement with the literature for pressure-atomized sprays with and without swirl and allow Lee and An [20] to reconstruct the droplet-size distribution from the droplet velocity distribution.

III. BIMODAL SIZE AND VELOCITY DISTRIBUTIONS

This section first gives a statistical description and the number PDF of the data from Felis-Carrasco [10] and then tackles their modeling in the framework of turbulence. The DTV measurements were obtained from positions along the jet axis located at $x/d_n = \{400, 500, 600, 700, 800\}$. At each axial position, measurements were made at different positions perpendicular to the jet. In order to capture all the spray development, the limit radial positions are different between the axial positions. At $x/d_n = 400$, the radial positions span from $y/d_n = -20$ to $y/d_n = 20$ and they span from $y/d_n = -32$ to $y/d_n = 32$ at $x/d_n = 800$. The measurements give access to the diameter d , the axial velocity u , and the radial velocity v of every droplet over a large section of the dispersion zone. Technically, the droplets are assumed to be spheroids and

TABLE II. Mean values of the distributions of d , u , and v .

x/d_n	400	500	600	700	800
$\langle d \rangle$ (μm)	96.82	91.22	95.60	93.63	97.89
$\langle d \rangle_V$ (μm)	125.0	126.2	129.3	125.0	121.7
$\langle \cdot \rangle_V / \langle \cdot \rangle$	1.29	1.38	1.35	1.33	1.24
$\langle u \rangle$ (m/s)	12.48	13.20	12.97	12.01	12.00
$\langle u \rangle_V$ (m/s)	21.53	20.35	19.78	18.17	16.72
$\langle \cdot \rangle_V / \langle \cdot \rangle$	1.72	1.54	1.52	1.51	1.39
$\langle v \rangle$ (mm/s)	2.1	-38.9	-16.7	-40.3	-2.9
$\langle v \rangle_V$ (mm/s)	-161.5	-210.4	-84.4	-129.6	-54.3
$\langle \cdot \rangle_V / \langle \cdot \rangle$	-76.9	5.41	5.05	32.2	18.7

the droplet volume V is estimated from the semiaxes given by the DTV measurements. Then the droplet diameter d is calculated as the diameter of the sphere of the same volume. Unless otherwise mentioned, the statistics given at a position x/d_n aggregate all the data over the positions y/d_n . For the sake of clarity, the number PDF of any variable ζ will be denoted by \mathcal{P}_ζ in the following.

A. Experimental distributions

As a first step, one could look at the mean values of the velocity distributions and the size distribution. Table II gives the algebraic mean $\langle \cdot \rangle$, the volume weighted mean $\langle \cdot \rangle_V$, and the ratio of the two for each distribution and each axial position. For any variable ζ , the volume-weighted average reads $\langle \zeta \rangle_V = \sum_{i=1}^{N_{tot}} V_i \zeta_i / \sum_{i=1}^{N_{tot}} V_i$, where i is the droplet index, N_{tot} the total number of droplets, V_i the volume, and ζ_i the ζ value of the i th droplet. While the ergodic condition can often be assumed, it is important to note here that both means systematically depart from each other for the three distributions. For the distribution of d , the volume-weighted mean is at least 24% larger than the algebraic mean, while this difference decreases from 72% to 39% for the distribution of u . Note as well that the means of u decrease along x/d_n . Concerning the distribution of v , the ratio of the two means shows a consequent variability, due to the proximity to zero of the mean values. Even if the variability is large, the means show at least one order of magnitude of difference. In the prospect of working with properly normalized variables, this systematic departure has to be accounted for in the choice of the mean to use for the normalizing procedure. The mass and energy conservation equations for the two-phase jet, introduced in Sec. II, rely on the phase indicator α_k . To ensure mass conservation in this context, the average of a variable ζ in the phase k must be expressed as $\langle \alpha_k \zeta \rangle$, which practically is equivalent to the volume-weighted mean. Thus, we choose the volume-weighted mean $\langle \zeta \rangle_V$ as the normalizing quantity of ζ . Doing so is equivalent to normalizing the droplet diameter by $d_{4,3}$ and the velocities by the bulk velocity of the dispersion phase. In the following, normalization is achieved by using the mean weighted by the droplet volume, except for the radial velocity v . Because $\langle v \rangle_V$ is close to 0 and could be misevaluated from the experimental measurements, the radial velocity v is normalized by $\langle u \rangle_V$.

Knowing how to properly normalize the present data, it is possible to compute the PDF of $d/\langle d \rangle_V$, $u/\langle u \rangle_V$, and $v/\langle u \rangle_V$ (see Fig. 2). The size distribution is computed over 1730 bins and the velocity distributions over 80 bins, with a total number of occurrences close to 400 000 on average. In addition to the mean, the three distributions are characterized by higher-order statistical moments. Figure 3 gives the evolution of the statistical moments up to the order 4 over the available x/d_n positions. The high-order moments under consideration here are the standard deviation σ , the skewness S , and the kurtosis κ , also referred to as flatness.

The size distribution $\mathcal{P}_{d/\langle d \rangle_V}$ presents an important skewness and a very large kurtosis. The former decreases along x from 10 to 5 and the latter decreases from 155 to roughly 35. Such values of skewness represent the fact that the distribution spans two decades $d/\langle d \rangle_V \in [0.1, 40]$ and that

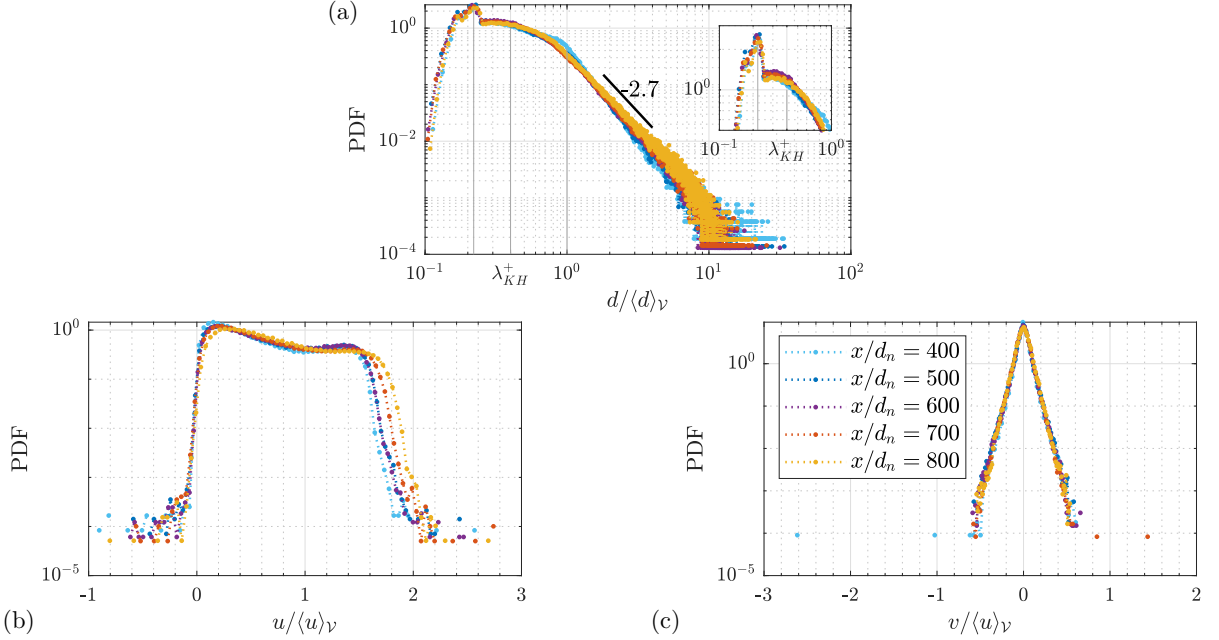


FIG. 2. Distributions of (a) $d/\langle d \rangle_V$, (b) $u/\langle u \rangle_V$, and (c) $v/\langle u \rangle_V$ for experimental data provided by Felis-Carrasco [10]. (a) A logarithmic scale and (b), (c) a semilogarithmic scale are used.

most of the droplets lie in the first decade, with the median value of $d/\langle d \rangle_V$ being equal to 0.51 on average. Regarding the kurtosis values, they are representative of the presence of large values, relative to the mean, in the tail of the distribution. Finally, the value of the standard deviation is almost constant over the five axial positions and equal to 0.93 on average, typical of distributions showing a region with concentrated data. Indeed, on average, the 25% and 75% quartiles are equal to 0.29 and 0.86 and the average interquartile is then 0.57, a range in which 50% of the droplets lie. Concerning the tail behavior, the distributions show a power-law decay scaling as $d/\langle d \rangle_V^{-2.7}$,

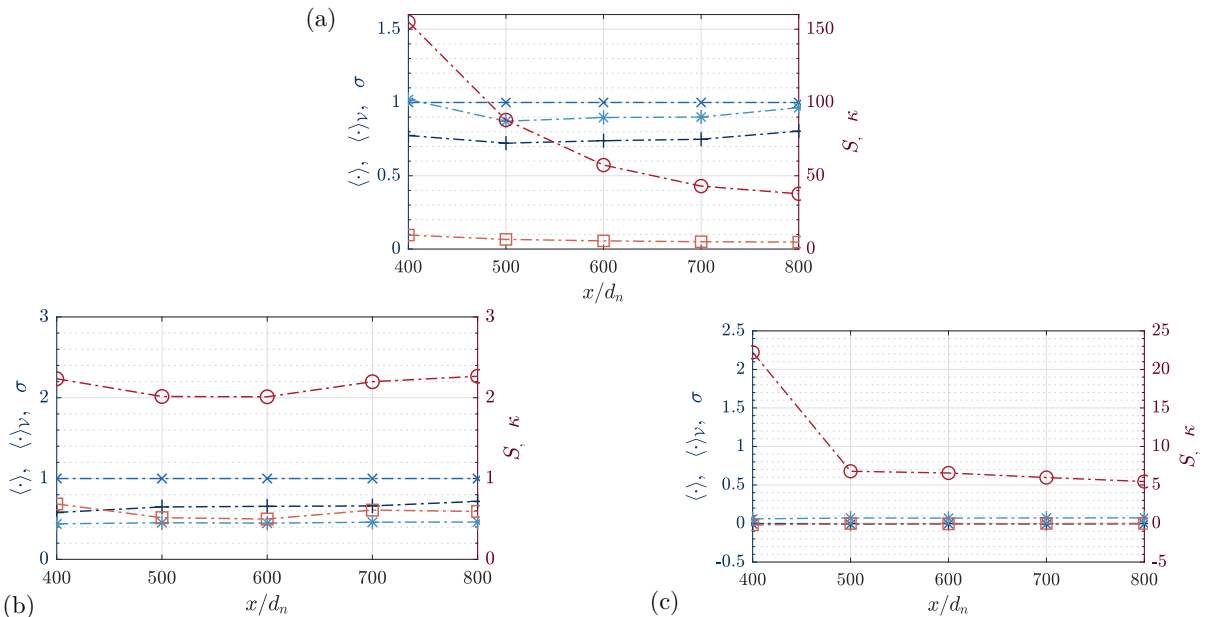


FIG. 3. Statistical moments of (a) $d/\langle d \rangle_V$, (b) $u/\langle u \rangle_V$, and (c) $v/\langle u \rangle_V$ for experimental data provided by Felis-Carrasco [10]. The blue lines represent $\langle \cdot \rangle$ (+), $\langle \cdot \rangle_V$ (x), and σ (*). The red lines represent S (□) and κ (○).

which departs from the exponential decay found by Simmons [37]. Furthermore, two modes can be seen on the distribution at each x/d_n : one for $d/\langle d \rangle_V \approx 0.2$ and the other for $d/\langle d \rangle_V \approx 0.4$. At the location $x/d_n = 400$, a third mode is also visible for $d/\langle d \rangle_V \approx 1.0$. Here it is worth noting that the second mode corresponds to the characteristic length scale of the Kelvin-Helmholtz instability [38]: $\lambda_{KH} = \sigma/\rho_g u_{inj}^2 = 49.6 \mu\text{m}$. Once normalized, this length scale is denoted by λ_{KH}^+ and $\lambda_{KH}^+ \approx 0.4$. We recall that λ_{KH} also respects $We_g = d_n/\lambda_{KH}$. Finally, close similarity is achieved for the distributions between $x/d_n = 500$ and $x/d_n = 800$ and characterizes a converged behavior with steady mechanisms in this range.

The distribution $\mathcal{P}_{u/\langle u \rangle_V}$ presents two modes for every x/d_n position as well. They are located around $u/\langle u \rangle_V \approx 0.2$ and 1.4 . In contrast to $\mathcal{P}_{d/\langle d \rangle_V}$, this distribution presents a slight departure between the tails on the right side and does not show any additional mode at $x/d_n = 400$. Except for this modest departure, the similarity is close for the five axial positions. Concerning the statistical moments, this PDF is characterized by lower skewness and kurtosis values than previously. Both are almost constant and on average are equal to 0.58 and 2.14 , respectively. This is representative of the fact that the distribution shows a minor asymmetry, due to a difference of predominance between the two modes, and that the distribution tails are short. The limited spanning of the distribution over $u/\langle u \rangle_V$ can be understood as a preponderant effect of the boundary conditions. The right limit might be enforced by the fact that the droplet velocity reaches a maximum on the centerline, close to the mean liquid velocity on the jet axis. The left limit might be enforced by the overall advection of the liquid phase towards increasing x/d_n , which prevent droplets from reaching negative values for u , i.e., moving back to the nozzle. As for the skewness and the kurtosis, the standard deviation of the distribution is almost constant and equal to 0.45 , characteristic once again of the data concentration. On average, the 25% and 75% quartiles are equal to 0.27 and 1.00 , and thus the average interquartile is 0.73 . Finally, the values of S and κ depart from the ones obtained in the case of a monophasic jet. The distribution of axial velocity for such jet is characterized by a skewness of -0.5 and a flatness of 2.8 , which is almost Gaussian. Here the present u distribution shows a reverse asymmetry and a shorter spanning.

The distribution $\mathcal{P}_{v/\langle u \rangle_V}$ presents only one maximum located at 0 . Its skewness is -0.05 on average and the distribution can be considered symmetric. The distribution kurtosis seems to tend to 5 but is equal to 9.39 on average as its value at $x/d_n = 400$ is relatively large, which is characteristic of a large tail span and a strong departure from Gaussianity. Finally, the standard deviation is almost constant over the axial positions with an averaged value of 0.069 , which shows a constant distribution width along x . This distribution seems to behave in a more classic manner than the distribution of $u/\langle u \rangle_V$ and $d/\langle d \rangle_V$ as it shows only one mode and characteristics similar to what can be found in the turbulence literature.

B. Modeling

Multiphase flows are inherently multidimensional. Their multidimensionality originates not only in the physical space but also in the phase space. Typically, every droplet of the present jet flow is, at first sight, characterized by three parameters: its size and two velocity components. Thus, in order to depict this population, one would need to propose a model able to capture the behavior of a three-dimensional joint PDF over the available axial positions. Doing so is very complex and it is easier to first have a closer look at the PDF of each parameter. This section proposes a model for the droplet-size distribution and the axial-velocity distribution.

1. Drop-size distribution

Sections II A and II B introduce two models of droplet distributions derived from different backgrounds. The first one, given by Eq. (8), is derived from a fine analysis of the ligament mechanics [22] experimentally studied in configurations like impacting droplets [25] or coaxial jet [12], close to the nozzle. The second one, given by Eq. (17), is derived from a phenomenological approach taking place in the framework of intermittent turbulence [16] and was initially developed

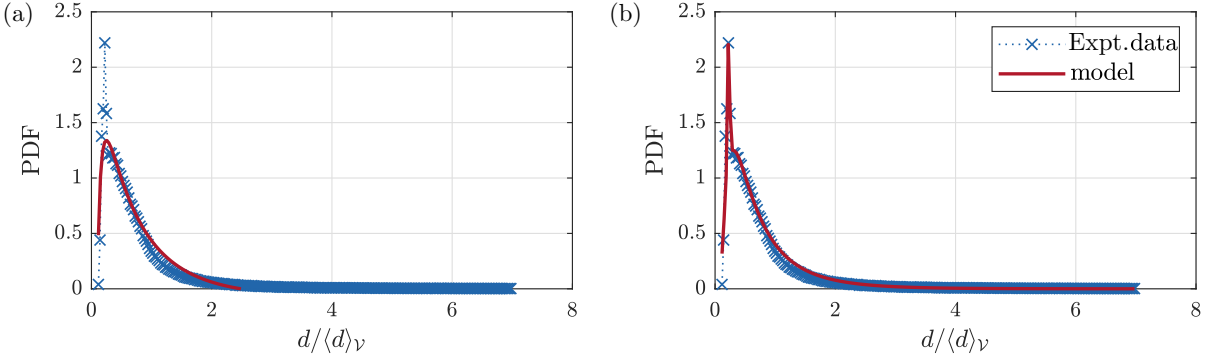


FIG. 4. Fit of the marginal distribution of $d/\langle d \rangle_V$ at the axial position $x/d_n = 800$ by the distributions from (a) Kooij *et al.* [26] and (b) Novikov and Dommermuth [15].

for turbulent spray around ships [15]. Those distributions will be respectively denoted by Prob_Γ and Prob_ϵ in this section.

A test campaign was carried out to compare the performance of each distribution to model the bimodal distribution obtained in Fig. 2. In order to reproduce the two modes of the experimental distribution, the fitting functions are defined as a linear combination of two reference distributions such that

$$f_\Gamma(x) = \alpha_1 \text{Prob}_\Gamma(x, m_1, n_1) + \alpha_2 \text{Prob}_\Gamma(x, m_2, n_2), \quad (22a)$$

$$f_\epsilon(x) = \alpha_1 \text{Prob}_\epsilon(x, a_1, \sigma_1) + \alpha_2 \text{Prob}_\epsilon(x, a_2, \sigma_2), \quad (22b)$$

where α_i , m_i , n_i , a_i , and σ_i are the fitting parameters. Note that both fit functions present the same number of fit parameters. The fitting algorithm used is the one of the EZYFIT toolbox developed by Moisy on MATLAB [39]. This algorithm is said to be able to capture a reference signal if the set of initial guesses is of the order of the set of converged parameters.

A fit is said to show good agreement with a given reference when the Pearson correlation coefficient, denoted by r , is close to 1. For a more discriminating criterion, one can use r^2 . The performance of the fitting functions to capture the experimental distribution is measured with r^2 . Both distributions are tested over 19 different initial guesses. The focus is on the region showing the two experimental modes, while the tail of the distribution is omitted. Thus the fitting procedure uses as reference the experimental distribution truncated at $d/\langle d \rangle_V = 7$ and the fitting is computed in the linear mode. Figure 4 gives the best results obtained from this campaign for each fitting function. The initial guesses, the final parameter values, and r^2 are given in Table III. The main difference between the two fitting functions is their ability to capture both peaks of the distribution. Using the algorithm from the EZYFIT toolbox, f_Γ systematically fails to capture the mode at $d/\langle d \rangle_V \approx 0.2$,

TABLE III. Initial guesses, final parameters, and r^2 for (a) Eq. (22a) and (b) Eq. (22b) given in Fig. 4. The parameter values are truncated at the third decimal.

f_Γ	(a)						
	α_1	m_1	n_1	α_2	m_2	n_2	r^2
initial	1	1	1	0.9	0.9	0.9	
final	5.26	1.04	1.20	-10.86	0.10	11.78	1.04
f_ϵ	(b)						
	α_1	a_1	σ_1	α_2	a_2	σ_2	r^2
initial	1	1	1	0.5	0.5	0.5	
final	0.99	0.79	0.66	0.05	0.22	0.01	0.97

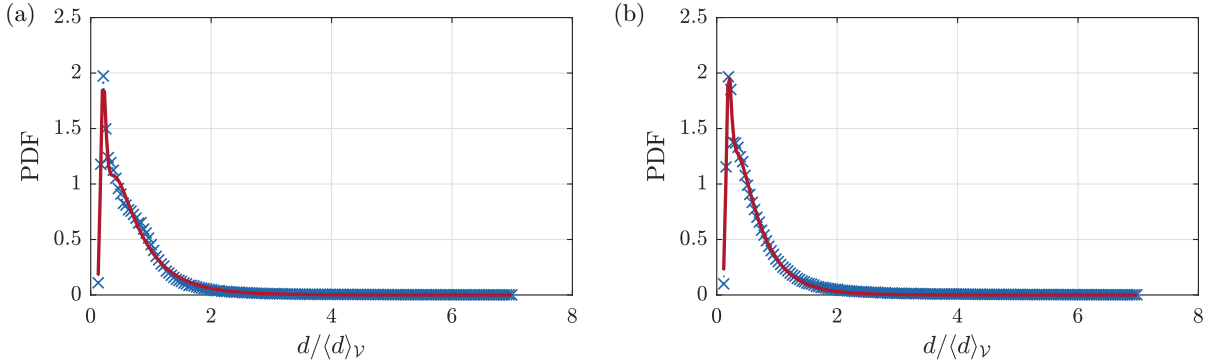


FIG. 5. Fit of the marginal distributions of $d/\langle d \rangle_V$ at the axial position (a) $x/d_n = 400$ and (b) $x/d_n = 600$ by the droplet-size distribution from Novikov and Dommermuth [15].

while f_ϵ is able to capture it for one set of initial guesses. One of the two amplitudes for the fitting f_Γ is negative. The fit is then not physical, as the objective is to model each mode with one distribution. This behavior is observed for a large part of the chosen sets of initial guesses. It could result from the optimization procedure for which a configuration with two modes does not perform as well as the one in Fig. 4. Improvements of the fitting algorithm could be done to implement, for example, parameter constraint or point weighting, to balance the weight of the points regarding their experimental importance. So far, under previous considerations and limits, the fitting function f_ϵ shows a better performance than f_Γ .

In order to test the reproducibility of this result, the function (22b) is tested over the four other x/d_n positions using the set of final parameters given in Table III as the initial guess. The fits for the positions $x/d_n = 400$ and 600 are given in Fig. 5. Their respective Pearson correlation coefficient values are $0.966\,87$ and 1.0026 . In both cases, the two modes located at $d/\langle d \rangle_V \approx 0.2$ and 0.4 are captured. The third mode of the distribution for $x/d_n = 400$ is not captured, which can be expected as f_ϵ is the combination of two distributions Prob_ϵ . The distributions for $x/d_n \in \{500, 700\}$ show behavior similar to the one at $x/d_n = 600$, which is consistent with the distribution similarity observed for $x/d_n \geq 500$.

The distribution derived by Novikov and Dommermuth [15] seems to model well the present experimental distribution, obtained from a turbulent flow, particularly for capturing both modes located at small $d/\langle d \rangle_V$. Conversely, under the limitations of the present campaign scope and methodology, the distribution from Kooij *et al.* [26] did not capture the higher and thinner peak of the experimental distribution.

2. Axial-velocity distribution

Similarly to the size distribution, the axial-velocity distribution shows two distinct modes. Looking at the distributions $\mathcal{P}_{u/\langle u \rangle_V}$ for different y/d_n positions, Fig. 6 reveals that only the mode for $u/\langle u \rangle_V \approx 0.2$ remains in the dispersion zone of the jet, while the mode for $u/\langle u \rangle_V \approx 1.4$ has importance only in the region close to the jet axis, i.e., for $y/d_n = \pm 8$. In addition, the distributions over the radial positions show symmetry with respect to the jet axis. The exploration of modeling is thus carried out differently in this section. The focus is first on modeling the axial-velocity distribution in the dispersion region of the jet. We choose the position $y/d_n = 20$ as it is the position farther away from the jet axis which is available for all x/d_n positions. The exploration is performed by testing the distributions considered in the study of Yoon [40] on the effects of the Weber number on the droplet-size distribution in a turbulent flow developing up to $x/d_n = 24$. Then the insights from this step are used to model the velocity mode $u/\langle u \rangle_V \approx 0.2$, while another distribution is proposed for the second mode, in order to depict the overall axial-velocity distribution.

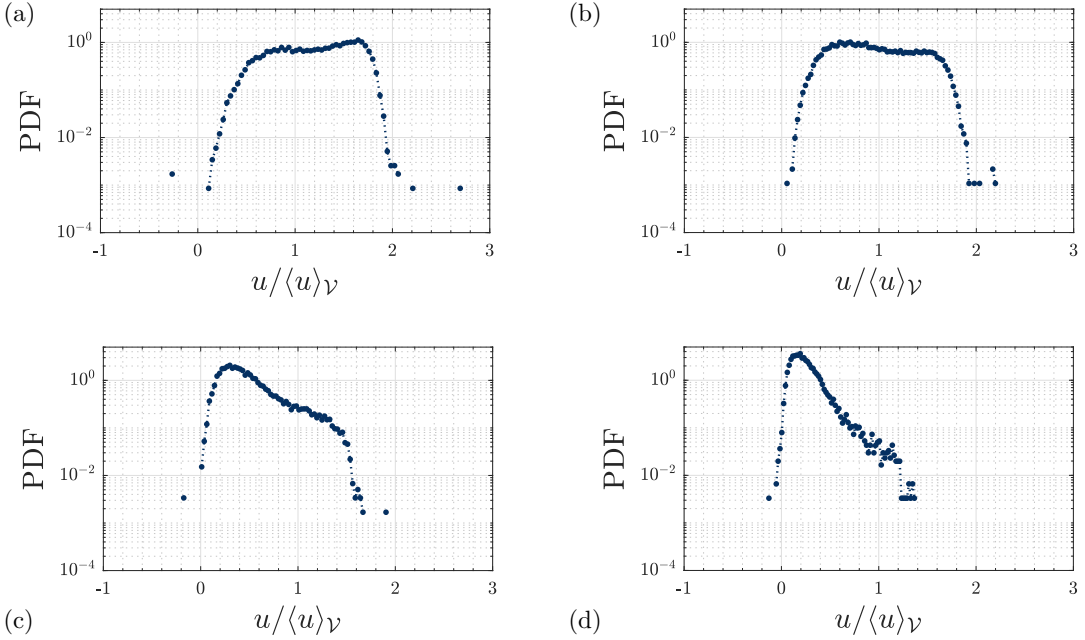


FIG. 6. Distributions of $u/\langle u \rangle_V$ for $x/d_n = 800$ at the radial positions (a) $y/d_n = 0$, (b) $y/d_n = -8$, (c) $y/d_n = -20$, and (d) $y/d_n = -32$.

In the aforementioned study, Yoon [40] considers three different PDFs to model the droplet velocity distributions: the Rosin-Rammler distribution f_{RR} , the log-normal distribution f_{LN} , and the Nukiyama-Tanasawa distribution f_{NT} . They are respectively defined by

$$f_{RR}(u) = \frac{qX^{q-1}}{X^q} \exp\left[-\left(\frac{u}{X}\right)^q\right], \quad (23a)$$

$$f_{LN}(u) = \frac{1}{\sqrt{2\pi}\sigma u} \exp\left(-\frac{[\ln(u) - \mu]^2}{2\sigma^2}\right), \quad (23b)$$

$$f_{NT}(u) = a \times u^p \exp(-bu^c) \quad (23c)$$

and show good agreement with experimental and numerical data for a round jet injected in quiescent air at high liquid Weber number, in the so-called atomization regime [1].

In order to model the axial-velocity distribution in the dispersion zone of the jet, the three distributions of Eq. (23) are tested at the radial position $y/d_n = 20$ over the five axial positions. To ensure the collapse of the PDF, the data have to be normalized by the averaged velocity at $y/d_n = 20$, denoted by $\langle u \rangle_V^{y/d_n=20}$. The fitting procedure is carried out in both the linear mode and logarithmic mode. Fitting with the log-normal distribution or the Nukiyama-Tanasawa distribution offers accurate results on the first try with initial guesses set as unity. However, several sets of initial guesses have to be tried for the Rosin-Rammler distribution to explore the performance of the fitting function.

The discriminating criterion used here is the average of r^2 over the x/d_n positions. The fitting function offering the r^2 value the closest to unity, on average, is the log-normal distribution f_{LN} computed in the linear mode. The fitting procedure gives $\mu = 0.78$ and $\sigma = 0.75$ as final parameter values. Over the five x/d_n positions, the correlation coefficient is such that $|r^2 - 1| \in [0.03, 0.28]$ and the mean r^2 is equal to 0.97. The upper bound of $|r^2 - 1|$ is obtained for $x/d_n = 400$. The fitting of the experimental data by f_{LN} is given in Fig. 7.

When looking closely at the distribution of $u/\langle u \rangle_V$ over the y/d_n positions, it appears that only the mode for $u/\langle u \rangle_V \approx 0.2$ remains in the dispersion zone of the jet. The previous tests show that the log-normal distribution fits well the experimental data at $y/d_n = 20$. In order to fit the distribution

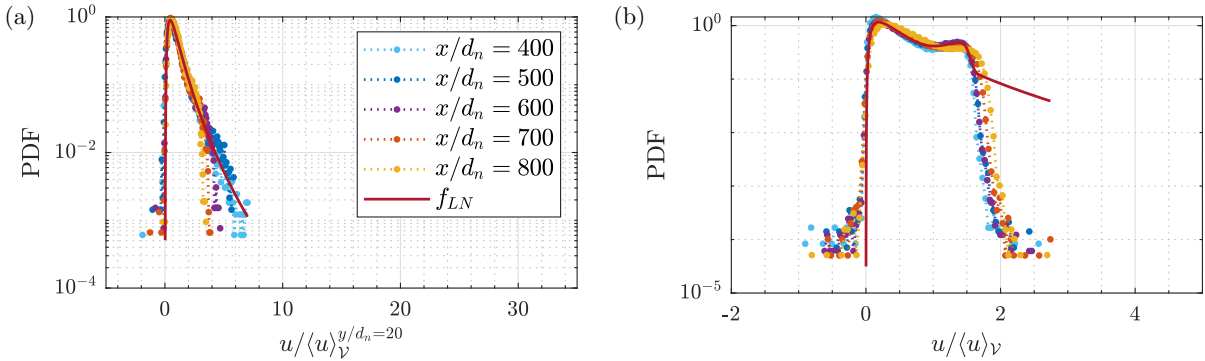


FIG. 7. (a) Fit of the distribution of $u/\langle u \rangle_v^{y/d_n=20}$ at the radial position $y/d_n = 20$ by a log-normal distribution (23b) and (b) fit of the distribution $\mathcal{P}_{u/\langle u \rangle_v}$ over all the radial positions by the model $f(u)$. The dotted lines represent the experimental data and the solid line represents the models. Both graphs use a semilogarithmic scale.

of $u/\langle u \rangle_v$ for each x/d_n position, as it was performed in the preceding section, it is possible to build a fitting function as a linear combination of the two distributions. Knowing the performance of f_{LN} to fit the mode $u/\langle u \rangle_v \approx 0.2$ in the dispersion region, we choose one of the two distributions to be a log-normal distribution with $\mu = 0.78$ and $\sigma = 0.75$. To be able to reproduce the right asymmetry of the mode for $u/\langle u \rangle_v \approx 1.4$, the second distribution is chosen to be a skewed normal distribution. This distribution is denoted by f_{SN} and is defined by

$$f_{SN} = \frac{1}{\sqrt{2\pi}\sigma} e^{-[(x-\mu)/\sqrt{2}\sigma]^2} \left[1 + \text{erf}\left(S \frac{x-\mu}{\sqrt{2}\sigma}\right) \right], \quad (24)$$

where μ , σ , and S are the mean, the standard deviation, and the skewness of the distribution, respectively. The fitting function is then

$$f(u) = \alpha_1 f_{LN}(u) + \alpha_2 f_{SN}(u). \quad (25)$$

The fit of the experimental data over all the radial positions by Eq. (25) is given in Fig. 7. As expected, the mode for $u/\langle u \rangle_v \approx 0.2$ is well captured by f and the fitting function reproduces the left boundary for $u/\langle u \rangle_v = 0$. Regarding the mode for $u/\langle u \rangle_v \approx 1.4$, the fitting function is able to capture the peak but fails to reproduce the right boundary for $u/\langle u \rangle_v \geq 1.5$. The overestimation of the distribution tail towards $+\infty$ is due to the participation of the log-normal distribution which does not decay fast enough. As a consequence, the fitting function f correctly captures the experimental axial velocity only over the range $u/\langle u \rangle_v \in [0, 1.50]$. As a reminder, the average interquartile range of $\mathcal{P}_{u/\langle u \rangle_v}$, given in Sec. III A, is $u/\langle u \rangle_v \in [0.27, 1.00]$. The validity range of f not is only larger than the average interquartile range but also contains it. So the fitting function f accurately depicts more than 50% of the droplet population.

Using the ability of the log-normal distribution to describe accurately the axial-velocity PDF in the dispersion region of the jet, a fitting function was built up as a linear combination of log-normal and skewed normal distributions to depict $\mathcal{P}_{u/\langle u \rangle_v}$ over all the radial positions. This fitting function captures both modes and accurately depicts more than 50% of the droplet population but fails to depict the distribution tail towards $+\infty$ and so the right boundary on the axial velocity.

IV. DROPLET-SIZE-VELOCITY JOINT DISTRIBUTION AND POPULATION SUBGROUPS

The presence of bimodal distributions for the droplet size and axial velocity was highlighted in the preceding section. The modes of each distribution could naturally represent a subgroup of droplets characterized by a given size or axial-velocity range. Thus, the present droplet population would present two subgroups with distinct velocities, $u/\langle u \rangle_v$ around 0.2 and 1.4, and two other subgroups with specific sizes, $d/\langle d \rangle_v$ around 0.2 and 0.3 (see Fig. 2). However, the PDFs of

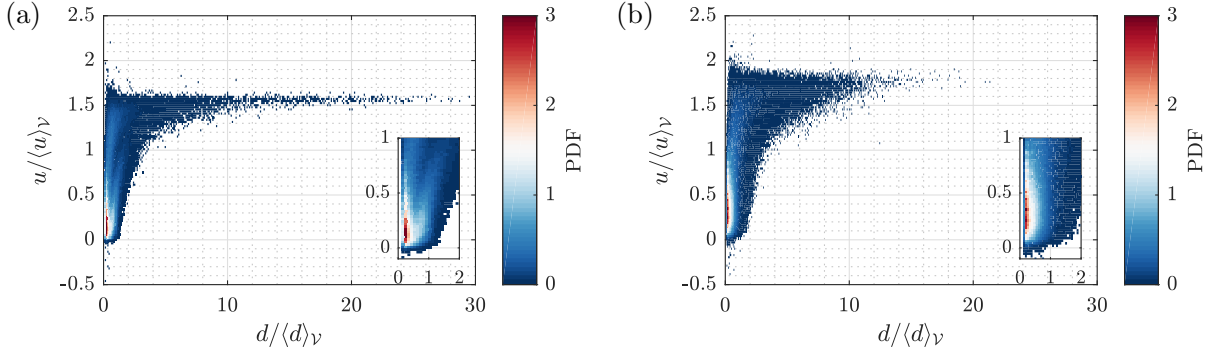


FIG. 8. Droplet-size–velocity joint PDF at (a) $x/d_n = 400$ and (b) $x/d_n = 800$.

$u/\langle u \rangle_V$ and $d/\langle d \rangle_V$ do not give any information about the correlation between the modes and thus the subgroups. In Sec. IV A the focus is on the droplet-size–velocity joint PDF to determine droplet subgroups. The validity of the quadratic formula given by Lee and An [20] to model the joint PDF for $x/d_n \geq 400$ is investigated in Sec. IV B.

A. Characterization of size-velocity subgroups

In a previous study, Felis *et al.* [8] highlighted the existence of different droplet behaviors depending on the droplet size and velocity. The Reynolds stress field, computed for different size classes, arbitrarily set, emphasizes that small droplets tend to show large velocity fluctuations while bigger droplets show a high axial mean velocity with almost zero fluctuations. The distributions of the droplet size and axial velocity presented in Sec. III show several modes, indicating the potential existence of droplet subgroups within the overall population. However, no information regarding the mode correlation is yet available. The influence of the size on the axial velocity and vice versa is given by the joint PDF of the droplet size and axial velocity, presented in Fig. 8 for the axial positions $x/d_n = 400$ and 800 .

First and foremost, a comment must be made on the joint PDF values being larger than one. Those quantities are computed with a regular sampling such that the axis along $d/\langle d \rangle_V$ is sampled in 340 sets and the axis along $u/\langle u \rangle_V$ in 150 sets. Consider the joint PDF at $x/d_n = 400$. Each axis respectively spans $[0.10, 33.59]$ and $[-0.92, 2.58]$. Thus the bin widths along $d/\langle d \rangle_V$ and $u/\langle u \rangle_V$ are equal to $\Delta_x = 9.85 \times 10^{-2}$ and $\Delta_y = 2.33 \times 10^{-2}$, respectively. In a given bin, the value of the joint PDF is calculated as the product of the probability in this bin and the inverse of the bin area. As probabilities are truly between 0 and 1, the PDF values lie between 0 and $(\Delta_x \Delta_y)^{-1} = 4.36 \times 10^2$. For $x/d_n = 400$, the maximum value of the joint probability is 7.9×10^{-3} . Then it is natural that the joint PDF values in Fig. 8 span up to around 3.

Both joint PDFs present a limited extension along the axis $u/\langle u \rangle_V$, included within $[-0.1, 2]$, while the extension along $d/\langle d \rangle_V$ is limited on 0 but spans towards large positive values, up to 30 for $x/d_n = 400$. This characterizes a data set with little dispersion along the velocity axis and important dispersion along the size axis, which corresponds to the behavior of the PDF of $u/\langle u \rangle_V$ and the one of $d/\langle d \rangle_V$. The maximum joint PDF values are concentrated in a relatively limited region located at small sizes and low axial velocities. The tail expansion along $d/\langle d \rangle_V$ is specific in the sense that it exists only for high axial velocities.

For both axial locations, the joint PDF tail tends toward a velocity asymptote located between 1.5 and 2. For $x/d_n = 400$, the tail reaches large values up to $d/\langle d \rangle_V = 30$ and is concentrated near this asymptote. For $x/d_n = 800$, the tail spans only up to $d/\langle d \rangle_V = 20$ and seems more dispersed near the asymptote. The reduction of the droplet-size maxima from 30 to 20 can be explained by the ongoing fragmentation process, which globally reduces the size of the water fragments and specifically the largest ones issued from the liquid core breakup. Regarding the velocity dispersion near the asymptote, one has to consider the non-normalized joint PDF in order to

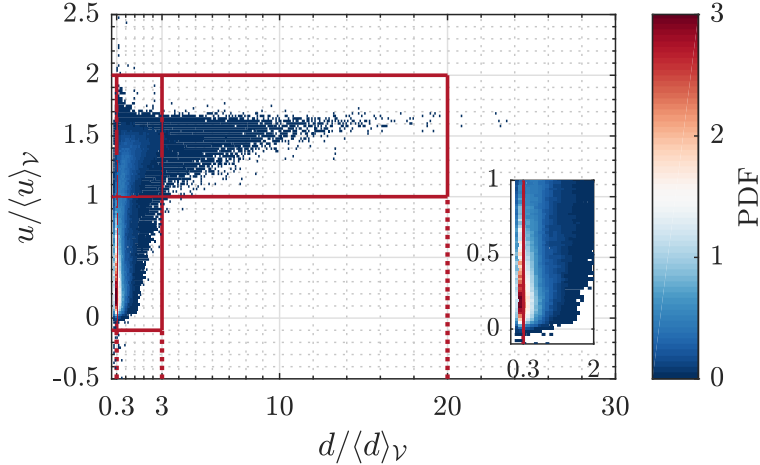


FIG. 9. Size-velocity joint PDF for $x/d_n = 600$ and droplet subsets discriminated with the characteristics of the size and axial-velocity distributions.

draw a conclusion independent of the evolution of $\langle u \rangle_V$ along x/d_n , given in Fig. 3. Furthermore, it is possible to observe a “path” of relatively large PDF values, colored in light blue, leaving from the maximum values of the joint PDF, leading to its tail, and following the elbow shape. A close look at the joint PDF for $x/d_n = 400$ even allows us to observe two paths. Concerning the correlation between $d/\langle d \rangle_V$ and $u/\langle u \rangle_V$, the large-size droplets show little correlation to their velocity and the low-velocity droplets show little correlation to their size, as both sets present a small dispersion along each axis, respectively. However, the in-between range of droplets seems to indicate a strong correlation between the size and the axial velocity.

Different droplet subsets can be derived from the description of the joint PDF. The maximum values of the joint PDF are representative of the most probable pairs $(d/\langle d \rangle_V, u/\langle u \rangle_V)$ and are concentrated in the region of low velocities and small sizes. Thus, it naturally depicts a first subset of droplets which are likely to behave like passive tracers. A second subset can be drawn by the tail expansion along the $d/\langle d \rangle_V$ axis. The tail along this axis exists only for high velocities and depicts the existence of a group of droplets characterized, at the same time, by a high velocity and a large size, which are likely to behave like ballistic objects. In addition, the joint PDFs show a third region of relatively high PDF values corresponding to the corner of the elbow. This region depicts a subset of droplets characterized by a high velocity and a small or intermediate size. While the first two droplet subsets cross-check the conjecture of Felis *et al.* [8], the existence of a third droplet subset is brought to light.

Knowing that subgroups with different physical behavior exist in the present droplet population, it could be possible to define them using some characteristics of the PDF of $d/\langle d \rangle_V$ and $u/\langle u \rangle_V$ like the spanning limits, the mode limits, and the dispersion. Consider the joint PDF for $x/d_n = 600$ as an example. In a straightforward manner, the spanning limits of the PDFs $\mathcal{P}_{d/\langle d \rangle_V}$ and $\mathcal{P}_{u/\langle u \rangle_V}$ give the outward limits of the possible droplet subsets: $0 < d/\langle d \rangle_V < 20$ and $-0.1 < u/\langle u \rangle_V < 2$. The modes of $\mathcal{P}_{d/\langle d \rangle_V}$ and $\mathcal{P}_{u/\langle u \rangle_V}$ depict specific sizes and velocities, potentially connected to distinct physical behaviors, and their delimitations can be used to discriminate subsets of the joint PDF. The value $u/\langle u \rangle_V = 1$ is chosen to delimit the axial-velocity modes, while the value $d/\langle d \rangle_V = 0.3$ is chosen to delimit the size modes. Finally, the delimitation of the size modes and the dispersion zone of $\mathcal{P}_{d/\langle d \rangle_V}$, i.e., its tail, is taken as $3\sigma_d \approx 3$. It is worth noting that the droplets whose size is between 0 and $3\sigma_d$ represent around 96% of the overall population, a percentage close to the Gaussian dispersion property. The delimitations detailed here are shown on the size-velocity joint PDF for $x/d_n = 600$ in Fig. 9.

Five subsets appear from those delimitations. Consider first the droplets showing a low axial velocity, i.e., a velocity corresponding to the first velocity mode $u/\langle u \rangle_V \approx 0.2$. Those droplets are

TABLE IV. Repartition of the droplet volume, number, and Stokes number of the joint PDF subsets at $x/d_n = 600$.

No.	$u/\langle u \rangle_V$	$d/\langle d \rangle_V$	Volume (%)	Number (%)	St
1	[0, 1]	[0, 0.3]	$O(10^{-2})$	25.2	0.83
2	[0, 1]	[0.3, 3]	3.69	48.8	7.92
3	[1, 2]	[0, 0.3]	$O(10^{-3})$	1.20	0.39
4	[1, 2]	[0.3, 3]	10.8	22.2	7.61
5	[1, 2]	[3, 20]	85.5	2.55	44.0

located in the bottom left corner of the joint PDF, $u/\langle u \rangle_V < 1$, and are depicted by two subsets: $(d/\langle d \rangle_V, u/\langle u \rangle_V)$ in $[0, 0.3] \times [-0.1, 1]$ and $[0.3, 3] \times [-0.1, 1]$. Two droplet populations seem to coexist in this range of velocities. Each of them is respectively characterized by a size $d/\langle d \rangle_V \approx 0.2$ with a little dispersion and a size $d/\langle d \rangle_V \approx 0.4$ with a larger dispersion. Thus the droplet set of low velocity and small size pointed out in [8] not only can be defined but is also made of two distinct droplet populations showing different characteristic sizes.

Now consider the droplets showing a high axial velocity, i.e., a velocity corresponding to the second velocity mode $u/\langle u \rangle_V \approx 1.4$. Those droplets are located in the upper part of the joint PDF, $u/\langle u \rangle_V > 1$, and are depicted by three subsets: $(d/\langle d \rangle_V, u/\langle u \rangle_V)$ in $[0, 0.3] \times [1, 2]$, $[0.3, 3] \times [1, 2]$, and $[3, 20] \times [1, 2]$. The top right subset presents a droplet population showing little dispersion in velocity, which increases slightly when the droplet size decreases. That is to say, the droplet size has little impact on the droplet axial velocity. Thus, the fragments of this population tend to decrease in size with an almost constant velocity, which cross-checks the existence of a group of droplets showing a ballisticlike behavior highlighted in [8]. The middle top subset presents relatively high joint PDF values, around 1. These values highlight the presence of a preferential droplet population. This population is characterized by a high axial velocity $u/\langle u \rangle_V \approx 1.5$ and an intermediate size $d/\langle d \rangle_V \approx 1$. Such velocity and size values respectively correspond to the second velocity mode and the third size mode, clearly visible for $x/d_n = 400$ in Fig. 2. In addition, this means as well that the third mode of $\mathcal{P}_{d/\langle d \rangle_V}$, visible for $x/d_n = 400$, also has importance for higher values of x/d_n . Finally, the last subset drawn by the chosen delimitations is the one on the top left corner. This subset presents joint PDF values less than 0.5. Such values are relatively low compared to the values of the nearby subsets, which are 1.5–3 for the bottom left subset and around 1 for the middle top subset. Thus, this subset could be considered as the expression of the tails of the nearby populations instead of depicting a droplet population characterized by a specific size and velocity.

Table IV gives for $x/d_n = 600$ the repartition of the droplet volume and number in the joint PDF subsets as well as the Stokes number associated with each subset. The low-velocity subsets in Fig. 9, $u/\langle u \rangle_V \leq 1$, are denoted by 1 and 2. The upper subsets are denoted by 3, 4, and 5. The ordering reads from left to right. The low-velocity subsets 1 and 2 represent 74% of the droplets but only 3.7% of the overall droplet volume. In contrast, for the high-velocity subgroups, subset 5 represents 85% of the overall droplet volume for only 2.55% of the droplets. Subset 4 aggregates 22.2% of the droplet population and 10.8% of the total volume. Such values are modest, but balanced, and could highlight the role played by this subset to link the populations of large and small droplet size. Finally, subset 3 only represents 1.2% of the population and a relative volume of $O(10^{-3})$. Such values are negligible compared to the other subsets and they support the interpretation of a subset being the “tail” of its neighbors.

The Stokes number St of each subset is calculated with the formulation from [10,41], using the Schiller-Naumann relation for the drag coefficient and the averaging operator $\langle \cdot \rangle_V$, which is written as

$$St = \frac{\tau_d}{\tau_t}, \quad \tau_d = \frac{\rho_l d^2}{18\mu_g(1 + 0.15 Re_d^{0.687})}, \quad \tau_t = \frac{y_{0.5u}}{\sqrt{\bar{R}_{11,g}}}, \quad Re_d = \frac{|u - \bar{u}_g|d}{v_G}, \quad (26)$$

TABLE V. Mean velocity values on the jet axis from the DTV measurements.

x/d_n	u_{axis} (m/s)
400	33.2
500	31.8
600	30.4
700	29.0
800	28.0

where Re_d is the Reynolds number seen by the droplet calculated using the gas mean velocity \bar{u}_g , τ_d is the droplet aerodynamic time constant, and τ_t is a turbulent timescale estimated from the axial standard deviation for the velocity fluctuations in the gas phase $\sqrt{\bar{R}_{11,g}}$ and the radial position $y_{0.5u}$ at which the fluid velocity is half the fluid velocity on the jet axis. The five droplet subsets are distributed over two decades of St and show three different trends. The Stokes number of subset 5, containing the droplets of high velocity and large size, reaches 44 and is representative of a ballistic behavior. The Stokes-number values for subsets 2 and 4 are between 7 and 8. As these values are larger than but close to unity, the droplets belonging to those subsets are in a ballistic regime but might be sensitive to large velocity fluctuations due to turbulence. Subsets 1 and 3 show a Stokes number less than unity, which makes those droplets the most sensitive to turbulence fluctuations. However, the droplets of this range might be unresponsive to the smallest scales of turbulence, as both Stokes numbers are relatively close to 1. It is important to note here that the velocity has little influence on the Stokes number. For example, subsets 2 and 4 present similar Stokes numbers whereas they are characterized by different velocities. The observation holds for subsets 1 and 3 as well, even if a slight departure due to the velocity difference is noticeable.

In addition to validating the conjecture drawn by Felis *et al.* [8] regarding the existence of two different droplet subgroups, this section precisely depicts and characterizes such groups among the overall droplet population. Specifically, a precise criterion is given for the low-velocity droplets which leads to the discrimination of two populations with different characteristic sizes. Furthermore, a subset of droplets showing high axial velocity and intermediate size is depicted and characterized. Complementarily, the weight of each subset in terms of droplet number and volume is given along with their Stokes number. Knowing the different subsets in the present droplet population now opens the way to understanding the underlying mechanisms leading to their existence.

B. Quadratic formula for joint PDF modeling

Section II C presented the work of Lee and An [20] and the quadratic formula (21) they derived to depict the relationship between the droplet velocity and the Sauter mean diameter $d_{3,2}$ for $x/d_n \leq 100$. In their study, the authors concluded that the good performance of the relationship enabled them to reproduce experimental and numerical data. In particular, this relationship is said to perform a good fitting of the centerline of a droplet-size–velocity joint PDF from Rimbert and Castanet [42], even if no mathematical definition of a joint PDF centerline is given. Finally, the authors claimed that the droplet-size PDF can be reconstructed from the diameters computed due to the quadratic formula. This section investigates the ability of this quadratic formula to fit the centerline of the present size–velocity joint PDF and the possibility to reconstruct the droplet-size distribution for $x/d_n \geq 400$. This investigation will consider the diameter d instead of $d_{3,2}$, as it is the available quantity in the present study for characterizing the droplet diameter. In addition, two reference velocities will be compared: the injection velocity u_{inj} and the mean liquid velocity on the jet axis at each x/d_n , denoted by u_{axis} . The values of the latter for each axial position are given in Table V.

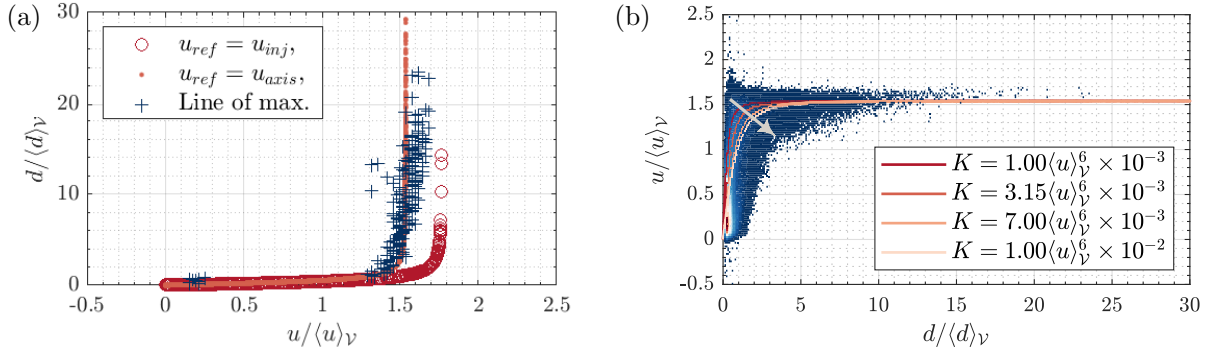


FIG. 10. (a) Comparison of two reference velocities for fitting the centerline of the size-velocity joint PDF at $x/d_n = 600$ by Eq. (27) where the fit parameter K is set to $3.15\langle u \rangle_V^6 \times 10^{-3}$. (b) Comparison of different values of K for fitting the centerline of the size-velocity joint PDF for $x/d_n = 600$ by Eq. (27). The arrow indicates increasing values of the fitting parameter K .

The reference velocity is denoted by u_{ref} and Eq. (21) is rewritten as

$$d = \frac{3\sigma_{l-g} + \sqrt{9\sigma_{l-g}^2 + K\rho_l\mu_l\bar{u}^2\frac{u_{ref}^2 - u^2}{2}}}{\rho_l\frac{u_{ref}^2 - u^2}{2}}. \quad (27)$$

Let us tackle first what the centerline of a joint PDF is. Considering the fitting of the joint PDF from Lee and An [20], the centerline of a joint PDF seems to be a line of PDF values such that it describes the main trend of the two-dimensional map. Here the centerline would correspond to the path of relatively large PDF values, visible in Fig. 8 and mentioned in the preceding section. The centerline would then correspond to local maximum values along each direction and could be defined by the zero values of the joint PDF gradient. As this path of relatively large PDF values spans large values of d , the gradient should be computed along d to capture all of the centerline. Thus, it could be possible to define the joint PDF centerline as the zero isoline of the joint PDF gradient computed along d .

Technically, there is an ambiguity when using the latter definition as the borders of the joint PDF also present gradient values close to zero. As a first approach, the centerline of the joint PDF is defined as the local maximum values of the PDF and is captured by searching for the local maximum in each bin along the direction d . The centerline produced by this approach is given in Fig. 10 and is referred to as the line of maxima. It is possible to observe a jump from $u/\langle u \rangle_V = 0.2$ to $u/\langle u \rangle_V = 1.4$ which is due to the existence of a local maximum in the region of low velocity and small size, corresponding to the bottom right subset in Fig. 9. Even if this estimation of the joint PDF centerline presents a discontinuity, it depicts well the overall trend of the joint PDF. Using this estimation, it is possible to compare the two reference velocities u_{inj} and u_{axis} for fitting the joint PDF centerline. A fitting procedure is carried out for the fit parameter K and gives a value of $3.15\langle u \rangle_V^6 \times 10^{-3}$. It appears in Fig. 10 that using the injection velocity as a reference overestimates the centerline. In contrast, using the mean liquid velocity on the jet axis leads to a more satisfactory result. The latter velocity u_{axis} is then used in the following as the reference velocity. In addition, it also appears that the quadratic formula proposed by Lee and An [20] performs nicely to capture the trend of the present joint PDF at large x/d_n , while it was initially derived for $d_{3,2}$ at small x/d_n distances.

Figure 10 presents the droplet-size velocity at $x/d_n = 600$ and Eq. (27) for different values of K . It can be seen that Eq. (27) qualitatively depicts the trend of the joint PDF for values of K between $1.00 \times 10^{-3}\langle u \rangle_V$ and $1.00 \times 10^{-2}\langle u \rangle_V$. This questions the value of K chosen to model the centerline in Fig. 10, especially under the limitation of discontinuity of the previous estimation.

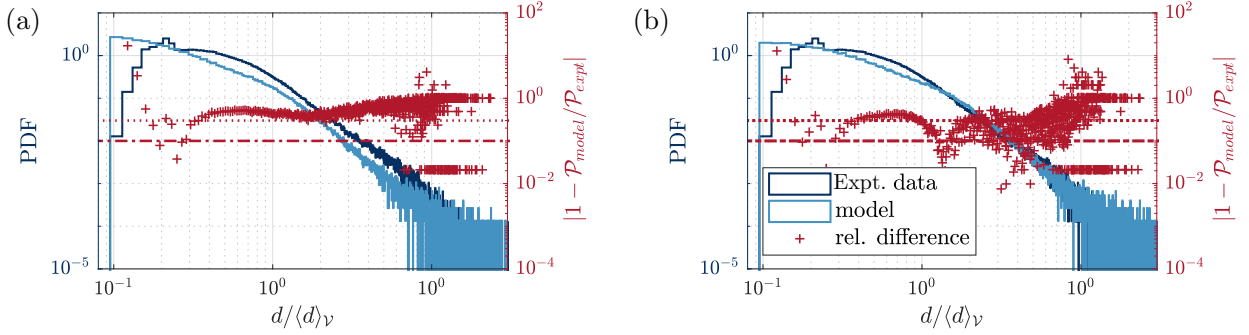


FIG. 11. Comparison of the experimental size PDF and the PDF reconstructed from the size given by Eq. (27) with (a) $K = 3.15\langle u \rangle_V^6 \times 10^{-3}$ and (b) $K = 7.00\langle u \rangle_V^6 \times 10^{-3}$. The pluses indicate the relative difference between the two PDFs. The dotted and dashed lines represent relative differences of 0.3 and 0.1, respectively.

In order to figure out a physically meaningful value of K , one could have a look at the reconstruction of the droplet-size PDF from the sizes given by Eq. (27). Figure 11 compares the experimental droplet-size PDF with the reconstructed PDF for two values of K : $3.15\langle u \rangle_V^6 \times 10^{-3}$ and $7.00\langle u \rangle_V^6 \times 10^{-3}$. In addition to comparing the experimental and model PDF, Fig. 11 gives the relative difference between the two, defined as $|1 - \mathcal{P}_{\text{model}}/\mathcal{P}_{\text{expt}}|$ and represented by the red pluses. An estimation is commonly considered as acceptable when the relative difference is less than 30% and considered as relatively good when it is less than 10%. Those two thresholds are indicated in Fig. 11 as well. On the one hand, the droplet-size PDF reconstructed with $K = 3.15\langle u \rangle_V^6 \times 10^{-3}$ reproduces a trend similar to the experimental PDF but shows an almost constant offset with a relative difference systematically larger than 0.3. On the other hand, the PDF reconstructed with $K = 7.00\langle u \rangle_V^6 \times 10^{-3}$ reproduces as well a trend similar to the experimental PDF and presents a smaller offset than previously. The relative difference is less than 0.3 up to $d/\langle d \rangle_V \approx 3$, where the distribution tail begins. However, in both cases, the relative difference between the two PDF tails presents large values, up to 10, and the model PDF is not able to capture the two modes for $d/\langle d \rangle_V \approx 0.2$ and 0.4. The box-and-whisker plot of the relative difference with $K = 7.00\langle u \rangle_V^6 \times 10^{-3}$ reveals that almost 50% of the relative difference values are under 0.3. It is worth noting that excluding the PDF tail would improve this result as most of the large values of relative difference are recorded in the tail region, whereas it represents only 4% of the total droplet number. Thus, the latter value of K enables us to estimate a joint PDF centerline which produces a droplet-size PDF close to the experimental one.

Even if Eq. (27) were derived in the context of turbulent combustion, i.e., for small x/d_n distances, and using the Sauter mean diameter $d_{3,2}$, good agreement is found by depicting the trend of the droplet-size–velocity joint PDF under the condition that the mean velocity on the jet axis u_{axis} is used as a reference. In addition, this formulation is able to produce a droplet-size PDF with a trend similar to the experimental one, if the value of the fitting parameter K is chosen in order to minimize the difference between the model and the experimental PDF. However, the model PDF fails to capture the first two modes in size.

V. CONCLUSION

In this work, it has been shown that, for agricultural-like jets lying in the second-wind-induced regime [1], both the droplet-size and axial-velocity distributions present distinct modes. On the one hand, the size distribution presents three modes for $d/\langle d \rangle_V \in \{0.2, 0.4, 1\}$, the second one corresponding to the Taylor scale, and a large dispersion towards $d/\langle d \rangle_V = 30$ with a decay scaling as $d/\langle d \rangle_V^{-2.7}$. On the other hand, the axial-velocity distribution presents two modes for $u/\langle u \rangle_V \in \{0.2, 1.4\}$ and a little dispersion. The dispersion of the latter is limited by two boundary conditions: the global advection of the water fragments and the mean axial velocity on the jet axis.

Regarding the distribution of $v/\langle u \rangle_V$, only one mode appears to exist and the distribution seems to behave in a more classical manner, similar to what can be found in the turbulence literature. Close similarity is observed for each distribution over the axial positions. Two theories have been tested to model the droplet-size distribution. The first one comes from the work of Villermaux *et al.* [22] based on a fine analysis of the ligament dynamics in low-turbulence fragmentation flows while the second one comes from Novikov and Dommermuth [15], who used intermittency in turbulence. In the limits of this study, it appears that, for $x/d_n \geq 400$, the distribution proposed by Novikov and Dommermuth [15] describes better the experimental size distribution and is able to capture the two modes at small $d/\langle d \rangle_V$. Regarding the modeling of the axial-velocity distribution, only the mode of low velocity $u/\langle u \rangle_V \approx 0.2$ exists in the dispersion zone of the jet. Among the three distributions derived for combustion applications, this mode is better depicted by the log-normal distribution. Taking benefit from this insight, a model PDF was proposed to depict the overall distribution of $u/\langle u \rangle_V$ at a given x/d_n . It does not capture the tails of the experimental distribution but describes nicely the two velocity modes, i.e., more than 50% of the overall droplet population.

Multimodal distributions suggest that different characteristic groups could exist in the droplet population. The analysis of the droplet-size–velocity joint PDF highlights the existence of three different behaviors. Two of them cross-check the conjecture of Felis *et al.* [8], who highlighted the existence of droplets behaving like passive tracers, with a small size and high-velocity fluctuations, or like ballistic objects, with a large size, high mean velocity, and almost zero fluctuations. In addition, this analysis reveals the existence of a third droplet group, characterized by a high axial velocity and an intermediary range of size. Using the characteristics of the size and axial-velocity PDF such as the spanning limits, the mode limits, and the distribution dispersion, it is possible to characterize precisely five subsets of droplets. Four seem to depict droplet groups with specific characteristic size and velocity while the last one seems to be the expression of the tails of the nearby populations. The Stokes numbers of those subsets follow three trends and span from 0.39 to 44, which corroborates the ballistic and passive tracer behaviors. However, this quantity presents a little dependence on the droplet velocity and is not able to discriminate droplet subsets with similar characteristic velocities. In the combustion framework, Lee and An [20] derived a quadratic formula to model the centerline of the joint PDF. After proposing a mathematical definition of such a centerline, the formula was tested on the present experimental data. It qualitatively described well the trend of the joint PDF. The size PDF reconstructed from this formula offers an acceptable description of the experimental data but fails to capture the two small size modes. It appears that results from combustion studies, developed in the region close to the nozzle, are valid as well in the dispersion region of agricultural-like configurations, i.e., far away from the nozzle.

Knowing the most probable droplet groups in the present flow opens the way to better understand the mechanisms at work. Several questions remain open. Which mechanism is responsible of the small-droplet-size mode? Which mechanism do the largest droplets undergo? Which mechanism produces such a power-law decay in the droplet-size distribution? Further works could focus on analyzing the turbulent energy spectra or on characterizing the droplet geometry in each subset of the size-velocity joint PDF to target such mechanisms. Complementary works could also be achieved to numerically reproduce similar configurations and investigate the ligament dynamics close to the nozzle.

ACKNOWLEDGMENTS

The authors thank F. Felis-Carasco and S. Tomas for making their data available. R.V. thanks E. Villermaux for fruitful discussion and comments.

[1] C. Dumouchel, On the experimental investigation on primary atomization of liquid streams, *Exp. Fluids* **45**, 371 (2008).

- [2] G. M. Faeth, Structure and breakup properties of spray, *Int. J. Multiphase Flow* **21**, 99 (1995).
- [3] P. K. Wu and G. M. Faeth, Aerodynamic effects on primary breakup of turbulent liquids, *Atomization Spray* **3**, 265 (1993).
- [4] P. K. Wu and G. M. Faeth, Onset and end of drop formation along the surface of turbulent liquid jets in still gases, *Phys. Fluids* **7**, 2915 (1995).
- [5] P. K. Wu, R. Miranda, and G. M. Faeth, Effects of initial flow conditions on primary breakup of nonturbulent and turbulent round liquid jets, *Atomization Spray* **5**, 175 (1994).
- [6] P. K. Wu, L. K. Tseng, and G. M. Faeth, Primary breakup in gas/liquid mixing layers for turbulent liquids, *Atomization Spray* **2**, 295 (1992).
- [7] C. Stevenin, S. Tomas, A. Vallet, M. Amielh, and F. Anselmet, Flow characteristics of a large-size pressure-atomized spray using DTV, *Int. J. Multiphase Flow* **84**, 264 (2016).
- [8] F. Felis, S. Tomas, A. Vallet, M. Amielh, and F. Anselmet, Experimental analysis of the flow characteristics of a pressure-atomized spray, *Int. J. Heat Fluid Flow* **85**, 108624 (2020).
- [9] E. Ruffin, R. Schiestel, F. Anselmet, M. Amielh, and L. Fulachier, Investigation of characteristic scales in variable density turbulent jets using a second-order model, *Phys. Fluids* **6**, 2785 (1994).
- [10] F. Felis-Carrasco, Atomization and dispersion of a liquid jet: Numerical and experimental approaches, Ph.D. thesis, Ecole Centrale Marseille, 2017.
- [11] E. Villermaux, Fragmentation, *Annu. Rev. Fluid Mech.* **39**, 419 (2007).
- [12] P. G. M. Marmottant and E. Villermaux, On spray formation, *J. Fluid Mech.* **498**, 73 (2004).
- [13] J. Eggers and E. Villermaux, Physics of liquid jets, *Rep. Prog. Phys.* **71**, 036601 (2008).
- [14] E. Villermaux and B. Bossa, Single-drop fragmentation determines size distribution of raindrops, *Nat. Phys.* **5**, 697 (2009).
- [15] E. A. Novikov and D. G. Dommermuth, Distribution of droplets in a turbulent spray, *Phys. Rev. E* **56**, 5479 (1997).
- [16] E. A. Novikov, Infinitely divisible distributions in turbulence, *Phys. Rev. E* **50**, R3303 (1994).
- [17] E. A. Novikov, Intermittency and scale similarity in the structure of a turbulent flow, *J. Appl. Math. Mech.* **35**, 231 (1971).
- [18] N. Rimbert and O. Sero-Guillaume, Log-stable laws as asymptotic solutions to a fragmentation equation: Application to the distribution of droplets in a high Weber-number spray, *Phys. Rev. E* **69**, 056316 (2004).
- [19] N. Rimbert and G. Castanet, Crossover between Rayleigh-Taylor instability and turbulent cascading atomization mechanism in the bag-breakup regime, *Phys. Rev. E* **84**, 016318 (2011).
- [20] T.-W. Lee and K. An, Quadratic formula for determining the drop size in pressure-atomized sprays with and without swirl, *Phys. Fluids* **28**, 063302 (2016).
- [21] O. Simonin, in *Combustion and Turbulence in Two-Phase Flows: Continuum Modelling of Dispersed Two-Phase Flows*, edited by M. Manna, VKI Lecture Series (von Karman, Institute for Fluid Dynamics, Sint-Genesius-Rode, 1996).
- [22] E. Villermaux, P. G. M. Marmottant, and J. Duplat, Ligament-Mediated Spray Formation, *Phys. Rev. Lett.* **92**, 074501 (2004).
- [23] M. Von Smoluchowski, Versuch einer mathematischen theorie der koagulationskinetik kolloider lösungen, *Z. Phys. Chem.* **92**, 129 (1917).
- [24] S. K. Friedlander, *Smoke, Dust, and Haze: Fundamentals of Aerosol Dynamics*, 2nd ed. (Oxford University Press, New York, 2000).
- [25] E. Villermaux and B. Bossa, Drop fragmentation on impact, *J. Fluid Mech.* **668**, 412 (2011).
- [26] S. Kooij, R. Sijs, M. M. Denn, E. Villermaux, and D. Bonn, What Determines the Drop Size in Sprays? *Phys. Rev. X* **8**, 031019 (2018).
- [27] A. N. Kolmogorov, The local structure of turbulence in an incompressible fluid for very large Reynolds numbers, *Dokl. Akad. Nauk SSSR* **30**, 299 (1941).
- [28] A. N. Kolmogorov, Energy dissipation in locally isotropic turbulence, *Dokl. Akad. Nauk SSSR* **32**, 19 (1941).
- [29] L. Landau and E. M. Lifshitz, *Fluid Mechanics*, A Course of Theoretical Physics Vol. 6 (Pergamon, Oxford, 1959).

- [30] A. N. Kolmogorov, *Colloques Internationaux du Centre National de la Recherche Scientifique* (CNRS, Paris, 1961), Vol. 108, pp. 447–458.
- [31] A. N. Kolmogorov, A refinement of previous hypotheses concerning the local structure of turbulence in a viscous incompressible fluid at high Reynolds number, *J. Fluid Mech.* **13**, 82 (1962).
- [32] A. M. Obukhov, Some specific features of atmospheric turbulence, *J. Fluid Mech.* **13**, 77 (1962).
- [33] U. Frisch, *Turbulence: The Legacy of A.N. Kolmogorov* (Cambridge University Press, Cambridge, 1995).
- [34] F. Anselmet, R. A. Antonia, and L. Danaila, Turbulent flows and intermittency in laboratory experiments, *Planet. Space Sci.* **49**, 1177 (2001).
- [35] W. Feller, *An Introduction to Probability Theory and its Applications*, 3rd ed. (Wiley, New York, 1971), Vol. 2.
- [36] H. Tennekes and J. L. Lumley, *A First Course in Turbulence* (MIT Press, Cambridge, 1972).
- [37] H. C. Simmons, The correlation of drop-size distributions in fuel nozzle sprays. Part II. The drop-size/number distribution, *J. Eng. Power* **99**, 315 (1977).
- [38] J. W. Hoyt and J. Taylor, Waves on water jet, *J. Fluid Mech.* **83**, 119 (1977).
- [39] F. Moisy, *EzyFit 2.44* (The MathWorks, Inc., Natick, 2020).
- [40] S. S. Yoon, Droplet distributions at the liquid core of a turbulent spray, *Phys. Fluids* **17**, 035103 (2005).
- [41] V. Ferrand, R. Bazile, J. Borée, and G. Charnay, Gas-droplet turbulent velocity correlations and two-phase interaction in an axisymmetric jet laden with partly responsive droplets, *Int. J. Multiphase Flow* **29**, 195 (2003).
- [42] N. Rimbert and G. Castanet, Liquid atomization out of a full cone pressure swirl nozzle, [arXiv:1008.2474](https://arxiv.org/abs/1008.2474).

3.3 Connecting the size-velocity joint distribution and the fragmentation mechanisms

The analysis concludes on the existence of different droplet subgroups characterized by specific pairs of size and velocity and opens the question of the fragmentation mechanisms generating droplets of such sizes. Consider again the droplet subsets as defined in the article, Sec. IV.A. Figure 3.1 reproduces Fig. 9 of the article, this time numbering the droplet subgroups. The subsets 1 and 2 present a low characteristic velocity, $u/\langle u \rangle_V \leq 1$, and the subsets 3, 4 and 5 a high one, $u/\langle u \rangle_V \geq 1$. Regarding the sizes, the subset 5 is characterised by large sizes, $d/\langle d \rangle_V \geq 3$. The subsets 2 and 4 are characterised by intermediate sizes, $0.3 \leq d/\langle d \rangle_V \leq 3$, and the subsets 1 and 3 by small sizes, $d/\langle d \rangle_V \leq 0.3$. The article notes as well that the subset 5 depletes between $x/d_n = 400$ and $x/d_n = 800$. Now that the groups are defined, it is possible to look at them separately by considering, for instance, the droplet size as an observable and computing its distribution. In order to keep some consistency with the size distribution of the overall droplet distribution, the distribution computed over the subset is slightly adapted by normalising with the total number of droplets in the spray instead of the number of droplets in a subset.

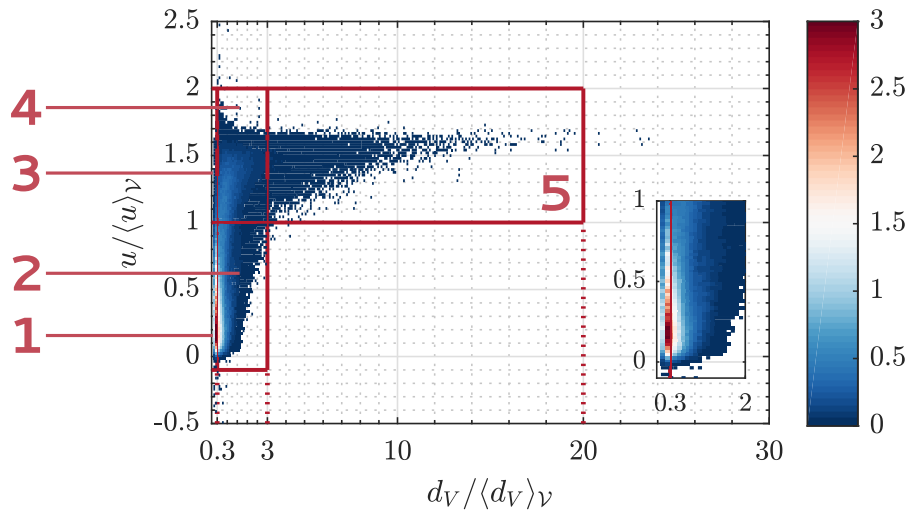


Figure 3.1: Size-velocity joint distribution for $x/d_n = 600$ and the droplets subsets numbered and discriminated with the characteristics of the size and velocity distributions.

3.3.1 Conjectures for the volume transfer between the droplet subgroups

Before diving in the analysis, let us go back to the experimental photographs of the fragmenting jet. Fig. 3.2 and 3.3 illustrate the two main sorts of break-up observed in the flow: the ligament-mediated and bag break-up regimes. Both regimes occur on ranges of several hundreds of nozzle diameters d_n . While the bag break-up regime starts to occur only once the liquid core pinched off and becomes less frequent for $x/d_n \gtrsim 600$, the ligament-mediated regime can occur all along the spray until the droplets become stable. This comes from the fact that the bag break-up regime is observed only on large, fast droplets having a relatively short existence time when

3.3. Connecting the size-velocity joint distribution and the fragmentation mechanisms

the ligament-mediated regime is observed on a widespread range of sizes and until the force equilibrium is such that no perturbation can overcome the surface tension and that no varicose perturbation can develop. Based on this observation, it is possible to conjecture at first that the droplets of the subset 5 are very likely to fragment in a bag break-up regime, as they are the largest and fastest droplets of the population, and that the droplets in the subset 1 are stable. On a first approximation, it is also possible to go further and conjecture that only the droplets of the subset 5 undergo bag break-ups while the droplets in the subsets 2, 3 and 4 undergo a ligament-mediated fragmentation.

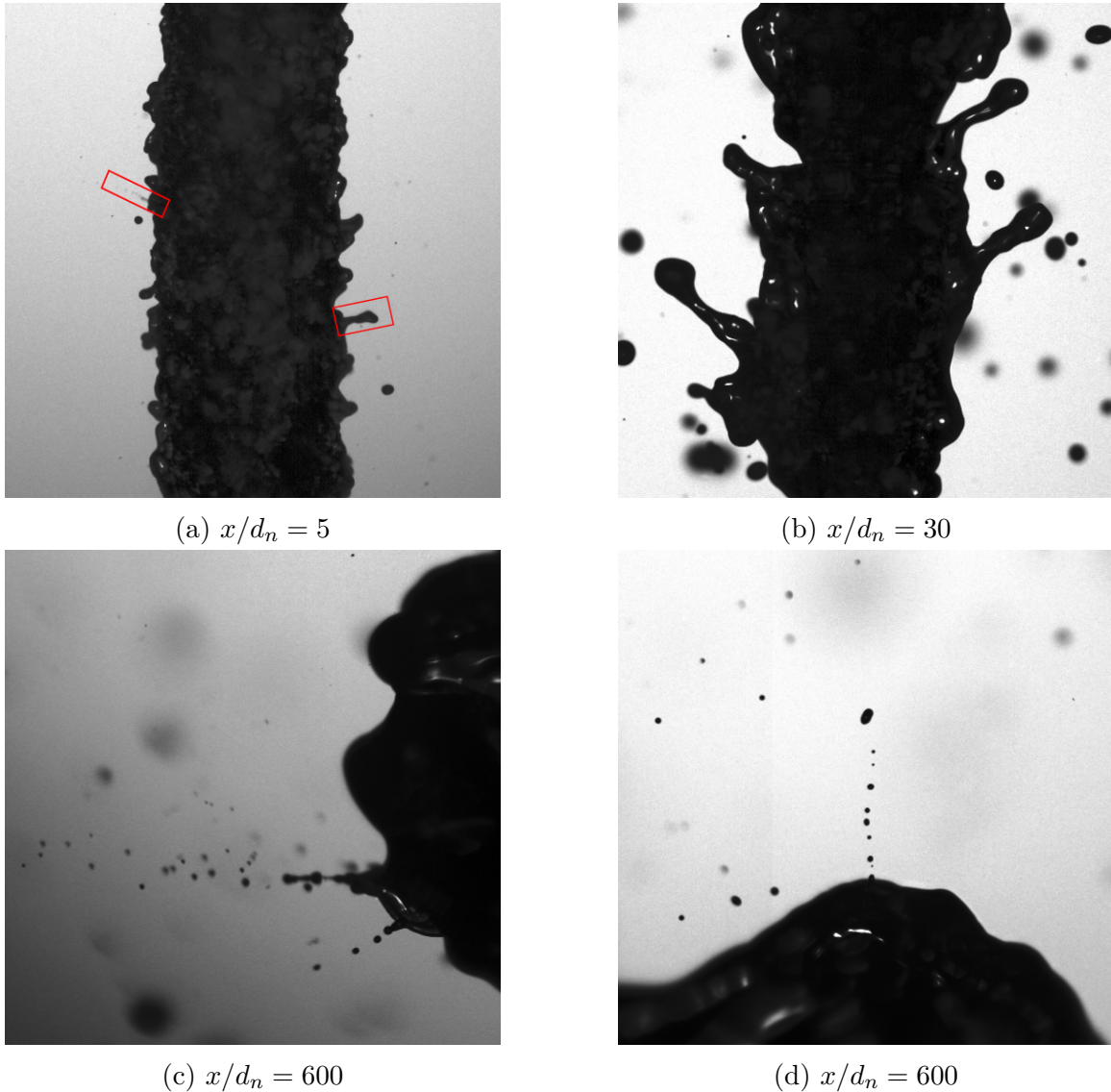


Figure 3.2: Photographs of ligaments ($3d_n \times 3d_n$).

Complementary to the fragmentation mechanisms, the question of the mass transfer between the subsets has to be tackled. Any droplet in a given subset which fragments generates smaller droplets and thus feeds the subset of smaller sizes. The subset 5 could here be seen as a volume reservoir pouring into the other subsets. During a bag break-up, the droplet takes a bag shape composed of a rim and a sheet. Rimbert & Castanet (2011) proposed a model to depict droplet bag break-ups relying on a crossover between the Rayleigh Taylor instability and the turbulent

cascade, respectively describing the fragmentation of the rim and the sheet. The authors also observed experimentally that the droplets coming from the sheet are much smaller than the ones coming from the rim.

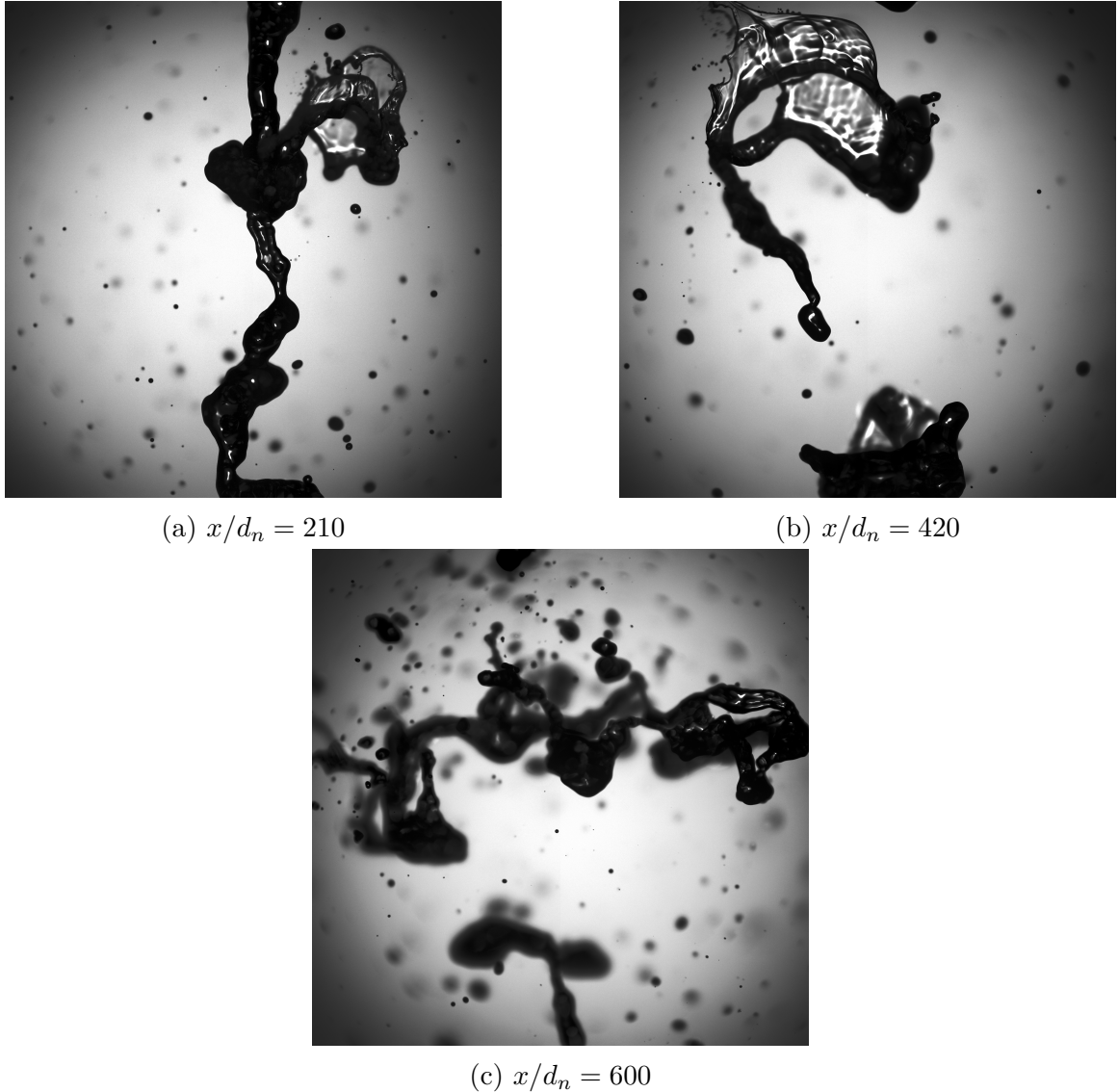


Figure 3.3: Photographs of bag break-ups ($12d_n \times 12d_n$).

With this in mind, it is possible to draw a second conjecture: the fragmentation of the droplets of the subset 5 generates droplets having the same velocity but of small and intermediate sizes, thus lying in the subsets 3 and 4. Regarding the subset 3, it was noted in the article that it may be the tail of the neighbouring subsets 1 and 4. This can be accounted for by adding an hypothesis and saying that the small droplets generated by a break-up undergo a fast decrease of velocity and, thus, feed the subset 1. The droplets of the subset 1 are assumed to be stable and cannot undergo further break-up. The droplets in the subset 4 still have a large velocity and can continue to fragment. Then, one could conjecture that they undergo ligament-mediated fragmentation and slow down at the same time. Depending of the droplet location in the size-velocity space, it could then feed the subset 1 or the subset 2. For instance, the volume of a droplet such that $u/\langle u \rangle_V \approx 1$ and $d/\langle d \rangle_V \approx 3$ is likely to pour into the subset

2. Conversely, the volume of a droplet such that $u/\langle u \rangle_V \approx 1.5$ and $d/\langle d \rangle_V \approx 0.3$ could pour into the subset 1. The later conjectures aim to depict the transfer of liquid volume contained in the large, fast droplets of the depleting subset 5 across the size-velocity space.

3.3.2 Exploring the size distributions of the subgroups

Now that the volume transfer between the subsets is conjectured, it is possible to test its validity by looking at each subset separately. To do so, one can consider, for instance, the droplet size as an observable and compute its distribution. In order to keep some consistency with the size distribution of the overall droplet distribution given in the article Sec. III.A, the distribution computed over the subset has to be slightly adapted. The count density, i.e. the number of occurrence divided by the bin width, is normalised by the total number of droplets in the spray instead of being normalised by the number of droplets in a subset of consideration. Following this method for computing the size distribution, Fig. 3.4 gives the droplet size distribution for each subset in a semi-logarithmic scale.

A striking observation is that the power-law decay observed in Sec. II.A is not visible anymore. The distributions of the subsets 2, 4 and 5 rather scale as an exponential respectively with $-7/2$, -1 and $-1/2$ as decay coefficient. This recalls at first the experimental observation made by Simmons (1977) that the tail of the size distribution of sprays commonly show an exponential decay. In a second time, such decays also recall the argument of random stripping introduced by Villermaux (2020). The random stripping argument relies on the ligament-mediated fragmentation. It explains the size distribution of droplets generated by a turbulent jet by modelling the distribution by the composition of a set of Γ distributions. This composition then results in a distribution with an exponential decay with a main mode at small sizes, similarly to Fig. 3.4d. Let us assume that the random stripping mechanism is relevant for our droplet production. Then, the droplets lying in the subsets 2 and 4 are likely to result from a ligament-mediated fragmentation, thus validating, in a first approximation, the production mechanisms conjectured for the subsets 2 and 4.

Checking the conjecture that the droplets of the subset 5 undergo a bag break-up fragmentation is straightforward. Indeed, droplets undergo this fragmentation mechanism when $We_p \geq 6$, with $We_p = \rho_g u^2 d_V / \sigma$. The gaseous Weber number associated to the points $(u/\langle u \rangle_V, d_V/\langle d_V \rangle_V) \in \{(3, 1.6), (8, 1)\}$ respectively equal 7.24 and 6.68. All the droplets above those points then undergo bag break-up. Thus, at first approximation, part of the subset 5 undergo bag break-up and the related conjecture is partly verified. It could be possible to improve this verification by considering the relative velocity of the droplet with the gas phase instead of u in the computation of We_p .

Consequently, part of the droplets in the subsets 2 and 4 are likely to result from the rim fragmentation during a bag break-up and part of the droplet in the subset 1 from the sheet fragmentation. This partly verify the conjecture that the rim fragmentation feeds the subsets 2 and 4 and that the sheet fragmentation feeds the subset 1. Further work has to be done to pinpoint more precisely the part of the droplets which actually result from the rim fragmentation and from the sheet fragmentation taking place in a bag break-up. Indeed, as not all the droplets of the subset 5 undergo a bag break-up, a part of the droplets in the subsets 1, 2 and 4 could also result from a classic ligament-mediated fragmentation.

An extra conclusion, which was not conjectured earlier, can be drawn about the large and fast droplets, lying in the subset 5. Fig. 3.4e indicates that the size distribution of the droplets

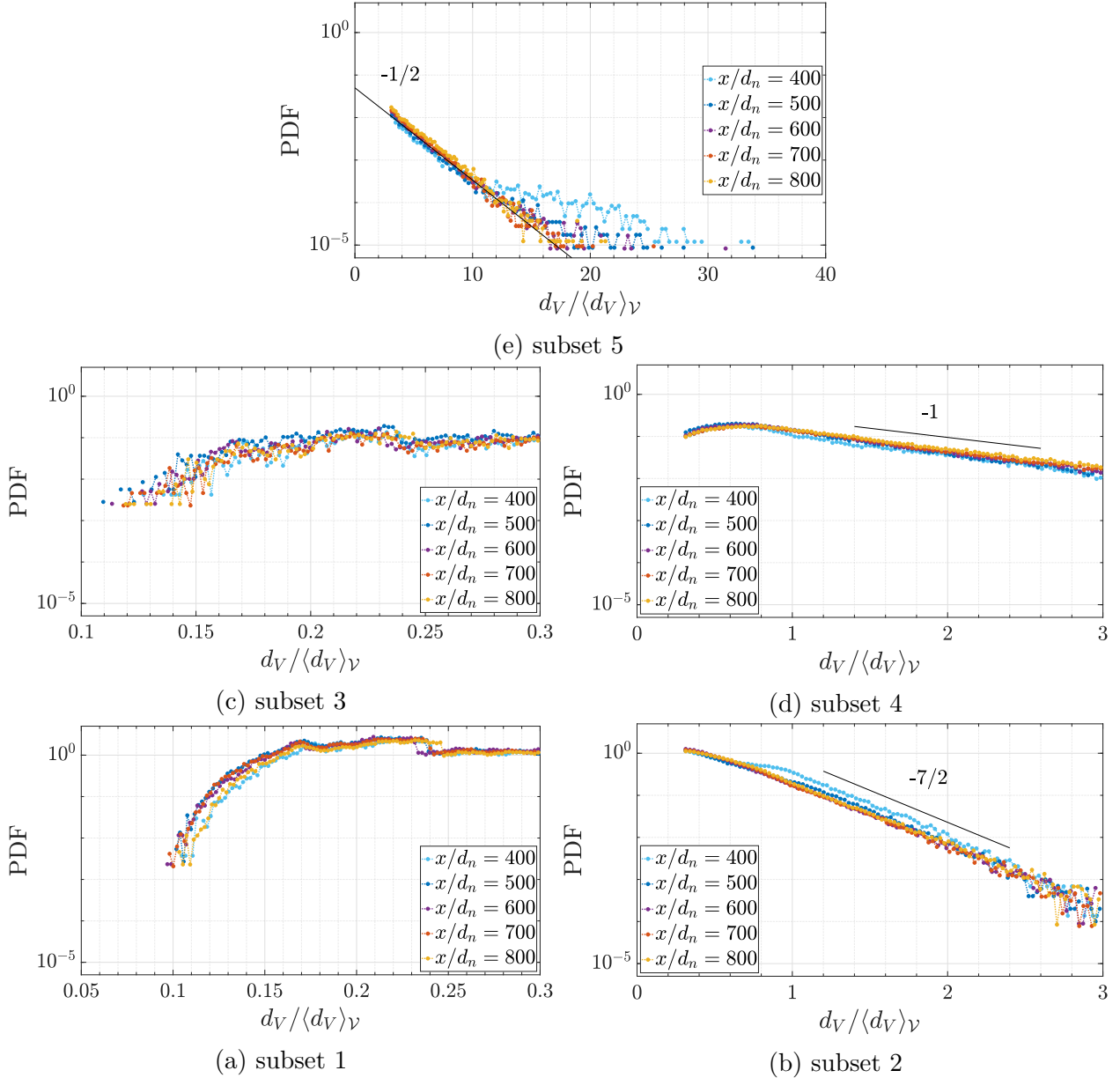


Figure 3.4: Size distribution of the droplets separated by subset for the five experimental positions.

in the subset 5 also follows an exponential decay. Following once again the random stripping argument, this could point out that the larger droplets of the jet fragmentation, mainly resulting from the liquid core pinch off, could also be described by a compound Γ distribution. In order to verify the overall volume transfer proposed above, two ways could be considered, either programmatically or analytically. Programmatically, one could implement an algorithm that, from an infinite source distribution as granted, the one of the subset 5 for example, generates a droplet population by reproducing the conjectured droplet fragmentations. The analytical way follows a similar logic but, instead of generating a droplet population step by step, one could compose the parametrised distributions resulting from each fragmentation mechanism and try to derive the overall population distribution. A strong limitation of the conjectured

volume transfer is that it aims to explain the distribution in the size velocity space of the droplets generated from the subset 5. Thus, no considerations are made regarding the droplets of smaller size existing prior to any bag break-up, for example the droplets generated by the peeling of the liquid core, Fig. 3.2a and 3.2b, or from large droplets, Fig. 3.2c and 3.2d.

Besides, in Sec. IV. A. of the article, several arguments pointed in the direction that the subset 3 could simply be the expression of the tail of the neighbouring subsets 1 and 4. In Fig. 3.4c, it is possible to distinguish reminiscences of the features of the size distribution of the subset 1, like the step at $d/\langle d \rangle_V \approx 0.24$, as well as the trend of the size distribution of the subset 4, for $d/\langle d \rangle_V \in [0.25, 0.3]$. And the arguments once again seem to point in the direction of a tail subset. This raises the question of the accuracy of the subset delimitation or the choice of the observables. While the subset delimitations seem to show some robustness, maybe further thinking on the observable to use could be advisable as the choice of the size and the velocity has some limitations. The major limitation related to the size velocity space and the subset delimitation developed above is that droplets experiencing different flow regimes can be found in the same subset. For example, two droplets having the same size but different velocities will interact differently, if not drastically differently, depending on the difference of velocity. Other observable which could be used are the particulate dimensionless numbers, in other words Re , We and Oh computed for each droplet with the droplet characteristic velocity and length, respectively the droplet velocity and its diameter. The use of the particulate Reynolds, Weber and Ohnesorge numbers is considered in Chap. 4 to describe the droplet phase space.

Chapter **4**

Weber dependency of jet fragmentation: a DNS investigation

Contents

4.1	Introduction	90
4.2	Flow modeling and parameter framing	92
4.3	Overall flow characteristics and droplet statistics	99
4.4	Dynamics of the jet and the droplets: a two speed fragmentation	115
4.5	Conclusion	128

The analysis presented here is aimed to be submitted for publication.

4.1 Introduction

We recall that jet fragmentation occurs in numerous natural mechanisms and industrial applications. It can appear in the form of an ocean spray when waves crash on the shore or a lava spray during volcanic eruption, yet, it is more common to find this physical mechanism in medication sprays, fuel injection systems of combustion engines or agricultural sprinkling. Jet fragmentation can be a challenging configuration to study numerically. Fragmentation flows of high Reynolds and Weber numbers present a large diversity of scales and fluid objects whose dynamics are partly governed by the surface tension and the turbulent characteristics, which gives them a high complexity. Their Direct Numerical Simulation (DNS) requires to solve the two phase Navier Stokes equations with surface tension. A fine resolution of the interfaces is of most importance and can be achieved with an optimized use of computing resources thanks to adaptative grids. Those multiphase flows result from the injection of a dense phase into a lighter phase through a nozzle of diameter d_n and produce a polydisperse spray. The phases are denoted by the subscript i which takes the value 1 for the injected dense phase and 2 for the lighter phase. Both phases are respectively renamed liquid and gas in the following. With the Reynolds (Re) and Weber (We) numbers, the Ohnesorge (Oh) number completes the list of governing dimensionless numbers. The first one represents the ratio of inertia over viscosity and the second one the ratio of inertia over surface tension. The latter relates to the droplet deformation and represents the ratio of viscosity over the product of the surface tension and inertia. Their respective expressions follow:

$$Re_i = \frac{\rho_i U_{inj} d_n}{\mu_i}, \quad We_i = \frac{\rho_i U_{inj}^2 d_n}{\sigma}, \quad Oh = \frac{\mu_1}{\sqrt{\rho_1 d_n \sigma}} \quad (4.1)$$

where ρ_i and μ_i denote the density and the dynamic viscosity of the phase i and σ the surface tension between the two phases, taken as constant.

Lefebvre & McDonell (2017) categorized five fragmentation regimes for non assisted fragmentation of round jets, whose delimitations mainly depend on the Weber number. The focus is given here on two of them: the second wind induced regime for which $We_2 \in [13, 40.3]$ and the so-called atomisation regime for which $We_2 > 40.3$. Complementary, the jet configurations are distinguished between large jets, with $d_n > 1\text{mm}$, and small jets. In addition, the fragmentation of a jet is often split into several breakup types: the primary and the secondary breakups. The former corresponds to the generation of elements only coming from the dense core while the latter considers large elements dumped from the core which undergo further fragmentation. Thus, the physical border of the two breakup types is the location where the dense core pinches off and generates large scale elements, which are unstable in flows of moderate or large liquid Reynolds number Re_1 and gaseous Weber number We_2 . Numerical studies of jet fragmentation mainly focus on the primary breakup region, close to the nozzle, due to limitations on computational resources and numerical challenges (Gorokhovski & Herrmann, 2008; Fuster *et al.*, 2009; Tryggvason *et al.*, 2011; Popinet, 2018). Zandian *et al.* (2017) realised DNS to study the evolution of a planar jet and specifically focused on the development of three dimensional instabilities. Ling *et al.* (2017a) studied a quasi planar gas-liquid mixing layer at moderate density ratio ($\rho_1/\rho_2 = 20$, $Re_1 = 160000$, $We_2 = 20$) thanks to finely resolved DNS. They were able to explain precisely the development of instabilities on the sheet interface. They captured the development of Taylor Culick instabilities as well as the fragmentation of a ligament into droplets and finally compared the droplet size distribution obtained for different

grid refinements with the logarithmic normal and Γ laws.

On the side of round liquid jets, the latest studies rely on DNS using the code Basilisk (Popinet & collaborators, 2013–2021) or the SPH method. Chaussonnet *et al.* (2018) used the latter to explore the droplet population produced by a twin-fluid atomizer at high pressure up to $x/d_n \approx 10$ ($\rho_1/\rho_2 = 93$, $Re_1 = 1.27 \times 10^7$, $We_2 = 1375$). Ling *et al.* (2017b) used Basilisk to observe the influence of viscosity on the fragmentation of a round biodiesel jet ($\rho_1/\rho_2 = 78.2$, $Re_1 = 1450$, $We_2 = 12.9$) developing up to $x/d_n \approx 20$ while testing different grid refinements. Zhang *et al.* (2020) observed the fragmentation of a round diesel jet injected through a solid G-spray injector developing up to $x/d_n \approx 20$ as well ($\rho_1/\rho_2 = 233$, $Re_1 = 13400$, $We_2 = 177$). Through their study, the authors were able to observe the fragmentation of the liquid core into droplets as well as the vortices spatial repartition along the core. In addition, the authors modeled the droplet size distribution relative to the azimuthal angle by a hyperbolic tangent function. Finally, both studies relying on Basilisk compared the logarithmic normal and the Γ laws, the latter being derived in the context of ligament mediated fragmentation (Villermaux *et al.*, 2004; Villermaux, 2020), to fit the droplet size distribution and concluded on the better performance of the fit with the logarithmic normal law in linear mode, i.e. fitting the signal as it is.

Later experimental studies (Stevenin *et al.*, 2016; Felis *et al.*, 2020) used specific droplet tracking velocimetry (DTV) and laser Doppler velocimetry (LDV) apparatus to explore the dispersed zone of agricultural like jets ($\rho_1/\rho_2 = 828.5$, $Re_1 = 41833$, $We_2 = 24$). The measurements were carried far away from the nozzle, $x \geq 400 d_n$, in the zone where the liquid core is fully atomized and where only the secondary breakup occurs. Based on those joint size-velocity measurements, Vallon *et al.* (2021) highlighted the multimodal nature of the droplet size distribution along with the existence of droplet subgroups, each of them being characterized by a specific pair of size and velocity.

The present chapter aims to complete the experimental campaigns by studying numerically the field close to the nozzle in similar flow conditions up to $x/d_n = 28$ in order to have a more global view of the fragmentation process that agricultural like jets undergo. To do so, Sec. 4.2 presents the flow modeling and the parameter framing. Sec. 4.3 is dedicated to the analysis of the overall flow characteristics. Sec. 4.4 focuses on the analysis of the droplet population statistics and the mechanisms from which they are generated.

4.2 Flow modeling and parameter framing

This section presents the governing equations, the numerical methods, the choice of the physical configurations, the numerical configuration and the computation cost. It finally introduces the selection of the most unstable mode of the jet, in order to stimulate the jet fragmentation.

4.2.1 Governing equations

Direct Numerical Simulations (DNS) aim to resolve all time and length scales by solving the Navier-Stokes equations. However, this resolution is often limited by the available computational resources. The fragmentation mechanism under consideration occurs at low Mach numbers neglecting gravitational forces and involves two immiscible, incompressible fluids. The flow dynamics is then governed by the unsteady Navier-Stokes equations and can be expressed in the theoretical framework of a one fluid flow with variable density and viscosity as:

$$\frac{\partial \rho \mathbf{u}}{\partial t} + (\mathbf{u} \cdot \nabla)(\rho \mathbf{u}) = -\nabla p + \nabla \cdot (\mu(\nabla \mathbf{u} + \nabla^T \mathbf{u})) + \mathbf{T}_\sigma \quad (4.2)$$

$$\frac{\partial \rho}{\partial t} + \nabla \cdot (\rho \mathbf{u}) = 0, \quad (4.3)$$

$$\nabla \cdot \mathbf{u} = 0 \quad (4.4)$$

where \mathbf{u} is the velocity, p the pressure and \mathbf{T}_σ the surface tension force, only defined on the liquid-gas interfaces. The two phases are taken into account in the one fluid framework through the phase indicator, named fraction field and denoted α in the following. The fraction equals 1 if a cell only contains liquid and 0 if it only contains gas. The one fluid viscosity and density are computed over the phase quantities by using α and follow $\mu = \alpha \mu_1 + (1 - \alpha) \mu_2$ and $\rho = \alpha \rho_1 + (1 - \alpha) \rho_2$.

4.2.2 Numerical methods

The DNS under consideration are computed with the solver developed by the Basilisk community. Basilisk is an open source project which aims to develop efficient solvers and methods which can be adapted to a large range of configurations (Popinet & collaborators, 2016–2021). This project is mainly led by Stéphane Popinet and benefits from the contribution of all the Basilisk community. The present study largely relies on the atomisation code available on the wiki of the project (Popinet & collaborators, 2016–2021).

The Navier-Stokes equations are solved for a biphasic flow with a constant surface tension using numerical schemes similar to Popinet (2003) & Lagrée *et al.* (2011). The resolution of the equations relies on time steps limited by the Courant-Friedrichs-Lowy (CFL) condition, the advection scheme of Bell-Collela-Glaz (Bell *et al.*, 1989) and an implicit solver for the viscosity. The gas-liquid interface is tracked with a Volume-Of-Fluid (VOF) scheme which is geometric, conservative and non diffusive (López-Herrera *et al.*, 2015). Regarding the surface tension, the interfacial force is calculated as $\mathbf{T}_\sigma = \sigma \kappa \mathbf{n} \delta_s$, where κ is the interface curvature and δ_s is the interface Dirac function. Considering the Continuum-Surface-Force (CSF) method and the Peskin immersed boundary method, the interfacial force can be approximated by $\mathbf{T}_\sigma = \sigma \kappa \nabla \alpha$ where κ is computed by the use of a height function (Abu-Al-Saud *et al.*, 2018). A projection

method is used to compute the centered pressure gradient and the acceleration field. The VOF scheme is combined with an octree adaptative grid (Agbaglah *et al.*, 2011) while the grid adaptation algorithm relies on a wavelet estimated discretization error, described by Popinet (2015) and used for atmospheric boundary layer simulations by van Hooft *et al.* (2018). Such grids present the advantage of finely resolving the gas-liquid interface while having a coarser resolution away from the interfaces, and thus enable an increase of the computational velocity. Finally, the droplet detection is achieved by a tag function which associates a different tag to each neighbourhood of connected cells respecting a threshold condition on the fraction field, set to $\alpha > 1 \times 10^{-3}$ in our DNS.

4.2.3 Physical configuration and parameters

The domain is a cubic box of dimension L_x . A liquid round jet is injected into a quiescent gas at a mean velocity U_{inj} , directed along the x -axis, through a disc of length l_x and diameter d_n . The latter disc is called nozzle in the following. The injection condition is set on the disc face located at $x = 0$ while a free stream condition is imposed at the location $x = L_x$. In addition, a Neumann condition on the normal velocity is imposed on the lateral faces. A sinusoidal perturbation is superimposed on the injection velocity in order to accelerate the development of the Kelvin Helmholtz instability on the interface. The perturbation has an amplitude α and a frequency f such that the injection velocity follows $u_{inj} = U_{inj}(1 + A \sin(2\pi f t))$. Finally, the advection time scale is defined by $T_a = d_n/U_{inj}$.

One aim of this study is to draw comparisons with the experiments of Felis *et al.* (2020). First and foremost, the turbulent property of the experimental inlet velocity profile is let aside and the numerical injection profile is set as laminar. Real world parameter values cannot be picked because the current computational resources do not allow to compute such configurations. For instance, the numerical constraints prohibit large values for the density ratio, $\rho_1/\rho_2 < 100$, the Reynolds number, $\max(Re) = O(10^4)$ and the surface tension, $\sigma = O(10^{-5})\text{N/m}$. Those constraints are denoted \mathcal{C}_0 , \mathcal{C}_1 and \mathcal{C}_2 . Even if the real world values are unreachable, a specific attention can be set on reproducing configurations with dimensionless numbers close to the experimental ones. The latter study carried out DTV and LDV measurements on a water jet lying in the second wind induced fragmentation regime (Lefebvre & McDonell, 2017). This regime is characterized by sharp limits on the gas Weber number: $13 < We_2 < 40.3$. The atomisation regime is also defined on the basis of the Weber number, $We_2 > 40.3$. The first priority is thus to make the DNS Weber numbers evolve over this range of values, which defines a third constraint \mathcal{C}_3 . In order to reproduce similar deformation regimes undergone by the droplets, focusing on the Ohnesorge number is also relevant. Experimentally $Oh = 3.4 \times 10^{-3}$, reproducing the same order of values makes a fourth constraint \mathcal{C}_4 . Reproducing a density ratio of $O(10^3)$, as for water injection in air, is impossible. Conserving the experimental viscosity ratio $\nu_2/\nu_1 = 15$ could also be interesting but it would slow down the fragmentation process, which goes against the optimisation of computer resources. One could then have a look at the conservation of the ratio $\gamma = \mu_1/\mu_2 = (\rho_1\nu_1)/(\rho_2\nu_2)$, where it is worth noting that the quantity $\rho_i\nu_id_n$ is homogeneous to a mass flow¹. Furthermore, γ rewrites as $\rho_1\rho_2^{-1}/(\nu_2\nu_1^{-1}) = We_1We_2^{-1}/(Re_1Re_2^{-1}) = We_1Re_1^{-1}/(We_2Re_2^{-1}) = Ca_1/Ca_2$, where Ca_i is the Capillary number of the phase i . Experimentally, γ equals 55 and can be seen such that the mass flow of the liquid phase is 55 times higher than the mass flow of the gas phase or equiva-

¹Indeed, $[\rho_i\nu_id_n] = \frac{\text{kg}}{\text{m}^3} \times \frac{\text{m}^2}{\text{s}} \times \text{m} = \text{kg} \times \text{s}^{-1}$. Also, $\rho_i\nu_id_n = \rho_iU_{inj}d_n^2/Re_i$.

ρ_1 (kg/m ³)	ρ_2 (kg/m ³)	ν_1 (m ² /s)	ν_2 (m ² /s)	σ (N/m)	d_n (m)	Oh
1	1/55	10^{-6}	10^{-6}	10^{-5}	4.48×10^{-3}	4.725×10^{-3}

Table 4.1: Fixed parameters and corresponding Ohnesorge number.

DNS	1	2	3	4	5	6	7	8	9	10
U_{inj} (m/s)	1.357	1.567	1.787	1.919	2.073	2.216	3.0	3.5	4.0	4.5
We_2 ($\times 10^1$)	1.5	2.0	2.6	3.0	3.5	4.0	7.33	9.98	13.03	16.5
Re_1 ($\times 10^3$)	6.1	7.0	8.0	8.6	9.3	10.0	13.4	15.7	17.9	20.2

Table 4.2: Injection velocities and corresponding gas Weber and liquid Reynolds numbers.

lently $Ca_1 = 55Ca_2$. Respecting this ratio makes a fifth constraint \mathcal{C}_5 . The list of constraints necessary to produce configurations close to the experiments is thus:

$$\left\{ \begin{array}{l} \mathcal{C}_0 : \rho_1/\rho_2 < 100 \\ \mathcal{C}_1 : \max(Re) = O(10^4) \\ \mathcal{C}_2 : \sigma = O(10^{-5}) \text{ N/m} \\ \mathcal{C}_3 : We_2 \in [13, 40.3] \text{ or } We_2 > 40.3 \\ \mathcal{C}_4 : Oh = O(10^{-3}) \\ \mathcal{C}_5 : \rho_1\nu_1/\rho_2\nu_2 = 55 \end{array} \right. \quad (4.5)$$

which let the parameters ρ_1 , ρ_2 , ν_1 , σ , U_{inj} and d_n free to choose. In order to keep a constant geometry between different DNS, the nozzle diameter is set as constant and only the injection velocity varies to cover the range of Weber and Reynolds of interest. Table 4.1 gives the values chosen for the parameters along with the corresponding Ohnesorge number. Table 4.2 lists the chosen injection velocities and the corresponding gaseous Weber and liquid Reynolds numbers. Note that the Ohnesorge number is constant over all the configurations. Thus, for all the DNS, the critical breakup Weber number for a given droplet size is constant (Hinze, 1955). Additionally, the breakup regimes in the secondary atomisation are defined on the same range of Weber numbers (Faeth *et al.*, 1995) for the 10 DNS. *In fine*, the breakup regimes of the droplets are set and identical for any pair (Re_1, We_1) and the DNS explore different breakup regimes of the jet by ranging from low to moderate Re and We numbers.

4.2.4 Most unstable modes for triggering the jet fragmentation

In order to trigger the jet fragmentation the earliest and save computational resources, it is interesting to destabilize the jet interface. Following the work of Yang (1992) on the growth of waves in round jets, it is possible to characterize the most unstable axisymmetric mode. In this work, the author studied the stability of an infinitesimal perturbation on the surface of a round jet of radius a . The notation follows the same convention as the one described below. In addition, the author considered that the gas phase can be injected at a velocity U_2 and that the fluids are incompressible and non viscous. In this section, U_{inj} is denoted U_1 .

The velocity and pressure fields can be split into an averaged part and a fluctuation part: $\mathbf{u}_i = \mathbf{U}_i + \mathbf{u}'_i$ and $p_i = P_i + p'_i$. Injecting this decomposition into the governing equations,

expressed in cylindrical coordinates (r, θ, z) , and applying the divergence operator gives the pressure disturbance equation :

$$\nabla^2 p'_i = 0, \quad \nabla^2 = \frac{1}{r} \frac{\partial}{\partial r} r \frac{\partial}{\partial r} + \frac{1}{r^2} \frac{\partial^2}{\partial \theta^2} + \frac{\partial^2}{\partial z^2} \quad (4.6)$$

Assuming a 3D disturbance with a normalised wavelength number ka and m in the streamwise and azimuthal directions, the perturbed quantities are $p'_i = p'_i(r) e^{i(kz+m\theta)+\alpha_{tg}t}$ and $\mathbf{u}'_i = \mathbf{u}'_i(r) e^{i(kz+m\theta)+\alpha_{tg}t}$, where α_{tg} is the temporal growth rate and m introduces the non axisymmetric variations of the disturbance. Eq. (4.6) then becomes:

$$\left(\frac{1}{r} \frac{\partial}{\partial r} r \frac{\partial}{\partial r} - \frac{m^2}{r^2} - k^2 \right) p_i(r) = 0 \quad (4.7)$$

Resolving this equation gives a solution for $p_i(r)$, Eq. (4.8), depending on the first and second type modified Bessel functions of order m , respectively denoted I_m and K_m . This solution can be used with the mass conservation equation for the linearised perturbation to derive a solution for \mathbf{u}'_i , Eq. (4.9).

$$p_i(r) = C_{i,1} I_m(kr) + C_{i,2} K_m(kr) \quad (4.8)$$

$$\mathbf{u}'_i = - \frac{\nabla (p_i(r) e^{i(kz+m\theta)+\alpha_{tg}t})}{\rho_i (\alpha_{tg} + ikU_i)} \quad (4.9)$$

where the four constants $C_{i,1}$ and $C_{i,2}$ have to be derived regarding the boundary conditions. The pressure is finite in the liquid at $r = 0$ and in the gas when $r \rightarrow +\infty$, thus $C_{1,2} = C_{2,1} = 0$. Let η_1 and η_2 denote the perturbed displacements of the interface and Δp_σ the pressure jump due to the surface tension σ . The pressure follows $\Delta p_\sigma = \sigma(1/R_1 + 1/R_2)$ with R_1 and R_2 the principal radii of curvature. The remaining two constants can be derived from the pressure jump, $p_1 - p_2 = \Delta p_\sigma$, and the interface displacement, $\eta_1 = \eta_2$. The perturbed displacements satisfy:

$$v_i = \frac{\partial \eta_i}{\partial t} + U_i \frac{\partial \eta_i}{\partial x} \quad (4.10)$$

with v_i the velocity component in the radial direction. By letting $\eta = \eta_1 = \eta_2 = \eta_0 e^{i(kz+m\theta)+\alpha_{tg}t}$, Yang (1992) showed that to the first order of η , $1/R_1 + 1/R_2 = 1/d_n - 1/d_n^2 [1 - m^2 - (ka)^2] \eta_0$. The continuity equations then become:

$$C_{11} \left(I_m(ka) - \frac{\sigma[1 - m^2 - (ka)^2]}{a^2} \frac{I'_m(ka)}{\rho_1(\alpha_{tg} + ikU_1)^2} \right) - C_{22} K_m(ka) = 0 \quad (4.11)$$

$$C_{11} \frac{I'_m(ka)}{\rho_1(\alpha_{tg} + ikU_1)^2} - C_{22} \frac{K'_m(ka)}{\rho_2(\alpha_{tg} + ikU_2)^2} = 0 \quad (4.12)$$

The latter equation system admits a non trivial solution when its determinant is zero. This condition gives the following dispersion equation:

$$(\rho_{1m} + \rho_{2m}) \alpha_{tg}^2 + 2ik\alpha_{tg} (\rho_{2m} U_2 + \rho_{1m} U_1) - k^2 (\rho_{2m} U_2^2 + \rho_{1m} U_1^2) - \frac{k\sigma}{a^2} [1 - m^2 - (ka)^2] = 0 \quad (4.13)$$

with:

$$\begin{cases} \rho_{1m} &= \gamma_m \rho_1 \\ \rho_{2m} &= \beta_m \rho_2 \\ \gamma_m &= k I_m(ka) / I'_m(ka) \\ \beta_m &= -k K_m(ka) / K'_m(ka) \\ I'_m(ka) &= \frac{dI_m(kr)}{dr} \Big|_{r=a} \\ K'_m(ka) &= \frac{dK_m(kr)}{dr} \Big|_{r=a} \end{cases} \quad (4.14)$$

The dispersion equation, Eq. (4.13), is a quadratic equation in α_{tg} and the expression of the adimensional temporal growth rate for the m -th transversal mode can be derived from it:

$$(\alpha_r^*)_m^2 = \frac{\gamma_m \beta_m Q \cdot (ka)^2}{(\gamma_m + \beta_m Q)^2} + \frac{ka}{We} \frac{1 - m^2 - (ka)^2}{\gamma_m + \beta_m Q} \quad (4.15)$$

where $(\alpha_r^*)_m^2 = (\alpha_r^2)_m / [(U_1 - U_2)^2 / d_n^2]$, $We = [d_n(U_1 - U_2)\rho_1] / \sigma$ and $Q = \rho_2 / \rho_1$. Conversely to the previous developments, the computation of the most unstable mode is straightforward. Figure 4.1 gives the evolution of $(\alpha_r^*)_m^2$ for $U_1 = 3.0$ m/s. The wavelength ka of such a mode corresponds to the wavelength for which the adimensional temporal growth rate is maximum. The mode pulsation ω is then given by α_i and the axisymmetric mode can be selected by setting $m = 0$. In addition, U_2 is set to 0 and a should be set to $d_n/2$. However, during the computation, a was set to d_n . The difference between the pulsation of the mode computed for $a = d_n$ and $a = d_n/2$ is of $O(1\text{rad/s})$ while the pulsations given by α_i are of $O(10^3\text{rad/s})$, i.e. the relative difference is of $O(10^{-3})$. Thus, the mode obtained with $a = d_n$ is not the most unstable mode but lies in the group of the most unstable modes. Table 4.3 lists the most unstable mode frequencies f for each selected configuration in Sec. 4.2.3, whose frequencies are used to parametrize the injection velocity of each DNS.

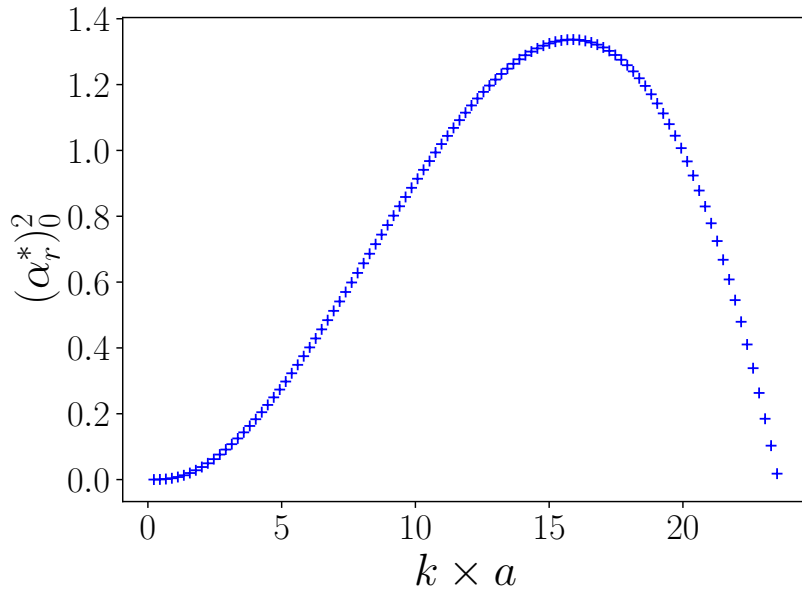


Figure 4.1: Evolution of the adimensional temporal growth rate $(\alpha_r^*)_m^2$ for $U_1 = 3.0$ m/s.

DNS		1	2	3	4	5	6	7	8	9	10
U_{inj}	(m/s)	1.357	1.567	1.787	1.919	2.073	2.216	3.0	3.5	4.0	4.5
ω	(10^3 rad/s)	2.137	2.853	3.693	4.247	4.995	5.667	10.471	14.278	18.676	23.441
f	(kHz)	0.340	0.454	0.587	0.676	0.795	0.901	1.666	2.272	2.972	3.730

Table 4.3: Pulsation and frequency of the most unstable mode for each jet configuration.

DNS	C_{tot} (10^6)	$\overline{\mathcal{V}_{num}}$ (10^6 cells/s)	t_{max}/T_a	$L_{j,max}/d_n$	N_{tot}
1	4.43	0.59	51.3	28	148
2	29.29	0.93	35.3	28	2345
3	53.83	2.23	35.5	28	7069
4	42.15	1.96	36.0	28	7958
5	51.41	1.73	37.7	28	4729
6	34.13	1.92	35.0	28	6180
7	77.45	2.45	24.0	21.5	17144
8	105.6	2.58	19.8	17.5	38538
9	141.7	2.58	17.3	15.2	68555
10	154.4	2.56	16.2	14.3	93755

Table 4.4: Numerical performances.

4.2.5 Numerical configuration and computational cost

The refinement level is set to 12 and the minimum cell size in an adaptative grid is given by $\Delta_{min} = L_x/2^{12}$. Hence the minimum cell size is $\Delta_{min} = 30.5 \mu m$ and $d_n/\Delta_{min} = 146.8$. The time step is set by the CFL condition, $|u_{max}| \Delta t / \Delta_{min} < C$, where the Courant number is initially set to 0.8. Running the 10 DNS summed a total of 431 256 scalar hours of computation. DNS 3 to 10 ran for 50 400 h while DNS 1 and 2 respectively ran for 12 600 h and 15 456 h. The computational performances can be tracked by checking the total number of cells used for each DNS, C_{tot} , the mean numerical velocity, $\overline{\mathcal{V}_{num}}$, the maximal physical time, t_{max}/T_a , the maximum jet elongation, $L_{j,max}/d_n$ and the total number of detected droplets, N_{tot} . Table 4.4 summarizes the related numerical performances. All the DNS are split into 3 runs and were computed on the Occigen HPC (CINES, France). An example of atomisation produced by DNS 10 is given in Fig. 4.2.

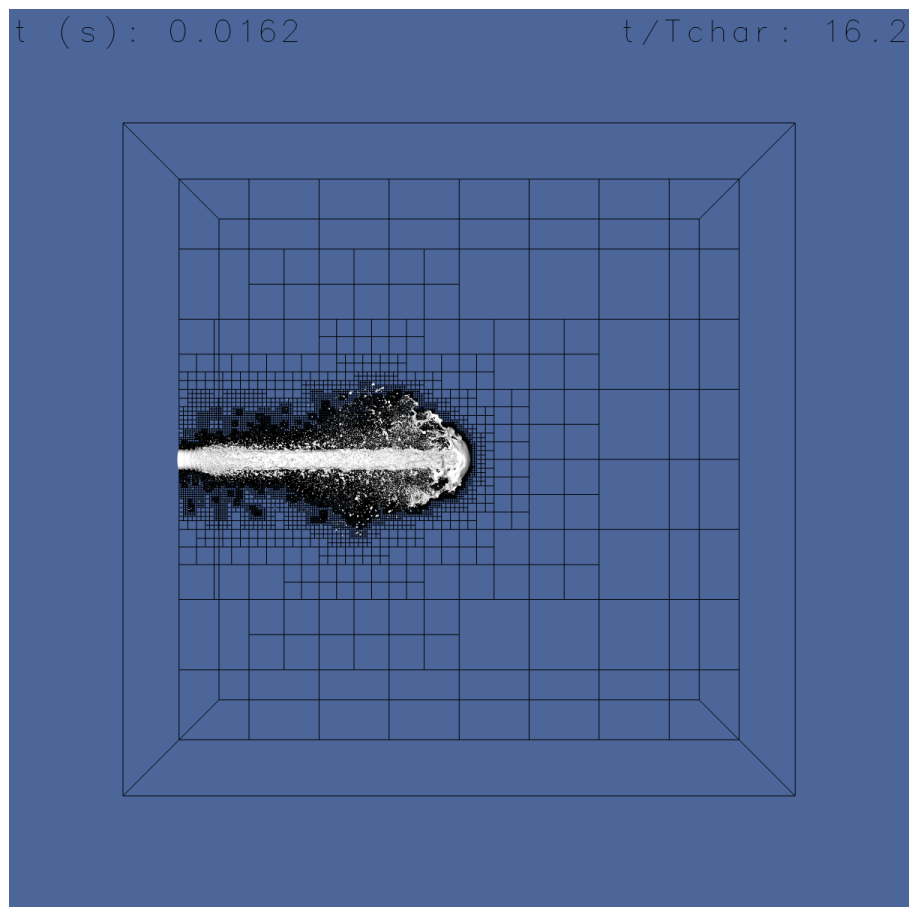


Figure 4.2: Atomisation and adaptative grid for $We_2 = 165$ (DNS 10) at $t/T_a = 16.2$.

4.3 Overall flow characteristics and droplet statistics

This section characterizes the Turbulent Kinetic Energy (TKE) in the domain, has a glance on the jet interface and introduces the statistics and PDF of the droplet population. In the following, the evolution of several variables relatively to t/T_a is analysed.

If the liquid core motion was the one of a solid cylinder, then the jet length would theoretically be $L_{j,\text{theo}} = d_n \times t/T_a$, i.e. $L_{j,\text{theo}}/d_n = t/T_a$. However, a lag of the jet tip relatively to this theoretical position is observed. In order to link t/T_a and the actual jet length L_j , Fig. 4.3 gives the temporal evolution of $L_j/L_{j,\text{theo}}$. Here, L_j is defined as the 99% quartile of the axial positions of the interface cells, $\alpha \in]0, 1[$, and not the maximum position. Doing so enables to exclude droplets which would exist on the upstream face of the jet tip as well as smooth out the effect of the grid refinement. Thus, the length of the jet equals in average 85% of the theoretical length, $L_j/d_n \approx 0.85 \times t/T_a$ and $T/T_a = 33$ corresponds to the instant when the jet exits the computational domain. Note that from $t/T_a \approx 5$, the ratio $L_j/L_{j,\text{theo}}$ is constant, which means that the jet front has a velocity equal to U_{inj} .

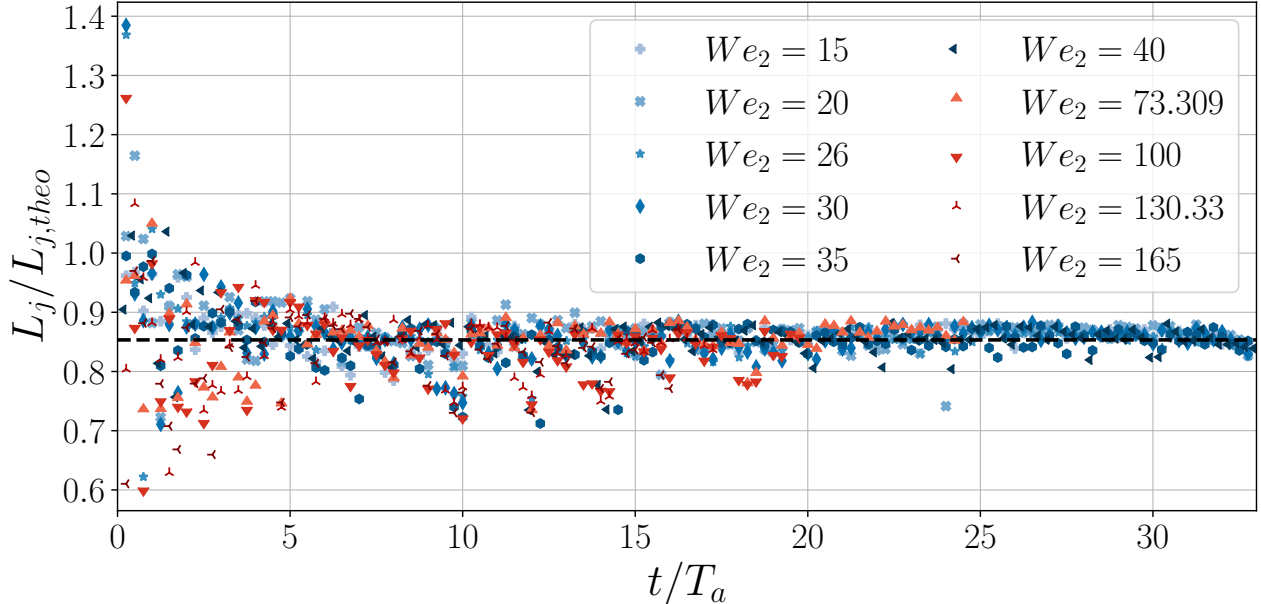


Figure 4.3: Temporal evolution of the jet length L_j compared to the theoretical jet length $L_{j,\text{theo}}$ for the 10 DNS. The black dashed line represents the mean value $L_{jet,max}/L_{jet,theo} = 0.853$ averaged over $t/T_a \in [0, 33]$. The blue colours denote the DNS in the second wind induced regime and the red colours the DNS in the atomisation regime.

4.3.1 Turbulent kinetic energy

One aim of this study is to draw conclusions on the statistics of the droplet population. To ensure converged statistics, the flow needs to reach a statistically steady state. Looking at the turbulent kinetic energy k_i enables to conclude about such a state, primarily the one of the gas phase. As shown in Table 4.4, the jet extension observed in the DNS 7 to 10 is smaller than the length L_x of the domain. Thus, a statistically steady state at the scale of the domain cannot

be achieved. Even so, it is possible to slice the domain in different sections along the x axis and conclude on the flow steadiness in each section.

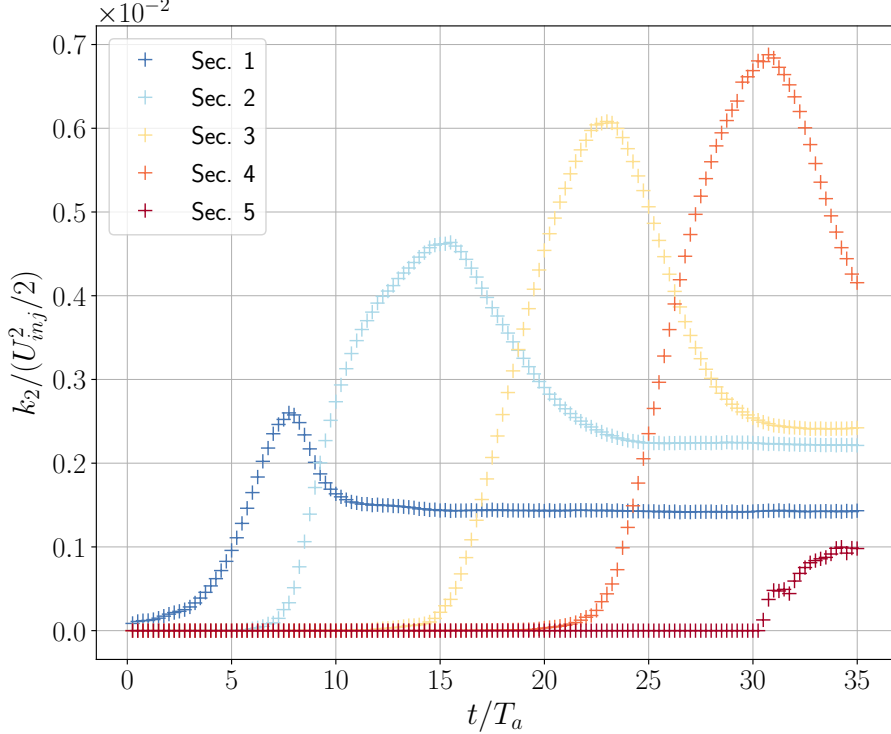


Figure 4.4: Turbulent kinetic energy in the gas phase for $We_2 = 40$ (DNS 6).

The domain of length L_x is sliced in 5 sections along the x axis. The fifth section represents the outlet side of the domain and its length is set to d_n . The rest of the domain is evenly sliced with a slice thickness equal to $(L_x - d_n)/4$. The sections are denoted from 1 to 5, going from the nozzle to the outlet face. The turbulent kinetic energy is computed for both the gas and the liquid following $k_i = \frac{1}{2} \int_{V_s} (u_{x,i}'^2 + u_{y,i}'^2 + u_{z,i}'^2) dV$ with V_s the volume of the section under consideration. Figure 4.4 shows the time evolution of the TKE for the DNS 6. The evolution is similar in each slice: k increases when the jet head enters the section, reaches a maximum, decreases when the head enters the following section and finally reaches a plateau. The time sampling is set with a step $\Delta(t/T_a) = 1/4$ and smooths the fluctuations out of the plateau region. The increase of the k_2 maximum and asymptote values between the slices is due to the ongoing fragmentation and the newly created droplets which increases the gas phase agitation. Thus, once the jet head fully exits a section, the flow reaches a statistically steady state. One could expect that the TKE around the jet head, measured from a Lagrangian point of view would reach an asymptote as well and, thus, a statistically steady state.

4.3.2 Close up on the jet interface

This section explores qualitatively the interface of the jet in two regions of interest: close to the nozzle where the unstable mode develops and around the tip of the jet where the front extends

DNS	1	2	3	4	5	6	7	8	9	10
We_2	15	20	26	30	35	40	73.3	99.8	130.3	165
Sr ($\times 10^{-6}$)	17.9	15.5	13.6	12.7	11.7	11.0	8.07	6.90	6.03	5.41

Table 4.5: Strouhal number based on the forcing and gaseous Weber number for the 10 DNS.

and fragments. It also includes the presentation of the method for computing the mean jet interface.

4.3.2.1 Development of the unstable mode

In order to check qualitatively the forcing implemented in the simulations and its outcome, one could have a look on the jet interface in the region of the nozzle, where the unstable mode excited by the forcing should develop. To compare the interface evolution between the different DNS, the x coordinate needs to be normalised by the characteristic length scale of the forcing, i.e. $U_{inj}f^{-1}$. Note here that $U_{inj}f^{-1} = Sr/d_n$, so $x/(U_{inj}f^{-1}) = (x/d_n)Sr$, where Sr is the Strouhal number based on the forcing, given in Table 4.5. Furthermore, the physical times chosen for the comparison have to be in phase relatively to the sinusoidal perturbation, i.e. the physical times should be chosen such that the perturbation waves superimpose on each other. Fig. 4.5 shows the jet interface sliced at $z = 0$ and for $y/d_n > 0$, normalised as explained.

For the 10 DNS, the perturbation waves collapse well after normalising by $U_{inj}f^{-1}$ and picking in-phase physical times. Consider first the second wind induced regime. The jet interfaces of the DNS 1 and 2 are represented separately from the DNS 3 to 6, Fig. 4.5a and 4.5b, to highlight the different behavior of the forcing between them, even if DNS 1 to 6 lie in the second wind induced regime. For the DNS 1 and 2, the development of the mode leads to waves which only break in large elements in the DNS 2 while they are attenuated in the DNS 1. Contrarily, the perturbation in the DNS 3 to 6 leads to the development of shorter waves which break into a wider droplet population. Here, the wave develops in the radial direction. While the wave extends radially, up to $y/d_n \approx 0.8$, its outskirt forms a rim and the space between the liquid core and the outer rim forms a sheet. The sheet becomes thinner the more the wave extends, before fragmenting for $x/(U_{inj}f^{-1}) \in [5.5, 7]$. Once the sheet has fragmented, the rim destabilizes and fragments as well. A similar wave development can be observed for the DNS 7 to 9, except that the wave extension is smaller than previously, up to $y/d_n \approx 0.6$, that the wave sheet fragments earlier, for $x/(U_{inj}f^{-1}) \in [5, 6]$, and that the rim fragments faster for DNS 7 or even hardly exists for DNS 8 and 9. Finally, no rim is created in the last DNS. Specific attention is required for the DNS 10. Fig. 4.5d indicates the presence of interface in the liquid core, meaning that the core is populated by some volume made of the lighter phase, i.e. bubbles. The bubbles are generated from $t/T_a \approx 10$ and could be generated by a cavitation effect triggered by the forcing or could originate from a numerical artefact. Note that bubbles also appear, but later on timewise, in the DNS 9. The presence of bubbles changes the fluid dynamics inside the core but appears to modify only slightly the interface dynamics in the time scope of the study and any perturbation would be smoothed out by considering the overall droplet population.

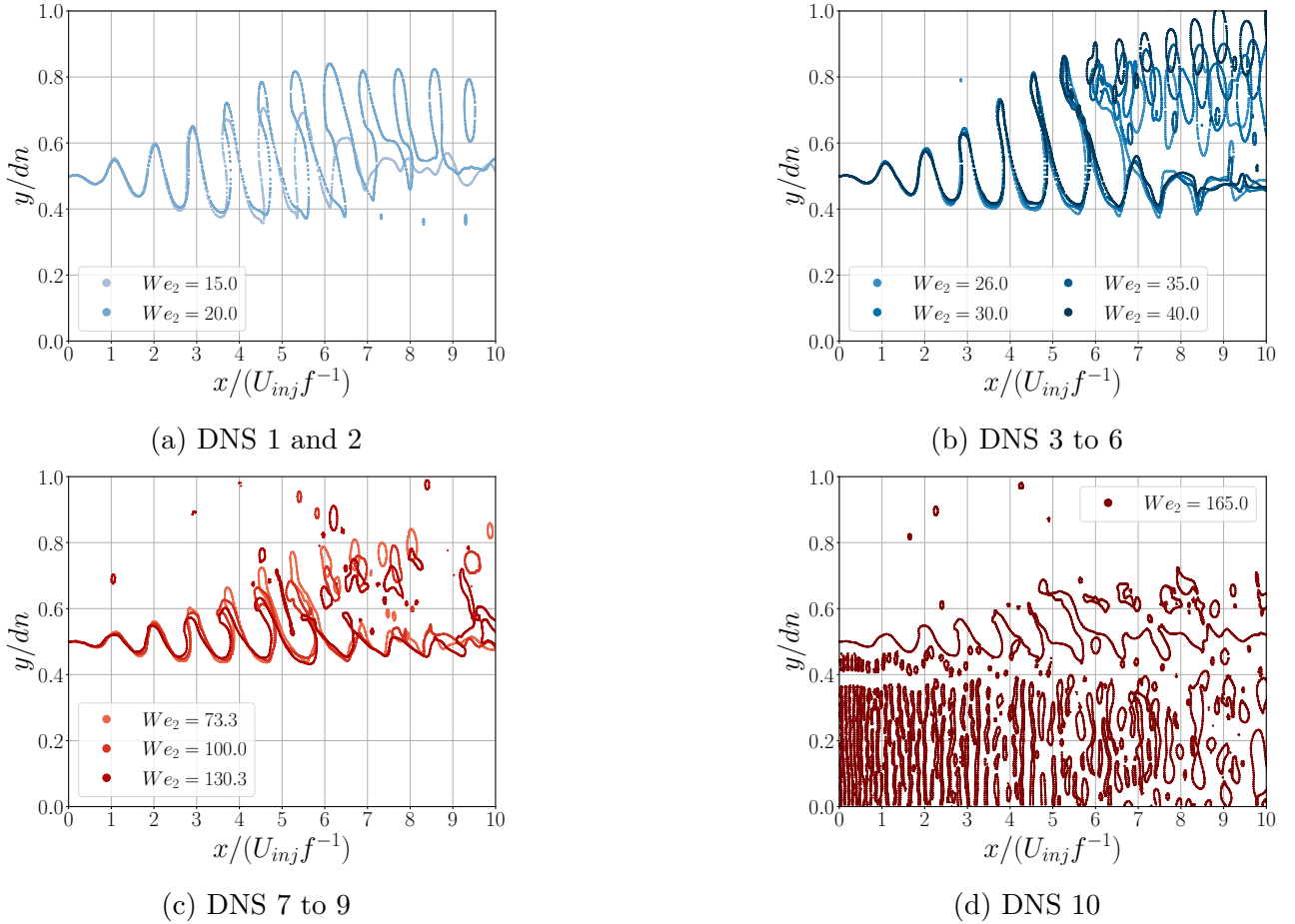


Figure 4.5: Superposition of the interface sliced at $z = 0$ in the region of the nozzle in the second wind induced regime (a,b) and the atomisation regime (c,d). The blue and red colors indicate the second wind induced and atomisation regimes respectively. The physical times are chosen such that the sinusoidal perturbations are in phase. As a reminder, $x/(U_{inj} f^{-1}) = (x/d_n) Sr$.

4.3.2.2 Development of the jet head

Complementarily to the development of the wave perturbation, it is possible to have a glance on the head of the jet. Fig. 4.6 presents the jet interface sliced at $z = 0$ in the region of the head of the jet for both regimes at the same physical time $t/T_a = 15$. What appears at first is the difference of geometry of the front between the two regimes. In the second wind induced regime, the front is plane while it is parabolic in the atomisation regime. This difference results from the force equilibrium between the liquid and gas phases depending on the injection velocity. In both regimes, the head extends up to $y/d_n \approx 2$ and experiences piercing (data not shown here) which could be due to the Taylor Culick instability. However, the dynamics of the head extension is quite different. In the second wind induced regime, the head extension can produce thick ligaments able to extend over distances of the order of d_n while, in the atomisation regime, the ligaments fragment once they are detached from the head sheet. The difference in the resulting droplet population is qualitatively visible in Fig. 4.6 where the droplets appear to be more numerous in the atomisation regime than in the second wind induced regime. Theoretical developments enable to estimate the thickness of the head to be of $O(10^{-4}\text{m})$, see Appendix A.

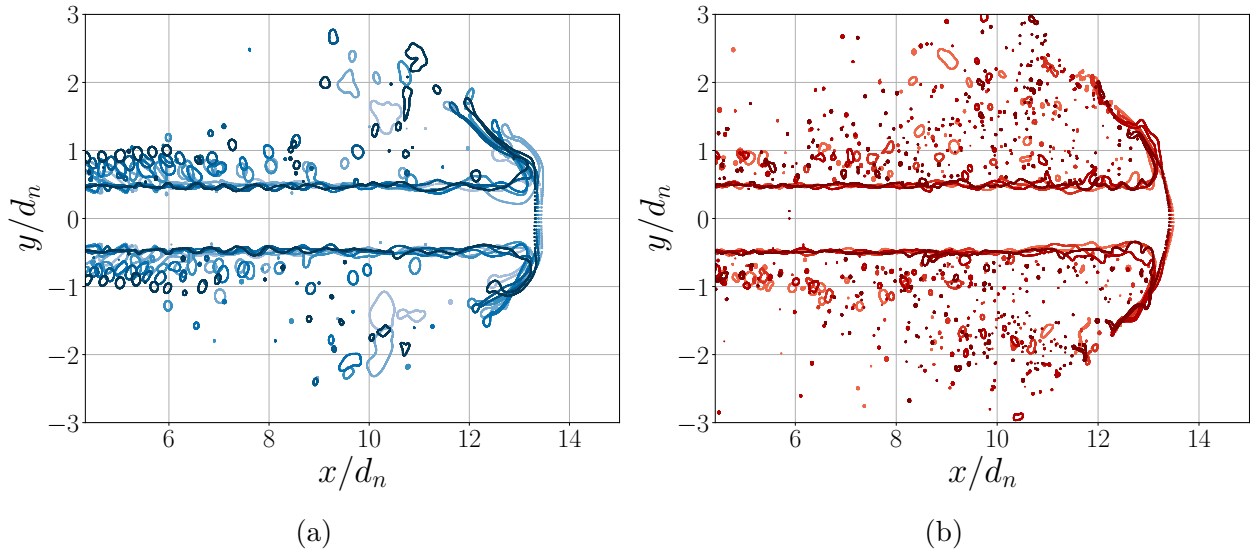


Figure 4.6: Superposition of the interface sliced at $z = 0$ in the region of the jet head in the second wind induced regime (a) and in the atomisation regime (b) at $t/T_a = 15$.

4.3.2.3 Computation of the mean interface

The discussion about the jet interface close to the nozzle and around the jet head were carried out while considering slices on the plane $z = 0$. In order to draw more general conclusions on the jet interface, for instance regarding the positions of the droplets along the jet like in Sec. 4.4.1 and 4.4.2, it is interesting to gather more global information as, for instance, the mean interface. Computing the latter is not straightforward and involves a bit of processing. To extract it, it is first necessary to compute the joint distribution of the interface points in the physical space $(x/d_n, r/d_n)$. Once computed, the mean interface can be extracted from the distribution by filtering out the most probable interface points. This extraction step however relies on the choice of a threshold. This threshold can be empirically chosen such that it enables to depict the mean interface while discarding most of the interface related to the droplets.

Fig. 4.7a and 4.7b respectively give the joint distribution of the interface points across the $(x/d_n, r/d_n)$ space and the interface filtered from the joint distribution with a threshold of 0.2, i.e. the interface points with a probability larger than 0.2. A way to refine the mean interface of the jet would be to consider the interface of the liquid core only, instead of considering all the interface points in the jet, i.e. the liquid core and all the droplets. The droplets would be then naturally discarded and the resulting interface would depict more precisely the mean interface around the jet head. Even so, the method used here is satisfactory for the following analysis.

4.3.3 Statistics of the droplet population

Figure 4.8 gives the number of droplets detected by the tag function implemented in Basilisk and denoted N_{tot} . First and foremost, the droplets produced in the DNS 1 and 2 do not exceed 1000 elements, which is not enough to draw conclusions on the statistics of those two populations. Thus, the DNS 1 and 2 are discarded in the following. All the other DNS show a total number of elements larger than 1000, which enable to carry out a statistical analysis.

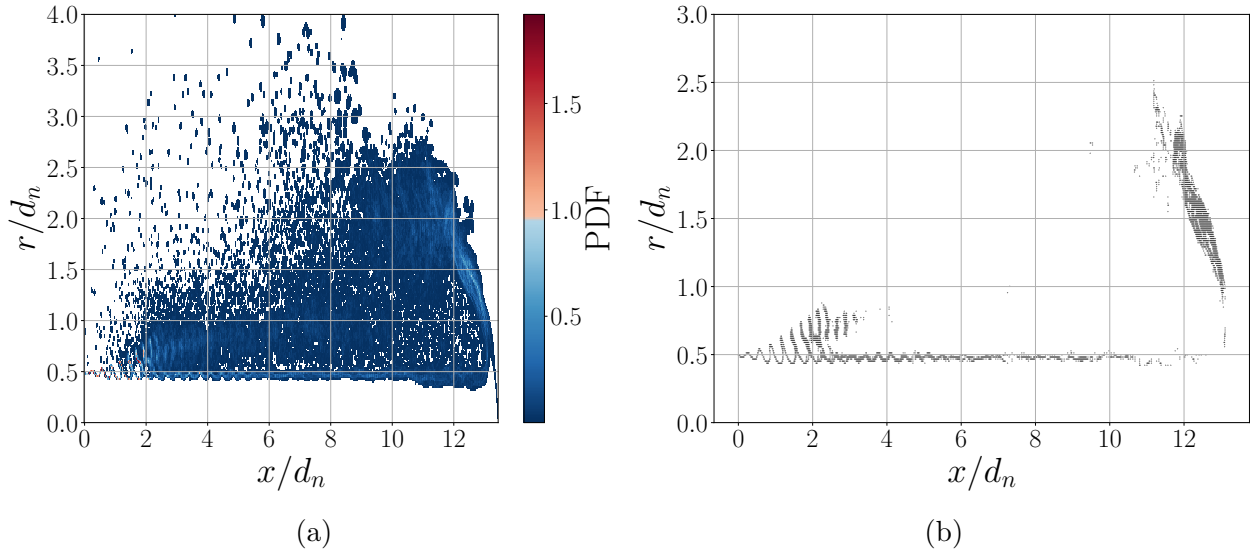


Figure 4.7: Joint distribution of the interface points in the $(x/d_n, r/d_n)$ space for $We_2 = 99.8$ (DNS 8) at $t/T_a = 15$ (a) and the interface filtered with a threshold of 0.2 (b).

The two regimes distinguish from each other by the total number of produced droplets. The total number is of $O(10^3)$ in the second wind induced regime whereas it is of $O(10^4)$ in the atomisation regime, reaching up to 5×10^4 elements for the DNS 10. Even so, after rescaling by $We_2^{1.8}$ the number of elements for the DNS 3 to 10 collapse all together and N_{tot} tends toward 6 $We_2^{1.8}$ for both regimes, excepted DNS 1 and 2. The transition to a steady production of droplets differs between the two regimes. In the second wind induced regime, the total number of elements quickly increases and drops down before reaching a steady rate. The observed decrease could be due to the interactions between the jet head development and the corollas induced by the mode forcing, interactions which bring the droplets back to the liquid core.

The arithmetic mean operator and the standard deviation are respectively denoted $\langle \cdot \rangle$ and σ while the skewness and the kurtosis are respectively denoted S and κ . Here, we considered the kurtosis subtracted by 3 such that the normal distribution has a zero kurtosis. Those four quantities represent the first four normalised statistical moments. Figure 4.9 gives the temporal evolution of the mean values of the size, the axial velocity and the radial velocity. Regarding the size and the axial velocity, after reaching a peak value for $t/T_a \in [5, 10]$, the mean values increase relatively steadily within the time scope under consideration. The time evolution of the mean of each DNS can be rescaled with We_2 . On one side, the mean size scaled by $We_2^{0.6}$ seems to evolve linearly with t/T_a . On the other side, it is possible to collapse the time evolution of the mean axial velocity for each regime by considering $\langle u_x \rangle We_2^{-1}$ for the second wind induced regime and $\langle u_x \rangle We_2^{-0.3}$ for the atomisation regime. The evolution of u_y is specific in the sense that the flow is statistically axisymmetric and $\langle u_y \rangle$ should naturally be set to zero, which is verified here asymptotically. Due to the flow symmetry, the mean of u_z behaves the same as the one of u_y . On the side of the standard deviations, those quantities reach a steady state faster than the mean values for the size and the velocities. Overall, the DNS in the second wind induced regime are close to a steady regime while the DNS in the atomisation regime are still evolving towards such a regime. This departure comes from the difference in the physical time reached by the DNS in each regime, directly depending on the flow complexity and the corresponding need of computational resources.

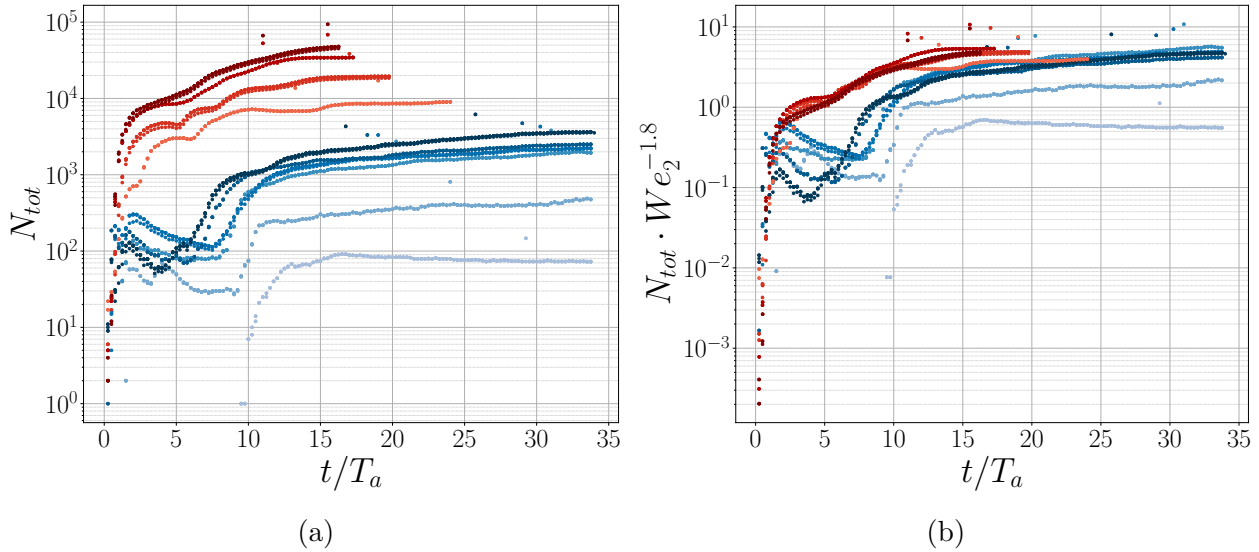


Figure 4.8: Total number of detected droplets, (a) unscaled and (b) scaled by $We_2^{-1.8}$. The blue colours denote the DNS in the second wind induced regime and the red colours the DNS in the atomisation regime.

Figure 4.10 gives the evolution along We_2 of the four first statistical moments along with the minimum and the maximum values for the size, the axial velocity and the transverse velocity at the time instants $t/T_a = 15$ and $t/T_a = 25$. First of all, the droplet tagging function implemented in Basilisk can return droplets with a volume V smaller than Δ_{min}^3 , the volume of the smallest grid cell. This behavior is expected and due to the cells having a volume fraction f between 10^{-3} and 1 and being disconnected to any liquid neighbourhood. To ensure physical consistency regarding the grid characteristics, all the droplets with a volume smaller than or equal to the minimum cell volume are discarded, i.e. any droplets such that $V \leq \Delta_{min}^3$. Assuming spherical droplets, this condition implies a minimum droplet diameter $d_{min} = \sqrt[3]{6/\pi}\Delta_{min} \approx 37.8 \mu\text{m}$.

Let us consider the statistical moments of the droplet size. Globally, both the mean and standard deviation decrease with We_2 and are of $O(100 \mu\text{m})$. Similarly, the maximum value decreases but is one order larger, $O(1 \text{ mm})$. Meanwhile, the skewness and the kurtosis slightly increase and are respectively of $O(1)$ and $O(10)$. An increase in We_2 corresponds to an increase of the inertial forces relatively to the surface tension forces. Then, the larger We_2 , the more likely the droplets undergo fragmentation and less sizes are stable. Thus, the mean diameter and the maximum diameter decrease and more droplets group around the mean diameter which, as a consequence, reduces the standard deviation. A decrease of the minimum diameter should also occur but the condition on the minimal droplet volume numerically filters out any diameter smaller than $37.8 \mu\text{m}$. In parallel, the increase in the skewness value, which is positive, points out that the droplet size distribution is slightly more skewed to the left with higher We_2 . This indicates that the right hand tail, towards sizes larger than $\langle d \rangle$, exists on a size range larger than the one on which the left hand tail exists. Finally, the positive sign and the increase of the kurtosis with We_2 indicates that the distribution tail increases in length relatively to the mean and the standard deviation or, equivalently, that the range of rare very large sizes, relatively to the mean, is both broader with higher We_2 and larger than the Gaussian distribution for which $\kappa = 3$. As the flow geometry remains the same for the different values of We_2 , the increase

in the kurtosis and the skewness is due to the depletion of large sizes in the benefits of small sizes, grouped around the mean diameter. However, even if d_{max} decreases, the large values of S and κ show that the larger droplet sizes do not disappear completely from the flow and still exist at higher values of We_2 .

Regarding the distribution of u_x , all the four statistical moments increase with We_2 . The increase in the mean and standard deviation indicates that the droplets are accelerated with We_2 , which is obvious as U_{inj} increases meanwhile, and that the dispersion in term of velocity is larger, which also seems natural as the relative velocity between the injection and the gas phase velocity increases too. The same observation holds to explain the evolution of u_x^{max} and u_x^{min} . Concurrently, the skewness is positive and increases with We_2 , thus the axial velocity distribution is skewed to the left with an increasing asymmetry. Compared to the skewness of the size distribution, the skewness of the distribution of u_x is much smaller and the distribution should be moderately skewed. Finally, the kurtosis not only increases but also changes sign for $We_2 \in [40, 70]$. The second wind induced regime is then characterized by a negative kurtosis, which indicates tails being shorter and a peak being flatter than the ones of the Normal distribution. Conversely, the kurtosis in the atomisation regime, for the values of We_2 under consideration, is positive, indicating larger tails and a sharper peak compared to the Normal distribution. Furthermore, the kurtosis is smaller than 3 and the distribution has tails shorter than the ones of the Gaussian distribution. Thus, each fragmentation regime shows a characteristic tail spanning for the distribution of u_x .

The interpretation of the evolution of the statistical moments for the distribution of u_y is straightforward. As discussed previously, the statistical axisymmetry of the flow enforces a zero mean value as well as a symmetric repartition of u_y around its mean, i.e. a zero skewness. Those two consequences of the flow symmetry are verified for each We_2 value and highlighted by the evolution of u_y^{min} and u_y^{max} . Similarly to the distribution of u_x , the standard deviation increases with the gaseous Weber number because of the increasing relative velocity between the liquid injection and the gas phase and thus the shear. The kurtosis, the one subtracted by 3, remains stable around 2 which indicates a steady behavior and tails being smaller than those of the Gaussian distribution.

Finally, the values of the skewness and the kurtosis of the size distribution are very large and one order of magnitude larger than the one of the velocity distributions. This indicates a wider spanning range for the size distribution than for the two velocity distributions, thus justifying the use of a loglog scale to visualise the size distribution.

4.3.4 Distributions of the size and the velocity

Complementary to the statistical moments, it is worth looking at the distributions of the size and the velocities of the droplets. For the sake of clarity, the number PDF of any variable ζ is denoted \mathcal{P}_ζ in the following. Even if the mean values of the size and the velocities are not fully converged, we consider the PDF of each variable normalised by its mean. However, u_y being close to zero in average, normalising by $\langle u_y \rangle$ is not relevant and $u_y/\langle u_x \rangle$ is considered instead. Figure 4.11 gives the PDF of $d/\langle d \rangle$, $u_x/\langle u_x \rangle$ and $u_y/\langle u_x \rangle$ at the time instants $t/T_a = 15$, where both regimes are computed, and $t/T_a = 25$, where only the second wind induced regime is computed. First of all, it is interesting to note that the PDF in each regime collapse for the three variables even if the mean values are not converged. From the three distributions, only that for $u_y/\langle u_x \rangle$ shows a similar behavior between the two regimes of fragmentation,

We_2	15	20	26	30	35	40	73.3	99.8	130.3	165
$\lambda (10^{-4}\text{m})$	10.31	8.93	7.84	7.29	6.75	6.32	4.67	4	3.5	3.11
$\lambda/\langle d \rangle_{t/T_a=15}$	7	3.47	3.36	3.29	2.85	2.83	3.37	3.65	3.52	3.28
$\lambda/\langle d \rangle_{t/T_a=25}$	2.50	2.21	3.28	2.62	2.37	2.37	—	—	—	—

Table 4.6: Estimation of the Taylor micro scale λ and its normalised values at $t/T_a = \{15, 25\}$.

excepting for the width and the slope of the tails. For both regimes, the PDF tails scale with $\exp(a \times u_y/\langle u_x \rangle)$ where $|a|$ nearly equals 6 in the second wind induced regime and nearly equals 3 in the atomisation regime. The difference in the tail width goes along with the difference between the exponential coefficient. Indeed, the larger the coefficient is, the smaller the tail width is. This can be explained once again with the increase of the relative velocity between the injection and the gas phase, and thus the shear, when We_2 increases. Note that, due to the flow symmetry, $\mathcal{P}_{u_z/\langle u_x \rangle}$ follows a trend similar to that of $u_y/\langle u_x \rangle$.

Regarding the size distribution, different modes appear clearly between the two fragmentation regimes. The size PDF derived from the atomisation regime shows one main mode centered on $d/\langle d \rangle = 0.5$ while the PDF for the second wind induced regime shows 3 modes centered on $d/\langle d \rangle = \{0.2, 1, 2.5\}$, denoted from 1 to 3 in Fig. 4.11b. Even if the main mode appears to be shifted towards larger $d/\langle d \rangle$ when We_2 increases, it refers to the same range of physical sizes d between 47 μm and 58 μm with a mean value of 55 μm , considering DNS 3 to 10. Tennekes & Lumley (1972) derived handy equations to estimate the turbulent Reynolds number Re_τ from the ratio of the extreme scales of the flow and the Taylor micro scale Reynolds number Re_λ : $Re_\tau \propto (d_n/\Delta_{min})^{4/3}$ and $Re_\lambda \approx \sqrt{Re_\tau}$ where $Re_\lambda = u_{RMS}\lambda/\nu_2$ and $\Delta_{min} = 30.5 \mu\text{m}$, see Sec. 4.2.5. With the chosen configuration, the estimation gives $Re_\tau \approx 775$ and $Re_\lambda \approx 27.8$. Besides, assuming that the turbulence intensity is around 20% of the injected velocity, i.e. $u_{RMS} = 0.2 U_{inj}$, it is possible to estimate the Taylor micro scale λ . Table 4.6 lists the estimation of λ for the 10 DNS.

The Taylor micro scale decreases with the gaseous Weber number We_2 , which is expected as Re_λ is set by the configuration and u_{RMS} increases with the injection velocity. Physically, the root mean square velocity increases with the injection velocity and the Taylor micro scale decreases. Most importantly, the normalised values of λ correspond to the third mode of $\mathcal{P}_{d/\langle d \rangle}$ at both $t/T_a = \{15, 25\}$ in the second wind induced regime, $We_2 < 40.3$, and indicate that the larger droplets observed in the DNS might be related to the most probable vortex size set by the gas turbulence. Finally, $\mathcal{P}_{d/\langle d \rangle}$ in both regime shows a similar tail evolution scaling as $(d/\langle d \rangle)^{-2.7}$, which was also observed experimentally (Vallon *et al.*, 2021), see Fig. 2 in Sec. 3.2. This power law scaling goes against the experimental observation of Simmons (1977) who remarked that the size distribution in industrial jet shows a tail scaling as an exponential. Fig. 4.12 gives the size distribution in a semi-logarithmic scale. The time instant $t/T_a = 20$ has been chosen over $t/T_a = 25$ in order to highlight the trend of the size distribution in the second wind induced regime thanks to the distribution of the DNS 7. It appears that, at both time instants, none of the size distribution follows a unique exponential decay. Instead, the distribution in the atomisation regime follows two exponential scalings, the first one for $d/\langle d \rangle \in [0.5, 2]$ and the second one for $d/\langle d \rangle \in [4, 8]$, with a transition region scaling as $d/\langle d \rangle^{-2.7}$ for $d/\langle d \rangle \in [2, 4]$. Following the analysis done in Sec. 3.3.2, the size distributions under consideration could be composed of several distributions whose decay follows an exponential scaling. The modeling of

the size PDF by theoretical distributions is achieved in Sec. 4.3.5.

The distribution of the axial velocity of the droplets shows some interesting behaviors. In jet fragmentation, it is often expected that the droplets show a positive axial velocity less than or equal to the injection velocity as they are globally advected towards increasing x/d_n . However, the $\mathcal{P}_{u_x/\langle u_x \rangle}$ shows large probabilities for a range of negative velocity, $u_x/\langle u_x \rangle \in [-2, 0]$, with a sharp peak at $u_x/\langle u_x \rangle = 0$. The right hand tail exists in both regimes on a range of velocities larger than the injection velocity U_{inj} . For instance, the droplet population from the DNS 6, $We_2 = 40$, lying in the second wind induced regime at $t/T_a = 25$ is such that $\langle u_x \rangle = 1$ m/s and $\mathcal{P}(2 < u/\langle u_x \rangle < 3) > 0$, meaning that there exist droplets with an axial velocity $u_x/U_{inj} \in [0.9, 1.35]$, thus being faster than the injection velocity $U_{inj} = 2.216$ m/s. The same conclusion can be drawn for the DNS in the atomisation regime. For the DNS 8 where $We_2 = 99.8$, there is $\langle u_x \rangle \approx 1.2$ m/s and $\mathcal{P}(3.75 < u_x/\langle u_x \rangle < 5) > 0$, then there exists droplets with an axial velocity such that $u_x/U_{inj} \in [1, 1.72]$, with $U_{inj} = 3.5$ m/s. Astonishingly, for the atomisation regime, the tail expansions in the regions of negative velocities and velocities larger than U_{inj} follow a similar trend scaling as $\exp(a \times u_x/\langle u_x \rangle)$ with $|a| = 4$. However, in the second wind induced regime, the left hand tail and the right hand tail present two different scalings: the former scales as $(u_x/\langle u_x \rangle)^7$ and the latter as $(u_x/\langle u_x \rangle)^{-2.5}$. The argument of the increasing relative velocity between the injection and the gas phase, and consequently in the standard deviation, could once again be used to explain the difference in the tail expansion between the two regimes. Finally, complementarily to the sharp peak for zero velocities, the axial velocity PDF is centered on $u_x/\langle u_x \rangle = 1$ in the second wind induced regime and presents a continuous decrease scaling as $\exp(-0.7 \times u_x/\langle u_x \rangle)$ in the atomisation regime. The specific characteristics of the velocity PDF, $u_x < 0$ and $u_x \geq U_{inj}$, are explored in Sec. 4.4.1.

4.3.5 Modeling the droplet size PDF

When it comes to modeling the distribution of the droplet size, one theoretical distribution is necessary to test: the Γ law derived from the ligament-mediated fragmentation framework (Villermaux, 2020) along with its refinement exposed by Kooij *et al.* (2018), here after denoted f_Γ and $f_{\Gamma B}$. While the former was specifically designed to describe the droplet size PDF resulting from the breakup of a ligament, the latter was designed to describe the size PDF resulting from the overall fragmentation of a jet. A previous study carried out by Vallon *et al.* (2021) highlighted the limits of those two distributions for modelling size PDF far away from the nozzle, $x/d_n \in [400, 800]$ in the context of agricultural like sprays, and the satisfying performance of the law derived by Novikov & Dommermuth (1997) in the framework of turbulence intermittency, denoted f_ϵ in the following. More details about each law and the related framework are given in Vallon *et al.* (2021). The three theoretical laws write as follow:

$$f_\Gamma : \quad \mathcal{P}(x = d/\langle d \rangle) = \frac{n^n}{\Gamma(n)} x^{n-1} e^{-nx}, \quad (4.16)$$

$$f_{\Gamma B} : \quad \mathcal{P}(x = d/\langle d \rangle) = \frac{2(mn)^{(m+n)/2} x^{(m+n)/1-1}}{\Gamma(m)\Gamma(n)} \mathcal{K}_{m-n}(2\sqrt{nm}x), \quad (4.17)$$

$$f_\epsilon : \quad \mathcal{P}(y = -\ln(l/l_1)) = \frac{a^{3/2}}{\sqrt{2\pi}\sigma y^{3/2}} \exp\left\{-\frac{a}{2\sigma^2} (ay^{-1/2} - y^{1/2})^2\right\}, \quad y \geq 0. \quad (4.18)$$

In the expression of f_Γ , ν represents the corrugations of a ligament before its breakup, corrug-

Regime	f_Γ			$f_{\Gamma B}$				f_ϵ			
	C	ν	r^2	C	m	n	r^2	C	a	σ	r^2
SWI	0.704	0.932	0.919	0.741	2.513	2.513	0.998	0.751	0.921	1.111	0.829
ATO	0.594	1.269	0.930	0.660	2.411	2.411	1.007	0.670	1.058	0.670	0.927

Table 4.7: Final parameters and r^2 , truncated at the third decimal, for the best fits given by f_Γ , $f_{\Gamma B}$ and f_ϵ at $t/T_a = 15$. The abbreviations ATO and SWI stand for atomisation and second wind induced.

gations which determine the size PDF resulting from the breakup (Villermaux *et al.*, 2004). The same logic takes place in the expression of $f_{\Gamma B}$. Additionally, the ligaments can show a large variety of sizes in the flow. This variety is taken into account by m which sets the order of the ligament size distribution (Kooij *et al.*, 2018). Finally, the expression is conditioned by the modified Bessel function of the second kind \mathcal{K} whose order is set by m and n . Regarding f_ϵ , Novikov & Dommermuth (1997) considered a cascade mechanism and the ratio between the initial size l_1 and the resulting size l of a fragmenting droplet where $a = \langle y \rangle$ and $\sigma = \langle (y - a)^2 \rangle$. It is worth noting that, even if f_ϵ relies on the cascade concept initially derived by Richardson (1922) and used in the seminal papers of Kolmogorov (1941a,c), the infinitely divisible nature of this distribution ensures that it is at no point close to a logarithmic normal distribution resulting from the Central Limit Theorem, see Sec. 1.5.1.1.

A systematic fit campaign is carried out to test the three distributions using the fitting algorithm of the EZYFIT toolbox developed by Moisy (2020) on MATLAB. This algorithm is said to be able to capture a given signal with a reference function when the parameters are set with initial values of the same order as the final values. Thus, the space of initial values has to be explored sufficiently to ensure that the optimum set of parameter values is captured for each theoretical distribution. To do so, the fit campaign is performed in two phases. In the first phase, 23 combinations of initial values are explored in linear and logarithmic modes, i.e. fitting the signal or its logarithmic transform. In the second phase, the best fits in each fitting mode and at the two time instants $t/T_a = \{15, 25\}$ are selected and tested a second time in order to improve the fit quality. Even if $\mathcal{P}_{d/\langle d \rangle}$ shows several modes in the second wind induced regime, the fit of the size distribution is carried out for the main mode only, i.e. with only one theoretical distribution at a time. Finally, each theoretical PDF is weighted by a coefficient C which is let free in the fitting algorithm. Generally speaking, a fit shows a good agreement with a given signal when the Pearson coefficient r is close to 1. One can also use r^2 as a more discriminating criterion. Figure 4.13 gives the best fits produced by f_Γ , $f_{\Gamma B}$ and f_ϵ in both fragmentation regimes at the time instant $t/T_a = 15$ while Table 4.7 gives the corresponding final parameters and r^2 .

Qualitatively, the three theoretical distributions capture well the size PDF in both regimes and describe with a good accuracy the right hand tail on the available range of sizes. No relevant comment can be drawn about the left hand tail as no physical droplet sizes are available in the DNS, see Sec. 4.3.3, and this range was discarded in the fit procedure. The light differences between the distributions then mainly lie in the description of the main mode. In both regimes, f_ϵ performs slightly better in capturing the main mode and the short left hand tail. Quantitatively, the values of r^2 bring a sharp light on the performance of each theoretical distribution. For both regimes, the law exposed by Kooij *et al.* (2018) shows r^2 values the

closest to 1 with a mean computed over the two better fits equal to 1.00025. Then follows the Γ law and the distribution derived by Novikov & Dommermuth (1997) with mean r^2 values respectively equal to 0.9245 and 0.878. Thus $f_{\Gamma B}$ better describes the size PDF in the flow region under consideration, close to the nozzle. Meanwhile f_ϵ shows a correct performance close to the nozzle, which completes its good performance for describing multimodal size PDF far away from the nozzle in the second wind induced regime (Vallon *et al.*, 2021).

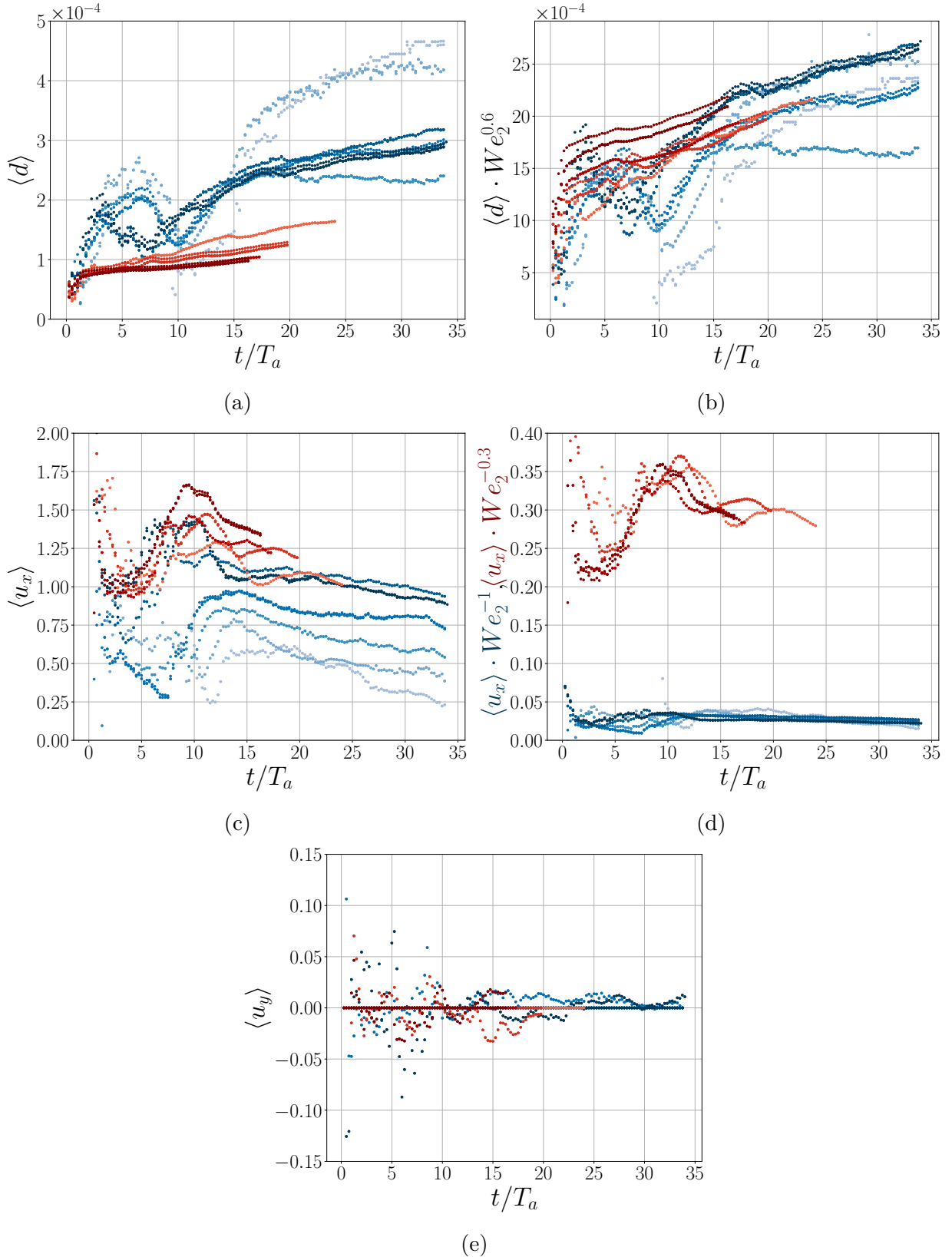


Figure 4.9: Temporal evolution of the mean $\langle \cdot \rangle$, unscaled (left) and scaled by We_2 (right) of the droplet size d (a,b), the axial velocity u_x (c,d) and the transverse velocity u_y (e). The units of the variables are the SI base units.

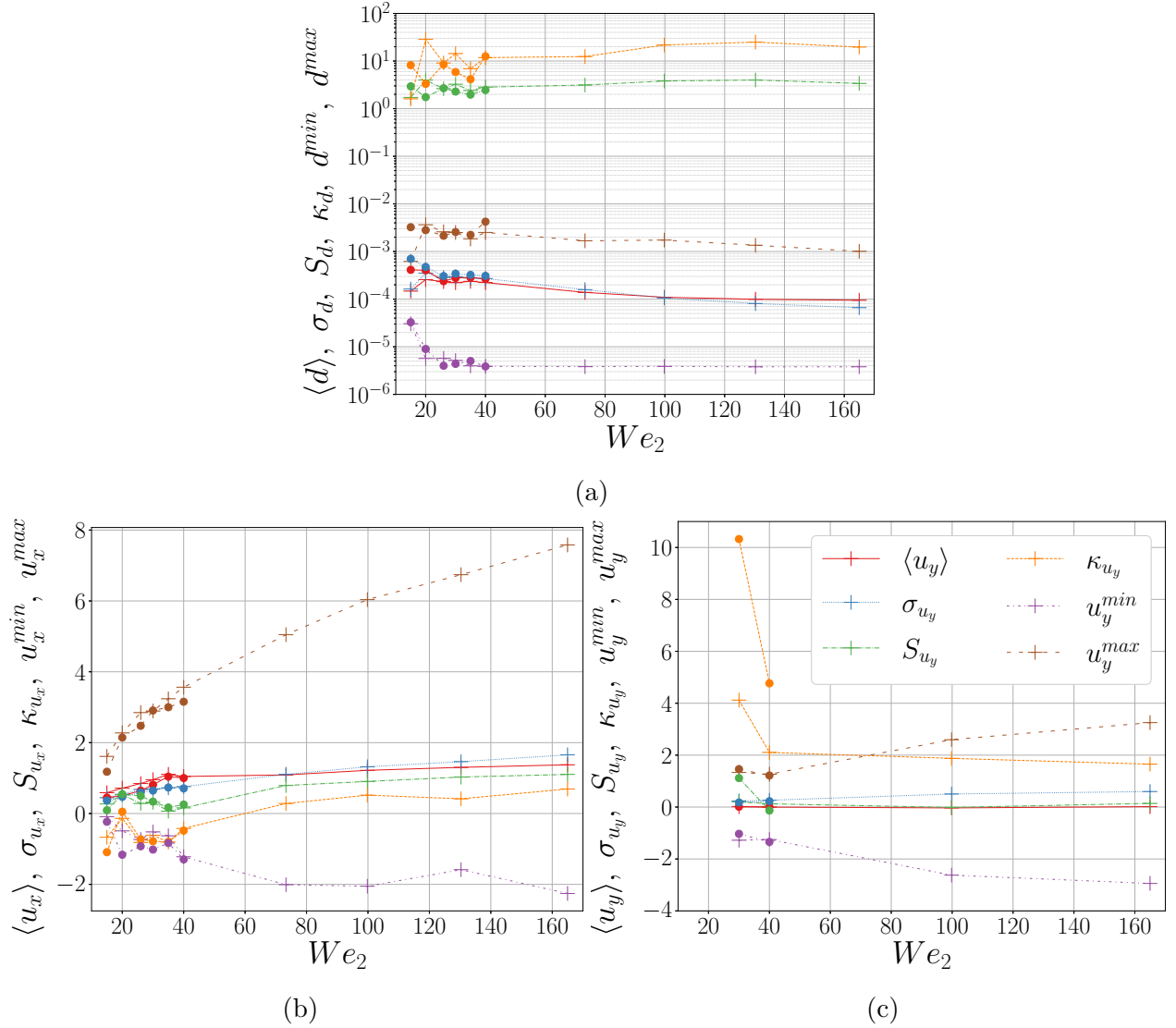


Figure 4.10: Evolution of $\langle \cdot \rangle$ (red), σ (blue), S (green), κ (orange), the minimum (purple) and maximum (brown) against We_2 for the size d (a), the axial velocity u_x (b) and the transversal velocity u_y (c). The pluses (+) correspond to $t/T_a = 15$ and the bullets (●) to $t/T_a = 25$. Note that S and κ are both dimensionless and that the dimensional variables are expressed with the SI base units.

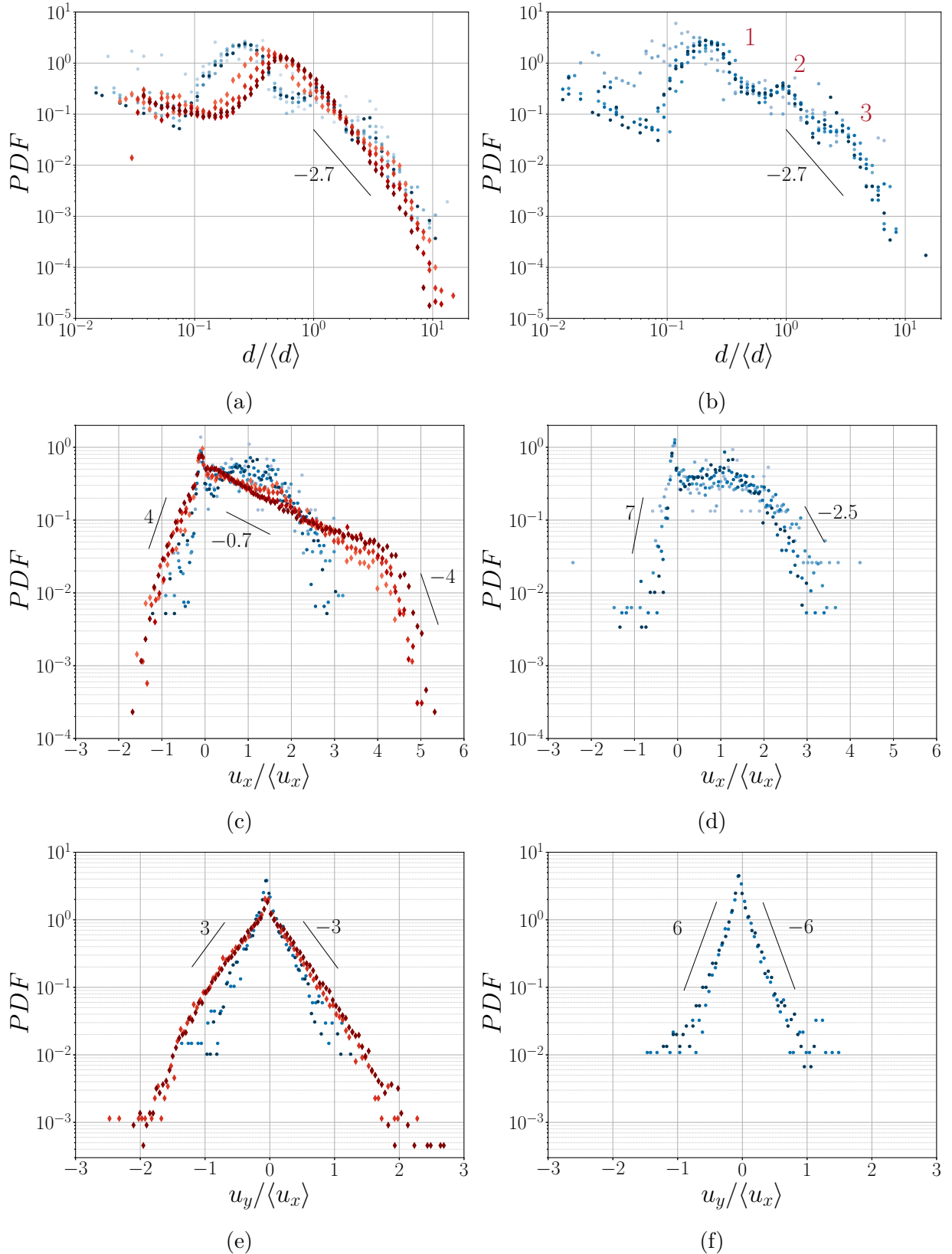


Figure 4.11: Distributions of $d/\langle d \rangle$ (a,b), $u_x/\langle u_x \rangle$ (c,d) and $u_y/\langle u_x \rangle$ (e,f) at $t/T_a = 15$ (left) and $t/T_a = 25$ (right). The blue bullets denote the DNS in the second wind induced regime and the red diamonds the DNS in the atomisation regime.

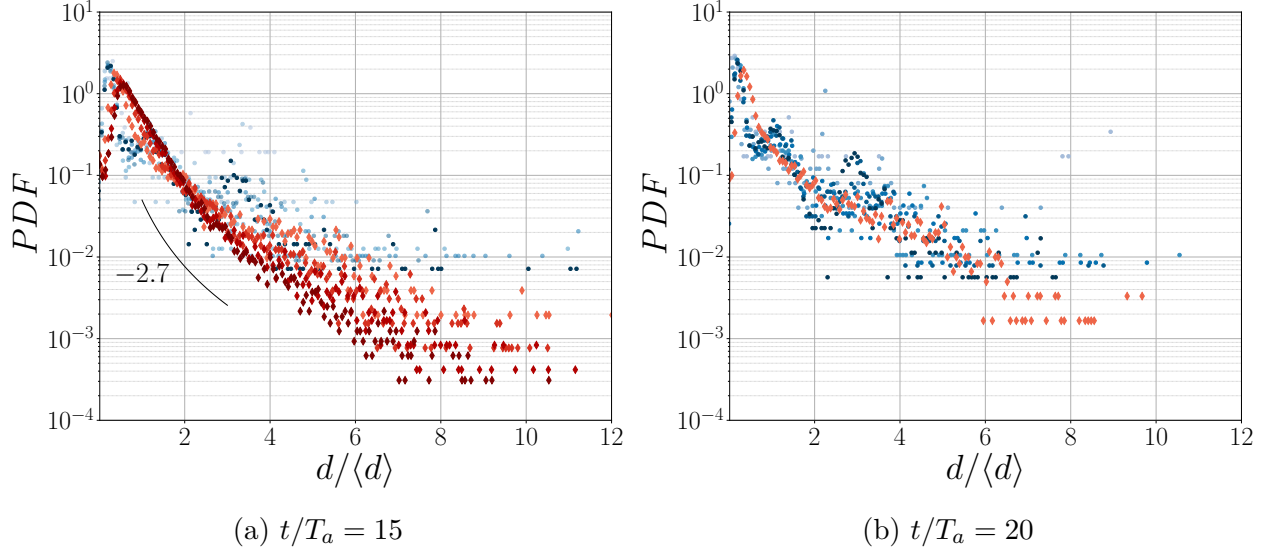


Figure 4.12: Distribution of $d/\langle d \rangle$ in semi-logarithmic scale at $t/T_a = 15$ and $t/T_a = 20$. The blue bullets denote the DNS in the second wind induced regime and the red diamonds the DNS in the atomisation regime. The solid black line corresponds to a power law of coefficient -2.7 , as in Fig. 4.11a and 4.11b.

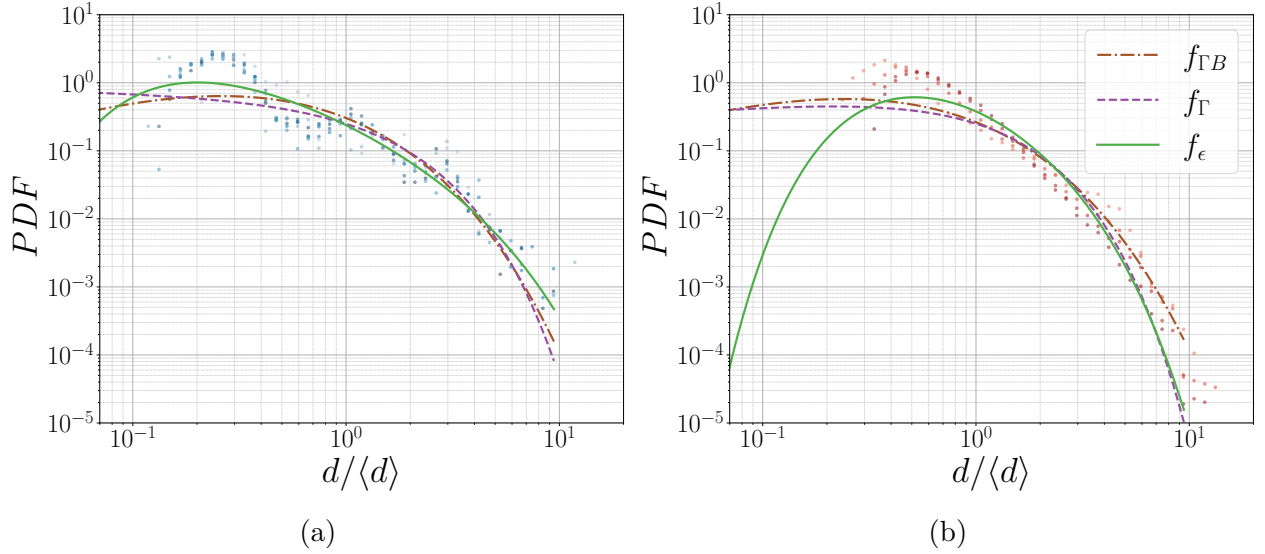


Figure 4.13: Fit of $\mathcal{P}_{d/\langle d \rangle}$ by f_Γ , $f_{\Gamma B}$ and f_ϵ in the second wind induced regime (a) and the atomisation regime (b) at $t/T_a = 15$. The fit procedure is carried on the data shown here and the best fit is represented over $d/\langle d \rangle \in [10^{-2}, 20]$.

4.4 Dynamics of the jet and the droplets: a two speed fragmentation

This section brings explanations about the specific features of the PDF of the droplet axial velocity in connection with the vortex ring theory and about the joint distribution of the droplet size and velocity. It also analyses the repartition of the droplets in the Reynolds - Ohnesorge phase space as well as compares it to the experiments. The section finally concludes on the drift velocity between the gas and liquid phases.

4.4.1 The axial velocity PDF and the jet head vortex ring

The analysis of the distribution of the axial velocity of the droplets in Sec. 4.3.4 highlighted the existence of droplets showing negative velocities and velocities larger than U_{inj} , two seldom features for a jet fragmentation. In order to investigate those two characteristics, it could be interesting to have a glance on the spatial repartition of the droplets such that $u_x/U_{inj} < 0$ or $u_x/U_{inj} > 1$. To do so, the cylindrical coordinates $(x/d_n, r/d_n, \theta)$ are preferred to the Cartesian coordinates.

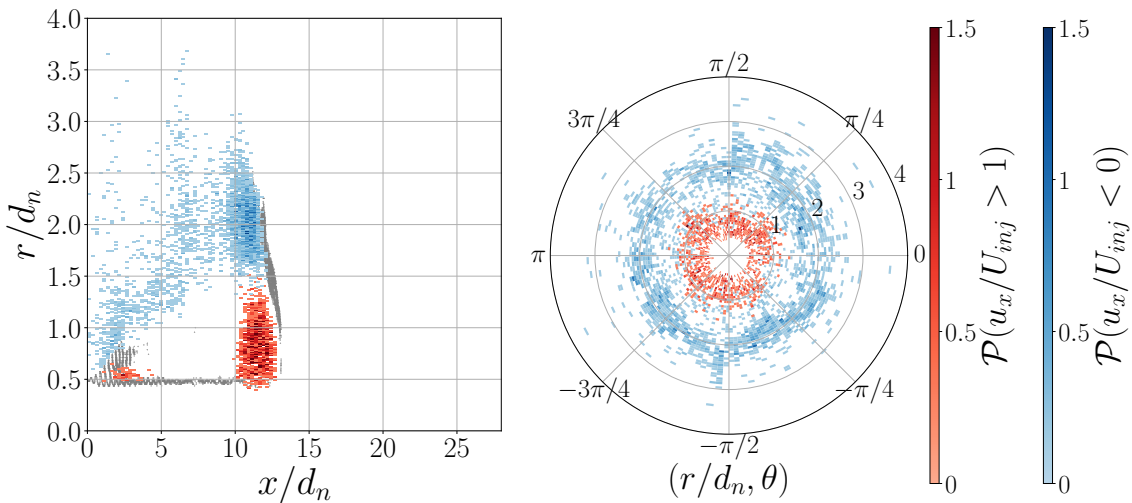


Figure 4.14: Spatial evolution of the probabilities $\mathcal{P}(u_x/U_{inj} < 0)$ and $\mathcal{P}(u_x/U_{inj} > 1)$ for $We_2 = 99.8$ (DNS 8) at $t/T_a = 15$ in cylindrical coordinates $(x/d_n, r/d_n, \theta)$. For each 2D graph, the probabilities are integrated on the third direction. On the $(x/d_n, r/d_n)$, the gray bullets represent the interface points with a presence probability larger than 0.2, i.e the mean jet interface and few droplets. See Sec. 4.3.2 for the computation method for the mean interface.

Figure 4.14 gives the spatial evolution in cylindrical coordinates of the probabilities $\mathcal{P}(u_x/U_{inj} < 0)$ and $\mathcal{P}(u_x/U_{inj} > 1)$. For each 2D graph, the probabilities are integrated on the third direction, e.g. along the θ direction in the $(x/d_n, r/d_n)$ graph. Note that the liquid core starts at $r/d_n = 0.5$ and that the jet extends up to $x/d_n \approx 12.5$. In the $(x/d_n, r/d_n)$ space, the droplets appear to be located in four regions. The ones being faster than U_{inj} are preferentially located next to the nozzle ($0 < x/d_n < 0.5, r/d_n = 0.5$) and at the backside of the jet head up to half of the head sheet extension ($10 < x/d_n < 15, 0.5 < r/d_n < 1.5$). The former are due to the jet forcing. Indeed, the forcing described in Sec. 4.2.3 is sinusoidal with a mean equal to

U_{inj} and some droplets issued from the corolla fragmentation can show velocities larger than U_{inj} . On the other side, the droplets showing negative velocities are preferentially located at the backside of the jet head from the half of the head extension up to its edge and located on a tail expanding over $x/d_n \in [0, 10]$ and $r/d_n \in [0.5, 2.5]$. The negative velocity or the velocity larger than U_{inj} of the droplets located at the downstream face of the jet head can be connected to the recirculation occurring behind it. Finally, the negative velocities along the tail towards $(x/d_n = 0, r/d_n = 0.5)$ can correspond to some droplets ejected from the recirculation region, with r/d_n increasing because of the increasing radius of the jet head in the time range $t/T_a \in [0, 15]$. The spatial repartition in the $(r/d_n, \theta)$ space shows homogeneity along the θ direction and a clear distinction between the two droplet groups along the r direction. The velocities larger than U_{inj} are concentrated in the boundary layer region, $r/d_n \in [0.5, 1]$, while the negative velocities spread over it, $r/d_n \in [1.5, 2.5]$.

Now that the droplets with, at first sight, unexpected axial velocities, $u_x/U_{inj} < 0$ and $u_x/U_{inj} > 1$, are located in the recirculation region behind the jet head, assessing this recirculation would help to explain why such velocities are reached. Looking at the distribution of u_x/U_{inj} is a time saver for this purpose, as it quantifies in a straightforward manner the range of velocities relatively to U_{inj} happening in this region. $\mathcal{P}_{u_x/U_{inj}}$ is given in Figure 4.15 and the ranges of unexpected velocities are $u_x/U_{inj} \in [-0.5, 0]$ and $u_x/U_{inj} \in [1, 1.5]$.

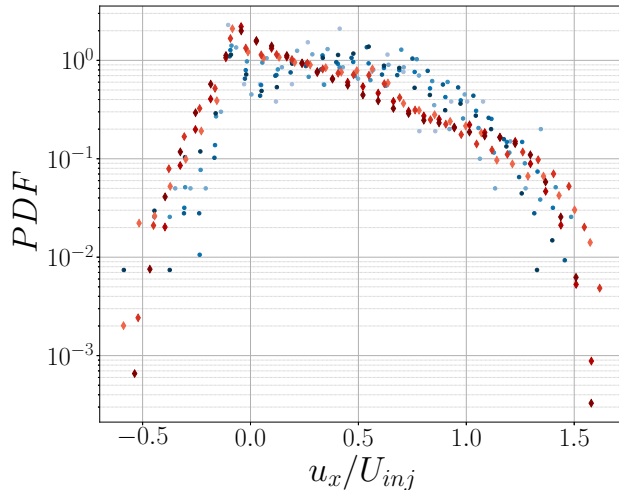


Figure 4.15: Distribution of u_x/U_{inj} at $t/T_a = 15$. The blue bullets represent the DNS in the second wind induced regime and the red diamonds represent the DNS in the atomisation regime.

Assuming that the recirculation observed behind the jet head behaves as a vortex ring behind a plate, it is possible to use the developments of Saffman (1992) which describe the dynamics of such unsteady objects. Let us consider a disc of radius a moving at a velocity U_d in the direction normal to the disc surface, denoted x hereafter, a vortex ring can develop on the downstream face and the velocity potential ϕ on the upstream face follows:

$$\phi = \mp \frac{2U_d}{\pi} \sqrt{a^2 - r^2}, \quad x = \pm 0, \quad y^2 + z^2 = r^2 < a^2 \quad (4.19)$$

If the disc dissolves, the vortex ring remains with a strength $\kappa(r) = 4U_d/\pi \times r/\sqrt{a^2 - r^2}$

and a vorticity $\omega = \kappa\theta\delta(x)$. The amplitudes of the hydrodynamic impulse² I in the x direction and the kinetic energy E are thus:

$$I = \frac{1}{2} \int (\mathbf{x} \times \boldsymbol{\omega})_x dV = \frac{1}{2} \int_0^a 2\pi r^2 \kappa dr = 8U_d a^3 / 3 \quad (4.20)$$

$$E = \frac{1}{2} \int \phi \frac{\partial \phi}{\partial n} dS = 4U_d^2 a^3 / 3 \quad (4.21)$$

In addition, the circulation Γ containing the disc while starting and ending at the disc center is such that:

$$\Gamma = \int_0^a \kappa dr = [\phi]_{r=0} = 4U_d a / \pi \quad (4.22)$$

Let us denote the vortex radius and the vortex core radius R and c and assume the conservation of the ring circulation and the hydrodynamic impulse. Knowing that the hydrodynamic impulse equals $\Gamma\pi R^2$ (Taylor, 1953), the combination of Eqs. (4.20) and (4.22) results in $R = \sqrt{2/3}a$. Further calculations give the expression of the vortex ring velocity U_{vr} and of its energy depending on Γ , R and c :

$$U_{vr} = \frac{\Gamma}{4\pi R} \left[\log \left(\frac{8R}{c} \right) - \frac{1}{2} + \int_0^c \left(\frac{\Gamma(s)}{\Gamma} \right)^2 \frac{ds}{s} + o\left(\frac{c}{R}\right) \right] \quad (4.23)$$

$$E = \frac{1}{2} \Gamma^2 R \left[\log \left(\frac{8R}{c} \right) - 2 + \int_0^c \left(\frac{\Gamma(s)}{\Gamma} \right)^2 \frac{ds}{s} + o\left(\frac{c}{R}\right) \right] \quad (4.24)$$

Combining the latter two equations with Eq. (4.21) enables to express the ratio of the vortex ring velocity U_{vr} along x and the disc velocity U_d :

$$\frac{U_{vr}}{U_d} = \frac{1}{4} + \frac{1}{\pi^2} \left(\frac{3}{2} \right)^{3/2} = 0.44 \quad (4.25)$$

The question of the velocity at the edge of the vortex core remains and is of most importance as it sets the droplet motion in the recirculation region. For a uniform core, c/R equals 0.19 while it equals 0.14 in the case of a hollow core. The velocity at the core edge, denoted u_c , can be expressed as a function of the circulation Γ , $u_c = \Gamma/2\pi c$. Using the expression of Γ given in Eq. (4.22) and $R = \sqrt{2/3}a$, u_c rewrites as:

$$u_c = \left(\frac{c}{R} \right)^{-1} \frac{2}{\pi^2 \sqrt{2/3}} U_d \quad (4.26)$$

With $c/R = 0.19$ and $c/R = 0.14$, u_c respectively equals $1.31 U_d$ and $1.77 U_d$. Taking $c/R = 0.165$, the mean value between 0.19 and 0.14, $u_c = 1.504 U_d$. In our flow, the jet head can be approximated as a disc behind which a vortex ring develops. Experimentally, we observed that the jet head has the same velocity as U_{inj} , $U_d = U_{inj}$. The velocity at the core edge then equals

²The concept of hydrodynamic impulse has a long history in theoretical hydrodynamics having been described by Lamb (1932). The advantage of the theory of hydrodynamic impulse is that it describes the physical origin of hydrodynamic forces and moments in terms of the vorticity generated at the body surface and its subsequent position in the fluid volume (Holloway & Jeans, 2020).

$\pm 1.5 U_{inj}$ and corresponds to the range of unexpected droplet velocities, $u_x/U_{inj} \in [-0.5, 0]$ and $u_x/U_{inj} \in [1, 1.5]$. Thus the negative velocities and velocities larger than U_{inj} result from the vortex ring dynamics taking place at the downstream side of the jet head.

4.4.2 Joint distribution of the droplet size and axial velocity

The fragmentation of a jet or droplets is governed by aerodynamic and surface tension forces. Depending on the equilibrium between those, droplets of a given size and velocity result. Those two quantities influence each other comparably to a two-way coupling mechanism. Thus, looking at the joint distribution of the size and the axial velocity could bring extra information to the analysis of the marginal PDF $\mathcal{P}_{d/\langle d \rangle}$ and $\mathcal{P}_{u_x/\langle u_x \rangle}$. Figure 4.16 gives the joint distribution of $d/\langle d \rangle$ and $u_x/\langle u_x \rangle$ for the DNS 6 and 9 respectively, in the second wind induced regime and the atomisation regime.

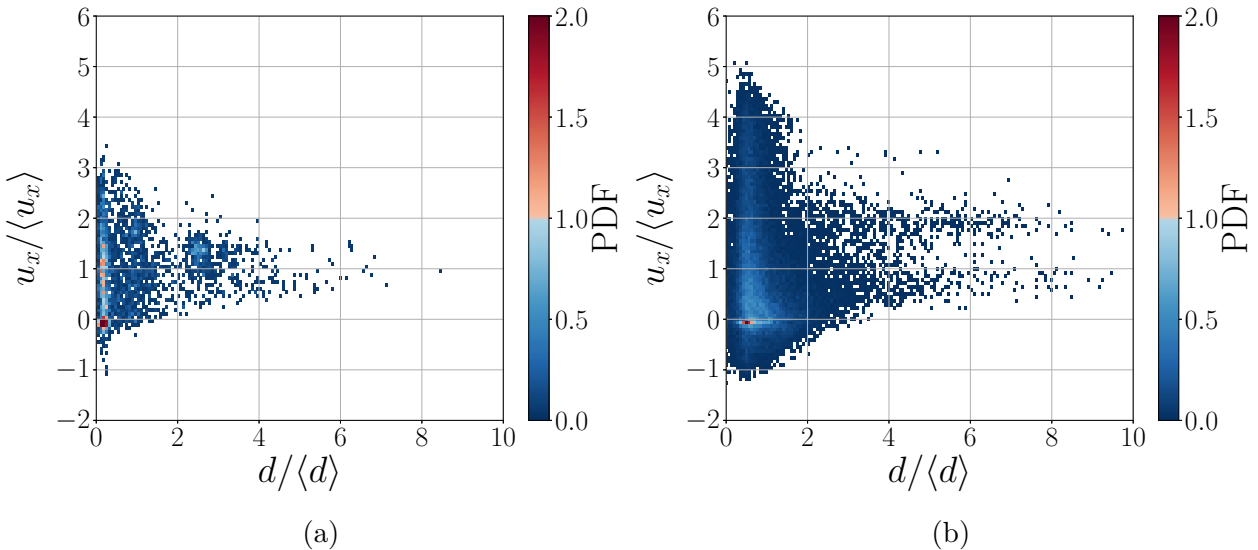


Figure 4.16: Joint distributions of the size and the axial velocity of the droplets for (a) $We_2 = 40$ (DNS 6) in second wind induced regime at $t/T_a = 30$ and for (b) $We_2 = 130.3$ (DNS 9) in atomisation regime at $t/T_a = 15$.

It is possible to recover the characteristics of the marginal PDF in the joint distributions. For instance, in the joint distribution of the DNS 6, three patches are noticeable along the size axis and correspond to the three modes of $\mathcal{P}_{d/\langle d \rangle}$ for which $d/\langle d \rangle \in \{0.2, 1, 2.5\}$. In addition, the negative velocities and velocities larger than U_{inj} described in Sec. 4.3.4 and explained in Sec. 4.4.1 are also noticeable. Observing so is expected as the marginal PDF are simply the projection of the joint PDF on the size or the velocity axes.

In the second wind induced regime, the negative axial velocities and the velocities larger than U_{inj} are preferentially observed for the first two size modes while the third size mode is concentrated around ($d/\langle d \rangle = 2.5, u_x/\langle u_x \rangle \approx 1.5$) and the tail, starting from $d/\langle d \rangle \approx 3$, seems to be centered on $u_x/\langle u_x \rangle = 1$. Globally, the smaller droplets appear to have, at the same time, a dispersion being large along the velocity axis and being short on the size axis. Conversely, the larger droplets show a large dispersion along the size axis and a short one along the velocity axis. This corresponds to the literature and the common behaviors of tracers and ballistic objects which are classically observed. In comparison, even if tracers and ballistic objects are

visible as well, the aspect of the joint distribution in the atomisation regime is different. Once again, the negative velocities and the velocities larger than U_{inj} are preferentially observed for the smaller droplets. However, the distribution shows two tails along the size axis, one centered on $u_x/\langle u_x \rangle \approx 0.75$ and the second one centered on $u_x/\langle u_x \rangle \approx 2$. Thus, the smaller and larger droplets still respectively behave like tracers and ballistic objects, but the ballistic objects show two traveling velocities. Conversely to the experimental observations (Vallon *et al.*, 2021), the joint distributions do not show a clear elbow shape. Also, drawing a third group of droplets showing a similar dispersion along the size and velocity axes, as in the experimental analysis, seems less manifest here. Such a group could be extrapolated from the joint distribution and the second size mode, $d/\langle d \rangle = 1$, in the second wind induced regime and for $d/\langle d \rangle \in [1.5, 2.5]$, while the velocity spans over $u_x/\langle u_x \rangle \in [0, 2]$ in both cases.

Similarly to Sec. 4.4.1, it is possible to check out the spatial repartition of the droplets corresponding to the tail of the joint distribution $\mathcal{P}_{(d/\langle d \rangle, u_x/\langle u_x \rangle)}$ of the DNS 9 in the atomisation regime. Those droplets are such that $d/\langle d \rangle > 4$ and are distinguished by their axial velocity being larger or smaller than $1.5\langle u_x \rangle$. Likewise the PDF of the axial velocity of the droplets, the joint distribution shows the same feature for the larger droplets for all the DNS in the atomisation regime. Once again, it is more practical to express the conditions on the size and the velocity independently from the arithmetic average but relatively to the injection conditions. Thus, the condition on the size writes as $d/d_n > 0.075$ and $0.4 U_{inj}$ is considered to be the threshold to distinguish the two tails. Figure 4.17 gives the spatial evolution in cylindrical coordinates of the probabilities $\mathcal{P}(d/d_n > 0.075, u_x/U_{inj} < 0.4)$ and $\mathcal{P}(d/d_n > 0.075, u_x/U_{inj} > 0.4)$. As for Figure 4.14, the liquid core starts at $r/d_n = 0.5$ and the jet extends up to $x/d_n \approx 12.5$. The droplets from each tail appear to exist in specific regions of the space. The large, fast droplets for which $d/d_n > 0.075$ and $u_x/U_{inj} > 0.4$ are preferentially located in the boundary layer region, $r/d_n \in [0.5, 1]$, from the nozzle to the jet head. The large, slow droplets for which $d/d_n > 0.075$ and $u_x/U_{inj} < 0.4$ are located on the downstream side of the jet head and around the maximal head sheet extension. The two groups show some overlapping in the recirculation region. It is possible that some droplets are caught in the vortex circulation, even if they preferentially behave as ballistic objects. In the $(r/d_n, \theta)$ space, the distributions are homogeneous along the azimuthal axis, which respects the flow symmetry, and the same repartition along the r/d_n axis appears between the two groups. Thus, the two tails of the joint distribution of the size and the velocity come from the existence of two sources of fragmentation in the flow: the head sheet edge and the corollas developing from the jet forcing.

4.4.3 Governing parameters at the droplet scale

The joint distribution of the size and the axial velocity of the droplets give some insights on the droplet dynamics in the flow. However, compared with the experiments, the numerical distributions show a slightly more complex trend and do not allow to distinguish droplets with different behaviors on the basis of the marginal PDF characteristics. Beyond this, it would be interesting to have a glance on the flow perceived by a droplet as well as the droplet deformation resulting from the droplet-flow interaction. Without detailing the flow around each droplet down to the smallest scales, it is possible to characterize such a flow by considering its governing parameters, the particulate Reynolds number and the particulate Ohnesorge number respectively expressed as:

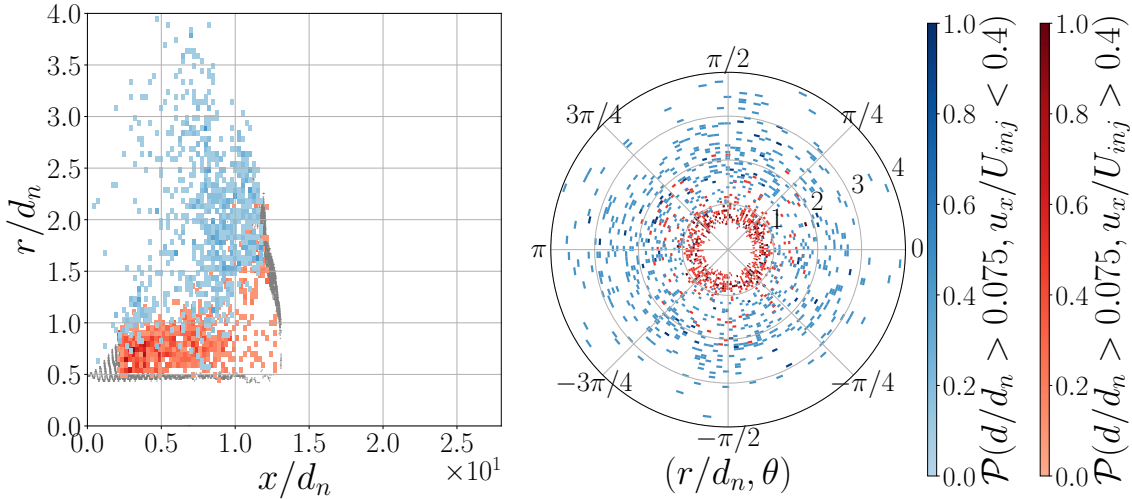


Figure 4.17: Spatial evolution of the probabilities $\mathcal{P}(d/d_n > 0.075, u_x/U_{inj} < 0.4)$ (blue) and $\mathcal{P}(d/d_n > 0.075, u_x/U_{inj} > 0.4)$ (red) for $We_2 = 99.8$ (DNS 8) at $t/T_a = 15$ in cylindrical coordinates. For each 2D graph, the probabilities are integrated on the third direction. On the $(x/d_n, r/d_n)$ graph, the gray boundary represents the interface points with a presence probability larger than 0.2, i.e the mean jet interface and few droplets. See Sec. 4.3.2 for the computation method of the mean interface.

$$Re_p = \frac{|u_{p,x} - U_{g,x}|d}{\nu_l}, \quad Oh_p = \frac{\mu_l}{\sqrt{\rho_l \sigma d}} \quad (4.27)$$

where d , $u_{p,x}$ and $|u_{p,x} - U_{g,x}|$ are the particle diameter, the particle axial velocity and its relative velocity compared to $U_{g,x}$, the x component of the gas phase velocity averaged over the domain. The particulate Reynolds number not only brings light on the balance between the inertial and viscosity forces at the scale of a droplet but it also brings information on the product of the droplet relative velocity and its diameter. By concatenating the size and the velocity of a droplet, the latter quantity could be seen as a potential of fragmentation. The higher the product $d \cdot |u_{p,x} - U_{g,x}|$ is, the more likely the droplet will fragment in multiple elements. It also enables to distinguish the droplet-flow interactions between droplets having the same size but different relative velocities, or equivalently having the same relative velocity and different sizes. In addition, the particulate Ohnesorge number characterizes the ratio between the viscosity forces and the product of the inertial and surface tension forces. This dimensionless number is usually used to characterize droplet deformation in a given flow. The larger is Oh_p , the less deformable is the droplet. Thus, even if they give global information on the droplet-scale flow, the combinations of Re_p and Oh_p could help to characterize the droplet behaviors depending on their possible deformation and potential of fragmentation. Figure 4.18 gives the normalised joint volume histogram of Re_p and Oh_p of the droplet population of the DNS 6 and 10 respectively at $t/T_a = 30$ and $t/T_a = 15$.

First of all, the Oh_p values larger than $Oh_{\Delta_{min}}$ correspond to the droplets smaller than the smallest cell size Δ_{min} and are not physically relevant. Considering the pair (Re_p, Oh_p) reshapes drastically the droplet data. Regarding the DNS 10, the two peaks present for the large sizes as well as the peaks around large velocities and negative velocities for the small sizes in Fig. 4.16 do not appear any more in the joint volume histogram of the particulate dimensionless numbers.

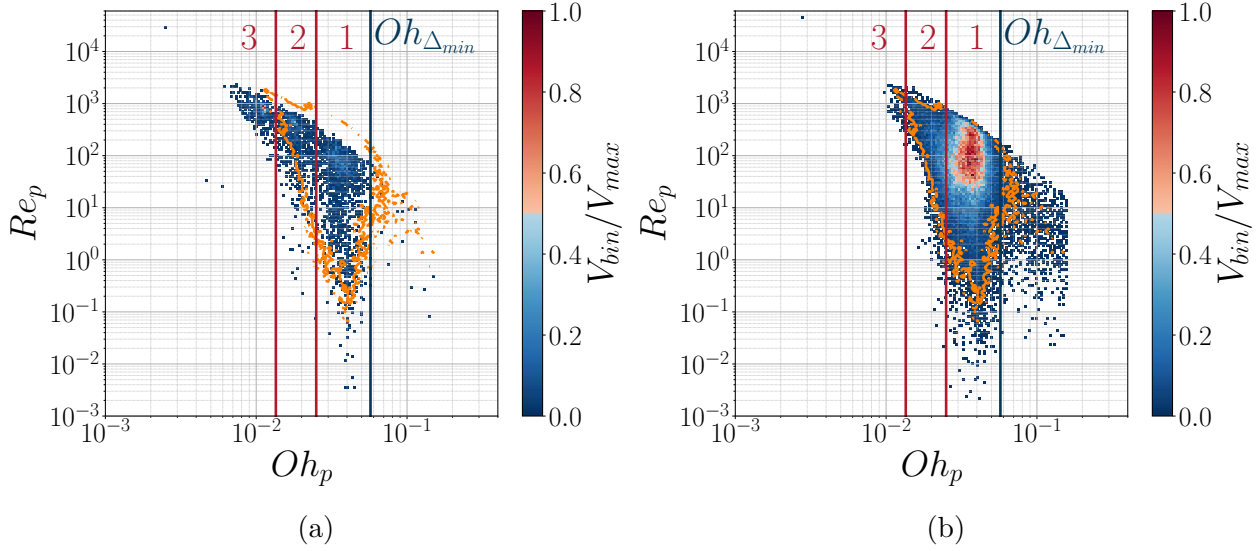


Figure 4.18: Joint volume histogram of Re_p and Oh_p for the droplet population for $We_2 = 40$ (DNS 6) at $t/T_a = 30$ (a) and for $We_2 = 165$ (DNS 10) at $t/T_a = 15$ (b). The Ohnesorge number corresponding to the smallest grid cell, $Oh_{\Delta_{min}}$, is indicated by the vertical blue line. The vertical red lines indicate the limits between the 3 modes of the size PDF of the DNS 6, Fig. 4.11b. The orange line represents the isovalue $V_{bin}/V_{max} = 0.03$ for the DNS 10.

In addition, while the trend of the size-velocity joint distributions are significantly different between the two fragmentation regimes, the limits of the joint volume histogram appear not only to be regular but also follow similar trends between the two fragmentation regimes, as shown by the comparison of the joint histogram of the DNS 6 and the edge contour of the DNS 10. Regarding the histogram values, different modes appear in the joint histogram of each DNS. For the DNS 6, in the second wind induced regime, it is possible to denote the three size modes, observed in Sec. 4.3.4, denoted from 1 to 3 and separated at $Oh_p \in \{1.35 \times 10^{-2}, 2.5 \times 10^{-2}\}$ by the red vertical lines. Each droplet group shows some dispersion along the Re_p direction, dispersion which increases when the droplet size decreases. The population thus shows three subgroups whose dynamics seems to mainly be governed by their size. From those three size subgroups, only the modes 1 and 2 remain in the joint volume histogram of the DNS 10, in the atomisation regime. The mode of large sizes, mode 3, does not exist in the atomisation regime because the corolla issued from the forcing cannot develop nor create rim leading to the generation of such droplet sizes. For the latter DNS, the mode 1, existing at large Oh_p and indicated by the red region in Fig. 4.18b, gains in importance and is the main size mode in the atomisation regime, existing for $Oh_p \in [2.5, 5] \times 10^{-2}$ and $Re_p \in [30, 400]$. Additionally, the dispersion of the modes for moderate and small Oh_p increases between the two regimes while respecting the same outer limits, as the droplet data spread over all the space delimited by the edge contour of the DNS 10. Finally, it is worth noting the absence of droplets in the region of large particulate Reynolds and small particulate Ohnesorge, $(Re_p, Oh_p) \in ([10^3, 10^4], [1, 7] \times 10^{-3})$, i.e. droplets whose size and axial velocity are of the order of d_n and U_{inj} .

The comparison of the edge contour of the DNS 10 with the joint volume histogram of the DNS 6 given by Fig. 4.18 suggests that the joint histograms follow similar borders regardless of the fragmentation regime. Figure 4.19 dives in a more detailed comparison of the joint histogram borders by superposing the edges for all the DNS and proposes a normalisation of

the two dimensionless numbers. The edges are obtained by sampling each joint histogram along the Oh_p direction and keeping for each sample the maximum of the ordinates and the ordinate of the percentile at 7 %. This technique enables to discard the outlier points existing at small Re_p . From the edges of the non normalised joint histograms, it appears clearly that the joint histograms evolve in the same phase space for both fragmentation regimes and that the borders only show a slight evolution with the gaseous Weber number We_2 . Note that the isolated points on the top left corner are the Re_p and Oh_p values correspond to the liquid core. Those points depart from Re_1 and Oh_1 because the liquid core has a volume larger than that of a sphere of diameter d_n . As a reminder, the injection dimensionless numbers are given Table 4.2

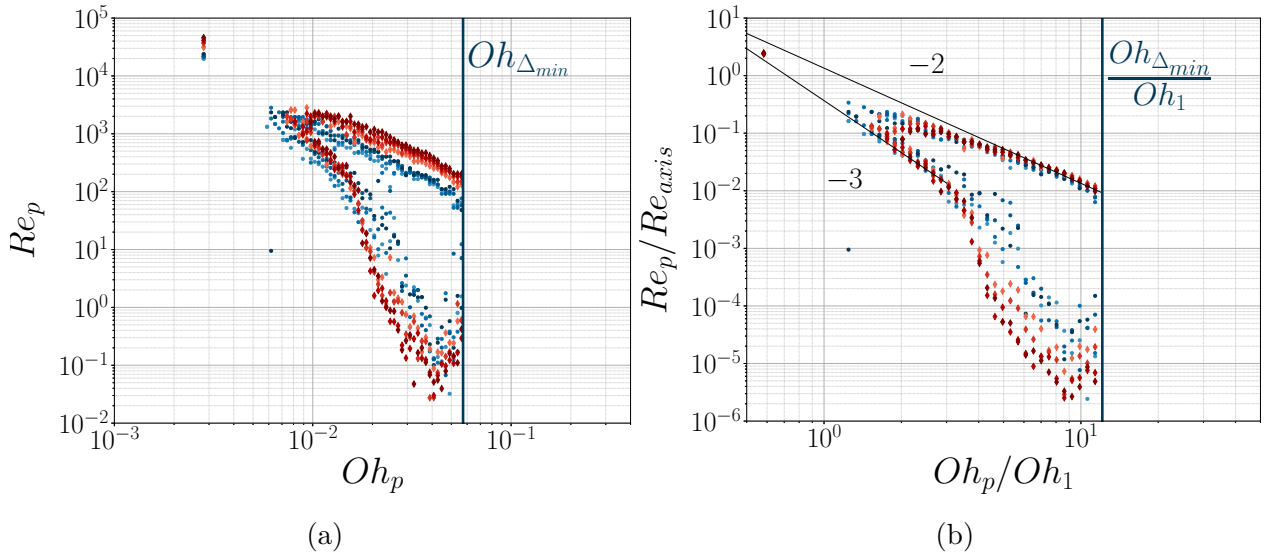


Figure 4.19: Edges of (a) the joint volume histograms and of (b) the normalised joint volume histograms at $t/T_a = 15$. The blue bullets represent the DNS in the second wind induced regime and the red diamonds the DNS in the atomisation regime.

In order to normalise Re_p and Oh_p , one can choose the Reynolds number on the jet axis Re_{axis} , computed with the nozzle diameter d_n and $u_{x, axis}$ the jet velocity on the x axis, and the injection Ohnesorge number Oh_1 computed with d_n . In our simulation, the velocity of the jet along the x -axis does not show any diminution, thus $u_{x, axis} = U_{inj}$ and $Re_{axis} = Re_1$. Making the distinction between the injection velocity and the jet velocity on the axis might appear auxiliary here but is relevant for comparing the numerical data with the experiments. Once normalised, all the upper borders and the lower borders of the joint histograms collapse. Not only those borders collapse but also show a power law dependency. The former scales such that $Re_p/Re_{axis} = 1.35(Oh_p/Oh_1)^{-2}$ and the latter scales such that $Re_p/Re_{axis} = 0.37(Oh_p/Oh_1)^{-3}$. The collapse however does not hold for the lower borders on the range $Oh_p/Oh_1 \in [4, 10]$, which could simply result from the difference in the relative velocity and the extreme values along the Re_p axis. Additionally, not only the isolated points corresponding to the liquid core collapse, but also they lie within the space delimited by the two power laws. Thus, a more developed spray in the same configuration could show a phase space delimited by those power laws and spreading from the liquid core towards the smallest droplets. Finally, as all the contours collapse in Fig. 4.19b, it could be possible to add that this cascade in the phase space ($Re_p/Re_{axis}, Oh_p/Oh_1$) is independent from the gaseous weber number We_2 .

Overall, the comparison of the joint volume histogram in the second wind induced regime, DNS 6, and in the atomisation regime, DNS 10, indicates that the dominant modes of the droplet population evolve with We_2 . Particularly, the mode for small Oh_p , i.e. large droplet sizes, does not exist in the atomisation regime. Also, the atomisation regime presents a larger dispersion in Oh_p and Re_p . This is expected as the increase in We_2 creates aerodynamic conditions in which large droplets are very unlikely to survive, or even be generated, and the increase of the relative velocity between the gas and the liquid induces an increase of the deviation of the size and the axial velocity, see Sec. 4.3.4. This analysis highlights the possibility to reshape the size and velocity data of the droplets into a regular shape even if the size-velocity joint distribution shows irregular boundaries and specific features. Additionally, it indicates that the values of the joint histogram of the particulate dimensionless numbers evolve with We_2 while respecting outer borders which are largely independent from We_2 . Normalising the particulate dimensionless numbers by the injection dimensionless numbers shows that the droplets exist over a steady phase space, delimited by power and exponential laws. Finally, this joint volume histogram opens the way for qualifying the different flow regimes undergone by the droplets and the consequent fragmentation mechanisms.

4.4.4 Droplet phase space: simulations and experiments

Vallon *et al.* (2021) proposed, among others, a detailed analysis of the experimental joint distribution of the size and axial velocity of the droplets in the case of a water jet injected into quiescent air at $We_2 = 24$ and lying in the second wind induced regime. The experimental apparatus used to perform simultaneous measurements of the size and the velocity of the droplets is detailed by Felis *et al.* (2020). The originality of that experimental campaign lies in the simultaneity of the DTV measurements and the distance where they were carried out: from 400 to 800 nozzle diameters along the jet axis. Complementarily, and following the insights of Sec. 4.4.3, it is possible to look at the experimental joint volume histogram of the particulate Reynolds and Ohnesorge numbers. Figure 4.20 gives the joint volume histogram for Re_p/Re_{axis} and Oh_p/Oh_1 derived from the experimental measurements of Felis *et al.* (2020). Note that the mean velocity of the liquid phase on the jet axis $u_{x, axis}$ is no longer equal to the injection velocity at such x/d_n but decreases by 20% at $x/d_n = 800$.

Once again, the borders of the joint volume histogram are well defined and can be easily modelled. The upper and lower borders split into two scalings. For $Re_p/Re_{axis} \geq O(10^{-3})$, the borders follow a power law while they follow an exponential scaling for smaller values of Re_p/Re_{axis} . The upper and lower borders are respectively denoted \mathcal{B}_{up} and \mathcal{B}_{low} and their scaling is such that:

$$\mathcal{B}_{up} : \begin{cases} \frac{Re_p}{Re_{axis}} = 0.215 \left(\frac{Oh_p}{Oh_1} \right)^{-2}, & \forall Oh_p/Oh_1 \in [1, 10] \\ \frac{Re_p}{Re_{axis}} = \exp \left(-0.1 \left(\frac{Oh_p}{Oh_1} + 45.1 \right) \right) - 1.90 \times 10^{-3}, & \forall Oh_p/Oh_1 \in [10, 20] \end{cases} \quad (4.28)$$

$$\mathcal{B}_{low} : \begin{cases} \frac{Re_p}{Re_{axis}} = 0.215 \left(\frac{Oh_p}{Oh_1} \right)^{-2.61}, & \forall Oh_p/Oh_1 \in [1, 3] \\ \frac{Re_p}{Re_{axis}} = \exp \left(-0.6 \left(\frac{Oh_p}{Oh_1} + 3.65 \right) \right) - 6.5 \times 10^{-3}, & \forall Oh_p/Oh_1 \in [3, 5] \end{cases} \quad (4.29)$$

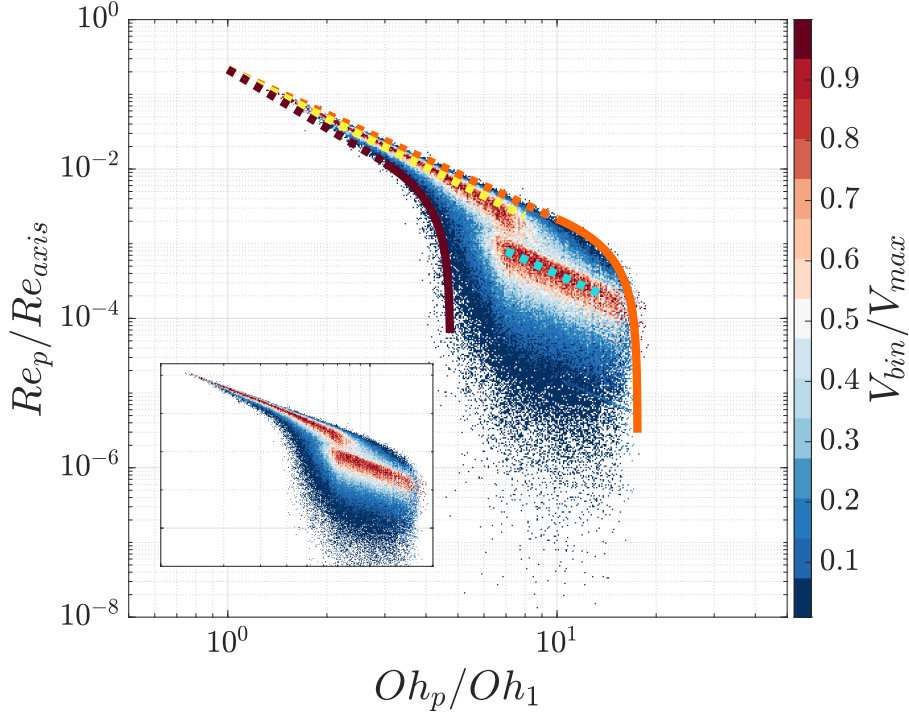


Figure 4.20: Experimental joint volume histogram of Re_p/Re_{axis} and Oh_p/Oh_1 at $x/d_n = 800$. The dash-dot lines represent the power law scalings while the solid lines represent the exponential scalings. The insert recalls the joint volume histogram without the modelled borders.

Note that, for a given value of Oh_p , the upper border describes the fastest droplets at a given size while, for a given value of Re_p , it describes the smallest droplets at a given velocity. Thus, the upper border can be seen as the border describing the smallest and fastest droplets in a given region of the phase space, the reverse logic holds for the lower border. Additionally, two main “paths” can be distinguished in the joint histogram. The first one lies in the power law region and the second one in the exponential region, respectively denoted \mathcal{P}_1 and \mathcal{P}_2 , both of them follow a power law scaling such that:

$$\begin{aligned} \mathcal{P}_1 : \frac{Re_p}{Re_{axis}} &= 0.215 \left(\frac{Oh_p}{Oh_1} \right)^{-2.175}, \quad \forall Oh_p/Oh_1 \in [1, 7] \\ \mathcal{P}_2 : \frac{Re_p}{Re_{axis}} &= 0.039 \left(\frac{Oh_p}{Oh_1} \right)^{-2}, \quad \forall Oh_p/Oh_1 \in [7, 14] \end{aligned} \quad (4.30)$$

Let us focus on the borders scaling as a power law. Starting from the expression of Oh_p , it is possible to rewrite Re_p as $Re_p = \sigma^{-1} \mu_l |u_{p,x} - U_{g,x}| Oh_p^{-2}$. Knowing that in this region $Re_p = C Oh_p^{-2-\alpha}$ with $C \in \mathbb{R}$, we then have $|u_{p,x} - U_{g,x}| = \sigma C Oh_p^{-\alpha}$, which is equivalent to $|u_{p,x} - U_{g,x}| \propto d^{\alpha/2}$. The droplets then show a velocity relative to the gas phase which increases with the droplet size. The coefficient α necessarily lies in \mathbb{R}^+ . Indeed a negative α would mean that the relative velocity of a droplet decreases when its size increases and consequently that larger objects would be more sensitive to the gas phase flow, which goes against the observation of ballistic objects in fragmentation flows. Consequently, the borders scaling as Oh^{-2} seem to result from dynamical limits. Regarding the lower border scaling as a power law, we have $\alpha \in \{0.4, 0.45, 0.5, 0.56, 0.61\}$ for $x/d_n \in \{400, 500, 600, 700, 800\}$. Inferring a rule on the evolution of the upper bound of α from the experimental data seems reckless.

Regarding the exponential scaling of the borders, it is interesting to note the existence of an offset along Oh_p and Re_p . The droplets being on the upper border preferentially have a smaller size and a larger relative velocity while those on the lower border have a larger size and a smaller relative velocity. In order to have all the droplets lying in a stable configuration, which corresponds to the region where $Re_p < O(10^{-3})$, the difference in the droplet dynamics has to be accounted for. This is what the offsets along Oh_p and Re_p in the exponential scaling enable to do.

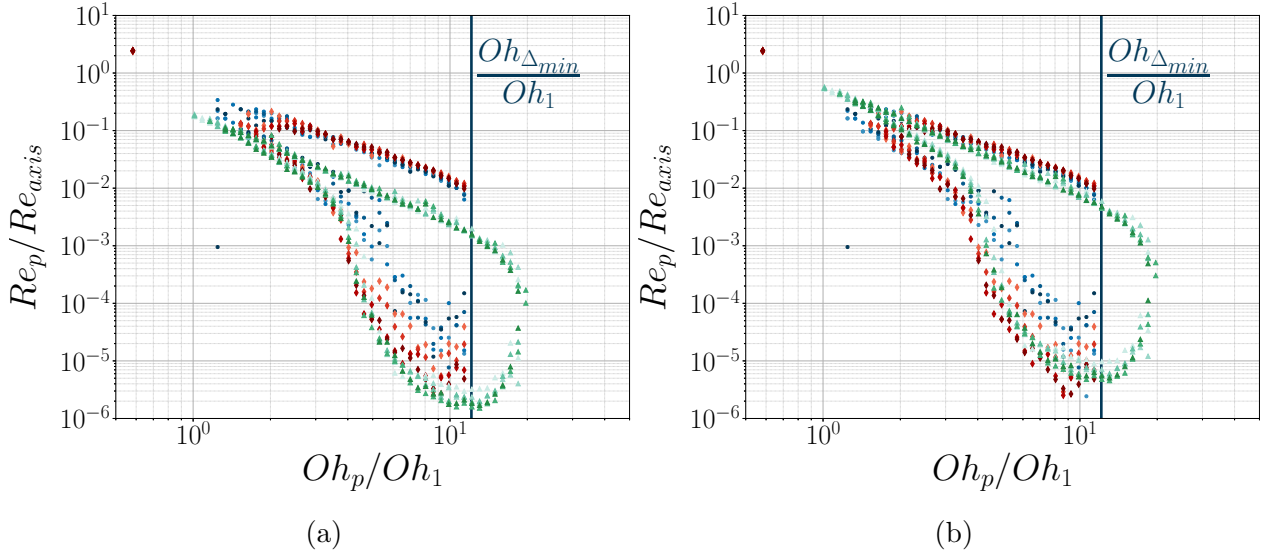


Figure 4.21: Comparison of the joint volume histograms obtained from the DNS campaign and from the experimental data of Felis *et al.* (2020), not corrected (a) and corrected by a multiplicative factor of 3 (b). The blue bullets and the red diamonds represent the DNS respectively in the second wind induced regime and the atomisation regime. The green triangles represent the experimental data.

Figure 4.21 compares the edge contour of the experimental and numerical joint volume histograms. When comparing the original experimental histograms and the numerical ones, it appears that the phase spaces in which the droplets evolve show ranges of existence being very similar between the experiments and the simulations. Even if an offset along the Re_p axis exists, they lie in the same range of sizes. By multiplying the edge contour of the experimental joint volume histogram by 3, the edges of the numerical and the experimental data collapse. Thus, we have $(Re_p/Re_{axis})_{num} = C \times (Re_p/Re_{axis})_{exp}$, where $C \approx 3$, which leads to:

$$\frac{|u_{p,x} - U_{g,x}|_{num} d_{num}}{|u_{p,x} - U_{g,x}|_{exp} d_{exp}} = C \frac{d_{n,num} u_{x,axis,num}}{d_{n,exp} u_{x,axis,exp}} \quad (4.31)$$

and results to $|u_{p,x} - U_{g,x}|_{num} d_{num} \approx 1.8 |u_{p,x} - U_{g,x}|_{exp} d_{exp}$, with $u_{x,axis,exp} = 0.8 \times U_{inj,exp} = 28 \text{ m/s}$ and $u_{x,axis,num} = U_{inj,num} = 4.5 \text{ m/s}$. The numerical and experimental contours lie in the same range of sizes. Thus, it can be assumed that $d_{exp}/d_{n,exp} \approx d_{num}/d_{n,num}$ which implies:

$$\frac{d_{num}}{d_{exp}} \approx 3.73, \quad \frac{|u_{p,x} - U_{g,x}|_{num}}{|u_{p,x} - U_{g,x}|_{exp}} \approx 0.48. \quad (4.32)$$

The experimental and numerical mean sizes are respectively $\langle d \rangle_{exp} = 95 \mu\text{m}$, averaged over the 5 x/d_n positions, and $\langle d \rangle_{num} \approx 300 \mu\text{m}$, at $t/T_a = 34$ in the second wind induced regime.

The ratio of the means equals 3.16, thus $\langle d \rangle_{num}/\langle d \rangle_{exp} \approx d_{num}/d_{exp}$ and verifies the previous result. The interpretation of the last three ratios must be made carefully. On the one hand, the way the measurements of the size and the velocity of the droplets is carried out greatly differs between the experiments and the simulations. In the simulations, once a droplet is detected thanks to the tag function of Basilisk, see Sec. 4.2.2, its volume and velocity are computed as the volume average in 3D of the cell values contained in the droplet. In the experiments, the measurements of the droplet size and velocity is carried out with a 2D laser sheet thanks to DTV. In addition, the measurement of the mean gas phase velocity also differs. While numerically it results from the velocity average over all the cells in the gas phase, the experimental mean gas phase velocity is estimated from LDV measurements at different radial positions and then averaged along those positions. On the other hand, it is important to keep in mind that the experimental and numerical data correspond to two drastically different physical spaces. The former were measured for $x/d_n = 800$ and the latter for $x/d_n \approx 20$. The difference could then reveal some dynamics occurring at the overall jet scale, for instance the overall slowdown of the droplet population when the droplet spray moves towards larger x/d_n . Another explanation could also be the choice of the normalisation for the Reynolds number. Using the Reynolds number computed over d_n and the averaged velocity of the dispersed liquid phase may help to make the numerical and experimental edge of the joint volume histograms collapse. Finally, the difference along the Re_p axis between the experimental and numerical joint histograms could also raise from the difference of the density ratios used in the simulations and in the experiments. Notwithstanding those limitations, it still seems legitimate to conclude that the joint histogram edges are self similar. This conclusion only holds for the edges and not for the joint histogram values which evolve very differently between the experiments and the simulations.

Yet, the two jet flows differ in term of fragmentation mechanisms. In the experimental flow, the bag breakup fragmentation plays an important role while it is totally absent in the numerical flows. In the experiments, the droplets undergoing bag breakup originate from the liquid core pinch off and are characterized by a large size and axial velocity. As the liquid core is still developing in the simulations, the absence of such droplets is expected. Even if the joint histogram edges are self similar, they slightly differ for large values of particulate Reynolds and Ohnesorge numbers where the experimental joint histograms exhibit a well defined tail. Besides, Sec. 4.3.5 shows that the ligament-mediated fragmentation describes well the droplet fragmentation in the numerical flows. Thus, it is tempting to conclude that the droplets are likely to undergo a bag breakup fragmentation when $Oh_p/Oh_1 < 2$ and a ligament mediated fragmentation when $Oh_p/Oh_1 \geq 2$.

4.4.5 Drift between the gas and liquid phases

At last, one could consider the drift velocity between the two phases, which has some importance regarding the accuracy of turbulent biphasic jet models (Simonin, 1996). Measuring the drift velocity between the phases is challenging, both experimentally and numerically. In the best case, one should achieve to measure the drift velocity between each droplet and its gaseous surrounding. Numerically, this can be done by computing the velocity tensor perceived by the particle under consideration (Pumir *et al.*, 2013; Loisy & Naso, 2017; Naso, 2019). Otherwise, a global approach enables to derive in an easier way a first approximation of the drift velocity between the phases by simply computing the difference between the velocity of each phase

averaged overall the computational domain or over cylindrical shells centered on the jet axis. Fig. 4.22 gives the temporal evolution of the averaged drift velocity computed for each gaseous Weber number We_2 along with the evolution of the injection velocity U_{inj} . First of all, the comparison of the evolution of the drift velocity for different We_2 between the phases is limited because of the difference in the maximum time evolution of the DNS. The DNS 7 to 10 have a shorter time evolution than the DNS 1 to 6. With the available data, it appears that the drift velocity lies between $0.8U_{inj}$ and U_{inj} , which is expected as the liquid jet is injected into a quiescent gaseous medium. Looking at the domain averaged velocities could here be misleading as it includes the jet injection. In order to discard the influence of the injection, it might be interesting to depict the drift velocity between the gaseous phase and disperse phase, i.e. the droplets, only. This can be achieved by sampling the computational space in cylindrical shells centered on the jet axis and computing the difference of the gas velocity and the droplet velocity averaged in each cylindrical shell.

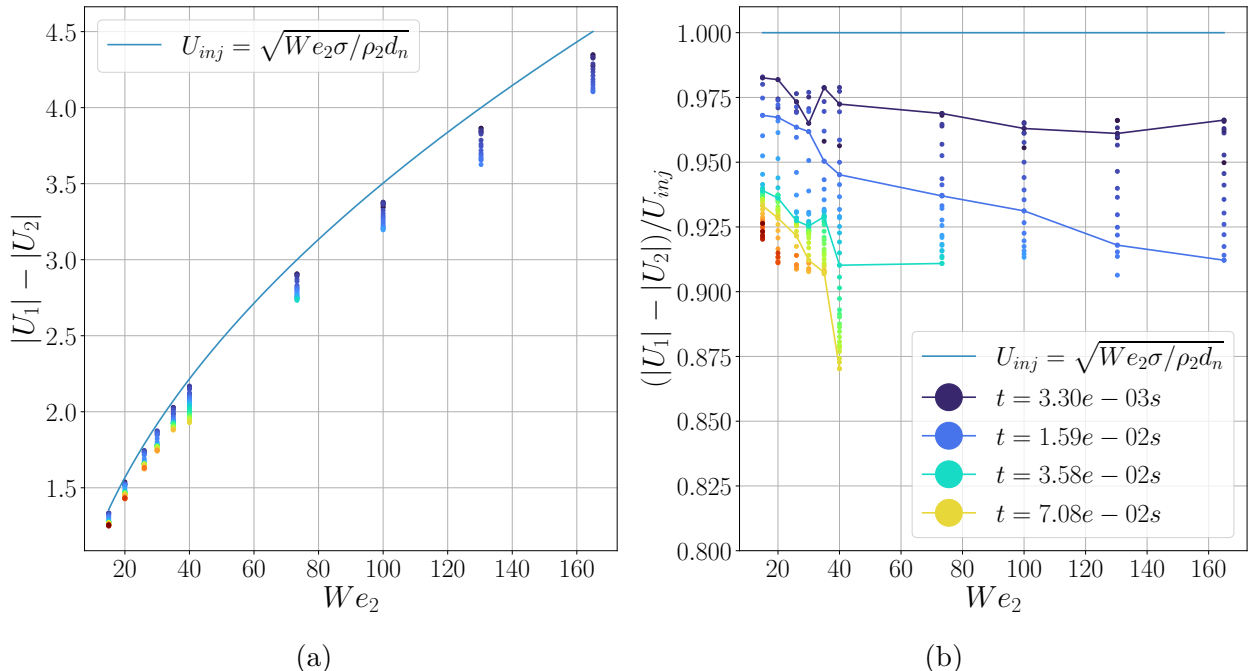


Figure 4.22: Velocity difference between the liquid and the gas phase averaged over the computational domain not normalised (a) and normalised (b). The color map indicates the time evolution with increasing values from dark blue to red. The solid lines on (b) indicate isovalues of t while the ice blue solid line indicates the injection velocity U_{inj} computed from We_2 .

4.5 Conclusion

In this work, the droplet population generated by the fragmentation of a round jet in a quiescent gas medium was studied numerically for different gaseous Weber number We_2 spanning the second wind induced regime and part of the atomisation regime. At first, the statistical moments of the size, the axial velocity and the radial velocity were depicted and their evolution with We_2 was detailed. The study of the distribution of the droplet size shows the existence of three modes in the second wind induced regime while only one mode exists in the atomisation regime. Complementary, the size distribution shows two exponential decays connected by a transition region scaling as a power law. Conversely to [Vallon et al. \(2021\)](#), the size distribution is better modelled by the law derived by [Kooij et al. \(2018\)](#) in the context of ligament-mediated fragmentation than by the law derived by [Novikov & Dommermuth \(1997\)](#) in the framework of turbulence intermittency. This could, at first sight, raise from the difference in the fragmentation mechanisms occurring in the region close to the nozzle, studied here, and the region far away from the nozzle studied previously. On the side of the axial velocity distribution, additionally to elucidating the scaling of the axial velocity distribution tails, the origin of the droplet velocities being negative and larger than the injection velocity U_{inj} is explained thanks to the vortex ring theory of [Saffman \(1992\)](#), vortex ring which sustains the recirculation region on the downstream side of the jet head. The existence of a double tail along the size direction for the size-velocity joint distribution is also explained by spatially separating the droplets evolving in the boundary layer and those ejected from the jet head.

The analysis also scaled down to the flow perceived by the droplets with the study of the droplet volume histogram over the phase space of the particulate Reynolds and Ohnesorge numbers. Properly scaled by the injection Ohnesorge number Oh_1 and the Reynolds number computed on the jet axis Re_{axis} , the boundaries of the joint volume histograms from the DNS collapse, thus indicating the weak dependence of the joint histogram boundaries on the gaseous Weber number. The collapse is also obtained between the numerical and the experimental joint volume histograms, with a slight correction along the Reynolds axis for the experimental one. This highlights the existence of a phase space properly bounded which contains the whole droplet population as well as the jet liquid core. Advantages could be taken from this result for modeling the turbulent jet fragmentation in terms of particulate dimensionless numbers or for improving the model of mass transfer proposed in [Chap. 3](#). Finally, the drift velocity between the phases, averaged over the computational domain, is computed and indicates a difference of the order of U_{inj} as expected. A more detailed analysis could enable to estimate the evolution of this drift velocity along the radial coordinate. Overall, the good accuracy of the statistical properties of the droplet population with the theoretical models as well as with the experimental data validate the accuracy of the simulations within the numerical limitations.

Further work could be done regarding the droplet dynamics and geometry. Now that the interface of the jet and the droplet population are described, it could be possible to focus on the size distribution resulting from specific fragmentation mechanisms, like the fragmentation of the rims in the second wind induced regime. This could help to understand the origin of the 3 modes observed for the size distribution in this regime. Also, performing a Lagrangian tracking of the rims in the DNS lying in the second wind induced regime would enable to verify the break-up of such toroidal ligaments and compare the resulting size distribution with the Γ distribution from the ligament-mediated fragmentation theory. Finally, a statistical analysis of the ligament geometry in the atomisation regime, specifically in the DNS with the highest

We_2 , could help to better describe the ligament size and corrugation distributions over the jet fragmentation.

Chapter **5**

Conclusions and perspectives

Contents

5.1	Main results	132
5.2	Thinking further	134
5.3	Closing words	142

5.1 Main results

This thesis aims at studying the droplet population generated by the fragmentation of a round liquid jet in the regions far away from and close to the nozzle. While experimental joint measurements of the droplet sizes and velocities using DTV are carried out in the far field, the close field is studied numerically thanks to DNS relying on the solver for the Navier-Stokes equations implemented in the C-based high level programming language Basilisk. For each study, the focus is given to the size and velocity distributions of the droplets. Two models of very different nature for the droplet size distribution, derived from the turbulence intermittency (Novikov & Dommermuth, 1997) and from the ligament-mediated fragmentation (Villermaux *et al.*, 2004), are tested out in both the far and close fields.

Multimodal distributions of agricultural-like sprays

The analysis of the DTV measurements of Felis *et al.* (2020) highlights the multimodal nature of both the size and the velocity distributions for agricultural-like sprays lying in the second wind induced regime for $400 \leq x/d_n \leq 800$. After precisely describing the statistical properties of both distributions, it appears from the systematic fit campaign that the size distribution from the intermittency framework performs the best. On the side of the bimodal velocity distribution, the low velocity mode is fitted with classic fragmentation distributions adapted to the velocity while a simple model is proposed for the second mode. Based on the joint distribution of the size and the velocity and the statistical properties of the marginal distributions, several subgroups of droplets are defined, each of them presenting a characteristic velocity and size and containing a consequent part either of the droplet number or of the volume of the disperse phase. Additionally, the main trend of the joint distribution is accurately described by the quadratic relationship of Lee & An (2016) between the size and the velocity. It is also possible to reconstruct the trend of the experimental size distribution thanks to this relationship.

Weber dependency of jet fragmentation

The DNS campaign focuses on round liquid jets in the second wind induced and the atomisation regimes. The distribution of the size and of the velocity differs between the two regimes up to $x/d_n = 28$. For the size, the former and the latter show a trimodal and a unimodal distributions respectively. Once again, the statistical properties of the distributions are detailed, power and exponential behaviours are highlighted and a fit campaign is carried out to test the distributions from the intermittency and ligament-mediated fragmentation frameworks. The latter offers a very accurate fit of the size distribution in the atomisation regime with a square Pearson coefficient r^2 of almost 1. The former performs less well quantitatively speaking but offers a better qualitative description of the trend, especially for the smallest sizes. At-first-sight, unexpected features of the velocity distribution and of the size-velocity joint distribution are respectively explained by the recirculation region quantified thanks to the vortex ring theory and by the characterisation of two sources of droplets: the forced corollas and the jet head. The volume joint histogram of the particulate Reynolds and Ohnesorge numbers shows sharp delimitations of the phase space in which the droplets evolve. Those limits appear to be independent of the gas Weber number and can be recovered experimentally too. Finally, a global

analysis of the slip velocity between the phases indicates a velocity approximately equal to 0.9 times the injection velocity.

5.2 Thinking further

Lessons from the fields

The nature of the two models for the size distribution tested out in the far and close fields is very different. One is derived from the framework of turbulence intermittency and is purely statistical while the other one is built over the experimental observations of the ligament dynamics. As said previously, the former shows a good accuracy for describing the size distribution in the far field region. In the close field region, the latter performs exceptionally well with a square Pearson coefficient r^2 almost equal to 1. However, the distribution derived from the intermittency framework offers a more satisfying qualitative trend for the smallest droplets.

In both fields, the size distribution presents a segment which follows a power law of coefficient -2.7 . Additionally, when the droplets are separated in different subgroups, either on the basis of the statistical properties of the velocity and size distributions or on the basis of the region of generation, the size distribution of the subgroups follows an exponential decay. Such exponential laws result from the composition of Γ laws in a way similar to the random stripping mechanism proposed by Villermaux (2020). Thus, as expected, the ligament mediated fragmentation is relevant to describe the size distribution of the subgroups in the far field, $400 \leq x/d_n \leq 800$, even if this region away from the nozzle is the theatre of a large spectrum of droplet sizes and of several different fragmentation mechanisms.

For its part, the numerical study in the close field indicates that the presence of two sources of fragmentation, the head of the jet and the corollas induced by the forcing, generates a size distribution with two exponential regimes, potentially resulting from two distinct random stripping mechanisms, as well as a transition region behaving as a power law of coefficient -2.7 . Complementary, the exponential decay of the size distribution of the subgroups related to the DNS in the second wind induced regime indicates that each exponential regime observed in the size distributions derives from a specific source of fragmentation.

In turbulent jet fragmentation like the one studied by Felis *et al.* (2020), the spectrum of fragmentation mechanisms is wide and includes among others the peeling and pinching of the liquid core, bag breakups of large, fast droplets and ligament mediated fragmentation of intermediate and small droplets. With this in mind, it could be possible to say that the subgroups observed experimentally result from different sources of fragmentation and, generally speaking, that the multiplication of fragmentation sources, like the ones listed above, leads to the combination of Γ compound distributions showing an exponential decay.

Regarding the validity of the distribution from Kooij *et al.* (2018) and Novikov & Dommermuth (1997), it appears that it is not only a question of distance from the nozzle but also of number of fragmentation sources. Indeed, the distribution from the intermittency framework performs well in the far field and offers a qualitatively satisfying trend in the close field while the distribution from the ligament-mediated fragmentation is very accurate in the close field and shows a good performance in the far field for less complex jets. Chap. 3 showed that two sources of droplets can be well identified and characterised in the close field. Thus, it is tempting to say that the intermittency distribution better describes the overall size distribution when several sources of fragmentation are active in the flow while the distribution from the ligament mediated fragmentation framework offers a more accurate description up to two sources of fragmentation.

Let us try to define more precisely the so-called sources of fragmentation. A source of fragmentation is, here, thought as a region of the phase space more than a spatial region. It could be correlated to a specific location in space, as the two sources identified in Chap. 4, but not necessarily. The example of the droplets studied in Chap. 3 provides a good illustration. Depending on the size and the velocity of the droplets, they do not experience the same flow conditions nor the same force balance and thus can fragment differently. Additionally, all the droplets of a given size do not necessarily fragment in the same region of space. Then, a source of fragmentation could be identified as a given region of the phase space constructed either over the size and the velocity of the droplets or the particulate Reynolds and Ohnesorge numbers.

It appears from this study that the distribution of Novikov & Dommermuth (1997) describes well the size distribution resulting from the combination of several Γ compound distributions resulting from the random stripping argument of Villermaux (2020). At the same time, the accuracy of the Γ distribution for describing the ligament-mediated distribution is not to be proven any more. Could an intermittency based fragmentation description improve the modelling of the size distributions resulting from turbulent jets? The results here suggest so. Furthermore, considering intermittency in fragmentation has some grounds.

Modelling the intermittency of the fragmentation process in a turbulent jet

A basic way to understand intermittency of small scales of turbulence is to consider it as a statistical description able to represent the discontinuous presence of the small scales in time and space, in other words that they are some times in different space locations and some times not. The example of ligament fragmentation on a fast, large droplet illustrated in Fig. 5.1a is typical. Similar formation can be found in DNS too, as illustrated by Fig. 5.1b. Contrary to the peeling occurring continuously on the liquid core from the nozzle until the core pinches off or the continuous fragmentation of the corollas in the DNS, such fragmentations appears discontinuously in time and space. Once this is said, two questions arise. What demonstration would be sufficient to prove that the fragmentation of a turbulent jet is actually intermittent? If it is intermittent, how can it be modelled? The first one is a fundamental requirement before searching further. Even so, it is possible to open the second question by looking backwards and consider the intermittency models developed in the turbulence community.

Without evaporation, the process of fragmentation is conservative. When a droplet breaks, the sum of the volume of the daughter droplets is equal to the volume of the initial droplet. There is no thing such as volume dissipation. Let us consider the intermittency models presented by Frisch (1995): the β -model, the bifractal model and the multifractal model based on the velocity. The β -model relies on the idea that the number of daughter eddies is set such that the fraction of volume occupied decreases by a fraction β , $0 < \beta < 1$. Applied to the fragmentation process, the sum of the volume of the daughter droplets would be smaller than the volume of the initial droplet. This breaks the volume conservation and makes the β -model unsuitable for describing droplet fragmentation. In the bifractal model, the physical space \mathbb{R}^3 is split in two regions characterised by two different scaling exponents, see 1.4.3, and fractal dimensions. In our context of fragmentation, this concept could be used. Instead of splitting regions of the physical space based on the velocity scaling exponent, one could split the phase space built over the size and the velocity of the droplets by regions in which a fragmentation regime is predominant. The multifractal model goes beyond by extending the bifractal model. Recalling that, in the inviscid limit, the Navier-Stokes equation is invariant under infinitely many scaling

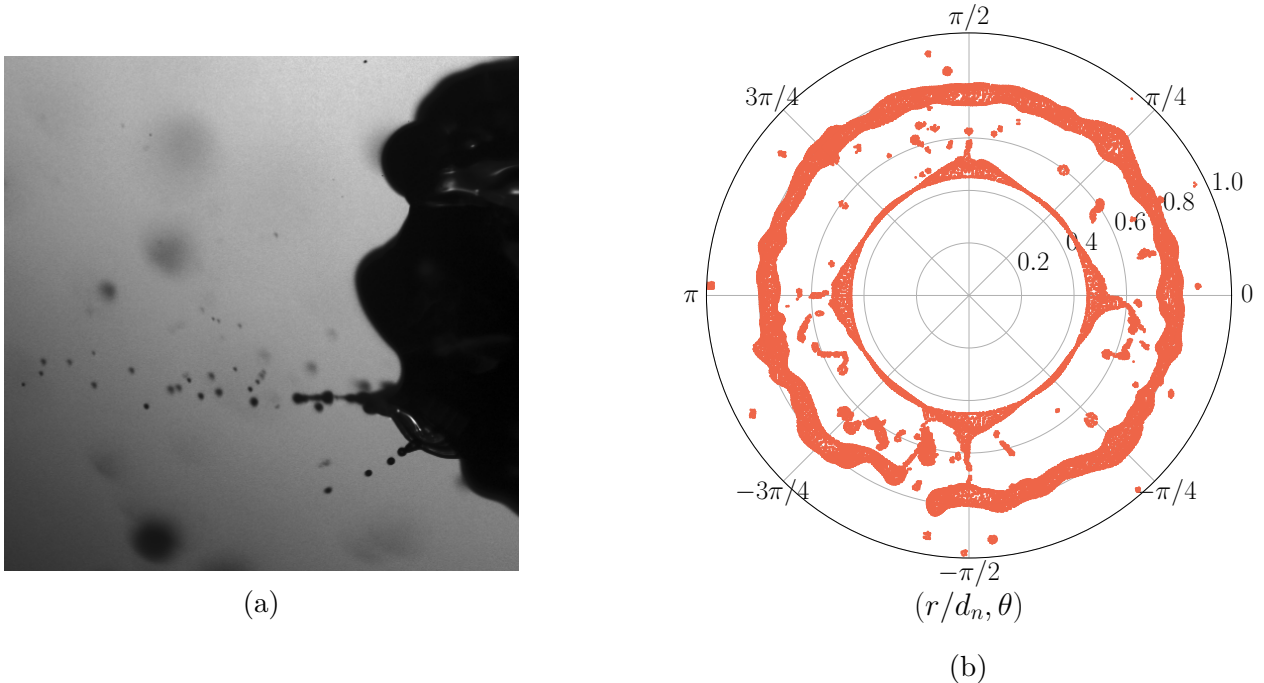


Figure 5.1: Examples of intermittent ligament fragmentation, experimentally at $x/d_n = 600$ (a) and numerically for the DNS 7, $We_2 = 73$, (b), visible at $-\pi/2$.

groups labelled by arbitrary scaling exponents, this model considers a continuous infinity of scaling exponents rather than a finite set. If a similar model could be derived for fragmentation, listing in an exhaustive manner all the possible fragmentation regimes would not be necessary. However, in the framework of turbulence, the multifractal model does not account for positive and negative increments. An equivalent for the droplet fragmentation could then not account for possible aggregation. This statement is to consider carefully as no one-to-one comparison can be accurately achieved here. Finally, the probabilistic formulation of the multifractal model overcomes the latter limit and could inspire a model for the size distribution resulting from a turbulent jet. It is important to note that those models were derived for describing the intermittency of the turbulent dissipation. In our context, no variable was identified as intermittent and we considered so far the intermittency of the fragmentation process, taken as a general concept. Let us consider two fragmentation mechanisms: the bag-breakup and ligament-mediated fragmentations. Each mechanism can be tracked in time by using their characteristics. Due to the existence of piercing, the droplets undergoing bag break-up can be detected by measuring their Euler characteristic, which is non zero when one or several holes exist. The droplets undergoing ligament-mediated fragmentation can be detected by computing their ellipticity which will get close to 1 as they deform into a ligament. Extra work on the droplet corrugations is however required to detect the formation of ligaments on large droplets, like in Fig. 5.1a. Once detected, the volume rate actually fragmented by one mechanism can be tracked in space and time. If this variable shows intermittency, it could potentially be used in an adaptation of the models for turbulence internal intermittency. Such an approach would take advantage of using a characteristic common to all, or at least several, fragmentation mechanisms, which for instance could be related to the ratio of the droplet surface and volume or related to the flow perceived by the droplets. If one considers a finite set of fragmentation

regimes, another idea could be to consider the resulting size distribution of a turbulent jet as the sum of the elementary distributions of each fragmentation regime weighted by its fractal dimension in the particulate Reynolds Ohnesorge phase space. Whatever the chosen option, reconstructing the multimodal size distribution obtained experimentally could be a test case for developing an intermittency based model for fragmentation. Improving the model of volume transfer proposed in Chap. 3 by using properly parametrised distributions resulting from specific fragmentation mechanisms could also bring further informations, for example about the relevance of the chosen fragmentation mechanisms.

The question of the flow perceived by the particles

Depending on the force balance, the aerodynamic conditions can play a critical role in the fragmentation process. In a turbulent flow, the role of vortices in fragmentation could also be investigated by looking at the spatial correlation between the droplets and the vortices. Fig. 5.2 illustrates this point. It shows the liquid interface of a fragmenting jet along with the turbulent vortices detected with the λ_2 criterion (Jeong & Hussain, 1995) and highlights two liquid fragments being spatially correlated with vortices. Following this, a more general way to explore the flow experienced by the droplets and the role of turbulence would be to study the velocity gradient tensor, which can be seen as an approximation of the velocity gradient acting in a small volume, perceived by the particles in numerical experiments. Computing this tensor experienced by each particle opens the way to depict precisely quantities like the droplet velocity relatively to the surrounding gas phase, the vorticity or the strain rate perceived by each droplet. This could be done using the pioneer developments of Pumir *et al.* (2013) and in a similar fashion as the study of bubbles in a turbulent flow done by Loisy & Naso (2017) and of the analysis of scale structures in rotating turbulence done by Naso (2019). Such an analysis would not only bring information on the flow perceived by each droplet but would also enable to carry out a statistical analysis to characterise different flow regimes and potentially connect them with droplet sizes and / or breakup regimes. Particularly, quantifying the vorticity perceived by the droplet would enable to better know the turbulence intensity and influence at the droplet scale.

The role of the droplet geometry

Complementary, the question of the geometry of the droplets remains open. Experimentally, the droplet geometry in 3D is not accessible easily and would require, if possible, several cameras as well as computationally costly spatial reconstruction. Even so, it is possible to study the projection of the droplets on the camera plane and compute both the length of the liquid fragment and its thickness. Numerically, the geometrical informations are much easier to access as the interfaces of the fragments also correspond to a limited set of spatial positions. The 3D geometry is then accessible and it would be easy to apply an homographic projection on a plane along the jet axis to reproduce the experimental data acquisition and compare the data sets. Doing such a geometrical study enables to better characterise the droplet population and to point out ligaments from the rest of the population. Once pointed out, it is possible to describe the statistics of the ligament population, starting by the distribution of their lengths, radii and corrugations which are missing in the framework of the ligament-mediated fragmentation. In this work, due to the 2D nature of the experimental data, it would not be possible to derive any

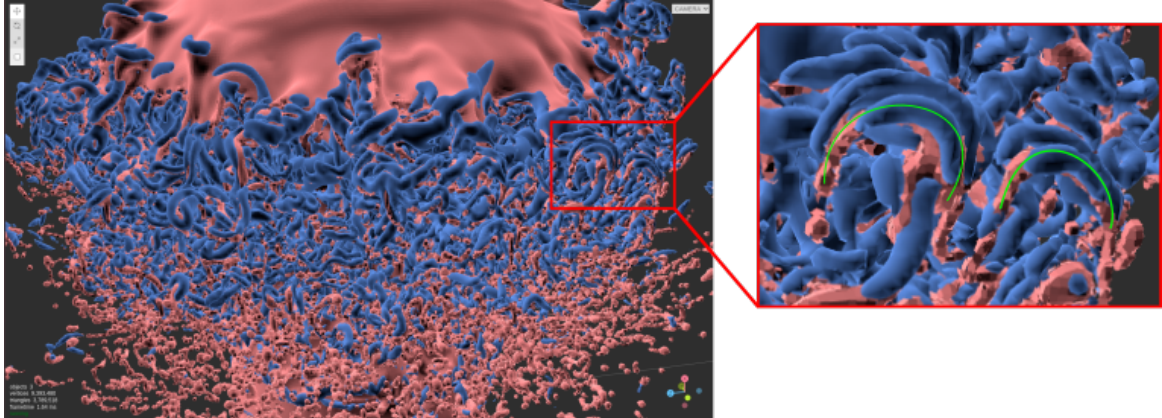


Figure 5.2: Visualisation of the jet head ($2d_n \times 3d_n$) in the DNS 10, $We_2 = 165$. The jet axis is vertical and the jet goes upward. The interface is coloured in red. The vortices, in blue, are detected with the λ_2 criterion (Jeong & Hussain, 1995). The two green lines in the close-up indicate the spatial correlation between a droplet and several vortices.

precise knowledges about the ligaments but they would serve to validate the numerical data instead.

Technical developments

On the side of the technique, a major progress in the study of droplets in turbulent jet fragmentation would be the ability of tracking the droplets and depict the different steps they undergo from their generation to their breakup. Doing so experimentally might enable to depict precisely the chain of mechanisms taking place in the fragmentation of large elements towards the smallest ones. Such tracking could be achieved thanks to time resolved stereo DTV measurements but a strong focus would be needed to overcome the complexity of 3D reconstruction (Gay, 2020). On the numerical side, performing a Lagrangian tracking of the liquid fragments also opens the way to fine observations of droplet fragmentation, under the classic limits of numerical computations and the difficulty to reach distances in the far field, typically $x/d_n = O(100)$. Combining a Lagrangian tracking with the tag routine of Basilisk enables to extract the time evolution of the interface. Once this is available, the time evolution of the fragment geometry and the corrugations developing on its interface can be studied. Implementing a routine to carry out a Lagrangian tracking of each droplet in Basilisk seems to be a challenge itself and might largely increase the computational cost. When the physics of the jet is better known, one could overcome this issue by carrying out a Lagrangian tracking of specific liquid fragments based on the evolution of some characteristic flow features, as illustrated by the proof of concept below.

Fig. 5.3 shows the tracking of the corollas induced by the forcing in DNS 6, $We_2 = 40$, as well as the detection and tracking of the rims resulting from the corolla development. The former are not formally detected. The travelling velocity of the corolla feet was observed to be the same as the injection velocity while the inclination angle was observed to be roughly the same in a given fragmentation regime. The corollas are then tracked based on their estimated axial displacement and bending. The interface points are then extracted on a slice following the corolla bending. Deriving such motion properties for the rims is more complicated. A close

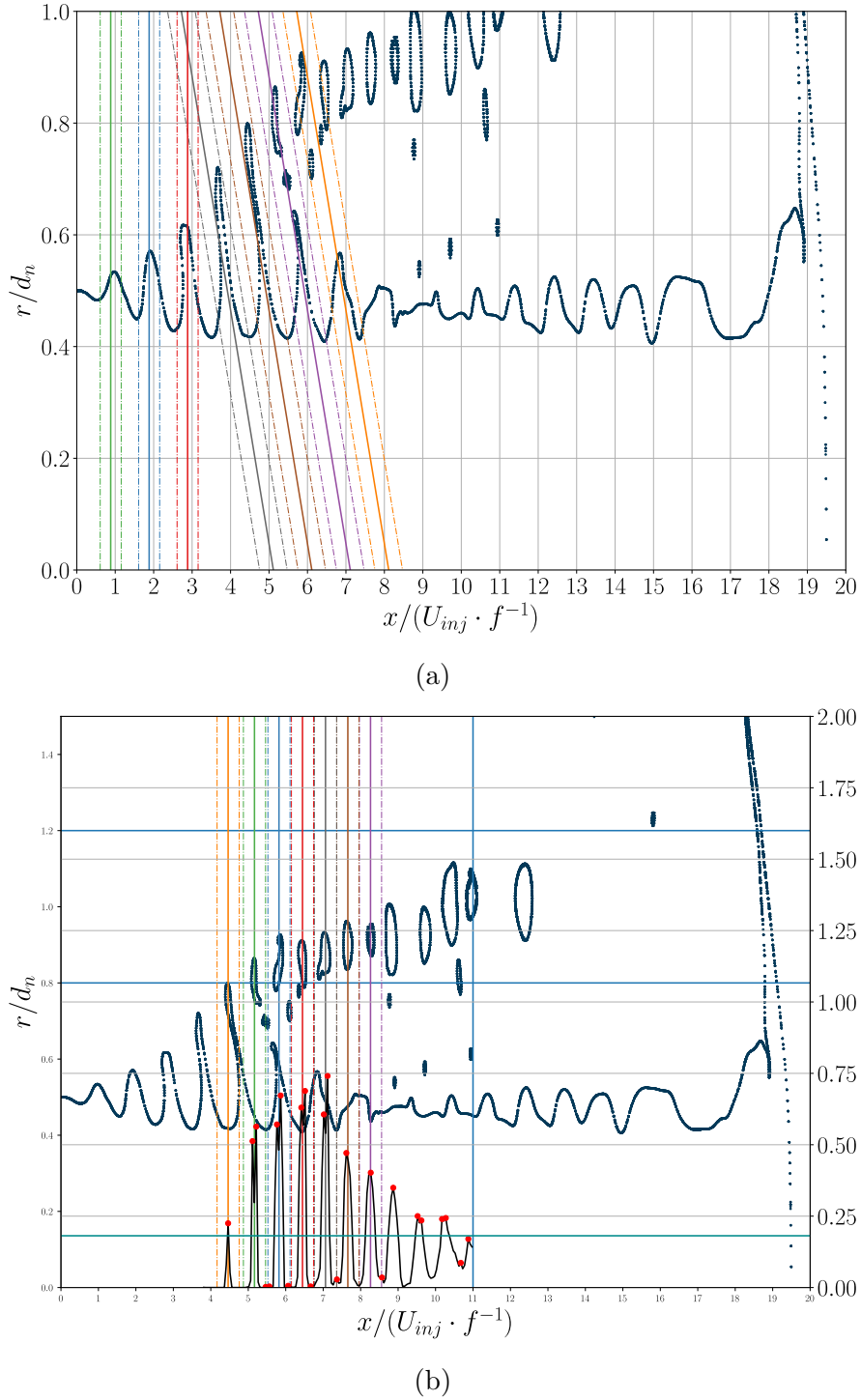


Figure 5.3: Illustration of the Lagrangian tracking of (a) the corollas and of (b) the rims for $We_2 = 40$ (DNS 6). The seven corollas are simultaneously tracked. The rims are detected only for $x/(U_{inj} \cdot f^{-1}) < 11$ and $0.8 < r/d_n < 1.2$, the region delimited by the blue lines. The black line in (b) represents the probability distribution of the interface points in the latter region. The red dots and the green line represent the peak of the distribution and the threshold for filtering the interface probabilities.

look at the interface evolution indicates that the rims are generated for $r/d_n \in [0.8, 1.2]$ and undergo fragmentation before $x/(U_{inj} f^{-1}) = 11$. Instead of guessing their spatial position, the rims are detected within the latter delimitations based on the value of the distribution of the interface points along the x -axis. The idea is to link each local maxima, i.e. each peak, of the interface point distribution to the presence of a rim. Note that the distribution and the peaks are represented by the black solid line and the red dots in Fig. 5.3b. Once the rim is detected, it can be extracted on the slice centred on the axial position of the peak. The distribution of the interface points can show minor peaks resulting from the presence of droplets in the region of interest. Those droplets can be discarded from the tracking by setting a threshold on the interface probability, indicated by the green line in Fig. 5.3b.

An example of tracking is given in Fig. 5.4 which shows the time evolution of one perturbation induced by the velocity forcing from the birth of the corolla until the fragmentation of its related rim. Using this technique led to detect 52 perturbations for the DNS 6 among which 35 show a complete evolution from the corolla birth to the rim fragmentation. This tracking method can be further improved by being implemented directly in Basilisk. Doing so would enable the computation of the time evolution of the ligament properties, such as its volume or its velocity, and the properties of the corrugations developing on its interface, which would be of first interest for the ligament-mediated fragmentation.

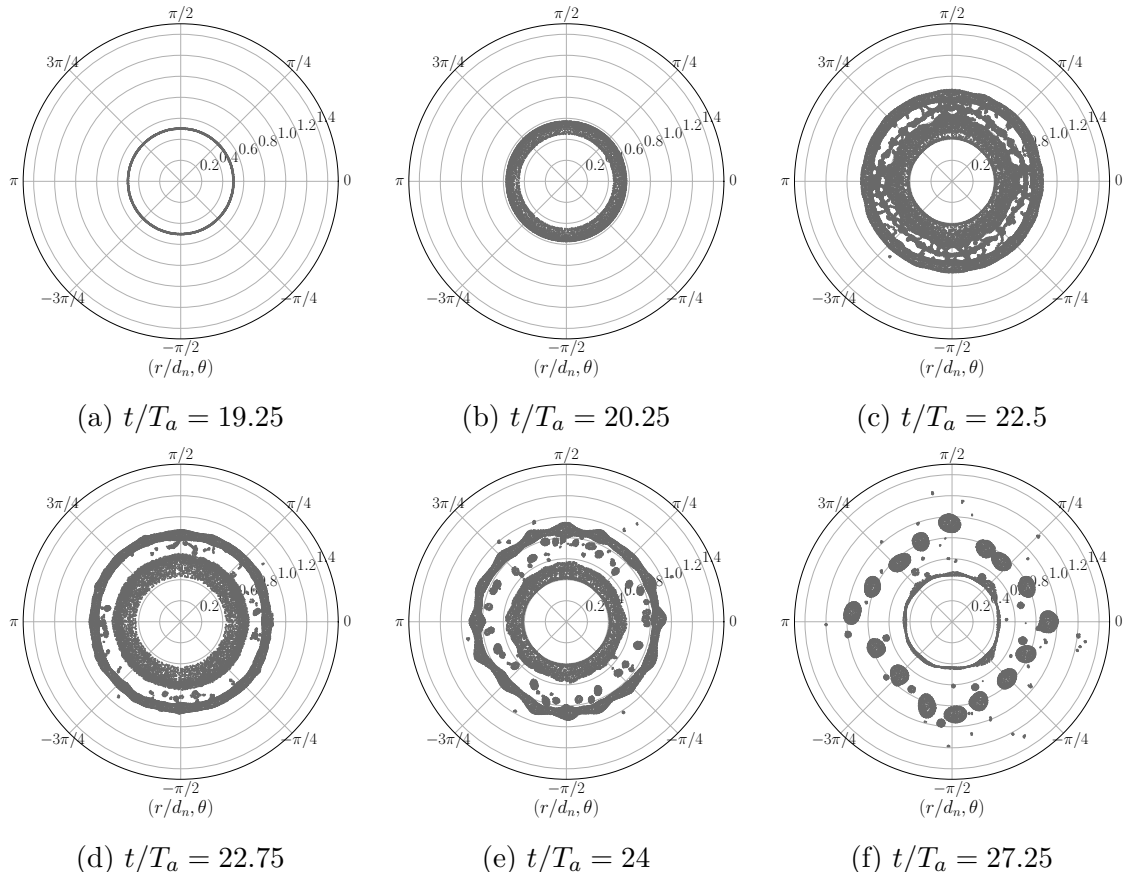


Figure 5.4: Time evolution of a corolla (a – c) and the corresponding rim (d – f) in the DNS 6, $We_2 = 40$.

Transporting the statistical moments

Exploring fragmentation can be done experimentally, numerically or theoretically, since the objective of describing the distributions of the droplet sizes or velocities remains. Thus, instead of transporting droplets in the physical space, one could transport the distribution of the internal variables. Marchisio & Fox (2013) detailed the mathematical framework to transport the moments of the distributions of different internal variables and this for different kinds of particle population, for example monodisperse or polydisperse phases. The most general formulation of the transport equation for distribution is the General Population Balance Equation (GPBE) which describes inertial polydisperse particles and can account for acceleration, growth, collision, aggregation and fragmentation. Instead of being expressed in terms of distribution, the GPBE can be rewritten in terms of the distribution moments. The resolution of such equations can be done thanks to the Quadrature Based Moment Methods (QBMM), like the ones presented by Fox (2018), or their high order counterparts (Fox, 2009). This approach has been proved successful in the context of combustion with the work of Fox *et al.* (2008) and Massot *et al.* (2010) for automotive engines and of Essadki *et al.* (2018) for cryogenic rocket engines. This approach could be tested out in the framework of agricultural-like sprays and compared with the DTV measurements and the DNS presented here.

5.3 Closing words

A better characterisation and modelling of the physics at play in fragmentation mechanisms are crucial for deepening our understanding of the processes, either natural or industrial, relying on it. Research work on fragmentation is necessary to gain knowledges on a widespread number of scientific fields which are highly relevant in today's society, like combustion in automotive engines, spraying in agriculture, sneeze flows for disease transmission or ocean sprays for climate modelling. Not only they are relevant today but those research topics will also grow in importance as climate change is catching up along with speeding disease emergence (Smith *et al.*, 2014; Stephens *et al.*, 2021). The last report of the working group I of the Intergovernmental Panel for Climate Change states bluntly that “it is unequivocal that human influence has warmed the atmosphere, ocean and land. Widespread and rapid changes in the atmosphere, ocean, cryosphere and biosphere have occurred” (Masson-Delmotte *et al.*, 2021). It also draws the possible incoming climate evolutions along with the global temperature evolution as a function of the greenhouse gases (GHG) emissions, see Fig. 5.5. The larger the global average temperature becomes, the wider and deeper the changes and their consequences will be. A deep understand of fragmentation constitutes a cornerstone to drastically reduce CO₂ emissions from combustion processes, efficiently control spraying irrigation under amplifying drought, quantify more precisely airborne transmission of diseases and better model tomorrow's climate dynamics as well as its impacts on future human societies.

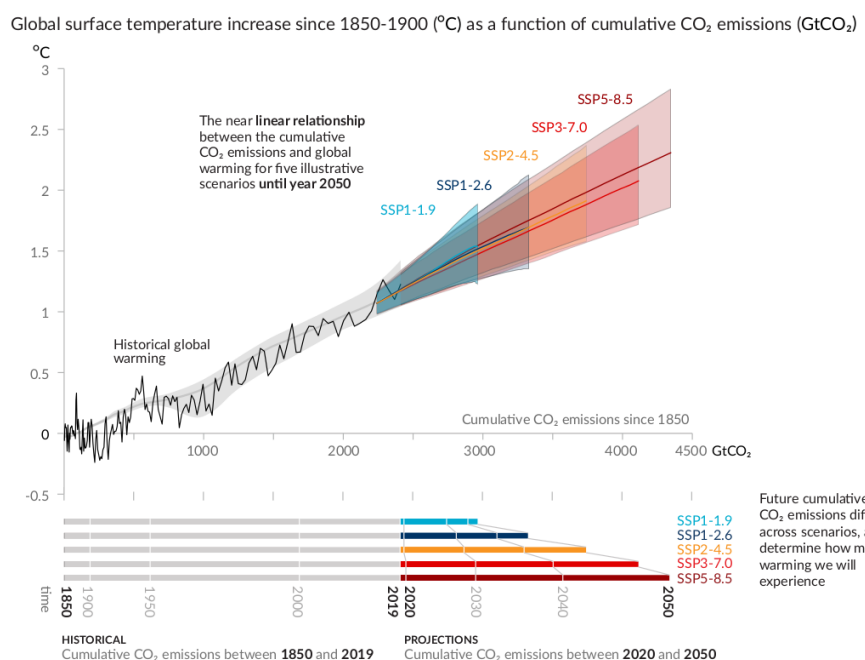


Figure 5.5: Relationship between the cumulative CO₂ emissions and the increase in global surface temperature. The top panel shows the historical evolution along with the projected range for different scenarios. The bottom panel gives the historical and projected cumulative CO₂ emissions for different scenarios. Taken from the work of Masson-Delmotte *et al.* (2021).

Bibliography

- Abid, M., F. Anselmet, & C. Kharif (2017). Instabilités Hydrodynamiques et Turbulence. Red. by C. Potel & P. Gatignol. *Sciences Mécaniques*. Toulouse: Cépaduès. 170 pp. ISBN: 978-2-36493-607-2. URL: <https://www.cepadues.com/livres/instabilites-hydrodynamiques-turbulence-9782364936072.html> (visited on 09/15/2021).
- Abu-Al-Saud, M. O., S. Popinet, & H. A. Tchelepi (2018). “A Conservative and Well-Balanced Surface Tension Model”. *Journal of Computational Physics* 371, pp. 896–913. ISSN: 00219991. DOI: [10.1016/j.jcp.2018.02.022](https://doi.org/10.1016/j.jcp.2018.02.022).
- Agbaglah, G., S. Delaux, D. Fuster, J. Hoepffner, C. Josserand, S. Popinet, P. Ray, R. Scardovelli, & S. Zaleski (2011). “Parallel Simulation of Multiphase Flows Using Octree Adaptivity and the Volume-of-Fluid Method”. *Comptes Rendus Mécanique* 339, pp. 194–207. DOI: [10.1016/j.crme.2010.12.006](https://doi.org/10.1016/j.crme.2010.12.006).
- Agostini, L. & M. Leschziner (2014). “On the Influence of Outer Large-Scale Structures on near-Wall Turbulence in Channel Flow”. *Physics of Fluids* 26.7, p. 075107. DOI: [10.1063/1.4890745](https://doi.org/10.1063/1.4890745).
- Agostini, L. & M. Leschziner (2018). “The Impact of Footprints of Large-Scale Outer Structures on the Near-Wall Layer in the Presence of Drag-Reducing Spanwise Wall Motion”. *Flow, Turbulence and Combustion* 100.4, pp. 1037–1061. ISSN: 1573-1987. DOI: [10.1007/s10494-018-9917-3](https://doi.org/10.1007/s10494-018-9917-3).
- Al Heidary, M., J. P. Douzals, C. Sinfort, & A. Vallet (2014). “Influence of Spray Characteristics on Potential Spray Drift of Field Crop Sprayers: A Literature Review”. *Crop Protection* 63, pp. 120–130. ISSN: 0261-2194. DOI: [10.1016/j.cropro.2014.05.006](https://doi.org/10.1016/j.cropro.2014.05.006).
- Anderson, J. D. (1995). Computational Fluid Dynamics - the Basics with Applications. *McGraw-Hill Series in Mechanical Engineering—McGraw-Hill Series in Aero- Aeronautical and Aerospace Engineering*. McGraw-Hill, Inc. 547 pp. ISBN: 0-07-001685-2.
- Anselmet, F., R. A. Antonia, & L. Danaila (2001). “Turbulent Flows and Intermittency in Laboratory Experiments”. *Planetary and Space Science* 49, pp. 1177–1191. ISSN: 0032-0633. DOI: [10.1016/S0032-0633\(01\)00059-9](https://doi.org/10.1016/S0032-0633(01)00059-9).
- Anselmet, F., Y. Gagne, E. J. Hopfinger, & R. A. Antonia (1984). “High-Order Velocity Structure Functions in Turbulent Shear Flows”. *Journal of Fluid Mechanics* 140, pp. 63–89. DOI: [10.1017/S0022112084000513](https://doi.org/10.1017/S0022112084000513).
- Atta, C. W. V. & T. T. Yeh (1973). “The Structure of Internal Intermittency in Turbulent Flows at Large Reynolds Number: Experiments on Scale Similarity”. *Journal of Fluid Mechanics* 59.3, pp. 537–559. ISSN: 0022-1120, 1469-7645. DOI: [10.1017/S0022112073001692](https://doi.org/10.1017/S0022112073001692).

BIBLIOGRAPHY

- Aulisa, E., S. Manservisi, R. Scardovelli, & S. Zaleski (2007). “Interface Reconstruction with Least-Squares Fit and Split Advection in Three-Dimensional Cartesian Geometry”. *Journal of Computational Physics* 225.2, pp. 2301–2319. ISSN: 0021-9991. DOI: [10.1016/j.jcp.2007.03.015](https://doi.org/10.1016/j.jcp.2007.03.015).
- Batchelor, G. K. (1967). An Introduction to Fluid Dynamics. *Cambridge Mathematical Library*. Cambridge University Press. 569 pp. ISBN: 0-521-66396-2.
- Bell, J. B., P. Colella, & H. M. Glaz (1989). “A Second-Order Projection Method for the Incompressible Navier-Stokes Equations”. *Journal of Computational Physics* 85, pp. 257–283. DOI: [10.1016/0021-9991\(89\)90151-4](https://doi.org/10.1016/0021-9991(89)90151-4).
- Benzi, R., S. Ciliberto, C. Baudet, & G. R. Chavarria (1995). “On the Scaling of Three-Dimensional Homogeneous and Isotropic Turbulence”. *Physica D: Nonlinear Phenomena* 80.4, pp. 385–398. ISSN: 01672789. DOI: [10.1016/0167-2789\(94\)00190-2](https://doi.org/10.1016/0167-2789(94)00190-2).
- Borrell, G. & J. Jiménez (2016). “Properties of the Turbulent/Non-Turbulent Interface in Boundary Layers”. *Journal of Fluid Mechanics* 801, pp. 554–596. ISSN: 0022-1120, 1469-7645. arXiv: [1606.08146](https://arxiv.org/abs/1606.08146). DOI: [10.1017/jfm.2016.430](https://doi.org/10.1017/jfm.2016.430).
- Bourouiba, L. (2016). *A Sneeze*. <https://doi.org/10.1056/NEJMicm1501197>.
- Bourouiba, L., E. Dehandschoewercker, & J. W. M. Bush (2014). “Violent Expiratory Events: On Coughing and Sneezing”. *Journal of Fluid Mechanics* 745, pp. 537–563. ISSN: 0022-1120, 1469-7645. DOI: [10.1017/jfm.2014.88](https://doi.org/10.1017/jfm.2014.88).
- Brackbill, J. U., D. B. Kothe, & C. Zemach (1992). “A Continuum Method for Modeling Surface Tension”. *Journal of Computational Physics* 100.2, pp. 335–354. ISSN: 0021-9991. DOI: [10.1016/0021-9991\(92\)90240-Y](https://doi.org/10.1016/0021-9991(92)90240-Y).
- Cattafesta, L. N. & M. Sheplak (2011). “Actuators for Active Flow Control”. *Annual Review of Fluid Mechanics* 43.1, pp. 247–272. ISSN: 0066-4189, 1545-4479. DOI: [10.1146/annurev-fluid-122109-160634](https://doi.org/10.1146/annurev-fluid-122109-160634).
- Chandrasekhar, S. (1961). Hydrodynamic and Hydromagnetic Stability. *International Series of Monographs on Physics Oxford, England*. New York, USA: Dover. ISBN: 978-0-486-64071-6.
- Charru, F. (2007). Instabilités Hydrodynamiques. *Savoirs Actuels*. Les Ulis, France, Paris, France: EDP Sciences, CNRS Éditions. ISBN: 978-2-86883-985-5. URL: <https://labo.utique.edpsciences.fr/en/product/97/9782759801107/Instabilites%20hydrodynamiques> (visited on 07/28/2021).
- Chaussonnet, G., S. Braun, T. Dauch, M. Keller, J. Kaden, T. Jakobs, C. Schwitzke, R. Koch, & H.-J. Bauer (2018). “Three-Dimensional SPH Simulation of a Twin-Fluid Atomizer Operating at High Pressure”. Proceedings of the 14th International Conference on Liquid Atomization & Spray Systems. ICLASS 2018. Chicago, IL, USA. URL: <https://publikationen.bibliothek.kit.edu/1000084437> (visited on 04/05/2021).
- Chehroudi, B., S.-H. Chen, F. V. Bracco, & Y. Onuma (1985). “On the Intact Core of Full-Cone Sprays”. *SAE Transactions* 94, pp. 764–773. ISSN: 0096-736X. JSTOR: [44467712](https://www.jstor.org/stable/44467712).
- Chen, X., D. Ma, V. Yang, & S. Popinet (2013). “High-Fidelity Simulations of Impinging Jet Atomization”. *Atomization and Sprays* 23.12. ISSN: 1044-5110, 1936-2684. DOI: [10.1615/AtomizSpr.2013007619](https://doi.org/10.1615/AtomizSpr.2013007619).
- Chigier, N. & R. D. Reitz (1996). “Regimes of Jet Breakup and Breakp Mechanisms (Physical Aspects)”. In: Kuo, K. K. Recent Advances In Spray Combustion: Spray Atomization and Drop Burning Phenomena. AIAA. ISBN: 1-56347-175-2.

- Choi, H., J. Lee, & H. Park (2014). "Aerodynamics of Heavy Vehicles". Annual Review of Fluid Mechanics 46.1, pp. 441–468. ISSN: 0066-4189, 1545-4479. DOI: [10.1146/annurev-fluid-011212-140616](https://doi.org/10.1146/annurev-fluid-011212-140616).
- Constante-Amores, C. R., L. Kahouadji, A. Batchvarov, S. Shin, J. Chergui, D. Juric, & O. K. Matar (2020). "Dynamics of Retracting Surfactant-Laden Ligaments at Intermediate Ohnesorge Number". Physical Review Fluids 5.8, p. 084007. ISSN: 2469-990X. DOI: [10.1103/PhysRevFluids.5.084007](https://doi.org/10.1103/PhysRevFluids.5.084007).
- Corke, T. C., C. L. Enloe, & S. P. Wilkinson (2010). "Dielectric Barrier Discharge Plasma Actuators for Flow Control". Annual Review of Fluid Mechanics 42.1, pp. 505–529. ISSN: 0066-4189, 1545-4479. DOI: [10.1146/annurev-fluid-121108-145550](https://doi.org/10.1146/annurev-fluid-121108-145550).
- Corrsin, S. (1959). "Outline of Some Topics in Homogeneous Turbulent Flows". Journal of Geophysical Research 64, p. 2134.
- Corrsin, S. & A. L. Kistler (1955). *Free-Stream Boundaries of Turbulent Flows*. 1244, p. 32.
- Cummins, S., M. Francois, & D. Kothe (2005). "Estimating Curvature from Volume Fractions". Computers and Structures 6–7.83, pp. 425–434. DOI: [10.1016/j.compstruc.2004.08.017](https://doi.org/10.1016/j.compstruc.2004.08.017).
- Dalin, P., N. Pertsev, S. Frandsen, O. Hansen, H. Andersen, A. Dubietis, & R. Balciunas (2010). "A Case Study of the Evolution of a Kelvin–Helmholtz Wave and Turbulence in Noctilucent Clouds". Journal of Atmospheric and Solar-Terrestrial Physics 72.14-15, pp. 1129–1138. ISSN: 13646826. DOI: [10.1016/j.jastp.2010.06.011](https://doi.org/10.1016/j.jastp.2010.06.011).
- Dan, T., T. Yamamoto, J. Senda, & H. Fujimoto (1997). *Effect of Nozzle Configurations for Characteristics of Non-Reacting Diesel Fuel Spray*. SAE Technical Paper 970355. Warrendale, PA, USA: SAE International. DOI: [10.4271/970355](https://doi.org/10.4271/970355).
- DeBar, R. (1974). *Fundamentals of the KRAKEN Code*. UCID-17366. Livermore, CA, USA: Lawrence Livermore Laboratory, California University.
- Desnyansky, V. N. & E. A. Novikov (1974). "The Evolution of Turbulence Spectra to the Similarity Regime". Izvestiya Akademii nauk SSSR. Fizika atmosfery i okeana 10.2, pp. 127–136.
- Drazin, P. G. & W. H. Reid (2004). Hydrodynamic Stability. 2nd ed. *Cambridge Monographs on Mechanics and Applied Mathematics, Cambridge Mathematical Library*. Cambridge University Press. ISBN: 978-0-521-52541-1. URL: <https://doi.org/10.1017/CBO9780511616938>.
- Dubrulle, B. (1994). "Intermittency in Fully Developed Turbulence: Log-Poisson Statistics and Generalized Scale Covariance". Physical Review Letters 73.7, pp. 959–962. ISSN: 0031-9007. DOI: [10.1103/PhysRevLett.73.959](https://doi.org/10.1103/PhysRevLett.73.959).
- Duguid, J. P. (1946). "The Size and the Duration of Air-Carriage of Respiratory Droplets and Droplet-Nuclei". The Journal of Hygiene 44.6, pp. 471–479. ISSN: 0022-1724. pmid: 20475760. DOI: [10.1017/S0022172400019288](https://doi.org/10.1017/S0022172400019288).
- Dumouchel, C. (2008). "On the Experimental Investigation on Primary Atomization of Liquid Streams". Experiments in Fluids 45.3, pp. 371–422. ISSN: 0723-4864. DOI: [10.1007/s00348-008-0526-0](https://doi.org/10.1007/s00348-008-0526-0).
- Dumouchel, C., J. Cousin, & K. Triballier (2005a). "Experimental Analysis of Liquid–Gas Interface at Low Weber Number: Interface Length and Fractal Dimension". Experiments in Fluids 39.4, pp. 651–666. ISSN: 1432-1114. DOI: [10.1007/s00348-005-1005-5](https://doi.org/10.1007/s00348-005-1005-5).

BIBLIOGRAPHY

- Dumouchel, C., J. Cousin, & K. Triballier (2005b). “On the Role of the Liquid Flow Characteristics on Low-Weber-Number Atomization Processes”. *Experiments in Fluids* 38.5, pp. 637–647. ISSN: 1432-1114. DOI: [10.1007/s00348-005-0944-1](https://doi.org/10.1007/s00348-005-0944-1).
- Eggers, J. & E. Villermaux (2008). “Physics of Liquid Jets”. *Reports on Progress in Physics* 71, p. 036601. ISSN: 0034-4885. DOI: [10.1088/0034-4885/71/3/036601](https://doi.org/10.1088/0034-4885/71/3/036601).
- Essadki, M., S. de Chaisemartin, F. Laurent, & M. Massot (2018). “High Order Moment Model for Polydisperse Evaporating Sprays towards Interfacial Geometry Description”. *SIAM Journal on Applied Mathematics* 78.4, pp. 2003–2027. ISSN: 0036-1399. DOI: [10.1137/16M1108364](https://doi.org/10.1137/16M1108364).
- European Union, United Nations, International Transport Forum, & OECD (2019). *Glossary for Transport Statistics*. 5th ed. ISBN: 978-92-76-06213-4.
- Faeth, G., L.-P. Hsiang, & P.-K. Wu (1995). “Structure and Breakup Properties of Sprays”. *International Journal of Multiphase Flow* 21, pp. 99–127. ISSN: 03019322. DOI: [10.1016/0301-9322\(95\)00059-7](https://doi.org/10.1016/0301-9322(95)00059-7).
- Felis-Carrasco, F. (2017). “Atomization and Dispersion of a Liquid Jet : Numerical and Experimental Approaches”. PhD thesis. IRPHE, Marseille: Ecole Centrale Marseille. URL: [http://theses.fr/2017ECDM0001](https://theses.fr/2017ECDM0001) (visited on 09/15/2021).
- Felis, F., S. Tomas, A. Vallet, M. Amielh, & F. Anselmet (2020). “Experimental Analysis of the Flow Characteristics of a Pressure-Atomized Spray”. *International Journal of Heat and Fluid Flow* 85, p. 108624. ISSN: 0142-727X. DOI: [10.1016/j.ijheatfluidflow.2020.108624](https://doi.org/10.1016/j.ijheatfluidflow.2020.108624).
- Feller, W. (1971). *An Introduction to Probability Theory and Its Applications*. 3rd. Vol. 2. New York: Wiley. URL: <https://doi.org/10.1002/bimj.19690110615>.
- Ferrand, V., R. Bazile, J. Borée, & G. Charnay (2003). “Gas-Droplet Turbulent Velocity Correlations and Two-Phase Interaction in an Axisymmetric Jet Laden with Partly Responsive Droplets”. *International Journal of Multiphase Flow* 29, p. 195.
- Fox, R. O. (2009). “Higher-Order Quadrature-Based Moment Methods for Kinetic Equations”. *Journal of Computational Physics* 228.20, pp. 7771–7791. ISSN: 0021-9991. DOI: [10.1016/j.jcp.2009.07.018](https://doi.org/10.1016/j.jcp.2009.07.018).
- Fox, R. O., F. Laurent, & M. Massot (2008). “Numerical Simulation of Spray Coalescence in an Eulerian Framework: Direct Quadrature Method of Moments and Multi-Fluid Method”. *Journal of Computational Physics* 227.6, pp. 3058–3088. ISSN: 0021-9991. DOI: [10.1016/j.jcp.2007.10.028](https://doi.org/10.1016/j.jcp.2007.10.028).
- Fox, R. O. (2012). “Large-Eddy-Simulation Tools for Multiphase Flows”. *Annual Review of Fluid Mechanics* 44.1, pp. 47–76. ISSN: 0066-4189. DOI: [10.1146/annurev-fluid-120710-101118](https://doi.org/10.1146/annurev-fluid-120710-101118).
- (2018). “Quadrature-Based Moment Methods for Multiphase Chemically Reacting Flows”. *Bridging Scales in Modelling and Simulation of Non-Reacting and Reacting Flows. Part I*. 1st ed. Vol. 52. Academic Press, pp. 1–50. ISBN: 978-0-12-815096-2. URL: <https://doi.org/10.1016/bs.ache.2018.01.001>.
- Francois, M., S. Cummins, E. Dendy, D. Kothe, J. Sicilian, & M. Williams (2006). “A Balanced-Force Algorithm for Continuous and Sharp Interfacial Surface Tension Models within a Volume Tracking Framework”. *Journal of Computational Physics* 1.213, pp. 141–173. DOI: [10.1016/j.jcp.2005.08.004](https://doi.org/10.1016/j.jcp.2005.08.004).

- Friedlander, S. K. & C. S. Wang (1966). "The Self-Preserving Particle Size Distribution for Coagulation by Brownian Motion". *Journal of Colloid and Interface Science* 22.2, pp. 126–132. ISSN: 0021-9797. DOI: [10.1016/0021-9797\(66\)90073-7](https://doi.org/10.1016/0021-9797(66)90073-7).
- Friedlander, S. K. (2000). *Smoke, Dust, and Haze: Fundamentals of Aerosol Dynamics*. 2nd ed. Oxford University Press, New York. ISBN: 978-0-19-512999-1.
- Frisch, U. (1995). *Turbulence: The Legacy of A.N. Kolmogorov*. Cambridge: Cambridge University Press. ISBN: 0-521-45713-0.
- Frisch, U., P.-L. Sulem, & M. Nelkin (1978). "A Simple Dynamical Model of Intermittent Fully Developed Turbulence". *Journal of Fluid Mechanics* 87.04, p. 719. ISSN: 0022-1120, 1469-7645. DOI: [10.1017/S0022112078001846](https://doi.org/10.1017/S0022112078001846).
- Fuster, D., G. Agbaglah, C. Josserand, S. Popinet, & S. Zaleski (2009). "Numerical Simulation of Droplets, Bubbles and Waves: State of the Art". *Fluid Dynamics Research* 41.6, p. 065001. ISSN: 0169-5983, 1873-7005. DOI: [10.1088/0169-5983/41/6/065001](https://doi.org/10.1088/0169-5983/41/6/065001).
- Gay, A. (2020). "Déformations de Fibres Flexibles En Écoulement Turbulent". PhD thesis. IRPHE, Marseille: Aix-Marseille Université. URL: <https://theses.fr/s163145> (visited on 09/03/2021).
- Gil, Y. & C. Sinfort (2005). "Emission of Pesticides to the Air during Sprayer Application: A Bibliographic Review". *Atmospheric Environment* 39.28, pp. 5183–5193. ISSN: 1352-2310. DOI: [10.1016/j.atmosenv.2005.05.019](https://doi.org/10.1016/j.atmosenv.2005.05.019).
- Ginzburg, I. & G. Wittum (2001). "Two-Phase Flows on Interface Refined Grids Modeled with VOF, Staggered Finite Volumes and Spline Interpolants". *Journal of Computational Physics* 2.166, pp. 302–335. DOI: [10.1006/jcph.2000.6655](https://doi.org/10.1006/jcph.2000.6655).
- Gorokhovski, M. & M. Herrmann (2008). "Modeling Primary Atomization". *Annual Review of Fluid Mechanics* 40.1, pp. 343–366. DOI: [10.1146/annurev.fluid.40.111406.102200](https://doi.org/10.1146/annurev.fluid.40.111406.102200).
- Griebel, M. & G. Zumbusch (2002). "Hash Based Adaptive Parallel Multilevel Methods with Space-Filling Curves". NIC Symposium 2001, Proceedings. NIC Symposium: Symposium, 5. - 6. December 2001. Ed. by H. Rolnik & D. Wolf. Vol. 9. NIC Series. Jülich: John von Neumann Institute for Computing, Jülic, pp. 479–492. ISBN: 978-3-00-009055-4.
- Guildenbecher, D. R., C. López-Rivera, & P. E. Sojka (2009). "Secondary Atomization". *Experiments in Fluids* 46.3, p. 371. ISSN: 1432-1114. DOI: [10.1007/s00348-008-0593-2](https://doi.org/10.1007/s00348-008-0593-2).
- Guyon, É., J.-P. Hulin, & L. Petit (2012). *Hydrodynamique Physique. Savoirs Actuels*. Les Ulis, France, Paris, France: EDP Sciences, CNRS Éditions. ISBN: 978-2-7598-0561-7.
- Haynes, W. M., ed. (2017). *CRC Handbook of Chemistry and Physics*. 97th ed. CRC Press, Taylor & Francis Group. ISBN: 978-1-4987-5429-3.
- Helmholtz, H. von (1868). "Überdiscontinuirliche Flüssigkeitsbewegungen". *Monatsberichte der Königlich preussischen Akademie der Wissenschaften zu Berlin* 23, pp. 215–28.
- Hilz, E. & A. W. P. Vermeer (2013). "Spray Drift Review: The Extent to Which a Formulation Can Contribute to Spray Drift Reduction". *Crop Protection* 44, pp. 75–83. ISSN: 0261-2194. DOI: [10.1016/j.cropro.2012.10.020](https://doi.org/10.1016/j.cropro.2012.10.020).
- Hinze, J. O. (1955). "Fundamentals of the Hydrodynamic Mechanism of Splitting in Dispersion Processes". *AICHE Journal* 1.3, pp. 289–295. ISSN: 1547-5905. DOI: [10.1002/aic.690010303](https://doi.org/10.1002/aic.690010303).
- Hirt, C. W. & B. D. Nichols (1981). "Volume of Fluid (VOF) Method for the Dynamics of Free Boundaries". *Journal of Computational Physics* 39.1, pp. 201–225. ISSN: 0021-9991. DOI: [10.1016/0021-9991\(81\)90145-5](https://doi.org/10.1016/0021-9991(81)90145-5).

BIBLIOGRAPHY

- Hoepffner, J. & G. Paré (2013). "Recoil of a Liquid Filament: Escape from Pinch-off through Creation of a Vortex Ring". *Journal of Fluid Mechanics* 734, pp. 183–197. ISSN: 0022-1120, 1469-7645. DOI: [10.1017/jfm.2013.472](https://doi.org/10.1017/jfm.2013.472).
- Holloway, A. & T. Jeans (2020). "Hydrodynamic Impulse Generated by Slender Bodies in Viscous Flow". *Ocean Engineering* 206, p. 106951. ISSN: 00298018. DOI: [10.1016/j.oceaneng.2020.106951](https://doi.org/10.1016/j.oceaneng.2020.106951).
- Hong, J. M., T. Shinar, M. Kang, & R. Fedkiw (2007). "On Boundary Condition Capturing for Multiphase Interfaces". *Journal of Scientific Computing* 33, pp. 99–125.
- Hoyt, J. W. & J. Taylor (1977). "Waves on Water Jet". *Journal of Fluid Mechanics* 83.119.
- Jeong, J. & F. Hussain (1995). "On the Identification of a Vortex". *Journal of Fluid Mechanics* 285 (-1), p. 69. ISSN: 0022-1120, 1469-7645. DOI: [10.1017/S0022112095000462](https://doi.org/10.1017/S0022112095000462).
- Jiménez Cisnero, B. E., T. Oki, N. W. Arnell, G. Benito, J. G. Cogley, P. Döll, T. Jiang, & S. S. Mwakalila (2014). "Freshwater Ressources". Climate Change 2014: Impacts, Adaptation, and Vulnerability. Part A: Global and Sectoral Aspects. Contribution of Working Group II to the Fifth Assessment Report of the Intergovernmental Panel on Climate Change. Cambridge, United Kingdom, and New York, NY, USA: Cambridge University Press, pp. 229–269.
- Jiménez, J. (1998). "Small Scale Intermittency in Turbulence". European Journal of Mechanics - B/Fluids. Special Issue Dynamics and Statistics of Concentrated Vortices in Turbulent Flow (Euromech Colloquium 364) 17.4, pp. 405–419. ISSN: 0997-7546. DOI: [10.1016/S0997-7546\(98\)80002-2](https://doi.org/10.1016/S0997-7546(98)80002-2).
- Jin, Y., M.-F. Uth, A. V. Kuznetsov, & H. Herwig (2015). "Numerical Investigation of the Possibility of Macroscopic Turbulence in Porous Media: A Direct Numerical Simulation Study". *Journal of Fluid Mechanics* 766, pp. 76–103. ISSN: 0022-1120, 1469-7645. DOI: [10.1017/jfm.2015.9](https://doi.org/10.1017/jfm.2015.9).
- Kamluk, A., A. Likhomanov, & A. Grachulin (2020). "Field Testing and Extinguishing Efficiency Comparison of the Optimized for Higher Expansion Rates Deflector Type Sprinkler with Other Foam and Foam-Water Sprinklers". *Fire Safety Journal* 116, p. 103177. ISSN: 0379-7112. DOI: [10.1016/j.firesaf.2020.103177](https://doi.org/10.1016/j.firesaf.2020.103177).
- Kang, M., R. Fedkiw, & X. Liu (2000). "A Boundary Condition Capturing Method for Multi-phase Incompressible Flow". *Journal of Scientific Computing* 3.15, pp. 323–360.
- Katz, J. (2006). "Aerodynamics of Race Cars". *Annual Review of Fluid Mechanics* 38.1, pp. 27–63. ISSN: 0066-4189, 1545-4479. DOI: [10.1146/annurev.fluid.38.050304.092016](https://doi.org/10.1146/annurev.fluid.38.050304.092016).
- Kelvin, L. (1871). "Hydrokinetic Solutions and Observations". *Philosophical Magazine* 4.42, pp. 362–77.
- Khokhlov, A. M. (1998). "Fully Threaded Tree Algorithms for Adaptive Refinement Fluid Dynamics Simulations". *Journal of Computational Physics* 2.143, pp. 519–543. DOI: [10.1006/jcph.1998.9998](https://doi.org/10.1006/jcph.1998.9998).
- Kolmogorov, A. N. (1941a). "Energy Dissipation in Locally Isotropic Turbulence". *Doklady Akademii Nauk SSSR* 32, p. 19.
- (1941b). "On The Logarithmic Normal Distribution of Particle Sizes Under Grinding". *Doklady Akademii Nauk SSSR* 31, pp. 99–101. DOI: [10.1007/978-94-011-2260-3_29](https://doi.org/10.1007/978-94-011-2260-3_29).
- (1941c). "The Local Structure of Turbulence in an Incompressible Fluid for Very Large Reynolds Numbers". *Doklady Akademii Nauk SSSR* 30.299.
- (1961). "Précisions sur la structure locale de la turbulence dans un fluide visqueux aux nombres de Reynolds élevés". *Colloques internationaux du Centre National de la Recherche*

- Scientifique. Mécanique de la Turbulence. Vol. 108. Institut de Mécanique Statistique de la Turbulence de Marseille: CNRS, pp. 447–458.
- (1962). “A Refinement of Previous Hypotheses Concerning the Local Structure of Turbulence in a Viscous Incompressible Fluid at High Reynolds Number”. *Journal of Fluid Mechanics* 13.1, pp. 82–85. ISSN: 0022-1120. DOI: [10.1017/S0022112062000518](https://doi.org/10.1017/S0022112062000518).
 - (1991a). “Dissipation of Energy in the Locally Isotropic Turbulence”. *Proceedings: Mathematical and Physical Sciences* 434 (1890,), pp. 15–17. JSTOR: [51981](#).
 - (1991b). “The Local Structure of Turbulence in Incompressible Viscous Fluid for Very Large Reynolds Numbers”. *Proceedings: Mathematical and Physical Sciences* 434 (1890,), pp. 9–13. JSTOR: [51980](#).
- Kooij, S., R. Sijs, M. M. Denn, E. Villermaux, & D. Bonn (2018). “What Determines the Drop Size in Sprays?” *Physical Review X* 8.3. ISSN: 2160-3308. DOI: [10.1103/PhysRevX.8.031019](https://doi.org/10.1103/PhysRevX.8.031019).
- Kraichnan, R. H. (1974). “On Kolmogorov’s Inertial-Range Theories”. *Journal of Fluid Mechanics* 62.2, pp. 305–330. ISSN: 1469-7645, 0022-1120. DOI: [10.1017/S002211207400070X](https://doi.org/10.1017/S002211207400070X).
- Kudryavtsev, V. N. & V. K. Makin (2011). “Impact of Ocean Spray on the Dynamics of the Marine Atmospheric Boundary Layer”. *Boundary-Layer Meteorology* 140.3 (3), pp. 383–410. ISSN: 1573-1472. DOI: [10.1007/s10546-011-9624-2](https://doi.org/10.1007/s10546-011-9624-2).
- Kumaran, V. & D. L. Koch (1993). “The Effect of Hydrodynamic Interactions on the Average Properties of a Bidisperse Suspension of High Reynolds Number, Low Weber Number Bubbles”. *Physics of Fluids A: Fluid Dynamics* 5.5, pp. 1123–1134. ISSN: 0899-8213. DOI: [10.1063/1.858598](https://doi.org/10.1063/1.858598).
- Lagrée, P.-Y., L. Staron, & S. Popinet (2011). “The Granular Column Collapse as a Continuum: Validity of a Two-Dimensional Navier–Stokes Model with a (*I*)-Rheology”. *Journal of Fluid Mechanics* 686, pp. 378–408. ISSN: 0022-1120, 1469-7645. DOI: [10.1017/jfm.2011.335](https://doi.org/10.1017/jfm.2011.335).
- Lamb, H. (1932). Hydrodynamics. sixth. New York, NY, USA: DoverPublications.
- Landau, L. & E. M. Lifshitz (1959). Fluid Mechanics. *A Course of Theoretical Physics*. Oxford: Pergamon Press. ISBN: 0-7506-2767-0.
- Lauga, E. (2016). “Bacterial Hydrodynamics”. *Annual Review of Fluid Mechanics* 48.1, pp. 105–130. ISSN: 0066-4189, 1545-4479. DOI: [10.1146/annurev-fluid-122414-034606](https://doi.org/10.1146/annurev-fluid-122414-034606).
- Launder, B. E. & D. B. Spalding (1974). “The Numerical Computation of Turbulent Flows”. *Computer Methods in Applied Mechanics and Engineering* 3, pp. 269–289. DOI: [10.1016/B978-0-08-030937-8.50016-7](https://doi.org/10.1016/B978-0-08-030937-8.50016-7).
- Lee, T.-W. & K. An (2016). “Quadratic Formula for Determining the Drop Size in Pressure-Atomized Sprays with and without Swirl”. *Physics of Fluids* 28.6, p. 063302. ISSN: 1070-6631. DOI: [10.1063/1.4951666](https://doi.org/10.1063/1.4951666).
- Lefebvre, A. H. (1989). Atomization and Sprays. New York, NY, USA: Hemisphere Publishing Corporation. ISBN: 0-89116-603-3.
- Lefebvre, A. H. & V. G. McDonell (2017). Atomization and Sprays. 2nd ed. *Combustion: An International Series*. CRC Press, Taylor & Francis. ISBN: 978-1-4987-3625-1. URL: <https://doi.org/10.1201/9781315120911>.
- Li, X., J. Zhang, S. Yang, Y. Hou, & R. Erdélyi (2018). “Observing Kelvin–Helmholtz Instability in Solar Blowout Jet”. *Scientific Reports* 8.1, p. 8136. ISSN: 2045-2322. DOI: [10.1038/s41598-018-26581-4](https://doi.org/10.1038/s41598-018-26581-4).

BIBLIOGRAPHY

- Lin, S. P. & R. D. Reitz (1998). "Drop and Spray Formation from a Liquid Jet". *Annual Review of Fluid Mechanics* 30.1, pp. 85–105. ISSN: 0066-4189, 1545-4479. DOI: [10.1146/annurev.fluid.30.1.85](https://doi.org/10.1146/annurev.fluid.30.1.85).
- Ling, Y., D. Fuster, S. Zaleski, & G. Tryggvason (2017a). "Spray Formation in a Quasiplanar Gas-Liquid Mixing Layer at Moderate Density Ratios: A Numerical Closeup". *Physical Review Fluids* 2.014005. DOI: [10.1103/PhysRevFluids.2.014005](https://doi.org/10.1103/PhysRevFluids.2.014005).
- Ling, Y., G. Legros, S. Popinet, & S. Zaleski (2017b). "Direct Numerical Simulation of an Atomizing Biodiesel Jet: Impact of Fuel Properties on Atomization Characteristics". *Proceedings ILASS-Europe 2017. 28th Conference on Liquid Atomization and Spray Systems. ILASS2017 - 28th European Conference on Liquid Atomization and Spray Systems.* Universitat Politècnica València. ISBN: 978-84-9048-580-4. DOI: [10.4995/ILASS2017.2017.5035](https://doi.org/10.4995/ILASS2017.2017.5035).
- Loisy, A. & A. Naso (2017). "Interaction between a Large Buoyant Bubble and Turbulence". *Physical Review Fluids* 2, pp. 014606–20. DOI: [10.1103/PhysRevFluids.2.014606](https://doi.org/10.1103/PhysRevFluids.2.014606).
- Lomax, H., T. H. Pulliam, & D. W. Zingg (2001). *Fundamentals of Computational Fluid Dynamics*. Berlin: Springer-Verlag. ISBN: 3-540-41607-2.
- López-Herrera, J., A. Gañán-Calvo, S. Popinet, & M. Herrada (2015). "Electrokinetic Effects in the Breakup of Electrified Jets: A Volume-Of-Fluid Numerical Study". *International Journal of Multiphase Flow* 71, pp. 14–22. ISSN: 03019322. DOI: [10.1016/j.ijmultiphaseflow.2014.12.005](https://doi.org/10.1016/j.ijmultiphaseflow.2014.12.005).
- Marchisio, D. L. & R. O. Fox (2013). Computational Models for Polydisperse Particulate and Multiphase Systems. *Cambridge Series in Chemical Engineering*. Cambridge University Press. ISBN: 978-0-521-85848-9. URL: <https://archive.org/details/statistica1fluid01moan> (visited on 09/15/2021).
- Marcotte, F. & S. Zaleski (2019). "Density Contrast Matters for Drop Fragmentation Thresholds at Low Ohnesorge Number". *Physical Review Fluids* 4.10, p. 103604. DOI: [10.1103/PhysRevFluids.4.103604](https://doi.org/10.1103/PhysRevFluids.4.103604).
- Marmottant, P. G. M. & E. Villermaux (2004). "On Spray Formation". *Journal of Fluid Mechanics* 498.1, pp. 73–111. ISSN: 0022-1120. DOI: [10.1017/S0022112003006529](https://doi.org/10.1017/S0022112003006529).
- "IPCC 2021: Summary for Policymakers" (2021). *Climate Change 2021: The Physical Science Basis. Contribution of Working Group I to the Sixth Assessment Report of the Intergovernmental Panel on Climate Change*. Ed. by V. Masson-Delmotte, P. Zhai, A. Pirani, S. L. Connors, C. Péan, S. Berger, N. Caud, Y. Chen, L. Goldfarb, M. I. Gomis, M. Huang, K. Leitzell, E. Lonnoy, J. B. R. Matthews, T. K. Maycock, T. Waterfield, O. Yelekçi, R. Yu, & B. Zhou. Cambridge University Press.
- Massot, M., F. Laurent, D. Kah, & S. de Chaisemartin (2010). "A Robust Moment Method for Evaluation of the Disappearance Rate of Evaporating Sprays". *SIAM Journal on Applied Mathematics* 70.8, p. 3203. DOI: [10.1137/080740027](https://doi.org/10.1137/080740027).
- Miesse, C. C. (1955). "Correlation of Experimental Data on the Disintegration of Liquid Jets". *Industrial & Engineering Chemistry* 47.9, pp. 1690–1701. ISSN: 0019-7866. DOI: [10.1021/ie50549a013](https://doi.org/10.1021/ie50549a013).
- Migdal, A. A. (1994). "Loop Equation and Area Law in Turbulence". *International Journal of Modern Physics A* 09.08, pp. 1197–1238. ISSN: 0217-751X, 1793-656X. DOI: [10.1142/S0217751X94000558](https://doi.org/10.1142/S0217751X94000558).
- Mittal, R., R. Ni, & J.-H. Seo (2020). "The Flow Physics of COVID-19". *Journal of Fluid Mechanics* 894. ISSN: 0022-1120, 1469-7645. DOI: [10.1017/jfm.2020.330](https://doi.org/10.1017/jfm.2020.330).

- Moisy, F. (2020). *EzyFit 2.44*. Natick: The MathWorks, Inc. URL: <https://www.mathworks.com/matlabcentral/fileexchange/10176-ezyfit-2-44>, %20MATLAB%20Central%20File%20Exchange.
- Monin, A. S., A. M. Yaglom, & J. L. Lumley (1975). Statistical Fluid Mechanics: Mechanics of Turbulence, Vol. 2. First English Ed. The MIT Press. ISBN: 978-0-262-13098-1. URL: <http://gen.lib.rus.ec/book/index.php?md5=9131f7e205d258933308ebe3e045ffd9> (visited on 10/01/2019).
- Naso, A. (2019). “Multiscale Analysis of the Structure of Homogeneous Rotating Turbulence”. *Physical Review Fluids* 4, pp. 024609–16. DOI: [10.1103/PhysRevFluids.4.024609](https://doi.org/10.1103/PhysRevFluids.4.024609).
- Néel, B. (2018). “Déstabilisation, Rupture et Fragmentation Spontanées et Stimulées de Films Liquides”. PhD thesis. IRPHE, Marseille: Aix-Marseille Université. URL: <http://www.teses.fr/2018AIXM0578> (visited on 07/22/2021).
- Nore, C., D. Castanon Quiroz, L. Cappanera, & J.-L. Guermond (2016). “Direct Numerical Simulation of the Axial Dipolar Dynamo in the Von Kármán Sodium Experiment”. *EPL (Europhysics Letters)* 114.6, p. 65002. ISSN: 0295-5075, 1286-4854. DOI: [10.1209/0295-5075/114/65002](https://doi.org/10.1209/0295-5075/114/65002).
- Notz, P. K. & O. A. Basaran (2004). “Dynamics and Breakup of a Contracting Liquid Filament”. *Journal of Fluid Mechanics* 512, pp. 223–256. ISSN: 1469-7645, 0022-1120. DOI: [10.1017/S0022112004009759](https://doi.org/10.1017/S0022112004009759).
- Novikov, E. A. (1970). “Intermittency and Scale Similarity in the Structure of a Turbulent Flow”. *Prikladnaya Matematika i Mekhanika* 35.2, pp. 266–277. ISSN: 0021-8928. DOI: [10.1016/0021-8928\(71\)90029-3](https://doi.org/10.1016/0021-8928(71)90029-3).
- (1990). “The Effects of Intermittency on Statistical Characteristics of Turbulence and Scale Similarity of Breakdown Coefficients”. *Physics of Fluids A: Fluid Dynamics* 2.5, pp. 814–820. ISSN: 0899-8213. DOI: [10.1063/1.857629](https://doi.org/10.1063/1.857629).
- (1994). “Infinitely Divisible Distributions in Turbulence”. *Physical Review E* 50.5, R3303–R3305. ISSN: 1063-651X. DOI: [10.1103/PhysRevE.50.R3303](https://doi.org/10.1103/PhysRevE.50.R3303).
- Novikov, E. A. & D. G. Dommermuth (1997). “Distribution of Droplets in a Turbulent Spray”. *Physical Review E* 56.5, pp. 5479–5482. ISSN: 1063-651X. DOI: [10.1103/PhysRevE.56.5479](https://doi.org/10.1103/PhysRevE.56.5479).
- Novikov, E. A. & R. W. Stewart (1964). “Intermittency of Turbulence and Spectrum of Fluctuations in Energy Dissipation”. *Izvestiya Akademii Nauk SSSR, Serya Geofizika* 3, pp. 408–413.
- Obukhov, A. M. (1962). “Some Specific Features of Atmospheric Turbulence”. *Journal of Fluid Mechanics* 13.77.
- Ohnesorge, W. V. (1936). “Die Bildung von Tropfen an Düsen Und Die Auflösung Flüssiger Strahlen”. *Zeitschrift für Angewandte Mathematik und Mechanik* 16.6, pp. 355–358. ISSN: 1521-4001. DOI: [10.1002/zamm.19360160611](https://doi.org/10.1002/zamm.19360160611).
- Parisi, G. & U. Frisch (1985). “On the Singularity Spectrum of Developed Turbulence”. *Turbulence and Predictability in Geophysical Fluid Dynamics*. Ed. by M. Ghil, R. Benzi, & G. Parisi. Amsterdam, Netherlands: North-Holland, p. 84. ISBN: UVA:X001402599.
- Pearson, B. R. & R. A. Antonia (2001). “Reynolds-Number Dependence of Turbulent Velocity and Pressure Increments”. *Journal of Fluid Mechanics* 444, pp. 343–382. DOI: [10.1017/S0022112001005511](https://doi.org/10.1017/S0022112001005511).

BIBLIOGRAPHY

- Perrie, W., X. Ren, W. Zhang, & Z. Long (2004). "Simulation of Extratropical Hurricane Gustav Using a Coupled Atmosphere-Ocean-Sea Spray Model". *Geophysical Research Letters* 31.3. ISSN: 1944-8007. DOI: [10.1029/2003GL018571](https://doi.org/10.1029/2003GL018571).
- Pitsch, H. (2006). "Large-Eddy Simulation of Turbulent Combustion". *Annual Review of Fluid Mechanics* 38.1, pp. 453–482. ISSN: 0066-4189. DOI: [10.1146/annurev.fluid.38.050304.092133](https://doi.org/10.1146/annurev.fluid.38.050304.092133).
- Popinet, S. & S. Zaleski (1999). "A Front-Tracking Algorithm for Accurate Representation of Surface Tension". *International Journal for Numerical Methods in Fluids* 6.30, pp. 775–793.
- Popinet, S. (2003). "Gerris: A Tree-Based Adaptive Solver for the Incompressible Euler Equations in Complex Geometries". *Journal of Computational Physics* 190.2, pp. 572–600. ISSN: 00219991. DOI: [10.1016/S0021-9991\(03\)00298-5](https://doi.org/10.1016/S0021-9991(03)00298-5).
- (2009). "An Accurate Adaptive Solver for Surface-Tension-Driven Interfacial Flows". *Journal of Computational Physics* 228.16, pp. 5838–5866. ISSN: 00219991. DOI: [10.1016/j.jcp.2009.04.042](https://doi.org/10.1016/j.jcp.2009.04.042).
- (2015). "A Quadtree-Adaptive Multigrid Solver for the Serre–Green–Naghdi Equations". *Journal of Computational Physics* 302, pp. 336–358. DOI: [10.1016/j.jcp.2015.09.009](https://doi.org/10.1016/j.jcp.2015.09.009).
- (2018). "Numerical Models of Surface Tension". *Annual Review of Fluid Mechanics* 50.1, pp. 49–75. DOI: [10.1146/annurev-fluid-122316-045034](https://doi.org/10.1146/annurev-fluid-122316-045034).
- Popinet, S. & collaborators (2013–2021). *Basilisk*. Basilisk. URL: <http://www.basilisk.fr/>.
- (2016–2021). *Basilisk-Atomisation*. Basilisk-Atomisation. URL: www.basilisk.fr/src/examples/atomisation.c.
- Pumir, A., E. Bodenschatz, & H. Xu (2013). "Tetrahedron Deformation and Alignment of Perceived Vorticity and Strain in a Turbulent Flow". *Physics of Fluids* 25. DOI: [10.1063/1.4795547](https://doi.org/10.1063/1.4795547).
- Purcell, E. M. (1976). "Life at Low Reynolds Number". *AIP Conference Proceedings* 28.1, pp. 49–64. ISSN: 0094-243X. DOI: [10.1063/1.30370](https://doi.org/10.1063/1.30370).
- Radhakrishna, V., W. Shang, L. Yao, J. Chen, & P. E. Sojka (2021). "Experimental Characterization of Secondary Atomization at High Ohnesorge Numbers". *International Journal of Multiphase Flow* 138, p. 103591. ISSN: 03019322. DOI: [10.1016/j.ijmultiphaseflow.2021.103591](https://doi.org/10.1016/j.ijmultiphaseflow.2021.103591).
- Ranz, W. E. (1956). "On Sprays and Spraying: A Survey of Spray Technology for Research and Development Engineers". Bulletin 65. Department of Engineering Research, Penn State University.
- Rayleigh, L. (1883). "Investigation of the Character of the Equilibrium of an Incompressible Heavy Fluid of Variable Density." *Proc. London Math. Soc.* 14, pp. 170–14.
- Reitz, R. D. (1978). "Atomization and Other Breakup Regimes of a Liquid Jet". PhD thesis. Princeton: Princeton University.
- Renardy, Y. & M. Renardy (2002). "PROST - A Parabolic Reconstruction of Surface Tension for the Volume-of-Fluid Method". *Journal of Computational Physics* 2.183, pp. 400–421. DOI: [10.1006/jcph.2002.7190](https://doi.org/10.1006/jcph.2002.7190).
- Reynolds, O. (1883). "An Experimental Investigation of the Circumstances Which Determine Whether the Motion of Water Shall Be Direct or Sinuous, and of the Law of Resistance in Parallel Channels". *Philosophical Transactions of the Royal Society* 174.82, p. 934.

- Richardson, L. F. (1922). Weather Prediction by Numerical Process. In collab. with University of California Libraries. Cambridge, The University press. 262 pp. URL: <http://archive.org/details/weatherpredictio00richrich> (visited on 10/03/2019).
- Rimbert, N. & G. Castanet (2011). "Crossover between Rayleigh-Taylor Instability and Turbulent Cascading Atomization Mechanism in the Bag-Breakup Regime". Physical Review E 84.1, p. 016318. ISSN: 1539-3755. DOI: [10.1103/PhysRevE.84.016318](https://doi.org/10.1103/PhysRevE.84.016318).
- Rimbert, N. & O. Sero-Guillaume (2004). "Log-Stable Laws as Asymptotic Solutions to a Fragmentation Equation: Application to the Distribution of Droplets in a High Weber-Number Spray". Physical Review E 69.5, p. 056316. ISSN: 1539-3755. DOI: [10.1103/PhysRevE.69.056316](https://doi.org/10.1103/PhysRevE.69.056316).
- Rode, S., J. Elgeti, & G. Gompper (2019). "Sperm Motility in Modulated Microchannels". New Journal of Physics 21.1, p. 013016. ISSN: 1367-2630. DOI: [10.1088/1367-2630/aaf544](https://doi.org/10.1088/1367-2630/aaf544).
- Rott, N. (1990). "Note on the History of the Reynolds Number". Annual Review of Fluid Mechanics 22.1, pp. 1–12. ISSN: 0066-4189, 1545-4479. DOI: [10.1146/annurev.fl.22.010190.000245](https://doi.org/10.1146/annurev.fl.22.010190.000245).
- Ruffin, E., R. Schiestel, F. Anselmet, M. Amielh, & L. Fulachier (1994). "Investigation of Characteristic Scales in Variable Density Turbulent Jets Using a Second-Order Model". Physics of Fluids 6.8, pp. 2785–2799. ISSN: 1070-6631. DOI: [10.1063/1.868167](https://doi.org/10.1063/1.868167).
- Saffman, P. G. (1992). Vortex Dynamics. Cambridge University Press. ISBN: 0-521-42058-X.
- Saidur, R., E. Abdelaziz, A. Demirbas, M. Hossain, & S. Mekhilef (2011). "A Review on Biomass as a Fuel for Boilers". Renewable and Sustainable Energy Reviews 15.5, pp. 2262–2289. ISSN: 13640321. DOI: [10.1016/j.rser.2011.02.015](https://doi.org/10.1016/j.rser.2011.02.015).
- Saito, Y. (1992). "Log-Gamma Distribution Model of Intermittency in Turbulence". Journal of the Physical Society of Japan 61.2, pp. 403–406. ISSN: 0031-9015, 1347-4073. DOI: [10.1143/JPSJ.61.403](https://doi.org/10.1143/JPSJ.61.403).
- Scardovelli, R. & S. Zaleski (1999). "Direct Numerical Simulation of Free-Surface and Interfacial Flows". Annual Review of Fluid Mechanics 31, pp. 567–603. DOI: [10.1146/annurev.fluid.31.1.567](https://doi.org/10.1146/annurev.fluid.31.1.567).
- Scardovelli, R. & S. Zaleski (2000). "Analytical Relations Connecting Linear Interfaces and Volume Fractions in Rectangular Grids". Journal of Computational Physics 164.1, pp. 228–237. ISSN: 0021-9991. DOI: [10.1006/jcph.2000.6567](https://doi.org/10.1006/jcph.2000.6567).
- Schneider, K. & O. V. Vasilyev (2009). "Wavelet Methods in Computational Fluid Dynamics". Annual Review of Fluid Mechanics 42, pp. 473–33.
- She, Z.-S. & E. Leveque (1994). "Universal Scaling Laws in Fully Developed Turbulence". Physical Review Letters 72.3, pp. 336–339. ISSN: 0031-9007. DOI: [10.1103/PhysRevLett.72.336](https://doi.org/10.1103/PhysRevLett.72.336).
- Simmons, H. C. (1977). "The Correlation of Drop-Size Distributions in Fuel Nozzle Sprays. Part II. The Drop-Size/Number Distribution". Journal of Engineering for Gas Turbines and Power 99.315-19. ISSN: 0022-1120. DOI: [10.1017/S0022112077001074](https://doi.org/10.1017/S0022112077001074).
- Simonin, O. (1996). "Combustion and Turbulence in Two-Phase Flows". VKI Lecture Series 1996-02.
- Smagorinsky, J. (1963). "General Circulation Experiments with The Primitive Equations: I. The Basic Experiment". Monthly Weather Review 91.3, pp. 99–164. ISSN: 1520-0493, 0027-0644. DOI: [10.1175/1520-0493\(1963\)091<0099:GCEWTP>2.3.CO;2](https://doi.org/10.1175/1520-0493(1963)091<0099:GCEWTP>2.3.CO;2).

BIBLIOGRAPHY

- Smith, J. D. & V. Sick (2006). "Real-Time Imaging of Fuel Injection, Evaporation and Ignition in a Direct-Injected Spark-Ignition Engine". 19th Annual Conference on Liquid Atomization and Spray Systems. ILASS Americas. Toronto, Canada, p. 7.
- Smith, K. F., M. Goldberg, S. Rosenthal, L. Carlson, J. Chen, C. Chen, & S. Ramachandran (2014). "Global Rise in Human Infectious Disease Outbreaks". *Journal of The Royal Society Interface* 11.101, p. 20140950. ISSN: 1742-5689, 1742-5662. DOI: [10.1098/rsif.2014.0950](https://doi.org/10.1098/rsif.2014.0950).
- Sommerfeld, A. (1908). "Ein Beitrag Zur Hydrodynamischen Erklärung Der Turbulenten Flüssigkeitsbewegung". Proceedings of the 4th International Congress of Mathematics. International Congress of Mathematics, 4th. Vol. 3. Rome, pp. 116–24.
- Stephens, P. R., N. Gottdenker, A. M. Schatz, J. P. Schmidt, & J. M. Drake (2021). "Characteristics of the 100 Largest Modern Zoonotic Disease Outbreaks". *Philosophical Transactions of the Royal Society B: Biological Sciences* 376.1837, p. 20200535. ISSN: 0962-8436, 1471-2970. DOI: [10.1098/rstb.2020.0535](https://doi.org/10.1098/rstb.2020.0535).
- Sterling, A. M. & C. A. Sleicher (1975). "The Instability of Capillary Jets". *Journal of Fluid Mechanics* 68.3, pp. 477–495. ISSN: 1469-7645, 0022-1120. DOI: [10.1017/S0022112075001772](https://doi.org/10.1017/S0022112075001772).
- Stevenin, C., S. Tomas, A. Vallet, M. Amielh, & F. Anselmet (2016). "Flow Characteristics of a Large-Size Pressure-Atomized Spray Using DTV". *International Journal of Multiphase Flow* 84, pp. 264–278. ISSN: 0301-9322. DOI: [10.1016/j.ijmultiphaseflow.2016.05.004](https://doi.org/10.1016/j.ijmultiphaseflow.2016.05.004).
- Taylor, G. I. (1935a). "Statistical Theory of Turbulence I". In: Batchelor, G. K. *The Scientific Papers of Sir G.I.Taylor*. Meteorology, Oceanology, Turbulent Flow. 1st ed. Vol. 2. Cambridge University Press.
- (1940). "Generation of Ripples by Wind Blowing over a Viscous Fluid". In: Batchelor, G. K. *The Scientific Papers of Sir G.I.Taylor*. Aerodynamics Etc. 1st ed. Vol. 3. Cambridge University Press, p. 244.
- (1950). "The Instability of Liquid Surfaces When Accelerated in a Direction Perpendicular to Their Planes. I." *Proceedings of the Royal Society A* 201.192-6.
- (1953). "Formation of a Vortex Ring by Giving an Impulse to a Circular Disk and Then Dissolving It Away". *Journal of Applied Physics* 24.1, pp. 104–104. ISSN: 0021-8979. DOI: [10.1063/1.1721114](https://doi.org/10.1063/1.1721114).
- Taylor, G. (1935b). "Statistical Theory of Turbulence . IV. Diffusion in a Turbulent Air Stream". In: Batchelor, G. K. *The Scientific Papers of Sir G.I.Taylor*: Meteorology, Oceanography and Turbulent Flow. 1st ed. Vol. 2. Cambridge University Press, pp. 288–306.
- Tennekes, H. & J. L. Lumley (1972). *A First Course in Turbulence*. Cambridge: MIT Press.
- Torrey, M., L. Cloutman, & R. Mjolsness (1985). *NASA-VOF2D: A Computer Program for Incompressible Flows with Free Surfaces*. Technical. Los Alamos Laboratory.
- Tryggvason, G., R. Scardovelli, & S. Zaleski (2011). *Direct Numerical Simulations of Gas-Liquid Multiphase Flows*. Cambridge University Press. ISBN: 978-0-521-78240-1. URL: <https://doi.org/10.1017/CBO9780511975264.002>.
- Vallon, R., M. Abid, & F. Anselmet (2021). "Multimodal Distributions of Agricultural-like Sprays: A Statistical Analysis of Drop Population from a Pressure-Atomized Spray". *Physical Review Fluids*, pp. 023604–23. DOI: [10.1103/PhysRevFluids.6.023604](https://doi.org/10.1103/PhysRevFluids.6.023604).
- Van Atta, C. W. & J. Park (1972). "Statistical Self-Similarity and Inertial Subrange Turbulence". *Statistical Models and Turbulence*. Ed. by M. Rosenblatt & C. Van Atta. Red. by

- J. Ehlers, K. Hepp, & H. A. Weidenmüller. Vol. 12. Lecture Notes in Physics. Berlin, Heidelberg: Springer Berlin Heidelberg, pp. 402–426. ISBN: 978-3-540-05716-1. DOI: [10.1007/3-540-05716-1_23](https://doi.org/10.1007/3-540-05716-1_23).
- Van Dongen, P. G. J. & M. H. Ernst (1985). “Dynamic Scaling in the Kinetics of Clustering”. *Physical Review Letters* 54.13, pp. 1396–1399. DOI: [10.1103/PhysRevLett.54.1396](https://doi.org/10.1103/PhysRevLett.54.1396).
- Van Hooft, J. A., S. Popinet, C. C. van Heerwaarden, S. J. A. van der Linden, S. R. de Roode, & B. J. H. van de Wiel (2018). “Towards Adaptive Grids for Atmospheric Boundary-Layer Simulations”. *Boundary-Layer Meteorology* 167.3, pp. 421–443. ISSN: 1573-1472. DOI: [10.1007/s10546-018-0335-9](https://doi.org/10.1007/s10546-018-0335-9).
- Vanyan, P. L. (1996). “Universality of Probability Distribution of Turbulent Energy Dissipation Rate”. *Oceanographic Literature Review* 5.44, p. 428. ISSN: 0967-0653. URL: <https://www.infona.pl/resource/bwmeta1.element.elsevier-3f397634-4bfb-309e-b45e-8ec4d6227ac8> (visited on 08/05/2021).
- Versteeg, H. K. & W. Malalasekera (2007). An Introduction to Computational Fluid Dynamics. Essex, England: Pearson Education Limited.
- Villermaux, E. (2007). “Fragmentation”. *Annual Review of Fluid Mechanics* 39.1, pp. 419–446. ISSN: 0066-4189. DOI: [10.1146/annurev.fluid.39.050905.110214](https://doi.org/10.1146/annurev.fluid.39.050905.110214).
- (2020). “Fragmentation versus Cohesion”. *Journal of Fluid Mechanics* 898. ISSN: 0022-1120, 1469-7645. DOI: [10.1017/jfm.2020.366](https://doi.org/10.1017/jfm.2020.366).
- Villermaux, E. & B. Bossa (2011). “Drop Fragmentation on Impact”. *Journal of Fluid Mechanics* 668, pp. 412–435. ISSN: 0022-1120. DOI: [10.1017/S002211201000474X](https://doi.org/10.1017/S002211201000474X).
- Villermaux, E., P. G. M. Marmottant, & J. Duplat (2004). “Ligament-mediated spray formation”. *Physical Review Letters* 92.7, pp. 074501–074501. ISSN: 0031-9007. DOI: [10.1103/PhysRevLett.92.074501](https://doi.org/10.1103/PhysRevLett.92.074501).
- Villermaux, E. & B. Bossa (2009). “Single-Drop Fragmentation Determines Size Distribution of Raindrops”. *Nature Physics* 5.9, pp. 697–702. ISSN: 1745-2473. DOI: [10.1038/nphys1340](https://doi.org/10.1038/nphys1340).
- Vledouts A., Vandenberghe N., & Villermaux E. (2015). “Fragmentation as an Aggregation Process”. *Proceedings of the Royal Society A: Mathematical, Physical and Engineering Sciences* 471.2184, p. 20150678. DOI: [10.1098/rspa.2015.0678](https://doi.org/10.1098/rspa.2015.0678).
- (2016). “Fragmentation as an Aggregation Process: The Role of Defects”. *Proceedings of the Royal Society A: Mathematical, Physical and Engineering Sciences* 472.2185, p. 20150679. DOI: [10.1098/rspa.2015.0679](https://doi.org/10.1098/rspa.2015.0679).
- Von Smoluchowski, M. (1917). “Versuch Einer Mathematischen Theorie Der Koagulationskinetik Kolloider Lösungen”. *Zeitschrift für Physikalische Chemie* 92, pp. 129–168. URL: <http://adsabs.harvard.edu/abs/1916ZPhy...17..557S> (visited on 01/17/2019).
- Wang, K. T. & C. F. Lee (2007). “Modeling Droplet Breakup Processes in Bio-Fuel Diesel Engines under Micro-Explosion Conditions”. 20th Annual Conference on Liquid Atomization and Spray Systems. ILASS Americas. Chicago IL., p. 8.
- Weber, C. (1931). “Zum Zerfall eines Flüssigkeitsstrahles”. *Zeitschrift für Angewandte Mathematik und Mechanik* 11.2, pp. 136–154. ISSN: 00442267, 15214001. DOI: [10.1002/zamm.19310110207](https://doi.org/10.1002/zamm.19310110207).
- Wilcox, D. C. (1993). Turbulence Modeling for CFD. La Canada, CA, USA: DCW Industries.
- Wilkinson, J. P. & J. W. Jacobs (2007). “Experimental Study of the Single-Mode Three-Dimensional Rayleigh-Taylor Instability”. *Physics of Fluids* 19.12, p. 124102. ISSN: 1070-6631, 1089-7666. DOI: [10.1063/1.2813548](https://doi.org/10.1063/1.2813548).

BIBLIOGRAPHY

- Wilson, R. J., P. A. Delamere, F. Bagenal, & A. Masters (2012). "Kelvin-Helmholtz Instability at Saturn's Magnetopause: Cassini Ion Data Analysis". *Journal of Geophysical Research: Space Physics* 117.A3. ISSN: 2156-2202. DOI: [10.1029/2011JA016723](https://doi.org/10.1029/2011JA016723).
- Witek, M. L., D. J. Diner, & M. J. Garay (2016). "Satellite Assessment of Sea Spray Aerosol Productivity: Southern Ocean Case Study". *Journal of Geophysical Research: Atmospheres* 121.2, pp. 872–894. ISSN: 2169-8996. DOI: [10.1002/2015JD023726](https://doi.org/10.1002/2015JD023726).
- Wyngaard, J. C. & Y. H. Pao (1972). "Some Measurements of the Fine Structure of Large Reynolds Number Turbulence". *Statistical Models and Turbulence*. Ed. by M. Rosenblatt & C. Van Atta. Red. by J. Ehlers, K. Hepp, & H. A. Weidenmüller. Vol. 12. *Lecture Notes in Physics*. Berlin, Heidelberg: Springer Berlin Heidelberg, pp. 384–401. ISBN: 978-3-540-05716-1. DOI: [10.1007/3-540-05716-1_22](https://doi.org/10.1007/3-540-05716-1_22).
- Yaglom, A. M. (1981). "Laws of Small-Scales Turbulence in Atmosphere and Ocean (in Commemoration of the 40th Anniversary of the Theory of Locally Isotropic Turbulence)". 17.919.
- Yang, H. Q. (1992). "Asymmetric Instability of a Liquid Jet". *Physics of Fluids A: Fluid Dynamics* 4, pp. 681–689. DOI: [10.1063/1.858287](https://doi.org/10.1063/1.858287).
- Yazar, A. (1984). "Evaporation and Drift Losses from Sprinkler Irrigation Systems under Various Operating Conditions". *Agricultural Water Management* 8.4, pp. 439–449. ISSN: 0378-3774. DOI: [10.1016/0378-3774\(84\)90070-2](https://doi.org/10.1016/0378-3774(84)90070-2).
- Zandian, A., W. A. Sirignano, & F. Hussain (2017). "Planar Liquid Jet: Early Deformation and Atomization Cascades". *Physics of Fluids* 29.6, p. 062109. ISSN: 1070-6631, 1089-7666. DOI: [10.1063/1.4986790](https://doi.org/10.1063/1.4986790).
- Zhang, B., S. Popinet, & Y. Ling (2020). "Modeling and Detailed Numerical Simulation of the Primary Breakup of a Gasoline Surrogate Jet under Non-Evaporative Operating Conditions". *International Journal of Multiphase Flow* 130, p. 103362. DOI: [10.1016/j.ijmulflo.2020.103362](https://doi.org/10.1016/j.ijmulflo.2020.103362).

Appendix A

Estimation of the sheet thickness in the region of the jet head

This appendix presents the formula and related derivation used in Sec. 4.3.2.2 to estimate the thickness of the sheet in the region of the jet head. The presentation is split within three parts. A simple model of the jet head development is presented first, Sec. A.1. Then the sheet thickness at its foot (the connection region between the sheet and the liquid core) and at its edge are theoretically derived, respectively in Sec. A.2 and Sec. A.3.

A.1 A simple model of the jet head development

Fig. A.1 gives a schematic representation of the jet head development. In the initial stage, Fig. A.1a, the jet is supposed to be a liquid semi infinite cylinder translating at a velocity U_{inj} in a quiescent gaseous medium at a pressure P_∞ . Due to the cylinder motion, an overpressure region is created at its upstream face and, in order to respect the local pressure equilibrium, is counterbalanced by an underpressure region surrounding the cylinder lateral face. This pressure difference compresses the layer of fluid behind the upstream face and imposes a radial motion to the fluid particles located in this area. The jet head thus deforms and shows a thin radial corrugation, Fig. A.1b. It appears legitimate here to assume that the corrugation thickness along the longitudinal direction, \vec{x} , is only set by the pressure equilibrium and is similar to the one in the compressed layer of liquid. This corrugation in turn triggers the development of the vortex ring. At this stage, the radial corrugation can extend with a radial velocity set by the vorticity of the recirculation region. The recirculation region, or equivalently the vortex ring, then radially extends along with the head sheet. The extension of both goes together. Due to the vortex ring, the gas motion is parallel to the head sheet and directed outwards. This imposes on the sheet some shear directed along the radial direction, \vec{r} , which benefits to the sheet extension and makes the ring extend too. During its extension, the sheet gets thinner until it undergoes piercing due to the Taylor Culick instability. At this development stage, the expansion stops and both the jet head and the vortex ring reach a steady dynamical behaviour and a stationary radial size, Fig. A.1c.

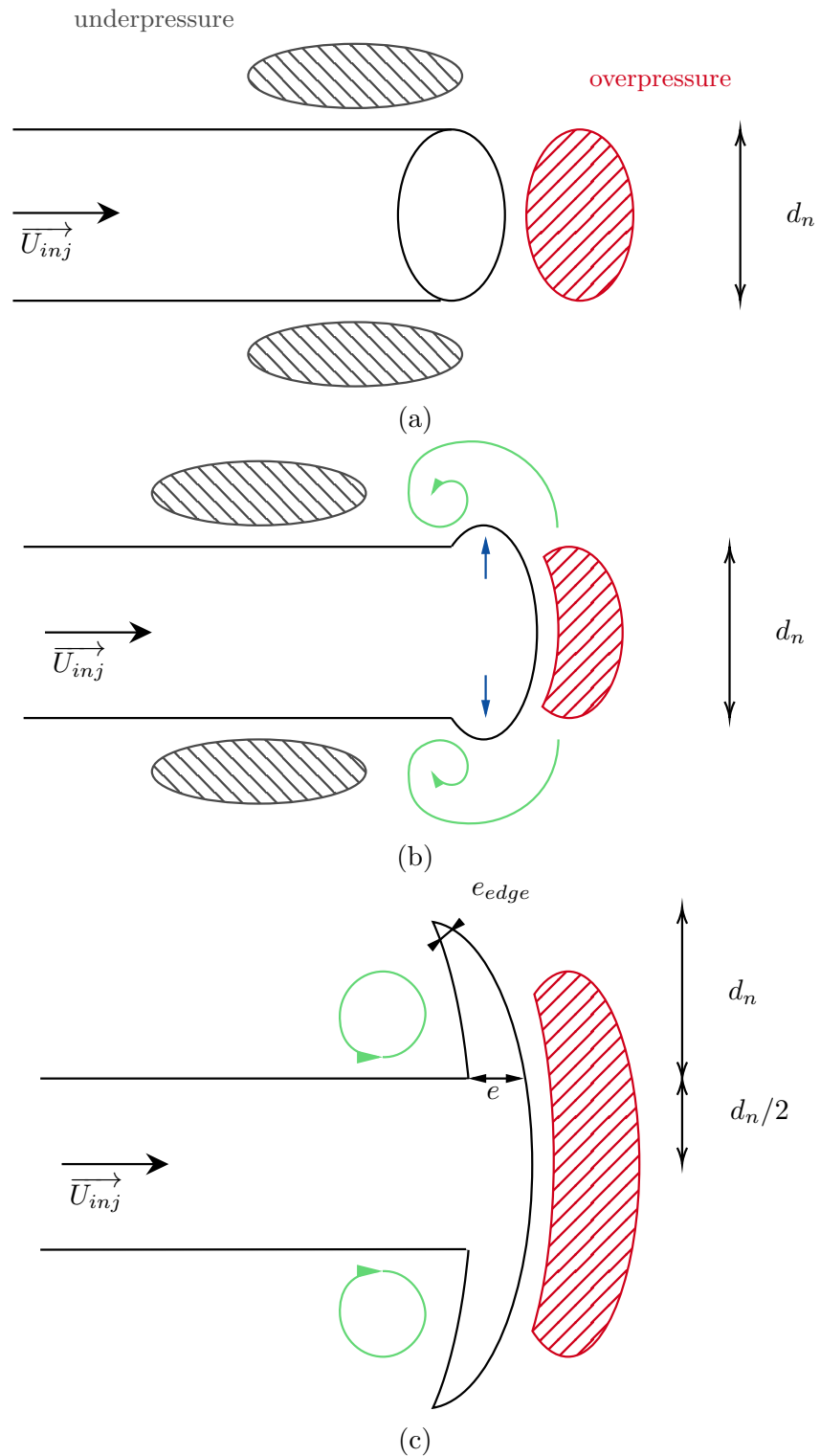


Figure A.1: Schematic representation of a simple model for the jet head development: (a) theoretical initial state, (b) trigger of the head expansion and (c) developed head sheet.

A.2 Estimation of the sheet thickness at its feet

Consider a control volume \mathcal{V} at the initial development stage explained above. This control volume is located behind the upstream face of the semi-infinite cylinder. Fig. A.2 gives a schematic representation of \mathcal{V} and the pressures applied on its faces. The pressures at play are:

- the Laplace pressure ΔP_σ applying on face 4,
- the dynamic pressure of the gas $P_{dyn,g}$ applying on face 3 and of the liquid $P_{dyn,l}$ applying on faces 1 and 3,
- the total upstream pressure P_{up} applying on face 3,
- the pressure on the lateral face P_{lat} , applying on face 4.

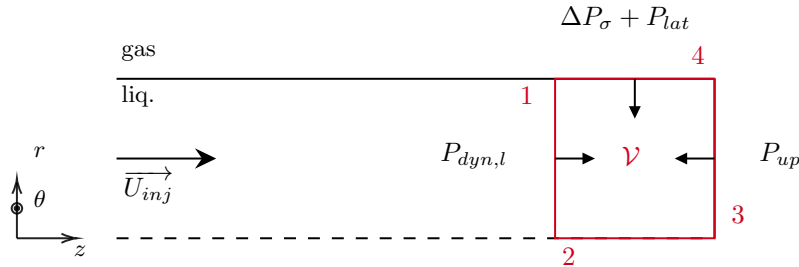


Figure A.2: Schematic representation of the cylinder jet at the stage (a) with the different pressures at play in the control volume. The dashed line represents the jet axis.

The expression of the liquid dynamic pressure is straightforward and writes as $P_{dyn,l} = 1/2\rho_l U_{inj}^2$. The dynamic pressure of the gas corresponds to the overpressure depicted previously and depends on $P_{dyn,l}$. It takes into account the drag applied on the upstream face through the drag coefficient C_x and writes as $P_{dyn,g} = C_x P_{dyn,l}$. The pressure applied on the upstream face of the cylinder is then the sum of the two dynamic pressures, $P_{up} = P_{dyn,l} + P_{dyn,g}$. In order to respect the local pressure equilibrium, the pressure on the lateral face is such that $P_{lat} \in [-P_{dyn,g}, 0]$. Finally, the Laplace pressure depends on the surface tension σ and the local curvature set by the curvature radii along \vec{x} and \vec{r} . It writes as $\Delta P_\sigma = \sigma R_x^{-1}$ for a cylinder along the x -axis and as $\Delta P_\sigma = \sigma(R_x^{-1} + R_r^{-1})$ when the cylinder is deformed like in Fig. A.3. Note that the pressures applying on face 2 are compensated due to the axisymmetry of the configuration.

The pressure difference between the faces 1 and 3, along the x -axis, writes as:

$$\begin{aligned}\Delta P_{dyn} &= P_{up} - P_{dyn,l} \\ \Delta P_{dyn} &= P_{dyn,g},\end{aligned}\tag{A.1}$$

thus, imposing a backward motion on the face 3 which, in turn, deforms the face 4 due to the fluid incompressibility. At the equilibrium, the pressures would verify $\Delta P_{dyn} = \Delta P_\sigma + P_{lat}$. The face 4 of the control volume then deforms if

$$\Delta P_{dyn} \geq \Delta P_\sigma + P_{lat}.\tag{A.2}$$

Let us denote e the thickness along x of the volume control \mathcal{V} . Complementary, assume that the upstream face is homogeneously pushed backward due to the pressure difference along the x axis, which creates an initial deformation. We also assume that this initial deformation has

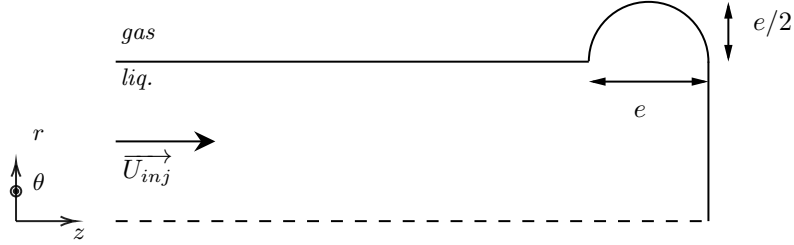


Figure A.3: Schematic representation of the initial deformation of the cylinder jet head.

an annular shape with a circular section of radius $e/2$, as illustrated in Fig. A.3. The curvature radii of the disturbed interface are then $R_x = d_n/2$ and $R_r = e/2$. The inequality A.2 then becomes

$$\begin{aligned}
P_{dyn,g} &> \sigma \left(\frac{2}{e} + \frac{2}{d_n} \right) + P_{lat} \\
\Leftrightarrow \frac{1}{2} \rho_g U_{inj}^2 C_x - P_{lat} &> 2\sigma \frac{d_n + e}{ed_n} \\
\Leftrightarrow \frac{1}{4} \frac{\rho_g U_{inj}^2 d_n}{\sigma} C_x - \frac{d_n}{2\sigma} P_{lat} &> \frac{d_n + e}{e} \\
\Leftrightarrow \frac{1}{4} We_g C_x - \frac{d_n}{2\sigma} P_{lat} &> \frac{d_n}{e} + 1 \\
\Leftrightarrow \frac{1}{4} \left[We_g C_x - 4 \frac{d_n}{2\sigma} P_{lat} - 4 \right] &> \frac{d_n}{e} \\
\Leftrightarrow 4 \left[We_g C_x - \frac{2d_n}{\sigma} P_{lat} - 4 \right]^{-1} &< \frac{e}{d_n} \tag{A.3}
\end{aligned}$$

Consider the corner between the faces 3 and 4. The pressure difference should be maximal at this position, when the disturbance starts to develop with the lateral pressure respecting $P_{lat} = -P_{dyn,g}$. Meanwhile the lower bound of e/d_n is minimal. Using this, Eq. A.3 rewrites as

$$\left[\frac{We_g C_x}{2} - 1 \right]^{-1} < \frac{e}{d_n}. \tag{A.4}$$

This condition thus sets an estimation of the minimum thickness e for which the difference of dynamical pressures overcomes the Laplace pressure and deforms the lateral surface of the cylinder. Considering $We_g = 100$ and $C_x = 0.4$ gives $e/d_n = 0.053$, i.e. a thickness approximately equal to 5% of the nozzle diameter d_n .

Assume that the jet is in a quasi steady regime. The previous calculation can be modified by considering the pressure to be at the equilibrium

$$P_{dyn,g} = \sigma \left(\frac{2}{e} + \frac{2}{d_n} \right) + P_{lat} \tag{A.5}$$

$$\Leftrightarrow \frac{e}{d_n} = 4 \left[We_g C_x - \frac{2d_n}{\sigma} P_{lat} - 4 \right]^{-1} \tag{A.6}$$

which gives the evolution of the feet thickness depending on the lateral pressure $P_{lat} \in [-P_{dyn,g}, 0]$. The normalised thickness is maximum when the lateral pressure is zero and minimum when the lateral pressure reaches its maximum. When $P_{lat} = 0$, e/d_n equals 0.11 and the thickness of the disturbance foot can not exceed this value. A limitation of the previous calculation is that the model does not account for any curvature between the upstream side of the disturbance and the rest of the jet, while such a curvature is observed experimentally. This results will be used in the following section to derive an expression of the sheet thickness at its edge.

A.3 Estimation of the sheet thickness at its edge

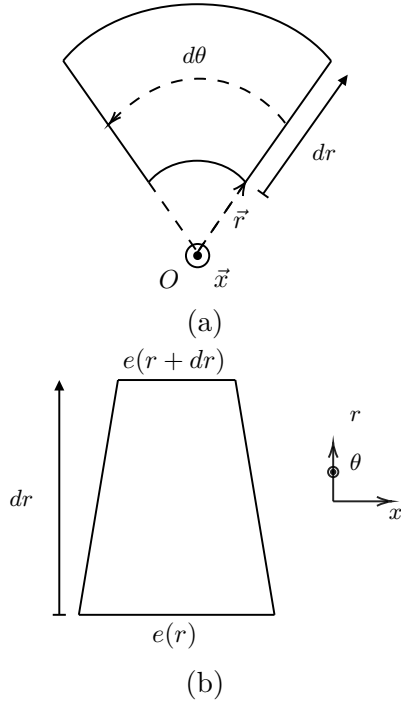


Figure A.4: Scheme of an infinitesimal element in cylindrical coordinates in the (r, θ) plane (a) and in the (x, r) plane (b).

Let us consider a plane circular sheet of center O with a cylindrical coordinate system centered on O . Fig. A.4 illustrates an infinitesimal element at a distance r from the center. The flow is directed from the center toward the edge of the sheet which extends from $r = r_0$ to $r = r_{max}$. The disk of center O and radius r_0 represents the jet core and $r_0 = d_n/2$. The thickness and surface of face and the velocity at the face are denoted $e(r)$, $S(r)$ and $U(r)$. By definition, the surfaces read

$$S(r) = e(r)r d\theta, \quad (\text{A.7})$$

$$(\text{A.8})$$

The conservation of mass flow between the two faces imposes

$$U(r)S(r) = U(r + dr)S(r + dr) \quad (\text{A.9})$$

$$\Leftrightarrow U(r)e(r)rd\theta = U(r + dr)e(r + dr)(r + dr)d\theta \quad (\text{A.10})$$

$$\Leftrightarrow \frac{U(r)}{U(r + dr)}e(r)r = e(r + dr)(r + dr). \quad (\text{A.11})$$

The surface of the flow evolving freely, one can assume that $U_i/U_o = 1$

$$re(r) = (r + dr)e(r + dr). \quad (\text{A.12})$$

Additionally, $(r + dr)e(r + dr)$ can be expressed thanks to a polynomial approximation at the first order such that:

$$(r + dr)e(r + dr) = re(r) + \frac{d(re(r))}{dr}dr, \quad (\text{A.13})$$

with Eq. A.12 it comes

$$\frac{d(re(r))}{dr} = 0 \Leftrightarrow e(r) = \frac{C}{r} \quad (\text{A.14})$$

with C a real constant. Let us denote e the thickness at the sheet foot, $r = r_0$. C can be expressed as $C = er_0$. The thickness of the sheet edge at $r = r_{max}$, denoted e_{edge} , finally writes

$$\frac{e_{edge}}{e} = \frac{r_0}{r_{max}} \quad (\text{A.15})$$

where $r_0 = d_n/2$ by definition. In the numerical experiments, the front sheet shows an unsteady behavior partly due to the development of Taylor Culick instabilities. If the maximal sheet extension is assumed to the extension such that the latter instabilities are not yet triggered, r_{max} can be estimated to be approximately equal to $3d_n/2$. Using this estimations gives $e_{edge}/e = 1/3$.

Combining Eq. A.15 and the expression of e/d_n obtained in the last section, Eq. A.6, it is possible to derive an analytical expression of the sheet thickness depending on d_n . It reads

$$\frac{e_{edge}}{d_n} = \frac{4 r_0}{r_{max} [We_g C_x - 2P_{lat} d_n / \sigma - 4]} \quad (\text{A.16})$$

Using the estimated maximal radial extension of the sheet while assuming that $P_{lat} = P_{dyn,g}$, the latter expression becomes:

$$\frac{e_{edge}}{d_n} = \frac{2/3}{We_g C_x - 2} \quad (\text{A.17})$$

With $We_g = 100$ and $C_x = 0.4$, the sheet thickness in the area where the Taylor Culick instabilities are triggered is such that $e/d_n = 0.0175$. In the numerical experiments the nozzle diameter is such that $d_n = 4.48 \times 10^{-3}$ m and then $e = 7.88 \times 10^{-5}$ m which is of the same order of magnitude as the experimental thickness at which Taylor Culick instabilities can be observed (Néel, 2018).

Abstract

The fragmentation of liquid jets takes place in numerous processes which can be either natural, like ocean sprays, sneezing or volcanic eruption, or industrial, like farming irrigation, ink printing or thermal engine injection. This thesis characterises the droplet population created by the fragmentation of a jet thanks to experimental data and numerical simulations in configurations close to those of agriculture. Experimentally, the data set comes from Droplet Tracking Velocimetry (DTV) measurements carried out prior to this thesis on a turbulent water jet injected into quiescent air. Numerically, a campaign of Direct Numerical Simulations (DNS) is carried out for different gaseous Weber numbers, i.e. different injection velocities in the same geometrical and physical configuration. The statistical study of the droplets for the experimental and numerical data shows results which are rather similar. It pays a specific attention to the joint statistics of the droplet size and velocity. Notably, the joint statistics enable to point out the existence of 5 well defined subgroups of droplets in the experimental data set and the existence of 2 sources of fragmentation in the numerical one. The study highlights the possible link between the subgroups and the different sources of fragmentation identified in the flow. Finally, two theoretical models of divergent nature are tested out to describe the droplet size distribution. The first one was derived from the analysis of the fine mechanics occurring at the scale of ligament-shaped droplets while the second one was derived from the framework of the internal intermittency of turbulence. Both of them propose an accurate description at different levels. The ligament-based model best describes the droplet size distribution in the close field and the distribution of the subgroups in the far field. The overall distribution in the far field is well described by the intermittency-based model, which also describes qualitatively well the size distribution in the close field. Thus, the validity of each model does not only depend on the distance from the nozzle but also on the number of fragmentation sources. Besides, it appears that the concept of turbulence intermittency for modelling the fragmentation process could improve the description of the atomisation of turbulent jets.

Résumé

La fragmentation des jets liquides est au cœur de nombreux processus naturels - création d'embrun, éternuement, éruption volcanique - ou industriels - irrigation agricole, impression à jet ou injection dans les moteurs thermiques. Cette thèse caractérise à l'aide de données expérimentales et de simulations numériques la population de gouttes créée par la fragmentation d'un jet dans des configurations proches de celles de l'agriculture. Du côté expérimental, les données proviennent de mesures vélocimétriques par suivi de gouttes (DTV) réalisées sur un jet d'eau turbulent injecté dans de l'air au repos. Du côté numérique, une série de Simulations Numériques Directes (DNS) a été réalisée pour différents Weber du gaz, c-à-d pour différentes vitesses d'injection avec une configuration géométrique et physique fixées. L'étude statistique des gouttes dans le cas de l'expérience et des simulations montre des résultats qui se corroborent. Une attention particulière est apportée aux statistiques jointes en taille et en vitesse des gouttes. Notamment, les statistiques jointes mettent en évidence l'existence de 5 sous groupes bien définis dans le jeu de données expérimentales et l'existence de 2 sources de fragmentation dans le jeu numérique. L'étude met en lumière le lien possible entre les différents sous groupes et les sources de fragmentation qui peuvent être identifiées dans l'écoulement. Enfin, deux modèles théoriques de nature très éloignée sont testés pour décrire la distribution en taille des gouttes. Le premier découle de la mécanique fine prenant place au niveau des ligaments et le second de l'intermittence interne de la turbulence. Tous deux se montrent pertinents à différents niveaux. Le modèle s'appuyant sur la mécanique des ligaments décrit au mieux la distribution en taille en champ proche et la distribution en taille de chaque sous groupe en champ lointain. La distribution en taille du jet en champ lointain est bien décrite par le modèle s'appuyant sur l'intermittence de la turbulence, modèle qui offre aussi une bonne description qualitative de la distribution en taille de la population en champ proche. Ceci montre que la validité de chaque modèle ne dépend pas seulement de la distance par rapport à la buse mais aussi du nombre de sources de fragmentation. En outre, il ressort qu'utiliser le concept d'intermittence de la turbulence pour modéliser le processus de fragmentation pourrait améliorer la description de l'atomisation des jets turbulents.